

Old Dominion University

## ODU Digital Commons

---

Modeling, Simulation and Visualization Student Past Proceedings of the MSV Student Capstone  
Capstone Conference Conference

---

Apr 19th, 12:00 AM

### Proceedings, MSVSCC 2018

Old Dominion University, Department of Modeling, Simulation & Visualization Engineering

Old Dominion University, Virginia Modeling, Analysis & Simulation Center

Follow this and additional works at: <https://digitalcommons.odu.edu/msvcapstone>



Part of the [Engineering Commons](#)

---

#### Recommended Citation

Old Dominion University. Department of Modeling Simulation & Visualization Engineering, & Virginia Modeling Analysis and Simulation Center. (2018, April 19). Proceedings, MSVSCC 2018. 12th Annual Modeling, Simulation & Visualization (MSV) Student Capstone Conference, Virginia Modeling, Analysis & Simulation Center, Suffolk, VA. 155 pp. <https://doi.org/10.25776/exgd-c079>

This Other is brought to you for free and open access by the Virginia Modeling, Analysis & Simulation Center at ODU Digital Commons. It has been accepted for inclusion in Modeling, Simulation and Visualization Student Capstone Conference by an authorized administrator of ODU Digital Commons. For more information, please contact [digitalcommons@odu.edu](mailto:digitalcommons@odu.edu).

# MISVISC

MODELING. SIMULATION. VISUALIZATION.

THE 12TH ANNUAL  
STUDENT  
CAPSTONE  
CONFERENCE  
April 19, 2018  
VMASC, SUFFOLK, VA 2018



## PROCEEDINGS



# VMASC



The Virginia Modeling, Analysis and Simulation Center (VMASC) is a university-wide multidisciplinary research center that emphasizes modeling, simulation, and visualization (MS&V) research, development and education.

VMASC is one of the world's leading research centers for computer modeling, simulation, and visualization. The mission of the Center is to conduct collaborative MS&V research and development, provide expertise to government agencies and industry, and to promote Old Dominion University, Hampton Roads and Virginia as a center of MS&V activities. Working with more than one hundred industry, government, and academic members, VMASC furthers the development and applications of modeling, simulation and visualization as enterprise decision-making tools to promote economic, business, and academic development. Annually, the Center conducts approximately \$10M in funded research.

Old Dominion University is a state-assisted institution and one of only four Virginia schools in the Carnegie Research Universities (high research activity) category. The University offers a complete range of Modeling & Simulation degree options from Bachelor's to Ph.D.

The Hampton Roads region is home to the Joint and Coalition Training (JCW), the US Army's Training and Doctrine Command, the Military Transportation Management Command, NATO Allied Command Transformation, the Armed Forces Staff College, the U.S. Navy's Commander Operational Test and Evaluation Force, the Naval Sea Systems Command, and the Space and Naval Warfare Center. In addition, the Department of Energy's Jefferson Lab, NASA-Langley Research Center and numerous regional industries are important users of MS&V technology. The economic value of MS&V-related business activity in Hampton Roads is estimated to be over \$500M.

VMASC concentrates on eight core modeling and simulation applied research areas:

- Transportation
- Homeland Security and Military Defense
- Virtual Environments
- Social Sciences
- Medicine & Health Care
- Game-based Learning
- M&S Interoperability
- System Sciences



# STUDENT CAPSTONE CONFERENCE

## MSVE

VMASC relocated to its new facility located at 1030 University Boulevard, Suffolk, VA on September 24, 2007. The Center also maintains an additional location on the main ODU campus in the Engineering and Computational Sciences building.

The Suffolk facility includes a multi-purpose computer laboratory with both Windows-based and Linux-based workstations for computer simulation development, labs dedicated to transportation, computational science, game-based learning, and a virtual simulator lab supporting live, virtual, and constructive simulation integration.

The main VMASC facility primarily supports military, defense and homeland security, social science, medical, computational science, and enterprise engineering research efforts plus administrative and program support. The facility on campus consists of approximately 6,000 square feet of lab space including two general-purpose labs, a visualization lab, a human factors lab, and a 74-seat virtual reality theater supporting both research and teaching requirements. This facility primarily supports the Center's visualization and medical research and development. It also serves as the on-campus presence for VMASC with linkages to the other departments throughout the university.

### The MSVE Department

Engineering and Computational Sciences Building on the Old Dominion University Norfolk Campus. In addition to the department and faculty offices, this facility also houses several instructional and research laboratories, a virtual reality theater, and a four-walled C.A.V.E. (Cave Automatic Virtual Environment). A significant resource to the department is the Virginia Modeling, Analysis and Simulation Center located adjacent to the University's Tri-Cities Higher Education Center in Suffolk, Virginia. VMASC occupies a two-story 60,000 square foot building designed to support state-of-the-art research in modeling, simulation and visualization. Some of the center's facilities are used in the department's educational programs; in addition, VMASC researchers teach courses and mentor students in the department's academic programs.







# KEYNOTE SPEAKER



## *Kane Crisler*

has studied graduate level Physics, Mathematics and Electrical/Communications Engineering. Kane is a former research scientist at AMRDEC US Government Laboratory, and served in Federal Law Enforcement. Presently, Kane is an Design Engineer and international lecturer in matters related to Cyber Security and RF communications. When not working, Kane can be found Skydiving, B.A.S.E. Jumping, Scuba Diving,

### **KEYNOTE: Understanding Host without Agent-Software: Packet Analysis Tools for Hunting**

Many of today's security applications require a distributed software-agent. From Anti-Virus to Operating System monitoring and management through proprietary protocols or Windows Powershell scripts. These tools are installed to monitor and report host behavior. Behaviors range from scanning a white-list of approved applications for installation to monitoring disk space. What happens when a machine is compromised, and the software-agent can no longer be trusted? What happens when the Operating System can no longer be trusted to report valid information about hardware peripherals, RAM and Disk Space? What happens when the code signing repository has keys added by an attacker?

Through packet analysis techniques, we remove the trust the self-reporting state of the software-agent and only rely on packets flowing over the network infrastructure. For in network band exfiltration and command and control, information must flow over network infrastructure. Monitoring the infrastructure and packet analysis using Deep Packet Inspection techniques allows a more insightful look into behavior than port based firewalls. Although many available Intrusion Detection Systems (IDS) and Intrusion Prevention Systems (IPS) exist, these systems are only as good as the rule sets and Yara configurations that defined them. How can better protect system from threats that have not been seen thousands of times before?

We do not rely on the subscription based rules alone, we hunt in our own networks, applying security based attack considerations to an internally massed big data set.

The tracks that the papers were divided up into included the following:

- Agent Based Modeling
- Gaming & Virtual Reality
- General Sciences & Engineering
- Transportation, Infrastructure Security & Military Application
- Medical Simulation

For each track there were awards given out: The Best Paper award, and the Best Presentation Award. Those recipients for best paper are listed below by track.

## **General Sciences & Engineering**

Brandon Waddell and James Leathrum: "Multi-Threaded Simulation Executive for Multi-Core Processors"

Saturnina Nisperos and Frederick Mckenzie: "A Sustainability Assessment Model for Crop Rotation Alternatives"

## **Transportation, Infrastructure Security & Military Application:**

Billingsley Pogue, Paulo Almeida, Andre Bergstein and Marisa Reyes: "Discrete Event Simulation and Analysis of the Plating Facility at the Corpus Christi Army Depot"

## **Medical Simulation:**

Thomas Tracey, John Asija, Brian Dilinila, Minh Dong, Michael Poteat, Jacob Richardson and Jake Webster: "Medical Workstation Evaluation Process"





### **Overall Best Paper- The Gene Newman Award**

The overall best paper is awarded the Gene Newman award. This award was established by Mike McGinnis in 2007; the award is given for overall best presentation, best paper, and research contribution. The Gene Newman Award for Excellence in M&S Research is an award that honors Mr. Eugene Newman for his pioneering effort in supporting and advancing modeling and simulation. Mr. Newman played a significant role in the creation of VMASC by realizing the need for credentialed experts in the M&S workforce, both military and industry. His foresight has affected both the economic development and the high level of expertise in the M&S community of Hampton Roads. The Students receiving this award will have proven themselves to be outstanding researchers and practitioners of modeling and simulation.

For the 2018 Student Capstone Conference, The Gene Newman Award went to:

***Daniel Perez***, for his paper entitled '*Deep Learning for Effective Quantification of Seagrass in Coastal Areas.*'



**PAGE 1** **AGENT BASED MODELING**

**PAGE 5** **GAMING & VIRTUAL REALITY**

**PAGE 10** **GENERAL SCIENCES & ENGINEERING**

**PAGE 88** **MEDICAL SIMULATION**

**PAGE 132** **TRANSPORTATION, INFRASTRUCTURE SECURITY, & MILITARY**



# STUDENT CAPSTONE CONFERENCE

2018

## AGENT BASED MODELING

- Page 2 Sara Simmons and Holly Graff  
***Old Dominion University***  
Agent-Based Modeling of Host-Vector-Pathogen Systems
- Page 4 Joshua Hastey  
***Old Dominion University***  
Power Shifts, Faits Accomplis, and Incomplete Information

# AGENT-BASED MODELING OF HOST-VECTOR-PATHOGEN SYSTEMS

Sara A Simmons  
Department of Biological Sciences  
Old Dominion University  
Norfolk, VA, US  
smcdo010@odu.edu

Holly D Gaff  
Department of Biological Sciences  
Old Dominion University  
Norfolk, VA, US  
hgaff@odu.edu

## ABSTRACT

The emergence of new tick-borne pathogens presents a potential increase in human infection risk that can be linked to tick vector range expansions. TICKSIM, an agent-based model designed in NetLogo, has provided a basis for exploring host-vector-pathogen dynamics and an opportunity to test the effects of different variables on the establishment of tick populations in new areas. An agent-based modeling approach is ideal for simulating interactions between individuals to capture the effects of these interactions on the system as a whole. Here we propose a modification of the TICKSIM model that integrates tick and pathogen genetics in a multi-host system to explore the potential co-evolutionary dynamics between these species. This model will provide insights to researchers seeking to reconstruct the history of range expansions and understand how new invasions influence pathogen prevalence and diversity.

**Keywords:** Agent-based modeling, range expansion, invasion biology, pathogen dynamics

## 1 INTRODUCTION

Tick range expansions have the potential to introduce new pathogen species to an area, which can then pose an infection risk to humans and other animals (Nadolny et al. 2011). This occurs when a small number of ticks attached to a host disperse across the landscape, drop off in a new location, and become the founders of a new tick population. Reconstructing the history of new introductions by gene flow analyses can help determine a point of origin. For example, haplotype networks use genetic information from a population sample to quantify relatedness of ticks within a population and show connectivity between populations. This technique has been useful in tracking the range expansions of some species, whereas results have been ambiguous for other species (Nadolny et al. 2015).

Agent-based modeling is a modeling approach in which agents operate autonomously within specified parameters (Sokolowski and Banks 2009). This approach is useful for modeling complex systems where agents model organisms driven by different cues and motivations. An example of this type of complex, multi-species system is the model TICKSIM, an agent-based model designed in NetLogo. TICKSIM is single host-parasite model that predicts prevalence of a tick-borne pathogen *Ehrlichia chaffeensis* under variable conditions (Gaff 2011). TICKSIM was modified to determine the minimum viable number of ticks to establish a new population was ten (Nadolny and Gaff 2013). A later version of the model introduced haplotype-tracking to track the genetic diversity in a population resulting from a founding haplotype (Nadolny and Gaff 2017). This model removes the pathogen prevalence component of the TICKSIM model with the intent to reincorporate this into future models (Nadolny and Gaff 2017).

Tick populations may persist in suitable environments, but changes in habitat, such as transitions from open meadows to forest appears change population and infection dynamics in some species. For this reason, a third unpublished model based on TICKSIM code incorporates dynamic change in host numbers as a consequence of habitat change to simulate this effect. Currently, an integrated model is needed to



reincorporate infection dynamics and to add more meaningful variability to host dynamics, such as population size and trends. This will improve the user's ability to calibrate the model for specific habitat types and to simulate change over time.

## 2 PROPOSED METHODOLOGY

The proposed model will reincorporate infection dynamics, improve the dynamic host population component, and introduce genotypes for the pathogen *Rickettsia parkeri*. Interactions can occur between several agents: hosts, ticks, and pathogens under varied initial conditions. Both ticks and pathogens will be tracked by lineage, a network of related individuals, across multiple instances of infection and subsequent transmission. The parameters that influence genetic structure of *Amblyomma maculatum*, the tick vector, and *R. parkeri* will be identified and tested with sensitivity analyses. These will be validated with real-world data from infected *A. maculatum* collected from island populations presumed to be isolated. Comparative analyses will determine whether the relative rate of change in the tick vector and the pathogen are comparable when both are introduced into the system together in an initial founding event. The model will be validated through comparison with internationally-collected data from closely related tick and pathogen systems. Statistical analyses will incorporate common measures of genetic diversity and structure.

## 3 EXPECTED RESULTS

The simulation will yield estimates of *R. parkeri* prevalence in hosts and genetic variation of *R. parkeri* based on initial genotypes. The degree of genetic change in *R. parkeri* lineages after a series of interactions between hosts and vectors is expected to be proportionate to the degree of genetic variation in the vector species *A. maculatum* regardless of host population dynamics. Results from the validated model will be used to select appropriate genetic analyses to study co-evolution between ticks and pathogens. These results should also illuminate mechanisms that consistently influence prevalence patterns.

## REFERENCES

- Gaff, H.D. 2011. "Preliminary analysis of an agent-based model for tick-borne disease." *Mathematical Biosciences and Engineering*, vol. 8(2), pp. 463-473.
- Gaff, H.D., and R.M. Nadolny. 2013. "Identifying requirements for the invasion of a tick species and tick-borne pathogen through TICKSIM." *Mathematical Biosciences and Engineering* vol. 10(3), pp. 625-635.
- Nadolny, R.M., C.L. Wright, W.L. Hynes, D.E. Sonenshine, and H.D. Gaff. 2011. "*Ixodes affinis* (Acari:Ixodidae) in southeastern Virginia and implications for the spread of *Borrelia burgdorferi*, the agent of Lyme disease." *Journal of Vector Ecology*, vol. 36(2), pp. 464-467. Available at: <http://dx.doi.org/10.1111/j.1948-7134.2011.00191.x>
- Nadolny, R., H. Gaff, J. Carlsson, and D. Gauthier. 2015. "Comparative population genetics of two invading ticks: Evidence of the ecological mechanisms underlying tick range expansions." *Infection, Genetics, and Evolution* 35:153-162. Available at: <http://dx.doi.org/10.1016/j.meegid.2015.08.009>
- Nadolny R., and H. Gaff. 2017. "Modeling the effects of habitat and host on tick invasions." *Letters in Biomathematics* vol. 5(1), pp. 2-29. Available at: <https://doi.org/10.1080/23737867.2017.1412811>
- Sokolowski J.A. , and C.M. Banks. 2009. "Agent - based modeling and social networks." In *Modeling and Simulation for Analyzing Global Events*, edited by Sokolowski J.A. , and C.M. Banks, pp. 63-79. Hoboken, NJ, John Wiley & Sons.

# **POWER SHIFTS, *FAITS ACCOMPLISH*, AND INCOMPLETE INFORMATION**

Joshua Hastey  
Graduate Program in International Studies  
Old Dominion University  
7045 Batten Arts & Letters  
Norfolk, VA, USA  
jhastey@odu.edu

## **ABSTRACT**

The fait accompli is an understudied form of low-intensity conflict. The unilateral revisions to the de facto status quo employed in Crimea and the Spratly Islands serve to highlight the longstanding importance of faits accomplis and raise important questions. When do faits accomplis trigger war or unilateral concessions? What conditions increase the likelihood of faits accomplis? This study is the first to establish conditions under which shifts in the distribution of power increase the likelihood of faits accomplis. It is also the first study to examine how faits influence the conditions under which such shifts are lead to preventive war or strategic concessions. The analysis demonstrates that accounting for faits accomplis weakens the conditions necessary for war presented in leading bargaining models of war. It also outlines several conditions that generate peaceful shifts, preventative war by the declining power, and opportunistic war by the rising power.



# STUDENT CAPSTONE CONFERENCE

2018

## GAMING & VIRTUAL REALITY

Page 6 Katherine Smith, Yuzhong Shen and Anthony Dean  
***Old Dominion University***  
Diegesis in Games for STEM Education

Page 8 Zinat Afrose and Yuzhong Shen  
***Old Dominion University***  
Parallelization of Adaptive Vector Median Filter for Point Cloud Denoising



# **DIEGESIS IN GAMES FOR STEM EDUCATION**

Katherine Smith, Yuzhong Shen, and Anthony Dean  
Department of Modeling, Simulation and Visualization Engineering  
Old Dominion University  
5115 Hampton Boulevard, Norfolk, VA, USA  
k3smith@odu.edu

## **ABSTRACT**

This abstract discusses incorporating educational elements diegetically in Science, Technology, Engineering, and Mathematics (STEM) games. While diegetic implementation enhances player engagement, it is important to balance concerns for player engagement with the goal of presenting material in a way that is clear and correct. In this work, two examples of diegetic implementation of educational elements are discussed.

**Keywords:** STEM education, game development, educational games, diegesis.

## **1 INTRODUCTION**

Developing games for STEM topics in higher education presents a number of challenges (Smith et al. 2017). One of these challenges is to maintain player engagement while simultaneously allowing them to learn and practice STEM concepts. One way to accomplish this is to incorporate educational elements diegetically (Murphy 2011). That is, as elements within the game scene rather than separate elements that are external to the game or part of the user interface. In Captivate, an educational STEM game, educational elements have been incorporated diegetically.

The remainder of this abstract will be organized as follows. First, the Methods section will describe how varying levels of diegesis for educational elements in games can contribute to player engagement. Then, the Results section will present two examples of how educational elements have been incorporated diegetically in a STEM educational game that is currently under development. Finally, the Conclusions and Discussions section will conclude the paper and discuss future work.

## **2 METHODS**

A key concern when incorporating educational game elements is balancing need to engage players with the need to limit player frustration. Sometimes the player may want to obtain information quickly and move on. In this case, a guide book or tutorial may be provided to the player that they can pause the game to reference. Of course, the most engaging way to incorporate educational elements is to have them as elements in the game scene that are part of the narrative. This becomes a challenge for STEM game development as not all educational elements lend themselves to being incorporated directly in the game scene.

## **3 RESULTS**

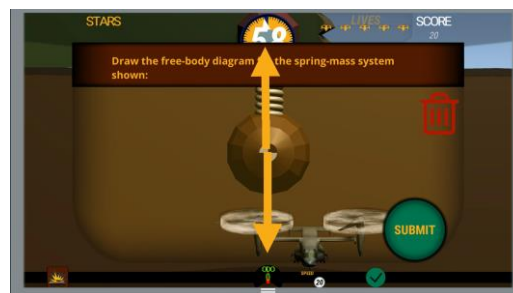
One of the games developed as part of Captivate is Physics Escape (Figure 1a, b). In Physics Escape, the player controls a drone as they try to escape from a damaged building. The drone itself is damaged and so

the player must answer physics questions to earn power ups that allow them to escape. The questions presented are about physics systems in the game world. When the player interacts with these systems, they are presented with a question that is overlaid on the system itself. One task the player must complete is to draw the free-body diagram directly on the system.

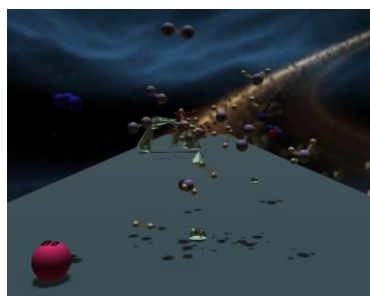
Another game developed for Captivate is Element Roll (Figure 1c, d). In this game, the player rolls through the game as an atomic element. The player can interact with different molecules, atomic particles and obstacles. When the player rolls through a cloud of molecules, they are asked to balance the chemical equation that corresponds to the molecules in the cloud.



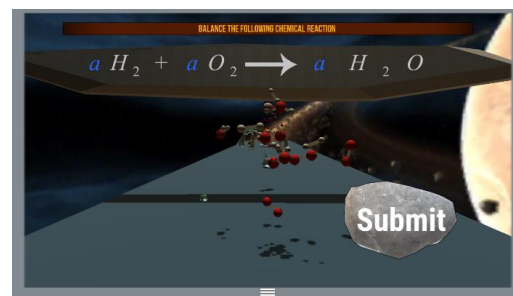
(a)



(b)



(c)



(d)

Figure 1. Physics Escape showing (a) play and (b) a player drawing a free-body diagram on a game object and Element Roll showing (c) play and (d) a question asking the player to balance a chemical reaction.

## 4 CONCLUSIONS AND DISCUSSION

The development of Captivate has involved incorporating educational game elements diegetically to enhance player engagement. Future work entails performing a study to determine the effect of diegesis on student learning.

## ACKNOWLEDGEMENT

This paper, and its associated research, was made possible through the Office of Naval Research STEM under ONR GRANT11899718.

## REFERENCES

- Murphy, Curtiss. 2011. "Why Games Work — the Science of Learning." *Modsim World 2011*.
- Smith, Katherine et al. 2017. "Overcoming Challenges in Educational Stem Game Design and Development." In *Proceedings of the 2017 Winter Simulation Conference*, eds. W. K. V. Chan et al. Las Vegas, NV.

# PARALLELIZATION OF ADAPTIVE VECTOR MEDIAN FILTER FOR POINT CLOUD DENOISING

Zinat Afrose and Yuzhong Shen

Department of Modeling, Simulation and Visualization Engineering  
Old Dominion University  
{zafro001,yshen}@odu.edu

## ABSTRACT

In this paper, we developed a method for filtering of noisy point cloud data using adaptive vector median filter and utilized Microsoft Parallel Patterns Library to accelerate the algorithm execution. The proposed algorithm adaptively adjusts the vector median value and the filter window size. If the vector median value in the present window is noisy, the filter window is expanded. This adaptive approach improves the performance of the proposed filter, with increased computational cost, especially for large data sets. Multi-core processor architecture contains several execution cores within a single processor package. Multi-core processors now are standard configuration on desktop and laptop computers, and even smartphones. To take advantage of multi-core architecture, software code must be parallelized. This paper discusses parallelization of adaptive vector median filter (AVM) using Microsoft Parallel Patterns Library. Experimental results demonstrated that AVM is well suited for parallelization and significant speedup using PPL was achieved.

**Keywords:** point cloud, denoising, filtering, parallel programming.

## 1 INTRODUCTION

Point clouds have become increasingly popular in various applications. Due to device limitation or influence of light, point cloud data are often contaminated by severe noise, which adversely affects the accuracy of surface reconstruction. Point cloud denoising or filtering is the process of removing noise in the point cloud data. In this paper, a point cloud denoising method to remove noise and outliers is proposed. The adaptive vector median filter is simple enough to process the point cloud quickly but overall computing cost can be expensive when dealing with larger datasets containing millions or even billions of points. Microsoft Parallel Patterns Library is utilized to execute AVM concurrently on multi-cores on the same processor, thus reducing computational time dramatically.

## 2 3D POINT CLOUD DENOISING USING ADAPTIVE VECTOR MEDIAN FILTER

Given a noisy point cloud and an initial window size, the adaptive vector median filter performs several steps. First, for each specified window, it calculates the vector median. Next, it checks if the point containing the vector median value is noisy based on the depth value (z component). If it is not noisy but the center point is noisy, then the center point is replaced by the vector median; if the center point is also not noisy, the filter output is the original center point. If both the vector median and the center point is noisy, the filter window is expanded and the above process is repeated. Figure 1(a) shows a noisy model with several outliers and Gaussian noise with 0.01 variance and 1(b) illustrates the result of the filtering.

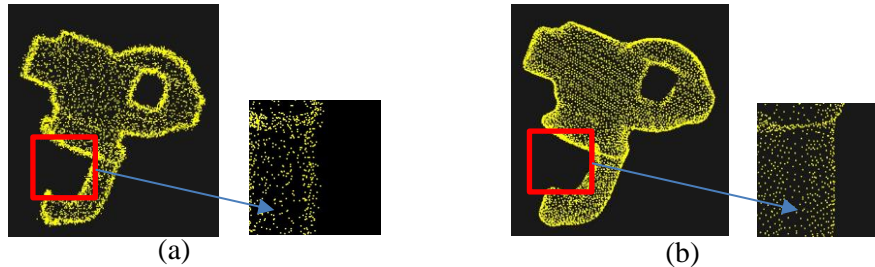


Figure 1: Denoising point cloud (a) Input noisy model, (b) Filtered result using AVM.



### 3 PARALLELIZATION WITH MICROSOFT PARALLEL PATTERNS LIBRARY

Microsoft's Parallel Patterns Library (PPL) provides features for multicore programming. Multicore programming is becoming popular for applications to scale up and improve performance. Point cloud datasets can contain millions or billions of points which can lead to huge amount of time for processing. This paper utilized PPL to accelerate AVM for execution on multi-cores. To evaluate the effectiveness of the proposed method, we extensively experimented with both serial and parallel versions of the algorithm and analyzed speed up performance. Experiments were carried out on 2 devices: Intel(R) Xeon(R) CPU E5-2687Wv3 10 cores, 3.10 GHz and Intel(R) Core(TM) i7-2760QM CPU 4 cores, 2.39GHz. Operating system for both of the devices was 64 bits Windows 7. In this experiment, the execution time and speed up ratio was collected using the adaptive vector median filter with different sets of point cloud data. Figure 2 shows the speedup ratio of the proposed algorithm using 4 physical cores and 10 physical cores respectively. The red line indicates the estimated curve line for speedup using Amdahl's law and the blue line indicates the resulted speedup using the proposed method. Amdahl's law can be defined in simple form as below:

$$\Psi(N) = \frac{t_{seq}}{t_{par}} \leq \frac{T}{(1 - \alpha)T + \alpha \frac{T}{N}} = \frac{1}{(1 - \alpha) + \frac{\alpha}{N}} \quad (1)$$

Here,  $T$  is the time needed for an application to execute on a single CPU,  $\alpha$  is the fraction of the computation that can be done in parallel so that  $1 - \alpha$  is the fraction that must be carried out on a single CPU and  $N$  is the number of processors. However, some intrinsic sequential part of the algorithm, communication cost, load balancing etc. can limit the achievable speedup. Experimental results show the behavior is linear for two different processors. The speedup performance clearly depends on the configurations of the processors. Table 1 shows the computation time both in serial and parallel for different point cloud data in a 4 cores device.

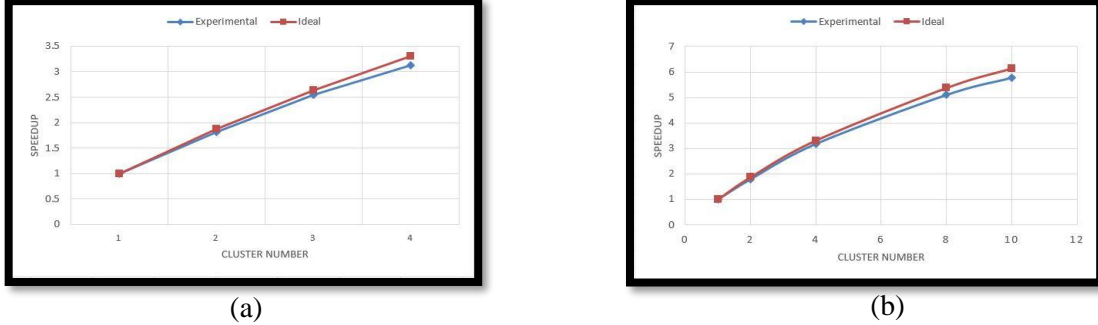


Figure 2: Experimental Speedup for a dataset using AVM with (a) 4 logical processors (b) 10 logical processors.

Table 1: Computation Time (in sec)

Model	No. of points	Serial (AVM)	Parallel (AVM)
Bunny	15726	0.12816	0.04116
Iron	85574	0.676	0.19150
Gear	6568	0.056	0.0172
ThaiStatue	4999996	40.733	13.577
Compressor	361043	3.117	0.9891

### 4 CONCLUSION

In this paper, we proposed a new algorithm- adaptive vector median filter to remove noise and outliers from noisy point cloud data and utilized Microsoft's Parallel Patterns Library to speed up the process. Experimental results showed that significant speed up of AVM can be achieved using multi-core processors.

# STUDENT CAPSTONE CONFERENCE

2018

## GENERAL SCIENCES & ENGINEERING

- Page 11 Aaron Walden, Mohammad Zubair, Jason Orender and Eric Nielsen  
***Old Dominion University and NASA Langley Research Center***  
Unstructured-Grid Algorithms for a Many-Core Landscape
- Page 13 Daniel Pérez, Kazi Islam, Victoria Hill, Blake Schaeffer, Richard Zimmerman and Jiang Li  
***Old Dominion University and U.S. Environmental Protection Agency***  
Deep Learning for Effective Quantification of Seagrass in Coastal Areas
- Page 23 Tunazzina Islam, Desh Ranjan, Mohammad Zubair, and Harold Riethman  
***Old Dominion University***  
REXTAL: Regional Extension of Assemblies Using Linked-Reads
- Page 25 Christos Tsolakis, Fotis Drakopoulos and Nikos P. Chrisochoides  
***Old Dominion University***  
Sequential Metric-Based Adaptive Mesh Generation
- Page 36 Wessam Elhefnawy  
***Old Dominion University***  
Hypoanalyzer: A Real Time Interactive Dashboard for Hypothesis
- Page 45 Brandon Waddell and James F. Leathrum Jr.  
***Old Dominion University***  
Multi-Threaded Simulation Executive for Multi-Core Processors
- Page 53 Erik Jensen and Masha Sosonkina  
***Old Dominion University***  
Comparison of Asynchronous Hybrid Parallel MPI-OpenMP Jacobi's Method Implementations
- Page 61 Collin D. Bowersock  
***Old Dominion University***  
Quantifying the Effect of an Unaccustomed Gait Pattern on Movement Variability
- Page 63 Anthony Williams and Ruhai Zhou  
***Old Dominion University***  
Stability Analysis of Active Suspensions of Liquid Crystals
- Page 76 Michelle E. Pizzo and Fang Q. Hu  
***Old Dominion University***  
Simulation of Sound Absorption by Scattering Bodies Treated With Acoustic Liners and the Assessment of its High-Performance Parallel Computing Capabilities

# UNSTRUCTURED-GRID ALGORITHMS FOR A MANY-CORE LANDSCAPE

Aaron Walden, Mohammad Zubair, Jason Orender

Eric J. Nielsen

Old Dominion University  
Norfolk, VA, 23529, USA  
{awalden,zubair,jorender}@cs.odu.edu

NASA Langley Research Center  
Hampton, VA, 23666, USA  
eric.j.nielsen@nasa.gov

Justin P. Luitjens

NVIDIA Corp.  
Salt Lake City, UT, 84101, USA  
jluitjens@nvidia.com

## ABSTRACT

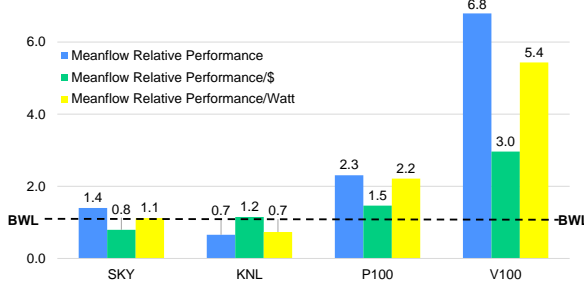
We explore the transition of a legacy, MPI-only, domain-decomposed unstructured-grid code highly optimized for multi-core systems to shared-memory MPI+OpenMP and MPI+CUDA models more suitable for a future high-performance computing landscape dominated by heterogeneous many-core architectures. We study node-level performance characteristics of compute-intensive kernels hand-optimized using CUDA and AVX512 vector intrinsics. Strong scaling results are presented which contrast the scalability of the original MPI-only model with that of the shared-memory models. We also compare scaling across a variety of different many-core architectures and high-performance computing systems.

**Keywords:** Parallel CFD applications, Heterogeneous computing, High-performance computing, Optimization.

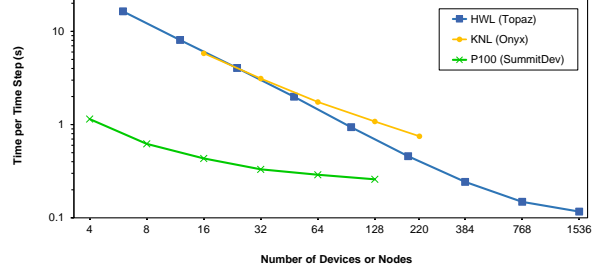
## 1 INTRODUCTION

NASA Langley Research Center’s FUN3D is an unstructured-grid computational fluid dynamics software suite used to tackle complex aerodynamics problems (Biedron, Carlson, Derlaga, Gnoffo, Hammond, Jones, Kleb, Lee-Rausch, Nielsen, Park, Rumsey, Thomas, and Wood 2017). The toolset enables multidisciplinary capabilities through coupling to variable fidelity models encompassing structural effects, multibody dynamics, acoustics, radiation, optics, propulsion, and ablation. FUN3D provides advanced adjoint-based design capability, enabling formal optimization of time-dependent moving-body simulations involving turbulent flows. The adjoint formulation is also used to perform rigorous mesh adaptation and error estimation.

FUN3D currently relies on explicit domain decomposition and a coarse-grained MPI-based communication paradigm optimized for multi-core systems. Practical considerations guiding the development of future exascale-class systems impose severe power constraints on their design (Simon 2013). This next generation of high-performance computing systems is likely to rely on many-core architectures offering substantially improved energy efficiency through higher degrees of concurrency and lower clock rates. These systems are also expected to lower the amount of memory available per core. Ultimately, these and other factors are



(a) Meanflow Single Node (1M grid points)



(b) Meanflow Strong Scaling (60M grid points)

likely to render legacy MPI-based paradigms inefficient, and it is widely recognized that such applications will require a transition to some form of hybrid parallelism to effectively leverage future exascale-class computing platforms.

In this work, we describe the transition of FUN3D from a pure MPI model to shared-memory hybrid MPI+OpenMP and MPI+CUDA models with support for heterogeneous architectures.

## 2 NODE-LEVEL PERFORMANCE

We detail the optimization of FUN3D’s two most computationally intensive kernels with particular emphasis on the development of custom CUDA and AVX512 vector intrinsic implementations. Race condition avoidance, vectorization, and memory bandwidth optimization are also discussed. We study performance at the node level for the following architectures: Intel Xeon Broadwell (BWL) and Skylake (SKY), Intel Xeon Phi Knights Landing (KNL), and NVIDIA Pascal P100 and Volta V100 GPUs. As shown in Figure 1a, speedups of nearly  $7\times$  over pure MPI on Broadwell are reported for the meanflow computation (apx. 80% of FUN3D’s PDE solver).

## 3 STRONG SCALING PERFORMANCE

We perform strong scaling studies of both conventional FUN3D and our hybrid shared-memory implementations across a variety of high-performance computing systems. In our strong scaling studies, we focus on the scalability of FUN3D’s multicolor point implicit linear solver, which performs the bulk of inter-node communication. In particular, the issue of MPI performance scaling with the number of ranks per node is studied. We also study load balancing in the context of mixed-element grids and the performance of intra-node and inter-node data movement in a heterogeneous CPU+GPU setting. Figure 1b compares strong scaling results across a Haswell system (HWL), KNL, and V100. Though V100 fails to strong scale due to its fast compute and MPI issues on the nascent SummitDev, we note that  $10\times$  the number of HWL nodes are required to achieve a speedup of  $4\times$  over V100 at scale.

## REFERENCES

- Biedron, R. T., J.-R. Carlson, J. M. Derlaga, P. A. Gnoffo, D. P. Hammond, W. T. Jones, B. Kleb, E. M. Lee-Rausch, E. J. Nielsen, M. A. Park, C. L. Rumsey, J. L. Thomas, and W. A. Wood. 2017. *FUN3D Manual 13.1*. NASA/TM-2016-219580.
- Simon, H. D. 2013. *Barriers to Exascale Computing*, pp. 1–3. Berlin, Heidelberg, Springer Berlin Heidelberg.



# DEEP LEARNING FOR EFFECTIVE QUANTIFICATION OF SEAGRASS IN COASTAL AREAS

Daniel Pérez<sup>1</sup>, Kazi Islam<sup>2</sup>, Victoria Hill<sup>3</sup>, Blake Schaeffer<sup>4</sup>, Richard Zimmerman<sup>3</sup> and Jiang Li<sup>2</sup>

<sup>1</sup>Department of Modeling, Simulation & Visualization Engineering, Old Dominion University, Norfolk, VA 23508

<sup>2</sup>Department of Electrical & Computer Engineering, Old Dominion University, Norfolk, VA 23508

<sup>3</sup> Department of Earth & Atmospheric Sciences, , Old Dominion University, Norfolk, VA 23508

<sup>4</sup> Office of Research and Development, U.S. Environmental Protection Agency

## ABSTRACT

Seagrass is a highly valuable component of coastal ecosystems ecologically and economically, yet reliable mapping of seagrass density is not available due to the high cost of data processing and spatial mapping. This paper presents a deep learning approach for quantification of leaf area index (LAI) levels of seagrass in coastal water using high resolution multispectral satellite images. Specifically, a deep convolutional neural network (CNN) for regression is proposed for quantification of seagrass LAI. The feasibility of the CNN is demonstrated when trained in nearby areas. In addition, a fine-tuning method is developed to transfer knowledge in a CNN trained at one location for seagrass quantification to different locations with minimum field observations, which saves a significant amount of time and resources in the mapping of seagrass LAI. Our experimental results show that the developed CNN is able to quantify seagrass LAI with less error than other machine learning models.

**Keywords:** Seagrass Quantification, Deep Learning, Convolutional Neural Network, Fine-tuning.

## 1 INTRODUCTION

Seagrass is an important ecological, economic and social well-being component of coastal ecosystems (Hemminga and Duarte 2000, Wicaksono and Hafizt 2013). Ecologically, seagrass provides multiple benefits such as pollution filtering, sediment trapping or organic fertilization. Economically, seagrass ecosystems are considered 23 and 33 times more valuable than terrestrial and oceanic ecosystems respectively. However, reliable information about the distribution of seagrass is not tracked in most parts of the world due to the high cost of comprehensive mapping (Wicaksono and Hafizt 2013).

In this paper, we propose a deep learning model for the detection of seagrass in a given area based on multispectral images taken from operational satellite remote sensing platforms. The developed method can quantify the leaf area index (LAI) for each valid pixel within a scene. LAI is defined as leaf area per square area (Breuer, L. and Freede, H. 2003), and it is considered one of the most important biophysical components of seagrass (Wicaksono and Hafizt 2013). The LAI index is expressed as a floating number ranging from 0 to 10, with '0' as no seagrass and '10' as the largest area of seagrass per area. The goal of this project is to develop a model that is able to quantify LAI from high resolution satellite imagery with limited field observations that may be ubiquitously applied to other localities.

The procedure to predict seagrass LAI is described as follows. First, high resolution satellite images of 3 different parts of the coast of Florida were obtained. These images were taken with the Worldview-2 (WV-2)

satellite, and they have a resolution of 1.24m in their 8 visible and near infrared (VNIR) bands. Historically, an experienced operator labeled the image as four different classes (sea, sand, seagrass and land) and applied a physics model (Hill et al. 2014) in the seagrass region to map LAI. Second, a 3-layer convolutional neural network (CNN) for regression is proposed to detect LAI in small patches of the images. Spatial information is used as we use 5x5 patches, while the spectral information includes 8 bands of multispectral images. Using this model, we aim to solve two different problems:

1. Whether we can use deep learning to detect LAI levels of seagrass by training a CNN and applying it in different parts of the same image.
2. Whether we can use the trained model in a completely different area than the one used for training. To improve the results for this case, a fine-tuning technique is proposed so that only a very small portion of each image is used for training.

The goal of this paper is to come up with a model that is able to predict seagrass level in any part of the world by just taking a few samples from the area. This would be significantly beneficial to entities interested on quantifying LAI in a given area, since it would save the time and resources allocated to map the whole space.

The remainder of the paper reviews the literature (Section 2), describes the methods in detail (Section 3), shows the results obtained (Section 4) and draws the conclusions from the produced work (Section 5).

## **2 RELATED WORK**

### **2.1 Deep Learning**

Applications of deep learning has been successful in numerous fields such as image classification (Krizhevsky et al. 2012, He et al. 2016), object detection and tracking (Redmon and Farhadi 2016, Ren et al. 2015), speech recognition (Hinton et al. 2012, Yu and Deng 2016), autonomous driving (Chen et al. 2015, Huval et al. 2015) and cybersecurity (Sommer and Paxson 2010, Najafabadi et al. 2015). Among different deep learning models, deep Convolutional Neural Networks (CNNs) are currently popular for various applications. A CNN consists of a set of convolutional layers followed by several fully connected layers. The convolutional layers learn effective representations for the raw data and the fully connected layers perform classification or regression based on the learned representations. Many CNN based image classification systems can perform an end-to-end learning in which feature extraction (representation learning) is jointly optimized with classification, and it is believed that this automatic feature learning process plays a critical role to achieve the performances of CNNs.

CNNs can also be utilized for regression by adding a regression layer on top of the representation layer. Though regression problems using CNNs are not as common as classification problems, some examples can be found in the literature. Niu et al. (Niu et al. 2016) proposed a multiple output CNN to perform ordinal regression for age estimation. Their network had a set of  $K-1$  output layers, where each output layer was a classification layer that predicted whether the age of facial image was larger than a rank of  $K$ , transforming a classification model into a ordinal regression model. Yuan et al. used a generic 2D CNN regression model for simultaneous face detection and segmentation (Yuan et al. 2014), proving that their model was as effective as a classification model. Girshick developed a fast region-based CNN method for object detection (Girshick 2015). He developed a CNN that produced two outputs: a softmax probability to classify the detected object over  $K$  classes, and a regression output consisting of 4 values that refined bounding box positions for one of the  $K$  classes. A similar method was used by Gidaris and Komodakis in (Gidaris and Komodakis 2015), where they developed a CNN model for bounding box regression, which

allowed the authors to refine the location of the detected objects. A regression CNN can also be used for estimating image data. In (Li *et al.* 2014), Li *et al.* developed a CNN to generate Positron Emission Tomography (PET) image scans from Magnetic Resonance Imaging (MRI) images to improve Alzheimer's disease diagnosis.

## 2.2 Seagrass LAI Mapping

The majority of the studies of seagrass mapping focus on assessing the accuracy of manually mapping methods (Phinn *et al.* 2008, Short and Coles 2001, Meehan *et al.* 2005). Yang *et al.* (Yang and Yang 2009) manually computed distribution of seagrass from satellite images using a remote sensing method. They obtained an accuracy slightly better than 80%. However, their approach only determined whether seagrass was found in a region instead of quantifying the LAI index. An automatic algorithm for seagrass LAI mapping was implemented by Wicaksono *et al.* (Wicaksono and Hafizt 2013). In this case, they provided regression results and obtained a best standard error of estimates of 0.72.

## 3 METHODOLOGY

### 3.1 Extraction of Patches from Satellite Images

We used three different multispectral and panchromatic images captured by the Worldview-2 (WV-2) satellite from the coastal areas of Florida. One of the images is used to train the CNN (Figure 1) and the other two are used for testing purposes (Figures 2-3). Each satellite image has an associated LAI mapping image obtained by the physics model (Hill *et al.* 2014). The LAI levels of the physics model are shown on Figures 1-3 in a colormap, where blue represents the pixels with no seagrass and red the pixels with the largest LAI. It is important to note that the extraction of patches was limited to those points with LAI information in the physics model.

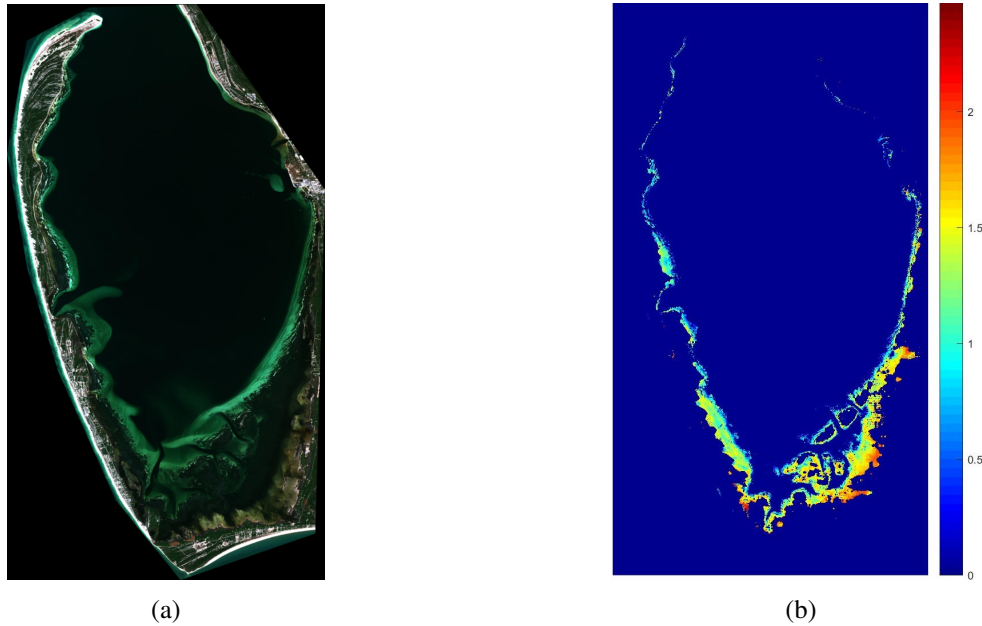


Figure 1: Satellite Image of Saint Joseph Bay (Florida, U.S.) taken on 11/10/2010 (a) with its corresponding ground truth for LAI (b).

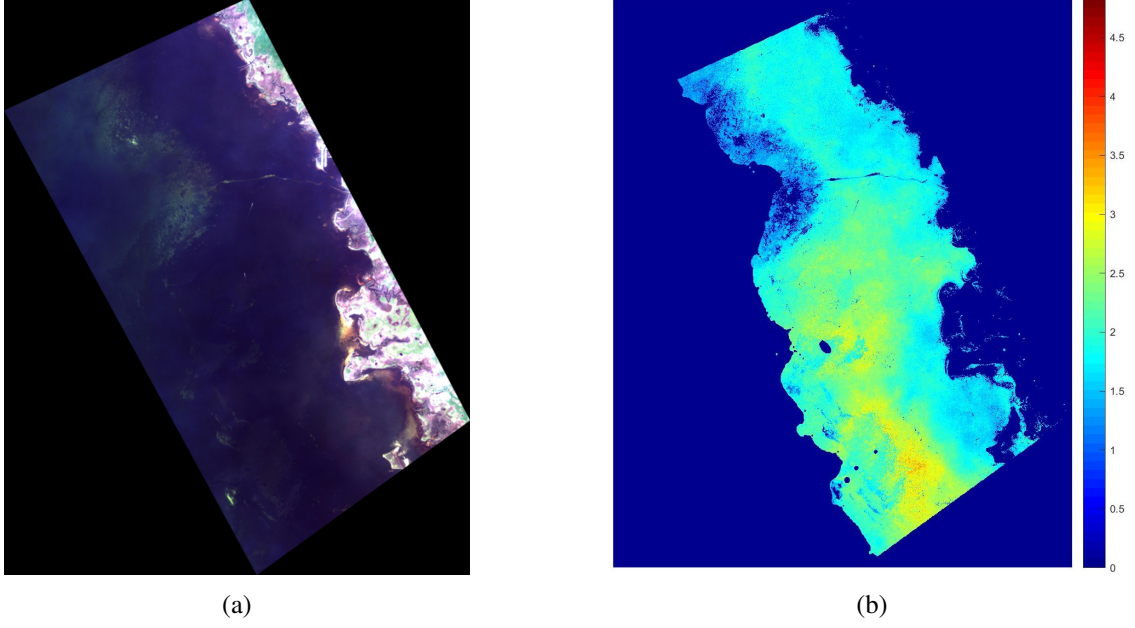


Figure 2: Satellite Image of Keeton Beach (Florida, U.S.) taken on 05/20/2010 (a) with its corresponding ground truth for LAI (b).

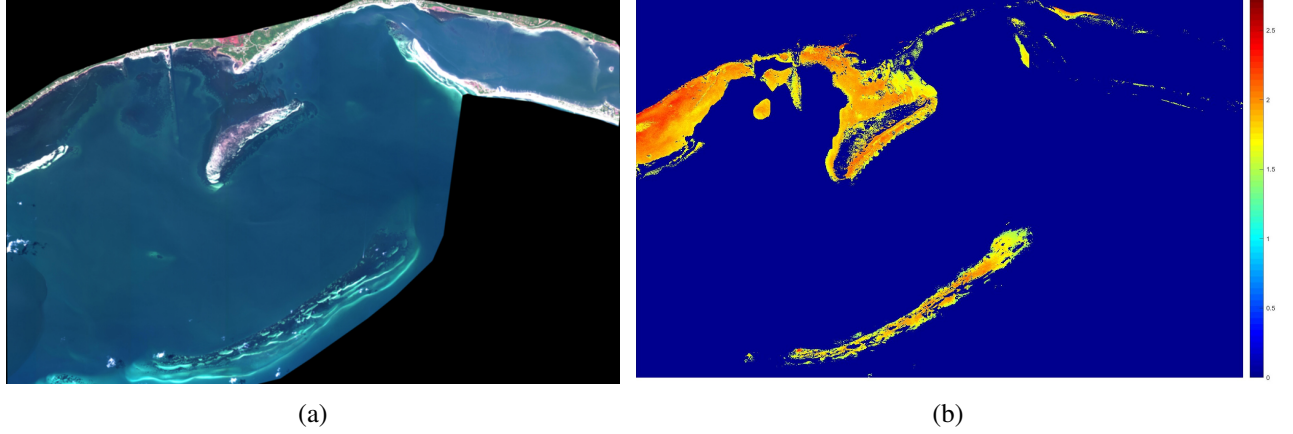


Figure 3: Satellite Image of Saint George Sound (Florida, U.S.) taken on 04/27/2012 (a) with its corresponding ground truth for LAI (b).

### 3.2 CNN Structure

Figure 4 shows the structure of the proposed CNN for seagrass LAI mapping. The CNN has 2 convolutional layers. The fully connected layer has 100 hidden unit and the last layer performs regression with a normal kernel initializer. The CNN was trained using 5x5x8 patches extracted from the satellite image of St. Joseph Bay (Figure 1).

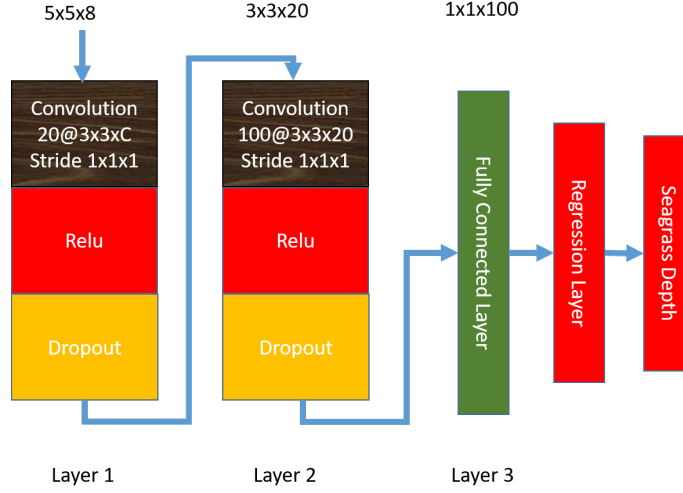


Figure 4: CNN structure LAI regression on the 8 channel pan-sharpened multispectral images.

### 3.3 Fine-tuning Method

The ultimate goal of this project is to develop a model that is able to quantify LAI from high resolution satellite imagery with limited field observations that may be ubiquitously applied to other localities, but the distribution of seagrass LAI at different locations shows a wide range of variation. It is difficult to collect enough ground truth data from each of the locations and train a machine learning model specific to the location. To solve this problem, we propose the following fine-tuning approach:

1. Train the model with all the patches from the training image (St. Joseph Bay).
2. Select 5 locations in the testing images and extract patches from an area of 50x50 pixels (approximately 13,000 total fine-tuning patches per testing image).
3. Freeze all the layers of the CNN but the last one (regression layer) and re-train the model with all the patches.
4. Compare the accuracy when fine-tuning with a subset of 50, 100 and 500 random patches.

The fine-tuning approach is applied for each of the testing images (Keeton beach and St. George Sound). Figure 5 shows the locations of the patches extracted for fine-tuning.

## 4 RESULTS

### 4.1 Cross-Validation Results

The first objective of this study is to be able to predict the level of seagrass in a location with a model that is trained using patches from the same area. To test the performance of our model, we performed a 4-fold cross validation (CV) in the training image taken on St. Joseph Bay. Figure 6 shows the results obtained with this method. To measure the error of the regression model, we consider the root-mean-square error (RMSE). The RMSE between the physics model  $m$  and the predictions  $p$  is defined in Eq. 1.

$$RMSE = \sqrt{\frac{\sum_{i=1}^n (m_i - p_i)^2}{n}} \quad (1)$$



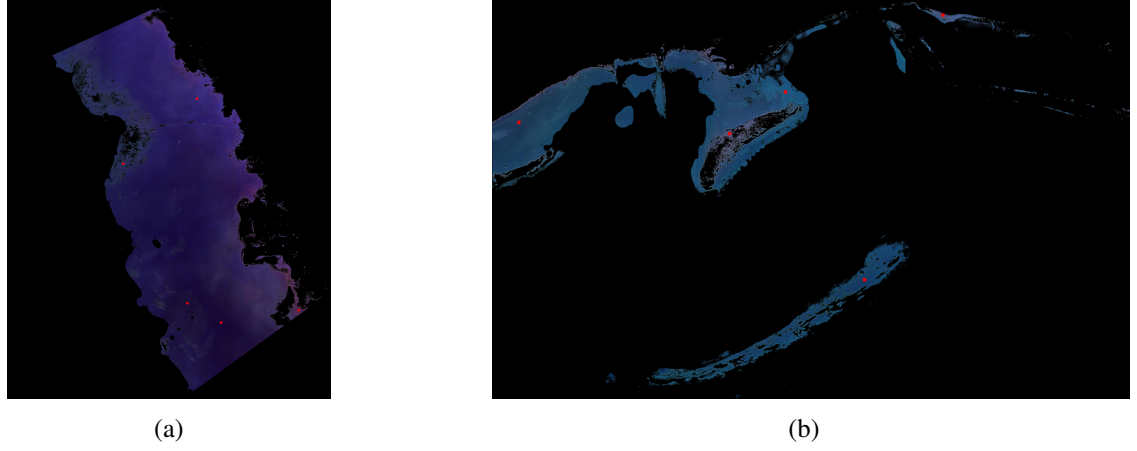


Figure 5: Location of the fine-tuning patches extracted from Keeton Beach (a) and St. George Sound (b)

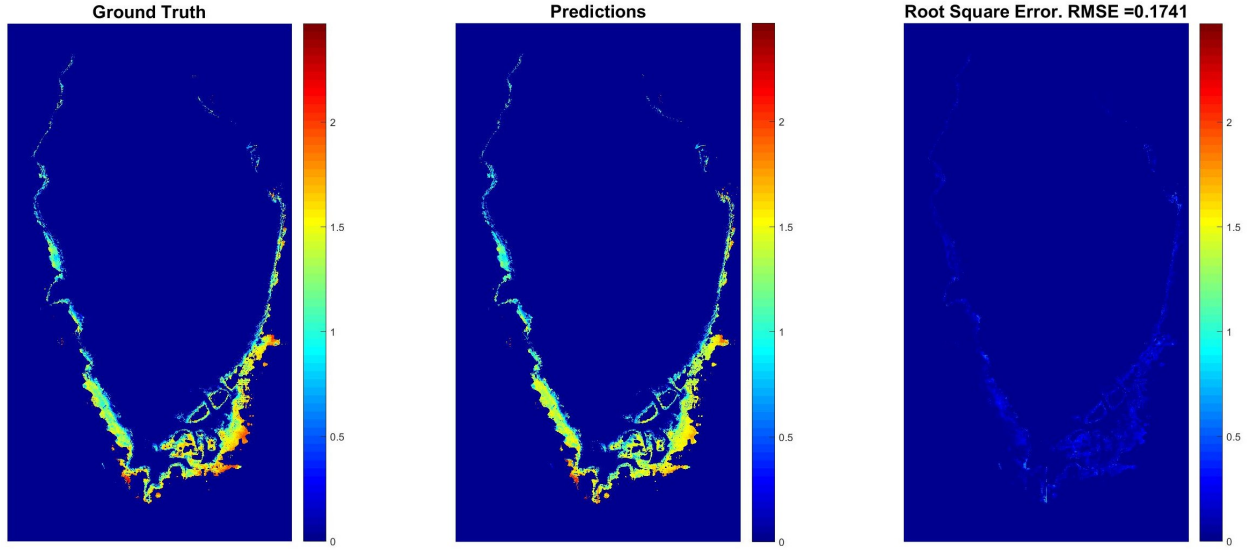


Figure 6: Results obtained on the 4-fold CV performed on St. Joseph Bay. The colormap of the ground truth from the physics model is displayed on the left, the predictions are included on the center, and the colormap in the right shows the RMSE.

#### 4.2 Patch Size Optimization

Figure 6 shows the 4-fold CV results obtained in the training image with a patch size  $5 \times 5 \times 8$ . We performed experiments with different patch sizes to determine which spatial size produced the best result. Table 1 shows the RMSE obtained by our model when the patch size is 3, 5, 7 and 9. While the variation of the RMSE is very small, it can be appreciated that the best results were obtained with patch size 5, which produced a RMSE of 0.17.

Table 1: RMSE Obtained for different patch sizes.

Patch Size	3	5	7	9
RMSE	0.180	<b>0.174</b>	0.180	0.178

Table 2: Average RMSE obtained using a regression model, a simple neural network and the CNN proposed by our method.

Method	RMSE
Linear Regression	0.237
Simple Neural Network	0.1815
CNN	<b>0.1779</b>

### 4.3 Comparison with Other Machine Learning Methods

To prove that a deep learning approach is the optimal solution for this problem, we performed experiments using other regression techniques. Specifically, we computed 4-folded CV results on St. Joseph Bay using linear regression and a simple neural network with 10 hidden units. Table 2 shows the RMSE obtained using each of the methods described above. In each case, the final RMSE was obtained by performing the average of the results using different patch sizes. Our method obtained a lesser error than any of the other comparison techniques. Thereby, we can determine that a deep CNN model is the optimal approach for the proposed problem.

### 4.4 Initial Results on Testing Images

The initial testing results are computed by using a model trained with all the data from st. Joseph Bay and applying it to the other two images. Figures 7 and 8 show the results obtained when the model was applied to Keeton Beach and St. George Sound respectively. It can be appreciated that the error increased significantly from the results obtained on the 4-fold CV approach.

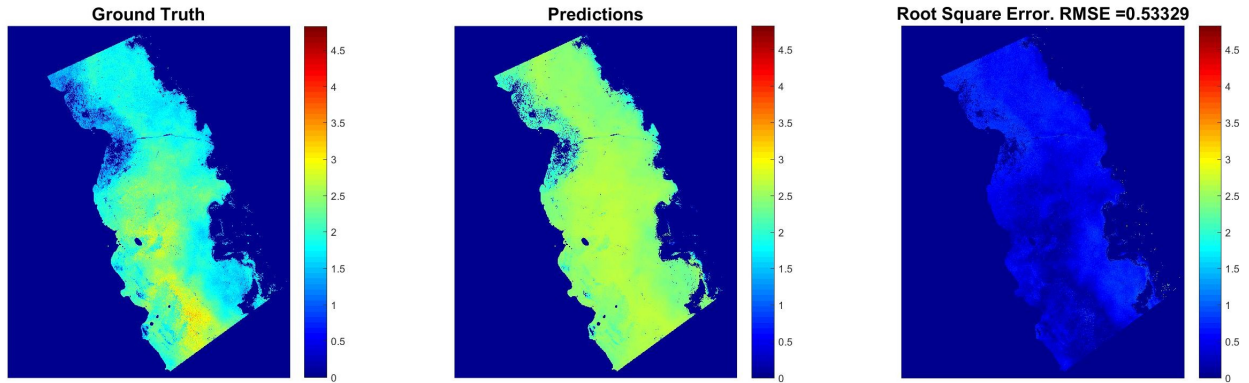


Figure 7: Initial results obtained on Keeton Beach. The colormap of the physics model is displayed on the left, the predictions are included on the center, while the colormap in the right shows the RMSE.

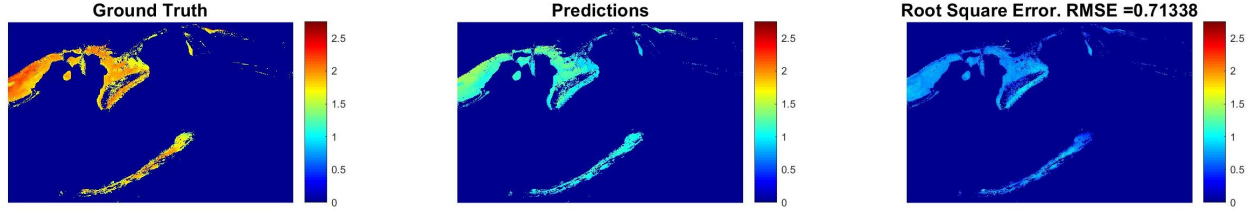


Figure 8: Initial results obtained on St. George Sound. The colormap of the physics model is displayed on the left, the predictions are included on the center, while the colormap in the right shows the RMSE.

#### 4.5 Testing Results after Fine-tuning

To reduce the error obtained on the initial results, we applied the fine-tuning approach described on Section 3.3. Figures 9 and 10 show the results obtained in the testing images when the CNN is fine-tuned with all the fine-tuning samples. It can be seen that the model performed significantly better than before, producing predictions that closely match the ground truth and with a rounded RMSE of 0.11 for both testing cases.

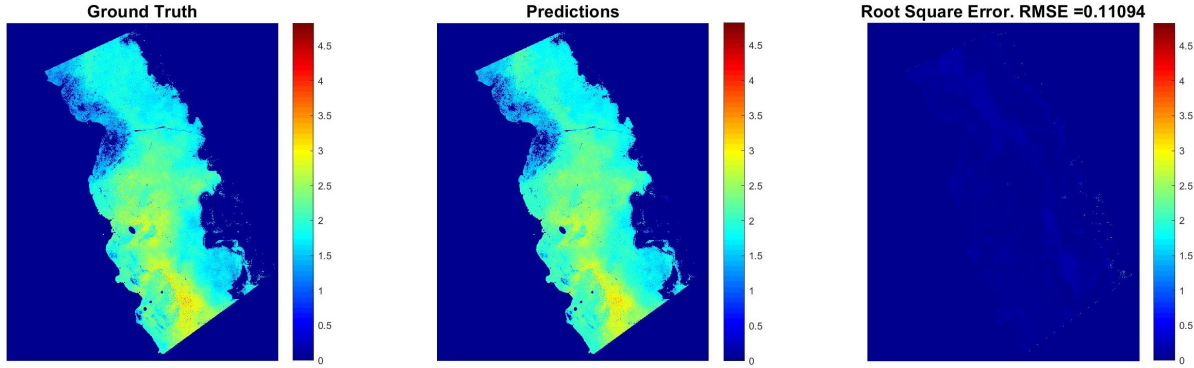


Figure 9: Results obtained on Keeton Beach after fine tuning. The colormap of the physics model is displayed on the left, the predictions are included on the center, while the colormap in the right shows the RMSE.

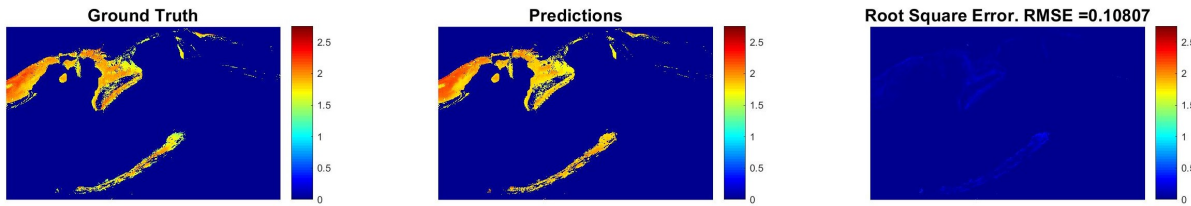


Figure 10: Results obtained on St. George Sound after fine-tuning. The colormap of the physics model is displayed on the left, the predictions are included on the center, while the colormap in the right shows the RMSE.

Figures 9 and 10 show the results when the last layer of the CNN was retrained with all the fine-tuning samples. Table 3 shows the comparison of the RMSEs obtained using a different number of fine-tuning patches. It can be noted that, when the model was applied to Keeton Beach, the least RMSE was obtained using 500 patches, while in the case of St. George Sound, the best performance was obtained when the model was fine-tuning with only 50 patches. This suggests that the fine-tuning patches have some noise that is cleared when we subsample the patches.

Table 3: Comparison of testing results.

Testing Image	0 Patches	50 Patches	100 Patches	500 Patches	All Patches
Keeton Beach	0.5333	0.1387	0.1385	<b>0.0944</b>	0.1109
St George Sound	0.7134	<b>0.1080</b>	0.1190	0.1122	0.1081

## 5 CONCLUSIONS

This paper presents a deep learning approach for quantification of seagrass LAI. Using our method, seagrass LAI can be predicted by analyzing a small set of samples on a given area, which saves the time and resources needed to analyze the whole space.

It was demonstrated that using a convolutional neural network for quantification of seagrass is a good approach that reduces the error when compared with other machine learning algorithms for regression (linear regression and neural network). The CNN obtained a best testing RMSE of 0.09 and 0.11 for Keeton beach and St. George Sound respectively, which beats the error obtained when performing 4-fold CV in the training image (0.17). This is reasonable given that the CNN was fine tuned with samples from 5 areas that were different and far from each other, while in the 4-fold CV the CNN is only trained with areas that are not as close.

The future work will be focused on implementing the Capsule network recently proposed by Sabour *et al.* (Sabour et al. 2017) to determine if the performance increases with this promising new model.

## ACKNOWLEDGMENTS

This paper is a result of ECE 807 - Machine Learning II. The work was supported by NASA under Grant NNX17AH01G.

## REFERENCES

- Breuer, L. and Freede, H. 2003. “Leaf Area Index - LAI”. <https://www.staff.uni-giessen.de/~gh1461/plapada/lai/lai.html>. Accessed March 16, 2018.
- Chen, C., A. Seff, A. Kornhauser, and J. Xiao. 2015. “Deepdriving: Learning affordance for direct perception in autonomous driving”. In *Computer Vision (ICCV), 2015 IEEE International Conference on*, pp. 2722–2730. IEEE.
- Gidaris, S., and N. Komodakis. 2015. “Object detection via a multi-region and semantic segmentation-aware cnn model”. In *Proceedings of the IEEE International Conference on Computer Vision*, pp. 1134–1142.
- Girshick, R. 2015. “Fast r-cnn”. In *Proceedings of the IEEE international conference on computer vision*, pp. 1440–1448.
- He, K., X. Zhang, S. Ren, and J. Sun. 2016. “Deep residual learning for image recognition”. In *Proceedings of the IEEE conference on computer vision and pattern recognition*, pp. 770–778.
- Hemminga, M. A., and C. M. Duarte. 2000. *Seagrass ecology*. Cambridge University Press.
- Hill, V., R. Zimmerman, W. Bissett, H. Dierssen, and D. Kohler. 2014. “Evaluating light availability, seagrass biomass and productivity using hyperspectral airborne remote sensing in Saint Joseph’s Bay, Florida”. *Estuaries and Coasts* vol. 37 (6), pp. 1467–1489.
- Hinton, G., L. Deng, D. Yu, G. E. Dahl, A.-r. Mohamed, N. Jaitly, A. Senior, V. Vanhoucke, P. Nguyen, T. N. Sainath et al. 2012. “Deep neural networks for acoustic modeling in speech recognition: The shared views of four research groups”. *IEEE Signal Processing Magazine* vol. 29 (6), pp. 82–97.

- Huval, B., T. Wang, S. Tandon, J. Kiske, W. Song, J. Pazhayampallil, M. Andriluka, P. Rajpurkar, T. Migmatsu, R. Cheng-Yue, F. Mujica, A. Coates, and A. Y. Ng. 2015. "An Empirical Evaluation of Deep Learning on Highway Driving". *CoRR* vol. abs/1504.01716.
- Krizhevsky, A., I. Sutskever, and G. E. Hinton. 2012. "Imagenet classification with deep convolutional neural networks". In *Advances in neural information processing systems*, pp. 1097–1105.
- Li, R., W. Zhang, H.-I. Suk, L. Wang, J. Li, D. Shen, and S. Ji. 2014. "Deep learning based imaging data completion for improved brain disease diagnosis". In *International Conference on Medical Image Computing and Computer-Assisted Intervention*, pp. 305–312. Springer.
- Meehan, A., R. Williams, and F. Watford. 2005. "Detecting trends in seagrass abundance using aerial photograph interpretation: problems arising with the evolution of mapping methods". *Estuaries* vol. 28 (3), pp. 462–472.
- Najafabadi, M. M., F. Villanustre, T. M. Khoshgoftaar, N. Seliya, R. Wald, and E. Muharemagic. 2015. "Deep learning applications and challenges in big data analytics". *Journal of Big Data* vol. 2 (1), pp. 1.
- Niu, Z., M. Zhou, L. Wang, X. Gao, and G. Hua. 2016. "Ordinal regression with multiple output cnn for age estimation". In *Proceedings of the IEEE Conference on Computer Vision and Pattern Recognition*, pp. 4920–4928.
- Phinn, S., C. Roelfsema, A. Dekker, V. Brando, and J. Anstee. 2008. "Mapping seagrass species, cover and biomass in shallow waters: An assessment of satellite multi-spectral and airborne hyper-spectral imaging systems in Moreton Bay (Australia)". *Remote Sensing of Environment* vol. 112 (8), pp. 3413–3425.
- Redmon, J., and A. Farhadi. 2016. "YOLO9000: Better, Faster, Stronger.". *arXiv: 1612.08242*.
- Ren, S., K. He, R. Girshick, and J. Sun. 2015. "Faster r-cnn: Towards real-time object detection with region proposal networks". In *Advances in neural information processing systems*, pp. 91–99.
- Sabour, S., N. Frosst, and G. E. Hinton. 2017. "Dynamic routing between capsules". In *Advances in Neural Information Processing Systems*, pp. 3857–3867.
- Short, F., and R. Coles. 2001. *Global seagrass research methods*, Volume 33. Elsevier.
- Sommer, R., and V. Paxson. 2010. "Outside the closed world: On using machine learning for network intrusion detection". In *Security and Privacy (SP), 2010 IEEE Symposium on*, pp. 305–316. IEEE.
- Wicaksono, P., and M. Hafizt. 2013. "Mapping seagrass from space: Addressing the complexity of seagrass LAI mapping". *European Journal of Remote Sensing* vol. 46 (1), pp. 18–39.
- Yang, D., and C. Yang. 2009. "Detection of seagrass distribution changes from 1991 to 2006 in Xincun Bay, Hainan, with satellite remote sensing". *Sensors* vol. 9 (2), pp. 830–844.
- Yu, D., and L. Deng. 2016. "Automatic Speech Recognition."
- Yuan, J., B. Ni, and A. A. Kassim. 2014. "Half-CNN: a general framework for whole-image regression". *arXiv preprint arXiv:1412.6885*.

# REXTAL: REGIONAL EXTENSION OF ASSEMBLIES USING LINKED-READS

Tunazzina Islam<sup>1</sup>, Desh Ranjan<sup>1</sup>, Mohammad Zubair<sup>1</sup>, and Harold Riethman<sup>2</sup>

<sup>1</sup>Department of Computer Science, Old Dominion University, Norfolk, VA; <sup>2</sup>School of Medical Diagnostic & Translational Sciences, Old Dominion University, Norfolk, VA.

## ABSTRACT

It is currently impossible to get complete de-novo assembly of segmentally duplicated genome regions using genome-wide short-read datasets. Here, we devise a new computational method called Regional Extension of Assemblies Using Linked-Reads (REXTAL) for improved region-specific assembly of segmental duplication-containing DNA, leveraging genomic short-read datasets generated from large DNA molecules partitioned and barcoded using the “Gel Bead in Emulsion” (GEM) microfluidic method[1]. We show that using REXTAL, it is possible to extend assembly of single-copy diploid DNA into adjacent, otherwise inaccessible subtelomere segmental duplication regions and other subtelomeric gap regions. Moreover, REXTAL is computationally more efficient for the directed assembly of such regions from multiple genomes (e.g., for the comparison of structural variation) than genome-wide assembly approaches.

**Keywords:** 10X sequencing, Linked-read sequencing, Subtelomere, assembly, segmental duplication, structural variation, genome gaps.

## 1 INTRODUCTION

Massively parallel short-read DNA sequencing has dramatically reduced the cost and increased the throughput of DNA sequence acquisition; it is now cheap and straightforward to do a variety of whole-genome analyses by comparing datasets of newly sequenced genomes with the human reference sequence. A recently developed approach pioneered by 10X Genomics generates short-read datasets from large genomic DNA molecules first partitioned and barcoded using the “Gel Bead in Emulsion” (GEM) microfluidic method [1]. The bioinformatic pipeline for assembly of these reads (“Supernova”; [2]) takes advantage of the very large number of sets of “linked reads”. Each set of linked reads is comprised of low-read coverage of a small number of large genomic DNA molecules (roughly 10) and is associated with a unique bar code. However, even with these new methods, evolutionarily recent segmentally duplicated DNA such as that found in subtelomere regions remain inaccessible to de novo assembly due to the long stretches of highly similar (> 95% identity) DNA. The problem for subtelomere DNA analysis is amplified by the relative lack of high-quality reference assemblies and abundance of structural variation in these regions. To address this problem and attempt to better assemble human subtelomere regions, we have developed a computational approach called Regional Extension of Assemblies Using Linked-Reads (REXTAL) to extend de novo assemblies from subtelomeric 1-copy DNA regions into adjacent segmentally duplicated and gap regions of human subtelomeres.

Supernova uses the barcode information after initial whole-genome assembly for bridging long gaps. We refer to this method as “genome-wide assembly method”. REXTAL differs from the genome-wide assembly method in that we use the barcode information for selection of reads from anticipated segmental duplication or gap regions adjacent to a specified 1-copy DNA segment before doing the assembly. REXTAL can be applied more generally for enriching region-specific linked reads and improving the assembly of any specified 1-copy genome region of an individual from any species for which a reference genome exists. For targeted region-specific assemblies from many individuals for which 10X datasets are available (e.g., analysis of structural variation at specific loci), REXTAL is faster and more accurate than genome-wide assembly method. In this scenario, for genome-wide assembly, we need to assemble the whole genome of the individuals and then extract the assembled portion of the specific region. But in our case, we first extract the specific region from the 10X dataset by aligning with a 1-copy segment of the reference genome, and then use our bioinformatic pipeline to do the assembly.



## 2 METHOD

The key input data is 10X Genomics linked-reads from individual human genomes, in our case from the genome of a publically available cell line GM19440. Our dataset has approximately 1.49 billion 10X Genomics linked-reads in paired-end format, with each read about 150bp. We processed the raw 10X Genomics data using Long Ranger Basic software developed by 10X Genomics (and freely available to any researcher) to generate barcode-filtered 10XG linked-reads. We used the UCSC browser [3] to access HG38 and selected subtelomere DNA segments for analysis. We used RepeatMasker [4] and Tandem Repeats Finder [5] to screen bait DNA segment sequences for interspersed repeats, low complexity DNA sequences, and tandem repeats to minimize the possibility of false-positive contaminant read identification in the initial selection of reads matching. We used BLAT (BLAST-like alignment tool) [6] with default parameter to do alignment of masked subtelomeric region with genome-wide reads from GM19440. We therefore initially collected all reads that shared a barcode with any read matching the 1-copy segment. We then empirically tested a variety of barcode frequency ranges meeting both of the above requirements for final read selection, using the ability of the selected reads to assemble the original bait region and extend into flanking DNA as the metric for optimization. To get the assembly of the selected paired-end barcode reads Supernova was used. To measure the quality of the assembly, we aligned specified subtelomeric regions of the reference sequence corresponding to our unmasked single-copy bait segments along with their flanking reference DNA segments as query with our generated assembled scaffolds as subject using NCBI BLAST [7], requiring high identity matches ( $\geq 98\%$ ) for retention of each local alignment.

## 3 RESULTS

We tested our read selection and regional assembly strategy on four human subtelomere regions with representative patterns of sequence organization (base pair coordinates listed are from HG38). The 2p subtelomere is a 500kb sized segment of 1-copy DNA (10001 to 500,000); 19p subtelomere has a very large segmental duplication region next to the telomere (10001-259447) followed by a 300kb-sized 1-copy region (259448-559447), 10p has a smaller segmental duplication region near the telomere (10001-88570) followed by a 300kb 1-copy region (88571-388571); 5p has multiple segmental duplication regions as well as multiple single copy regions. 1st segmental duplication region is 10,001-49,495bp, 1st 1-copy region is 49,496-210,595bp, 2nd segmental duplication region is 210,596-305,378bp, and 2nd 1-copy region is 305,379-677,959bp. We tested a wide variety of Barcode ranges empirically for their ability to select read sets capable of generating high-quality regional assemblies corresponding to the bait segment itself as well as extending assemblies of the bait segment into adjacent DNA. For 2p we chose barcode range 10-60 and for 19p, 10p and 5p we chose barcode range 3-70. We showed that using REXTAL, it is possible to extend assembly of single-copy diploid DNA into adjacent, otherwise inaccessible subtelomere segmental duplication regions.

## 4 CONCLUSION

In future experiments, using larger source DNA molecules for barcode sequencing approaches could further extend assemblies into and through segmental duplications, and optical maps of large single molecules extending from the 1-copy regions through segmental duplications and gaps could be used to optimally guide and validate these assemblies.

## REFERENCES

1. Zheng, G. X.-L.-P. et al., (2016). Haplotyping germline and cancer genomes with high-throughput linked-read sequencing. *Nature biotechnology*, 34, 303--311.
2. Weisenfeld NI, Kumar V, Shah P, Church DM, Jaffe DB. (2017). Direct determination of diploid genome sequences. *Genome research*, 27, 757--767.
3. Kent WJ, Sugnet CW, Furey TS, Roskin KM, Pringle TH, Zahler AM, Haussler D. (2002). The human genome browser at UCSC. *Genome research*, 12, 996--1006.
4. Smit, A. F. (1996). 2010 RepeatMasker Open-3.0. URL: <http://www.repeatmasker.org>.
5. Benson, G. (1999). Tandem repeats finder: a program to analyze DNA sequences. *Nucleic acids research*, 27, 573.
6. Kent, W. J. (2002). BLAT—the BLAST-like alignment tool. *Genome research*, 12, 656--664.
7. Altschul SF, Madden TL, Schäffer AA, Zhang J, Zhang Z, Miller W, Lipman DJ. (1997). Gapped BLAST and PSI-BLAST: a new generation of protein database search programs. *Nucleic acids research*, 25, 3389--3402.
8. Gurevich A, Saveliev V, Vyahhi N, Tesler G. (2013). QUAST: quality assessment tool for genome assemblies. *Bioinformatics*, 29, 1072--1075.
9. Li H., Durbin R. (2009). Fast and accurate short read alignment with Burrows--Wheeler transform. *Bioinformatics*, 25, 1754--1760.
10. Li H, Handsaker B, Wysoker A, Fennell T, Ruan J, Homer N, Marth G, Abecasis G, Durbin R; 1000 Genome Project Data Processing Subgroup (2009). The sequence alignment/map format and SAMtools. *Bioinformatics*, 25, 2078--2079.

# SEQUENTIAL METRIC-BASED ADAPTIVE MESH GENERATION

Christos Tsolakis, Fotis Drakopoulos and Nikos P. Chrisochoides

CRTC Lab Computer Science Department  
School of Sciences  
Old Dominion University  
{ctsolakis,fdrakopo,nikos}@cs.odu.edu

## ABSTRACT

In this work, CDT3D an in-house developed isotropic mesh generator is extended to include metric based mesh adaptation. Mesh operations perform the same topological transformations but all criteria are evaluated in a transformed space. Details on the required modifications at each meshing step are included as well an evaluation of the new method on metric functions given in analytic form.

**Keywords:** Anisotropic Mesh Generation, Metric Adaptation, Mesh Adaptation

## 1 INTRODUCTION

Generating anisotropic meshes translates into generating a mesh in which the desired sizing depends on the direction. In many computational areas including both areas of Finite Elements Analysis and visual graphics, there are cases where the function to be interpolated exhibits high variation in only one direction. For example, meshing the surface of a cylinder with elongated elements aligned with the axis of the cylinder can produce a surface mesh with high fidelity and low number of elements at the same time. In contrast, creating a surface mesh only with isotropic elements will require a significant higher number of elements in order to achieve the same fidelity. In the context of Computation Fluid Dynamics (CFD) simulations, the traditional approach to simulations is to generate a mesh which will be passed to a solver in order to approximate the solution of the problem. After, a number of iterations the solver will request a new mesh from the mesh generation component while providing information about the error of the solution on the previous mesh. For reasons, similar to the above example it has been found that aligning elements taking into consideration the variation of the solution in each direction can yield a lower interpolation error with fewer elements.

CDT3D (Drakopoulos 2017, Drakopoulos, Tsolakis, and Chrisochoides 2017) is designed to be the speculative component of the telescopic approach to mesh generation presented in (Chrisochoides 2016). However, parallel performance is only one part of the numerous needs of the meshing community, offering functionality that meets the needs of the CFD community is another one. In this paper, the mesh generation algorithm is extended so it can handle the feedback coming from the solver as described above. In the presented work, input to the algorithm is not only the surface mesh as before but also an error estimator at each point in the form of a matrix. The goal is to use this information in order to create a mesh that adapts to the provided information as good as possible. While only the sequential version of the algorithm has been implemented and tested, all the modifications of the code relate to local evaluations, so extending the method in the future, to the parallel version of CDT3D should be straightforward.

## 1.1 Related Work

One of the first attempts to create anisotropic elements appears in (Peraire, Vahdati, Morgan, and Zienkiewicz 1987), where the authors extract information about the error of the evaluation solution of the PDE and encapsulate it into an error estimator. The estimator is then used to guide their advancing front point creation method by producing a spacing that suites the needs of the problem.

The first use of the 2D Delaunay method to create anisotropic elements appears in (Mavriplis 1990). The author captures anisotropy via a two-dimensional control surface in the three-dimensional space. The control surface is then linearly discretized and a stretch vector for each linear component is evaluated. Local operations like Delaunay cavity evaluation are modified in order to correspond to isotropic evaluations on the high order surface.

Creating anisotropic meshes with the Delaunay method was revisited in (George, Hecht, and Vallet 1991), but this time the error estimator was provided in the mesh generation algorithm in a form of a symmetric positive definite matrix that can induce a metric operator. This representation combines naturally with notions of differential geometry as it is presented below.

Moving forward to present, there is a plethora of mesh adaptation software that uses this representation and properly modified meshing operators in order to produce anisotropic meshes. A non-exhaustive list includes, `Bamg` (Hecht 2018) in two dimensions `mmgs` for surface meshes and `mmg3d` for volume meshes in three dimensions (MMG developers 2018, Dobrzynski and Frey 2009) `Feflo.a` from INRIA (Loseille and Löhner 2009), `refine` from NASA, (Park 2018, Park and Darmofal 2008), `Omega_h` (Ibanez 2018, Ibanez and Shephard 2016), `pragmatic` (Gorman 2018, Gorman, Rokos, Southern, and Kelly 2015) and `EPIC` from Boeing (Michal, Babcock, Kamenetskiy, Krakos, Mani, Glasby, Erwin, and Stefanski 2017, Michal and Krakos 2012). Most of the cited software is designed for high performance sequential mesh adaptation and many of the mesh operations used are optimized for this purpose only. In this work, in contrast, CDT3D which is built from the ground up to be a core part of the telescopic approach of the CRTC group is extended in order to support mesh adaptation. Inspired from the approach presented in (Alauzet and Marcum 2017), metric adaptation is introduced to the mesh generation software while keeping the mesh operations same by evaluating quality quantities and criteria in the metric space.

## 2 METRIC SPACES IN THE CONTEXT OF MESH GENERATION

The proposed method uses the notion of the Euclidean and Riemannian metric spaces, as models for the transformed space.

Informally, the Euclidean metric space can be thought as a transformed space near the vicinity of a point. In the context of mesh generation, the mesh in the vicinity of the point is transformed through affine transformations in order to create an isotropic mesh in the transformed space. Selecting the transformations appropriately, results in a mesh that exhibits the desired sizing in each direction in the physical space. The notion of Riemannian metric space can be seen as a global metric space which is locally a Euclidean metric space and varies smoothly within the domain.

A short reference of the most relevant to this work definitions follows. For a complete treatment see (Loseille and Alauzet 2011).

**Definition 1** (Positive Definite Matrix). *A real symmetric  $3 \times 3$  matrix  $M$  is called positive-definite if  $\forall u \in \mathbb{R}^3, u \neq 0 \implies u^T M u > 0$ .*

**Remark:** For a positive-definite matrix  $\mathcal{M}$ , the bilinear function  $\langle u, v \rangle_{\mathcal{M}} := u^T \mathcal{M} v$  defines an inner product in  $\mathbb{R}^3$ .

**Remark:** It can be shown that every inner product on a real vector space can induce a vector space norm by the map  $\|u\|_{\mathcal{M}} = \sqrt{\langle u, u \rangle_{\mathcal{M}}}$  and subsequently a metric via the formula  $d_{\mathcal{M}}(x, y) = \|x - y\|_{\mathcal{M}}$ .

The pair  $(\mathbb{R}^3, \mathcal{M}) := (\mathbb{R}^3, d_{\mathcal{M}})$  consists therefore a metric space. For the rest of the paper it will be called a **Euclidean Metric Space** or simply a **Euclidean Space**. In a metric space, notions like length, angle, area and volume which are of particular interest in mesh generation can be defined as usual by substituting the usual metric with the one induced by the positive-definite matrix  $\mathcal{M}$ :

$$\text{length of a segment} \quad \ell_{\mathcal{M}}(x, y) = d_{\mathcal{M}}(x, y) \quad (1)$$

$$\text{angle between non-zero vectors} \quad \cos(\theta_{\mathcal{M}}) = \frac{\langle u, v \rangle_{\mathcal{M}}}{\|u\|_{\mathcal{M}} \|v\|_{\mathcal{M}}}, \quad \theta_{\mathcal{M}} \in [0, \pi] \quad (2)$$

Although these two functions can be used to evaluate most of the required quantities during mesh generation, a general transformation map from physical space  $(\mathbb{R}^3, \mathcal{I})$  to the Euclidean space  $(\mathbb{R}^3, \mathcal{M})$  would be useful both for speeding up calculations and for allowing more complicated expressions. The first step to derive this map is given by the spectral theorem of linear algebra:

**Theorem 1** (Spectral Decomposition). *If  $M \in \mathbb{R}^{n \times n}$  is a symmetric matrix then it can be factorized as  $M = PDP^T$  where  $P$  is a orthogonal matrix whose columns are eigenvectors of  $M$  and  $D := \text{diag}(d_1, d_2, \dots, d_n)$  the diagonal matrix of the eigenvalues of  $M$ .*

The spectral decomposition enables the definition of the map

$$D^{\frac{1}{2}} P^T : (\mathbb{R}^3, \mathcal{I}) \rightarrow (\mathbb{R}^3, \mathcal{M})$$

$$x \mapsto D^{\frac{1}{2}} P^T x, \quad \text{where } D^{\frac{1}{2}} := \text{diag}(\sqrt{d_1}, \sqrt{d_2}, \sqrt{d_3})$$

that maps a vector from the physical space to the Euclidean space induced by  $\mathcal{M}$ . Using the above map in conjunction with common geometric formulas, one can transform results from physical space to the Euclidean space, for example using the algebraic properties of the cross product one gets:

$$x \times_{\mathcal{M}} y = \left( D^{\frac{1}{2}} P^T x \right) \times \left( D^{\frac{1}{2}} P^T y \right) = \det \left( D^{\frac{1}{2}} P^T \right) \cdot \left( \left( D^{\frac{1}{2}} P^T \right)^T \right)^{-1} (x \times y) = \sqrt{\det \mathcal{M}} \left( D^{-\frac{1}{2}} P^T \right) (x \times y)$$

since,  $PP^T = \mathcal{I}$ . Finally, using the cross product the volume of a parallelepiped  $K$  in the Euclidean metric space can be evaluated  $\mathbb{R}^3$ :

$$|K|_{\mathcal{M}} = \langle x, (y \times_{\mathcal{M}} z) \rangle_{\mathcal{M}} = \sqrt{\det \mathcal{M}} \cdot |K|_{\mathcal{I}_3} \quad (3)$$

where  $|K|_{\mathcal{I}_3}$  is the volume of the parallelepiped in the physical space.

## 2.1 Riemannian Metric space

In the case of the Euclidean space the metric tensor is a constant matrix, if one allows the metric tensor to vary smoothly over the computational domain, then the **Riemannian Metric space** or simply **Riemannian space** is defined. Even though in a Riemannian space there is no global definition of the inner product, it is still a useful construct for mesh adaptation purposes since in most applications the metric varies within the domain. First, in order to be able to define a metric tensor for every point of the domain an interpolation scheme on the input background mesh must be needed.

In this work, the Log-Euclidean framework introduced in (Arsigny, Fillard, Pennec, and Ayache 2006) is used as interpolation scheme. One of the main advantages of this scheme over the previous used in the literature is that the interpolation operator is commutative simplifying thus the interpolation procedure during mesh generation. Moreover, in (Michal and Krakos 2012) the Log-Euclidean framework was found to be superior in comparison to the power average and the simultaneous matrix reduction method in various numerical evaluations.

## 2.2 Metric Interpolation Log-Euclidean Framework

Let  $x_i, i = 1 \dots k$  be a set of vertices and  $\mathcal{M}_i = (\mathcal{M}(x_i))$  their corresponding metrics. Then, for a point  $x$  of the domain with barycentric coordinates  $a_i$ :

$$x = \sum_{i=1}^k a_i \cdot x_i, \quad \text{with} \quad \sum_{i=1}^k a_i = 1$$

the interpolated metric is defined by:

$$\mathcal{M}(x) = \exp \left( \sum_{i=1}^k a_i \ln \mathcal{M}_i \right) \quad (4)$$

Note that since  $\mathcal{M}_i$  is positive definite it has positive eigenvalues therefore the exponential and logarithm of the metric are well defined and given by

$$\ln(\mathcal{M}) := P \ln(D) P^T \quad \exp(\mathcal{M}) := P \exp(D) P^T$$

Where  $\mathcal{M} = P D P^T$  is the spectral decomposition of  $\mathcal{M}$ .

## 2.3 Computation of Edge Length in Metric Space

The length of a segment in an adapted mesh plays critical role in the quality of the mesh and it is one of the metrics used in this work to quantify the quality of the generated mesh. For this reason an accurate estimate is needed. In differential geometry the length of a vector  $\mathbf{u} = xy$  is computed using the integral

$$\ell_{\mathcal{M}}(xy) = \int_0^1 \|\gamma'(t)\|_{\mathcal{M}} dt = \int_0^1 \sqrt{\mathbf{u}^T \mathcal{M}(x + t\mathbf{u}) \mathbf{u}} dt \quad \text{where } \gamma(t) = x + t \cdot \mathbf{u}$$

However, this computational expensive evaluation can be approximated using a variational law presented in (Alauzet 2010):

**Definition 2.** Let  $e = p_1 p_2$  be an edge of the mesh and  $\mathcal{M}_1 := \mathcal{M}(p_1), \mathcal{M}_2 := \mathcal{M}(p_2)$  the corresponding metric tensor on the endpoints of the edge, Without loss of generality assume that  $\ell_{\mathcal{M}_1}(e) > \ell_{\mathcal{M}_2}(e)$  and define  $a = \frac{\ell_{\mathcal{M}_1}(e)}{\ell_{\mathcal{M}_2}(e)}$  then,

$$\ell_{\mathcal{M}}(e) = \ell_{\mathcal{M}_1}(e) \frac{a-1}{a \ln(a)} \quad (5)$$

## 2.4 Computation of Element Volume

Finally, many quality measures and validity tests in mesh generation use the value of the volume of a tetrahedron, therefore a formula for the computation of element volume is needed. Formally, in a Riemannian

space the volume is evaluated using a continuous version of formula (3). However, in order to avoid the expensive calculations the same approach as in (Alauzet and Marcum 2017) is used, that is, interpolating the metric on the centroid of the element and using the Euclidean volume formula (3).

### 3 CDT3D

#### 3.1 Isotropic Mesh Generation

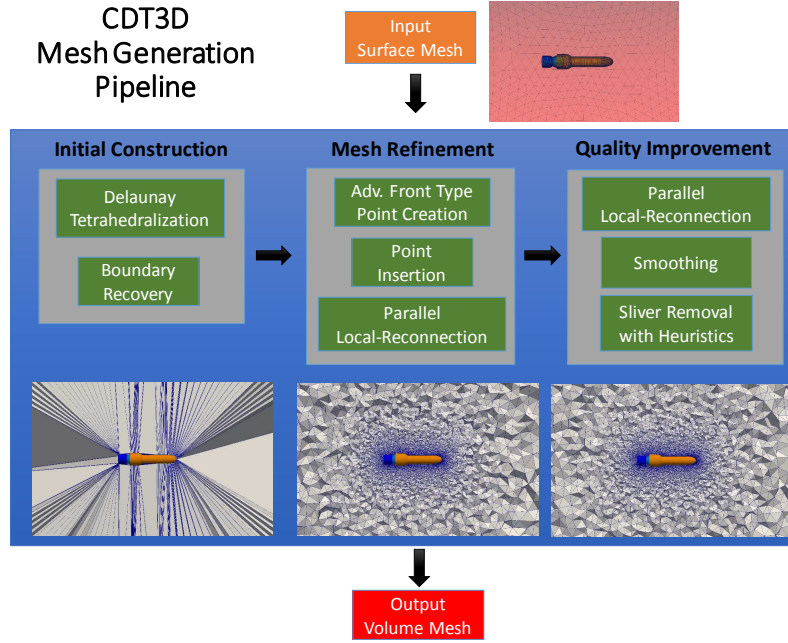


Figure 1: High level mesh generation pipeline of the CDT3D software.

The presented work is based on the isotropic CDT3D mesh generation software (Drakopoulos 2017, Drakopoulos, Tsolakis, and Chrisochoides 2017). The pipeline of CDT3D can be divided into three parts Initial Mesh Construction, Mesh Refinement and Mesh Optimization (see Figure 1).

The first step creates a Delaunay mesh of the input boundary points and Boundary recovery modifies the Delaunay mesh in order to contain all the initial edges and faces of the input surface triangulation with no or very low number of Steiner points.

Mesh Refinement inserts new points into the mesh until the desired point distribution function is satisfied. New points are created using advancing-front point type placement and direct insertion is used to introduce them into the mesh. A local reconnection step containing edge and face flips is performed in parallel optimizing a combined Delaunay and Min-Max type (maximization of the minimum Laplacian edge weight) criterion. These three steps are performed repetitively until no point is inserted.

During the final stage of the pipeline, the mesh quality is improved repetitively using a combination of vertex smoothing, local reconnection and point insertion with heuristics to remove isolated bad shape elements.



### 3.2 Anisotropic Mesh Generation

The adaptive version of the code follows the same steps as in figure 1 but performs all the evaluations of distances, angles and volumes using the formulas presented in section 2. Vertex Insertion remains unmodified since it uses direct insertion which modifies the mesh using only mesh connectivity information. Sliver removal has not been implemented in the adaptive version since the heuristics used, depend heavily on the uniformity of the physical space. The rest of the steps are modified as follows:

**Vertex Creation** During vertex creation, between each pair of active and inactive tetrahedra a candidate point is generated by advancing from the common face in a distance that will create an equilateral element based on an appropriate length scale. Since in the adapted version the quality is specified by the metric tensor, the distance is evaluated in the metric space. More specifically, a candidate point  $P$  is created on the centroid of the face between the two tetrahedra. The metric is interpolated on  $P$  producing  $\mathcal{M}_P$ .  $P$  is then advanced perpendicular to the face by a unit distance as measured by the Euclidean length (equation (1)) using  $\mathcal{M}_P$ . As with the isotropic case  $P$  will be rejected if it is too close to the boundary, to existing vertices or to other candidate points. For evaluating the distances in this case formula (5) is used, since all the pre-existing vertices and candidate points have already a metric tensor assigned to them.

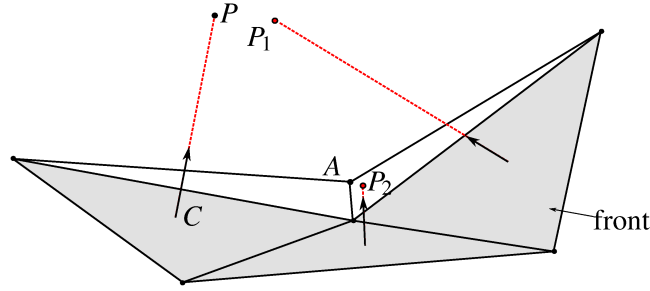


Figure 2: On the left face:  $C$  is the centroid of the face and the initial position of  $P$ .  $P$  is then advanced normal to the face and by a distance unit in the metric on  $C$ , ( $\|CP\|_{\mathcal{M}_C} = 1$ ).  $P_1, P_2$  are generated in a similar manner but they are both rejected.  $P_1$  is too close to a candidate point ( $\ell_{\mathcal{M}}(PP_1) < eps$ ).  $P_2$  is too close to a mesh vertex ( $\ell_{\mathcal{M}}(AP_2) < eps$ ). Where  $eps$  is a user defined threshold. they are too close to a candidate it

**Local Reconnection** Local Reconnection consists of modifying the connectivity of the mesh while optimizing some criteria. In CDT3D, 2-3,3-2 and 4-4 flips are used coupled with the in-sphere or the Min-Max criterion. To introduce anisotropy to these calculations the criteria have been adapted as follows:

The in-sphere test of a point  $y$  against a tetrahedron  $K = (x_1, x_2, x_3, x_4)$  is replaced with the weighted one presented in (Dobrzynski and Frey 2009) :

$$\left\{ \begin{array}{l} \alpha_{\mathcal{M}_y}(y, K) < 1 \\ \sum_{i=1}^4 \alpha_{\mathcal{M}_{x_i}}(y, K) + \alpha_{\mathcal{M}_Q}(y, K) < 5 \end{array} \right. \quad \text{where} \quad \begin{array}{l} \alpha_{\mathcal{M}_R}(R, K) = \frac{\|O_K y\|_{\mathcal{M}_R}}{\ell_{\mathcal{M}_R}(r_K)} \\ O_K \text{ circumcenter of } K \\ r_K \text{ circumradius of } K \end{array}$$

In isotropic configurations evaluating the Laplacian Edge Weight for an element  $K$  consists in evaluating the following quantity:

$$Q(K) = \max_{i=1 \dots 6} \frac{\langle n_{F_{i,1}}, n_{F_{i,2}} \rangle}{6|K|}$$

where  $n_{F_{i,1}}, n_{F_{i,2}}$  are the 2 faces attached to the  $i$ -th edge.

For the anisotropic case, the formula for  $Q(K)$  is adapted using a metric tensor  $\mathcal{M}$  evaluated on the centroid of  $K$ . Moreover, a formula that uses only inner products is used (Marcum and Alauzet 2013), to avoid the expensive evaluation of cross products:

$$Q_{\mathcal{M}}(K) = \max_{i=1\dots 6} \frac{\langle e_i, e_j \rangle_{\mathcal{M}} \cdot \langle e_i, e_k \rangle_{\mathcal{M}} - \langle e_i, e_i \rangle_{\mathcal{M}} \cdot \langle e_j, e_k \rangle_{\mathcal{M}}}{6|K|_{\mathcal{M}}} \quad (6)$$

**Vertex Smoothing** One of the most effective parts of mesh quality improvement in CDT3D is the one of mesh smoothing. In this work, the optimal point placement smoothing algorithm was used. The optimal point placement repositions each vertex of the mesh to the average of  $k$  optimal positions, where  $k$  is the number of boundary faces. In the metric space the optimal position for a face with vertices  $a, b, c$  is evaluated using:

$$E_{abc} = C_{abc} + \sqrt{\frac{2}{3}} \cdot \frac{\vec{n}}{\|\vec{n}\|_{\mathcal{M}}} \cdot \frac{1}{3} \left( \|\vec{ab}\|_{\mathcal{M}} + \|\vec{bc}\|_{\mathcal{M}} + \|\vec{ca}\|_{\mathcal{M}} \right)$$

where  $C_{abc}$  is the centroid and  $\vec{n}$  the normal of the face. Similar to the isotropic case, the final position of the point is found by evaluating the average out of the  $k$  optimal points.

## 4 RESULTS

The adaptive algorithm was evaluated on metric tensors given as analytical functions. During the evaluation of the algorithm it became apparent that if the boundary mesh is also adapted then the final mesh has better quality. For this reason, the open source MMGS library (Dobrzynski and Frey 2009, Dapogny, Dobrzynski, and Frey 2014, MMG developers 2018) was used to adapt the input surface mesh to the provided metric as pre-processing step.

In this work the quality of the meshes is assessed using the edge lengths of the tetrahedra as evaluated by the metric and the mean ratio (Liu and Joe 1994) in the metric space:

$$\eta(K) = \frac{12(3|K|_{\mathcal{M}})^{\frac{2}{3}}}{\sum_{i=1\dots 6} \ell_{\mathcal{M}}^2(e_i)} \in [0, 1]$$

where  $\mathcal{M}$  is the metric tensor interpolated at the centroid of the tetrahedron. The constants in this formula are selected in a way that the mean ratio of an ideal element is 1.0. For the edge lengths, since the goal is to create a mesh as uniform as possible in the metric space, ideal value of edge length is also 1.0. The presented method is compared against two of the open source mesh adaptation methods mentioned in the introduction. `refine` (Park 2018) developed at NASA, and `Omega_h` currently developed at Sandia National Labs (Ibanez 2018). Both of these mesh adaptation codes are used for large scale real time applications.

The qualitative statistics was generated using the `ref_histogram.sh` script of `refine`.

### 4.1 Linear Metric field in unit cube

The first example is a simple linear function with anisotropic stretching centered on the plane  $z = 0$  (Ibanez, Barral, Krakos, Loseille, Michal, and Park 2017). The analytic form is:

$$\mathcal{M}(x, y, z) = \begin{pmatrix} \frac{1}{h_x^2} & 0 & 0 \\ 0 & \frac{1}{h_y^2} & 0 \\ 0 & 0 & \frac{1}{h_z^2} \end{pmatrix}$$

where,  $h_x = 0.1, h_y = 0.1, h_0 = 0.001, h_z = h_0 + 2(0.1 - h_0)|z - 0.6|$

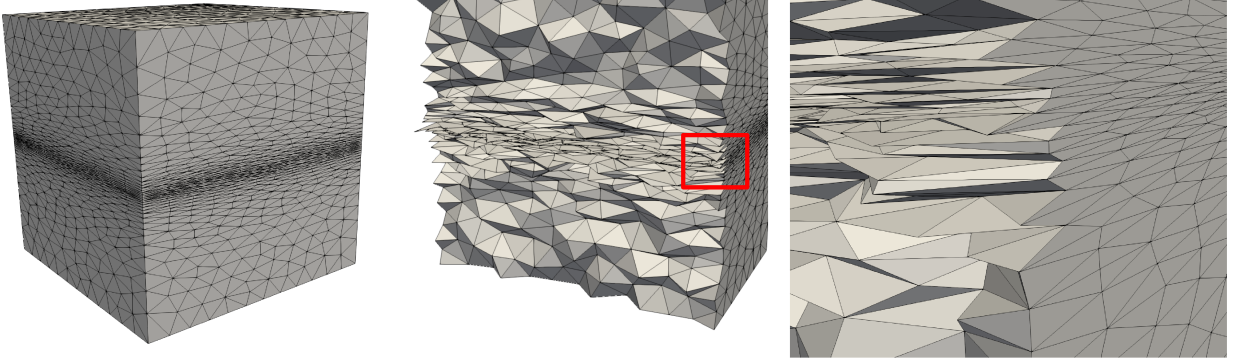


Figure 3: Generated mesh for the linear case: Surface , cross-cut and zoom-in view of the red section.

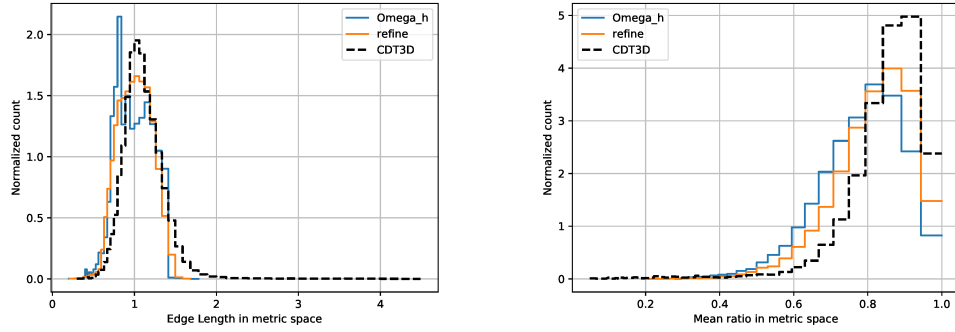


Figure 4: Quality statistics in the metric space for generated volume mesh. For the proposed method, 94% of the edges has length between  $[0.5, 1.5]$ . For refine and Omega\_h the percentages are 96% and 99% respectively. For the mean ratio 95% of the elements have quality higher that 0.7. For refine and Omega\_h the percentages are 90% and 85% respectively.

## 4.2 Quarter Cylinder Metric Function

In the second example curvature is introduced. The domain is again the unit cube, the function enforces a stretching around a cylinder along the  $z$ -axis. The analytic formula is taken from (Alauzet and Marcum 2017):

$$\mathcal{M}(x, y, z) = \begin{pmatrix} \frac{1}{h_x^2} \cos^2 \theta + \frac{1}{h_y^2} \sin^2 \theta & \left( \frac{1}{h_x^2} - \frac{1}{h_y^2} \right) \cos \theta \sin \theta & 0 \\ \left( \frac{1}{h_x^2} - \frac{1}{h_y^2} \right) \cos \theta \sin \theta & \frac{1}{h_x^2} \sin^2 \theta + \frac{1}{h_y^2} \cos^2 \theta & 0 \\ 0 & 0 & h_z \end{pmatrix}$$

where,  $h_x = \min(0.002 \cdot 5^a, h_{max})$ ,  $h_y = \min(0.05 \cdot 2^a, h_{max})$ ,  $h_z = h_{max}$ ,  $h_{max} = 0.1$ ,  $\theta = \arctan(x, y)$ ,  $a = 10 \cdot |0.75 - \sqrt{x^2 + y^2}|$

In both examples, the distribution of both criteria is very close to the other two mesh adaptation methods. There is though a small number of low quality elements in the mean ratio quality metric as well as some edges longer as they should. Future versions of the algorithm will target on eliminating those elements.

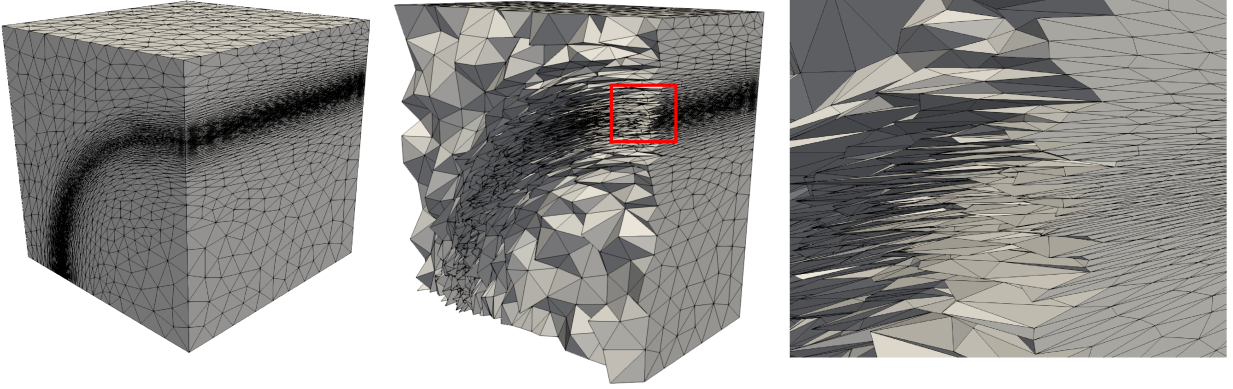


Figure 5: Generated mesh for the quarter cylinder case: Surface , cross-cut and zoom-in view of the red section.

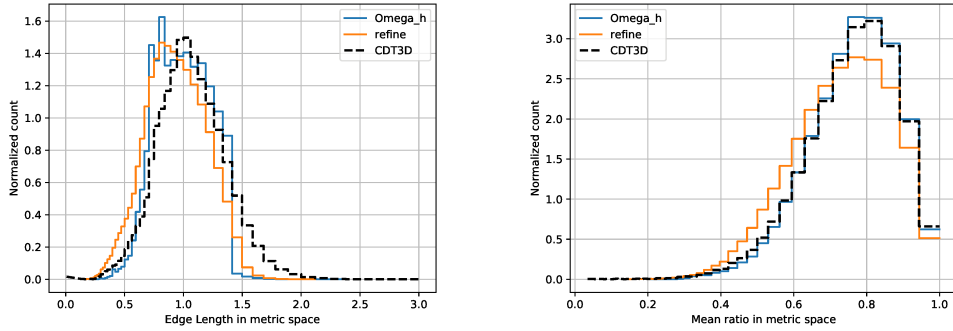


Figure 6: Quality statistics in the metric space for generated volume mesh. For the proposed method, 91% of the edges has length between  $[0.5, 1.5]$ . For refine and Omega\_h the percentages are 98% and 99% respectively. For the mean ratio 78% of the elements have quality higher than 0.7. For refine and Omega\_h the percentages are 69% and 79% respectively.

## 5 CONCLUSION

In this work, CDT3D, an in-house isotropic mesh generator was modified to support mesh adaptation based on a metric tensor. The modifications on the code were minimal. Topological transformations remain the same but qualitative evaluations are adapted in two ways. Whenever a local evaluation is needed, the Euclidean formulas are used based either on the metric tensor of the point itself or on the metric tensor of an interpolated point. On the other hand, when the length of a segment is needed the Riemannian framework was used in order to take into consideration the metric of both endpoints. Initial results on analytic metrics look promising although there is room for improvement:

To eliminate long edges an additional step could be added targeting only on those or alternatively the edge/face flip criteria could be modified to take into account not only the element quality as a whole but also the lengths of the individual edges. Additionally, it has been shown that metric orthogonal strategies for generating metric adapted meshes offer better quality (Alauzet and Marcum 2017, Loseille 2014). Given the modularity of CDT3D this point creation method could be created with low effort.

In contrast to the provided examples, in most simulation settings the analytic form of the metric is not available. In these cases metric information is given in a form of a coarse background mesh. Although, metric interpolation is already implemented interpolating from a background mesh requires some extra steps that need to be implemented.

## REFERENCES

- Alauzet, F. 2010. “Size Gradation Control of Anisotropic Meshes”. *Finite Elements in Analysis and Design* vol. 46, pp. 181–202.
- Alauzet, F., and D. Marcum. 2017. “Metric-Aligned and Metric-Orthogonal Strategies in AFLR”. In *23rd AIAA Computational Fluid Dynamics Conference*. Denver, Colorado, American Institute of Aeronautics and Astronautics.
- Arsigny, V., P. Fillard, X. Pennec, and N. Ayache. 2006, aug. “Log-Euclidean Metrics for Fast and Simple Calculus on Diffusion Tensors”. *Magnetic Resonance in Medicine* vol. 56 (2), pp. 411–421.
- Chrisochoides, N. P. 2016. “Telescopic Approach for Extreme-Scale Parallel Mesh Generation for CFD Applications”. In *46th AIAA Fluid Dynamics Conference*. American Institute of Aeronautics and Astronautics.
- Dapogny, C., C. Dobrzynski, and P. Frey. 2014. “Three-dimensional adaptive domain remeshing, implicit domain meshing, and applications to free and moving boundary problems”. *Journal of Computational Physics* vol. 262, pp. 358 – 378.
- Dobrzynski, C., and P. Frey. 2009. “Anisotropic Delaunay Mesh Adaptation for Unsteady Simulations”. In *Proceedings of the 17th International Meshing Roundtable*, edited by R. V. Garimella, pp. 177–194. Springer Berlin Heidelberg.
- Drakopoulos, F. 2017. *Finite Element Modeling Driven by Health Care and Aerospace Applications*. Ph. D. thesis, Computer Science, Old Dominion University.
- Drakopoulos, F., C. Tsolakis, and N. P. Chrisochoides. 2017. “Fine-Grained Speculative Topological Transformation Scheme for Local Reconnection Methods”. In *AIAA Aviation Forum*, pp. accepted.
- George, P. L., F. Hecht, and M. G. Vallet. 1991. “Creation of Internal Points in Voronoi’s Type Method. Control Adaptation”. *Advances in Engineering Software and Workstations* vol. 13 (5), pp. 303–312.
- Gorman, Gerard J. 2018. “pragmatic GitHub site”. <https://meshadaptation.github.io>.
- Gorman, G. J., G. Rokos, J. Southern, and P. H. J. Kelly. 2015. “Thread-Parallel Anisotropic Mesh Adaptation”. In *New Challenges in Grid Generation and Adaptivity for Scientific Computing*, SEMA SIMAI Springer Series, pp. 113–137. Springer, Cham.
- Hecht, Frédéric 2018. “BAMG - Bidimensional Anisotropic Mesh Generator”.
- Ibanez, Dan 2018. “Omega\_h GitHub site”. [https://github.com/ibaned/omega\\_h](https://github.com/ibaned/omega_h).
- Ibanez, D., N. Barral, J. Krakos, A. Loseille, T. Michal, and M. Park. 2017, January. “First Benchmark of the Unstructured Grid Adaptation Working Group”. *Procedia Engineering* vol. 203, pp. 154–166.
- Ibanez, D., and M. Shephard. 2016. “Mesh Adaptation for Moving Objects on Shared Memory Hardware”. *Procedia Engineering*, pp. 5.
- Liu, A., and B. Joe. 1994, June. “Relationship between Tetrahedron Shape Measures”. *BIT Numerical Mathematics* vol. 34 (2), pp. 268–287.
- Loseille, A. 2014, January. “Metric-Orthogonal Anisotropic Mesh Generation”. *Procedia Engineering* vol. 82 (Supplement C), pp. 403–415.

- Loseille, A., and F. Alauzet. 2011. “Continuous Mesh Framework Part I: Well-Posed Continuous Interpolation Error”. *SIAM Journal on Numerical Analysis* vol. 49 (1), pp. 38–60.
- Loseille, A., and R. Löhner. 2009. “On 3D Anisotropic Local Remeshing for Surface, Volume and Boundary Layers”. In *Proceedings of the 18th International Meshing Roundtable*, pp. 611–630. Springer, Berlin, Heidelberg.
- Marcum, D. L., and F. Alauzet. 2013. “Unstructured Mesh Generation Using Advancing Layers and Metric-Based Transition for Viscous Flowfields”. In *21st AIAA Computational Fluid Dynamics Conference*. American Institute of Aeronautics and Astronautics.
- Mavriplis, D. J. 1990, October. “Adaptive Mesh Generation for Viscous Flows Using Triangulation”. *Journal of Computational Physics* vol. 90 (2), pp. 271–291.
- Michal, T., and J. Krakos. 2012. “Anisotropic Mesh Adaptation Through Edge Primitive Operations”. In *50th AIAA Aerospace Sciences Meeting Including the New Horizons Forum and Aerospace Exposition*. American Institute of Aeronautics and Astronautics.
- Michal, T. R., D. Babcock, D. S. Kamenetskiy, J. Krakos, M. Mani, R. S. Glasby, T. Erwin, and D. Stefanski. 2017. “Comparison of Fixed and Adaptive Unstructured Grid Results for Drag Prediction Workshop 6”. In *55th AIAA Aerospace Sciences Meeting*. American Institute of Aeronautics and Astronautics.
- MMG developers 2018. “Mmg Platform”. <https://www.mmgtools.org>.
- Park, Mike 2018. “refine GitHub site”. <https://github.com/nasa/refine>.
- Park, M., and D. Darmofal. 2008. “Parallel Anisotropic Tetrahedral Adaptation”. In *46th AIAA Aerospace Sciences Meeting and Exhibit*. American Institute of Aeronautics and Astronautics.
- Peraire, J., M. Vahdati, K. Morgan, and O. C. Zienkiewicz. 1987, October. “Adaptive Remeshing for Compressible Flow Computations”. *Journal of Computational Physics* vol. 72 (2), pp. 449–466.



# HYPOANALYZER : A REAL TIME INTERACTIVE DASHBOARD FOR HYPOTHESIS

Wessam Elhefnawy  
Department of Computer Science  
Old Dominion University  
4700 Elkhorn Ave, Suite 3300, Norfolk, VA, USA  
welhefna@cs.odu.edu

## ABSTRACT

Web annotation systems have been receiving more attraction, such systems help sharing knowledge among web visitors as they are allowed to annotate the web resources and provide personal comments. Some of existing web annotation systems such as Hypothes.is has limited information insight. In this work, we introduce an interactive dashboard aims to provide a unified and dynamic representation by bring together analysis and visualization of web annotated resources. Data mining and machine learning methods are employed to find dependencies and relation between annotated web resources to give hypothes.is users deep insight to web resources. Our dashboard provides global overview for domains common patterns, connectivity of web domains, and annotated web resources distribution.

**Keywords:** web annotation, visualization , dynamic dashboard, real time analysis.

## 1 INTRODUCTION

In the visual analysis process, where analysts access information from multiple sources to combine insights, a well-designed interactive visualization is very essential. Since, the process of visual analysis may last for many weeks and given the limits of human memory [1]. Thus, the importance of gaining insights into the data, identify patterns, and make decisions given by the interactive visualizations are vital for visual analysis.

Dashboards, collections of multiple visual components on a single view, are the most popular visualization tools in the domain of annotation analysis [2]. The researches on annotation analysis has increased significantly in the past few years, however most of the created work engaged the visualization and analysis to facilitate the search, query and navigation but didn't provide any correlation aggregation or statistical representation for the data. One example of such researches [3] where the analysis of large bodies of texts were supported by interactive techniques and visualization of annotations. Another ex-ample [4] which uses machine learning methods integrated with visual interface to allow non-experts to benefit from the given system.

This paper presents HypoAnalyzer dashboard that aims to overcome the shortage in the previous researches by providing users with the facility to interpret the annotation results using visual exploration of the patterns in the annotation domain. The provided system filters out the unimportant information and speed up the task of analysis of Hypothes.is online annotation repository.

The presented dashboard aims at integrating a set of data mining and visualization functionalities into a powerful tool, which provides new insights and discoveries. The presented system supports discovery by combining the following tasks: getting an overview of the whole annotation repository, correlation and aggregation patterns by internet domains or tags, comparing and contrasting the characteristics of different annotations patterns, showing patterns in the context of the annotation where they appear, seeing their distributions in different levels across internet domains or documents.

The paper is structured as follows. Section 2 describes the motivation of the proposed work. Section 3 present some related research work. Section 4 explain the data collection and analysis of the system, where the data cleaning is introduced and the data collection and analysis architecture were presented. Section 5 provides a comprehensive description about the design of the visualization system. The conclusion and future work are stated in Section 6.

## **2 MOTIVATION**

Manual annotation is used in most software packages and web-based annotation services (e.g. [hypothes.is](http://hypothes.is)), including the ability to set up a hierarchical list of categories and add resources to those categories, and adding free text comments. Although, being useful for the online domain all these features make it difficult to search or to use in semantic meaning extraction. However, research can't ignore the manual annotation as it can deliver a highly accurate information about the annotated re-source. Manual annotation can also simplify the understanding of resources and giving more attention to the important resources.

Hypothes.is is an open platform online system for manual annotation which allow tagging, comments and re-plies. It is characterized by the increasing number of users, annotated domains, and digital documents. All this make the data set on Hypothes.is a dynamically changing data set over time. Due to the importance of annotation there is a need to provide a system to give us information about these annotated data.

The best way to provide good information about all these data is to use interactive visualization along with deep data analysis (such as correlation, aggregation, and statistical analysis). Providing such a visualization system makes Hypothes.is data repository, much readable, easy to explore, analysis, and derive relations between annotations as well as support the global system overview.

## **3 RELATED WORK**

Visualization has succeeded to retrieve, compare, and rank computer programs [5], and entire text documents [6]. These visualizations depends on visualizing repetitions in sequence and patterns in text. Also some visualization techniques have been developed for biological sequence analysis such as arc diagrams, repeat graphs and dot plots[7, 8].

Several visualization and web annotation tools appear in the web community. Here is a short overview about some of them that are similar or related to Hypothes.is annotation visualization. One of the tools for web annotation and visualization is Portege[9], which offers an editing environment with several third party plug-ins. Portege also support a graphical visualization that is provided by Onto Viz tab plug-in, where the hierarchy of annotation is visualized as an RDF graph. Another web annotation tool is Knowledge and Information Management (KIM) plat-form [10] which targets automatic annotation of web re-sources and annotation population. In KIM plugin the an-notated parts of the text are colored with respect to a given annotation. Also, the KIM plugin supports browsing annotation. Additional tool is Magpie [11], is a framework supporting the analysis of web pages that is integrated in the standard web browser. Magpie user interface components visualize objects found in the page and allow users to interact with the services through contextual menus.

## 4 ANALYSIS

### 4.1 Data Collection and Wrangling

Hypothes.is annotation repository is a dynamic data source storing a structured annotations as a JavaScript object (JSON). Each notation holds several items, and every item consist of the attribute and its value. Due to the dynamic properties of the data this require the separation between the data collection, analysis, and visualization which is taken into consideration on the design of the proposed dashboard. Figure 1 shows the proposed system architecture. The figure shows the three stages of the system: Data Collector and analysis, Web Server, and Web Browser Based Visualization.

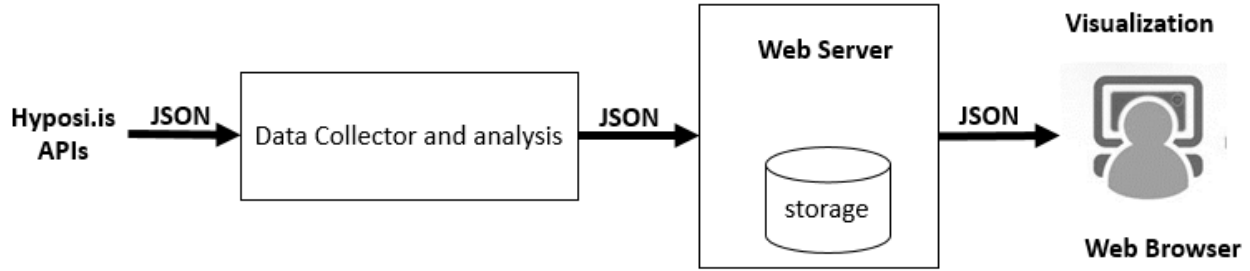


Figure 1 The proposed system architecture

Data collector and analysis stage is a background process that uses the Hypothes.is APIs to receive the raw annotation stream as JSON object and analysis it. Then it produce a JSON stream holding the extracted information. The web server stage is the link between the user and the data analysis, as it gets the extracted information form the data collector and analysis stage and provide the user with information to render it in the client side. Figure 2 shows the data collector and analysis stage design where it consists of three main modules Data Collection, Data Analysis, and Derived Data. The Data Collection module plays the main rule by collecting the data and periodic check for any changes to update the data using the Hypothes.is data repository APIs. Also it caches the raw data to reduce the reading time. When the Data Collection module is done caching the date the data analysis module starts its job. The data analysis module extract the important items for each annotation record and clean the unwanted items. It also validate and analyses the extracted data by doing a basic statistical analysis based on availability of tags and comments in each validated an-notation record. Then, the derived data module takes the output of the Data Analysis module validated annotation record and calculate the relation, grouping and extract facts.

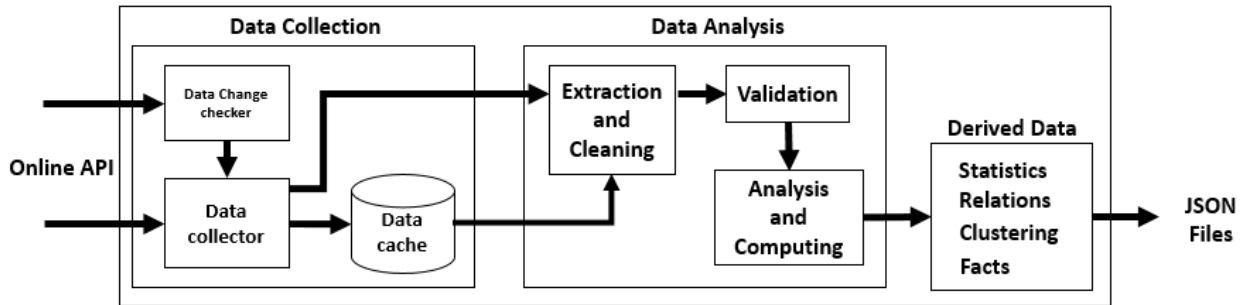


Figure 2 The data collection and analysis module internal structure.

During data extraction and cleaning unwanted items are removed from the raw data to save the storage and speed up the processing time. Figure 3 shows the most important items that is used to represent each annotation highlighted in blue. The ID item holds the annotation identification number which is very important to keep the identity of each annotation. The Created and Update items are used in the process of updating the changed annotations. URI (Universal Resource Identifier) item holds the resource type and the

annotation address. The Tags item holds the key words attached with the annotation, while the Text item holds the comments attached with the annotation.

TARGET		
Source	Selector	Pos
USER		
CREATED		
DOCUMENT		
Link	Title	
PERMISSIONS		
Delete	Update	Read Admin
URI		
TAGS		
CONSUMER		
ID		
TEXT		
UPDATED		

Figure 3 The annotation data record, the blue items are used in the proposed system to extract the information.

## 4.2 Data Abstraction

According to our data analysis for hypothes.is repository, three items can be useful to build interactive visualization system. These items are: URI, Tags, and Text. While the URI provide the resource access and Categories the annotation source into URL (web annotation), URN (multimedia an-notation) and Blob (local annotation). Tag provides a summary list of the most important words, while Text add description or additional context to the annotation.

Table 1 What-Why-How model for HypoAnalyzer dashboard.

System	HypoAnalyzer dashboard
What : Data	Structure dynamic stream JSON objects
What : Derived	Clustering, connectivity, statistics
Why : Tasks	Identify, Compare, and Summaries; distributions and correlation.
How: Encode	Bubble chart, Chord Chart, Bar Chart, and Stacked bar Chart
How: Manipulate	Select, Highlight
How: Facet	Juxtaposed four windows, view clustering, statistics, links with highlighting and size, popup details view
How : reduce	Filter to reduce the number of visualized domains based on number size of the domain
Scale	All annotations in hypothes.is repository are grouped by domain name

URI is beneficial to group annotations in three categories URL, URN, and BLOB. Figure 4 shows the Structure of URL format which provides three important information : protocol type, domain name and domain suffixes, and resource identification. Using the domain name and domain suffix as identifiers allows grouping of URL based annotations in internet domains groups. Whereas using the domain suffix cluster the online domains in Effective Country Code Top level (Effective CCTL), Top-level do-main(TLD),and Country Code Top-level domain (CCTLD).

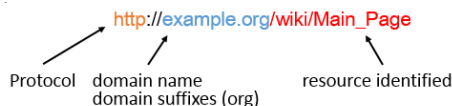


Figure. 4 URI format for online resource.

The Tags item holds the important keywords which is useful to find the dependency relation, correlation, and similarity between different online domains, as shown in Table 2. Combining tags and comments make it possible to find the distribution per cluster, and the distribution per the online do-main. Also the proposed system uses this combination to calculate statistical probability, which gives the user summarized information about the availability of annotations. In addition it was also useful to validate the output of visualization, Table 1 show the What-Why-How model.

**Table 2 Actions and Targets for data abstraction**

Annotation Item	Actions	Targets
URI	Identify	Correlation
	Compare	Similarity
	Summarize	
TAGS	Identify	Topology
	compare	paths
	derive	Dependency correlation
TAGS + TEXT	Discover	Distribution
	derive	
	compare	

Table 2 shows actions and targets for each selected item from the annotation record. The targets given in the table is what we aim to get to the user from the visualization system.

### 4.3 Data Visualization Decisions

Nowadays there are many different types of visualization charts, but not all charts are suitable to represent massive information efficiently. For that, In HypoAnalyzer dashboard choosing a good visualization chart is important to the visualization task. One of the options is to visualize the data using directed force tree. As directed force tree is a useful visualization tool to show topological relationship. Directed force tree in Figure 5 consists of a collection of nodes and edges, where the nodes are used to encode the size of domain in the whole data set and its color encode the category. The edges represent the connectivity between the nodes, the size encode the weight of the connectivity. Although the usefulness of the directed force tree in relation representation, it suffers from many problems in dynamic information representation. One of these problems is the need to change lots of configuration parameters with any small change in the data, which make the chart suffer from collision and overlapping between nodes and edges. Solving such a problem by self-tuning methods is very difficult and not efficient especially with a dynamically changing data.

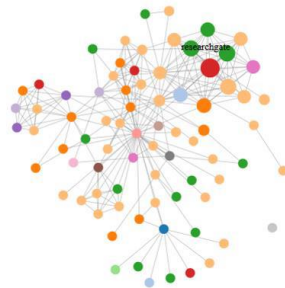


Figure. 5 shows a directed force tree, nodes size encodes the size of domain, nodes color encodes categories, and links encode the relationships between domains.

After exploring the back draw of using directed forced tree we came to a conclusion that a single chart will not be sufficient to give a good visualization of the data. For that, In HypoAnalyzer an interactive multiple chart are connected together to overcome any shortage of single chart visualization.

## 5 HYPOANALYZER DASHBOARD

Since HypoAnalyzer dashboard aims to provide an online dynamic visualization dashboard, web technologies were used in the implementation. The dashboard developed using html5, JavaScript, and D3. In this section we provide a comprehensive description for the visualization charts used in the presented dashboard.

## 5.1 Layout

The presented visualization system consists of four inter-active juxtapose visualization to show the relation between the annotations as shown in Figure 6. The main chart of the system is an interactive bubble chart that represents the clusters of the annotations (Cluster Chart). The chord chart is used along with the bubble chart to illustrate the relation between domains (Relation Chart). The bar chart is used to show the part of whole relation between cluster and dataset (Availability Chart). The stacked bar chart provides a statistic as a part of whole relationship between domain, cluster and whole dataset (Statistics Chart). A control panel is attached to the system to choose the clustering method and control the dynamic features of the visualization system.

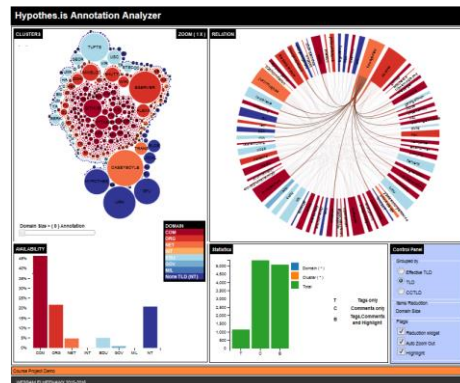


**Figure. 6 Hypothes.is annotation analyzer visualization system**

## 5.2 Annotated Web Resources Clusters

In Figure 7, clusters of domains are visualized using interactive bubbles chart where each domain is presented as a bubble and each coherent groups of domains are represented by unique color. The distribution of domain is encoded by the size of the bubble, while the color is used to encode the cluster distribution. The domains are clustered based on effective CCTL, TLD, and CCTLD specification of annotated domains in Hypothes.is repository.

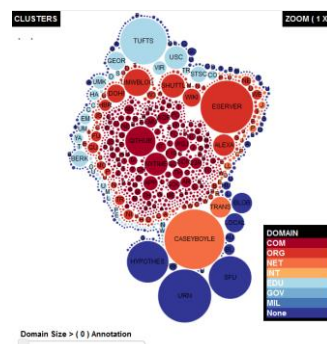


**Figure. 7 The Cluster chart, a bubble based chart shows domains and related clusters.**

### 5.3 Domains Connectivity

The connectivity of domains is represented by a dynamic chord chart shown in Figure 8, each chord is a domain. The connectivity between domains is measured by common tags, comments, and resource similarity. The links between cords represent the connectivity, the quadratic weighted link encode the weighted relation between chords. The weight of link normalized to degree of connectivity. Tooltip provides user by more information about relation between domains (e.g. weight of relation, tags).



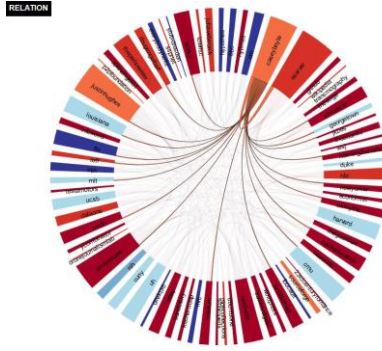


Figure. 8 The relation chart, a chord based visualization shows links between domains in Hypothes.is dataset.

## 5.4 Domains Distribution

In Figure 9, a dynamic bar chart is used to show the part of whole relationship between the clusters and the whole Hypothes.is data set where the chart keys represent the different clusters and the bar height represents the percentage of availability. This chart dynamically changes with the selected method for clustering.

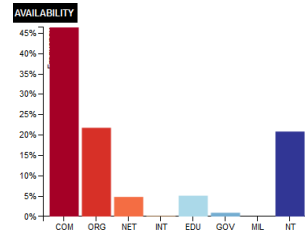


Figure 9 The availability chart, a bar chart shows the part of whole relation between cluster and whole Hypothes.is dataset.

## 5.5 Domain Annotated Resources Distributions

Figure 10 shows distribution of annotated web resources: tags (T), comments (C) and both tag and comment (B). This chart is supported by summary table showing the percentage of each resource in the selected domain to its cluster and total Hypothes.is dataset.

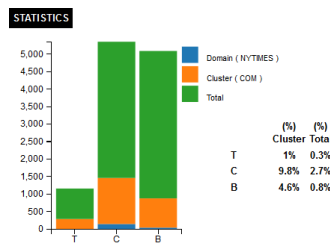


Figure 10 The statistics chart, a stacked bar chart shows summary statistics for each domain relative to cluster and Hypothes.is dataset.

## 5.6 Color Scheme

In HypoAnalyzer dashboard charts have common color scheme. The change in any of charts reflected in the corresponding charts as shown in Figure 5. The consistency in color schemes improves the connection between dashboard charts which makes them correlated and readable. The color schemes is examined by the colorbrewer2 [12] to avoid the color selection problems.

## 5.7 Data Reduction

The dashboard of HypoAnalyzer is supported by an interactive filters to allow the user to control the view of the dashboard. All of the domains in the Hypothes.is repository are shown by default at the start of a session to provide an global overview, and the interactive filter manipulates the clusters to reformulate

the view queries. This filter is well suited to browsing the repository information, where the user formulate the view query according to analysis process directions. Figure 11 show the effective usage of domain filter, and the reflection of the filter on the connectivity chart where the filtered out domains are deleted from the clusters chart and them color are changed to gray scale in the connectivity chart.

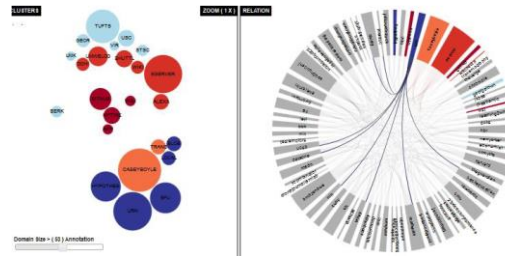


Figure 11 The interactive slider at the bottom of the clusters chart used to filter out or add back the clusters domains, and reflect the changes to the relation chart, only domains have more 53 annotations are encoded.

## 5.8 Interaction

HypoAnalyzer allows several types of interactions as an integral part of the system. The user can enable or disable these features using the control panel options. Moving the mouse pointer over the clusters chart make focus on the hovered bubble cluster. Similar domains bubbles are highlighted by fading out unrelated clusters while the selected bubble is highlighted by surrounding it with a strong black circle. This selection process updates other charts based on the selected domain information. Double clicking any domain bubble activates the geometric zoom and the highlighting feature as shown in Figure 12. Moving the mouse out of the bubble reset the view and remove the highlighting and zooming effect from the clusters chart. The user may also move the mouse over bubble, chords and links for additional detailed information.

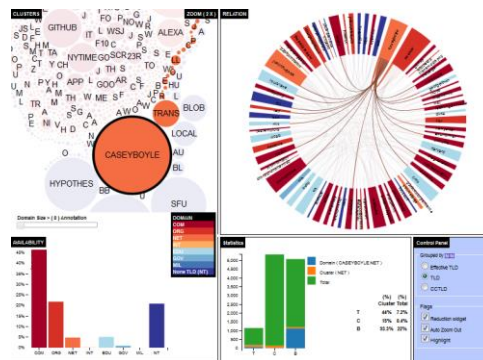


Figure 12 Interactive features of Hypothes.is annotations analyzer selection, highlight and geometric zooming.

The dashboard is designed for rapid exploration, with the goal of encouraging easy movement between different views, and allow users took advantage of this interactivity.

## 6 CONCLUSION

HypoAnalyzer is a dynamic web based visualization dashboard for exploring the hypothes.is annotation repository. The dashboard provide a real time interactive domain analysis over the annotated web resources using data mining and machine learning. HypoAnalyzer architecture designed to speed up the online dynamic data visualization and reduce the memory usage. By incorporate multi-interactive visualization charts, HypoAnalyzer allows users to get deep insight with annotated web resources. Finally, this paper has outlined a number of promising directions for future research that build on the real time dynamic data

analysis and interactive methodology used by HypoAnalyzer. Some of these directions could be to make the dashboard design more reactive, incorporate spatial information such as hosting , design efficient idiom to utilize the topology analysis such as indirect relationship among Hypothes.is users, or provide online API to allow easy access for the derived information.

## REFERENCES

- [1] Cowan, N. Attention and Memory: An Integrated Framework, vol. 26 of Oxford Psychology Series. Oxford University Press, 1998.
- [2] Cutroni, J. Google Analytics. O'Reilly Media, Inc., 2007.
- [3] Fekete, J. and Dufournaud, N., Compus: visualization and analysis of structured documents for understanding social life in the 16th century. In Proc. of the Fifth ACM Conference on Digital Libraries, 47-55. 2000.
- [4] Plaisant, C. and Rose, J. and Yu, B. and Auvil, L. aKirschenbaum, M. and Smith, M. and Clement, T. and Lord, G., Exploring Erotics in Emily Dickinson's Correspondence with Text Mining and Visual Interfaces, in Proc. of the 6th ACM/IEEE-CS Joint Conference on Digital Libraries, 141-150. 2006.
- [5] G. Lommerse, F. Nossin, L. Voinea, A. Telea, the Visual Code Navigator: An Interactive Toolset for Source Code Investigation. In Proc. IEEE InfoVis'05, 24-31. 2005.
- [6] Wise, J. A. and Thomas, J. J. and Pennock, K. and Lantrip, D. and Pot-tier, M. and Schur, A. and Crow, V., Visualizing the non-visual: spatial analysis and interaction with information from text documents, In proc IEEE Symposium on Information Visualization 1995, 51-58. 1995.
- [7] Frank, A. C., Amiri, H., Andersson, S., Genome Deterioration: loss of repeated sequences and accumulation of junk DNA. *Genetica*, Vol. 115, No. 1, 1-12. 2002.
- [8] Kurtz, S & Schleiermacher, C. REPuter: fast computation of maximal repeats in complete genomes. *Bioinformatics* 15, 426-427. 1999.
- [9] Noy, N., Sintek, F., Decker, M., S., M., R. W., Fergers on and M. Musen. A. Creating Semantic Web Contents with Protege-2000. *IEEE Intelligent Systems* 16(2):60-71, 2001.
- [10] Popov, B., Kiryakov, A., Ognyanoff, D., Manov D. and A. Kirilov. KIM -a semantic platform for information extraction and retrieval. *Journal of Natural Language Engineering*, Vol. 10, Issue 3-4, Sep 2004, pp. 375-392, Cambridge University Press
- [11] Dzbor, M., Domingue, J. and Motta, E. Magpie -Towards a Semantic Web Browser. 2nd International Semantic Web Conference (ISWC2003) 20-23 October 2003, Sundial Resort, Sanibel Island, Florida, USA <http://kmi.open.ac.uk/projects/magpie/main.html>
- [12] Color Brewer 2: Color Advice for Maps. Cynthia Brewer, Mark Harrower and the Pennsylvania State University. <http://color-brewer2.org/>

# MULTI-THREADED SIMULATION EXECUTIVE FOR MULTI-CORE PROCESSORS

Brandon Waddell

James F. Leathrum Jr.

Department of Modeling, Simulation, and Visualization Engineering

Old Dominion University

5115 Hampton Blvd

Norfolk, VA, USA

bwadd006@odu.edu

jleathru@odu.edu

## ABSTRACT

Classical Parallel Discrete Event Simulation (PDES) increases simulation performance by distributing the simulation application across multiple computing platforms. A burden is placed on the developer to partition the simulation. This work focuses instead on identifying available parallelism within the simulation executive, thus removing the burden from the developer. Event scheduling and event execution natural parallelism with each other; future events may be scheduled with the simulation executive while the currently executing event continues. The execution and scheduling are dealt with as multiple threads, taking advantage of multicore architectures. This paper identifies the available parallelism between event scheduling and execution, highlight points of contention between the two, and present algorithms to take advantage of the parallelism.

**Keywords:** Discrete Event Simulation, Parallel Discrete Event Simulation, Simulation Executive, Event Scheduling, Event Execution, Multi-threading, Resource Contention

## 1 INTRODUCTION

Discrete Event Simulations (DES) are developed for many systems. A DES consists of a reusable simulation executive and a simulation application. The simulation executive is responsible for event list management while the simulation application is responsible for defining event functionality. A standard DES is developed to run serially which inherently have longer execution times as the system grows larger. Historically distributed simulation is utilized to increase performance by partitioning the system across many processors. With the partitioning of the system, significant modifications to the simulation application are required; this leaves developers with substantial development overhead (Fujimoto 2000).

An alternative approach to partitioning the system across multiple processors is to utilize multiple cores on single processor by creating multiple threads of execution that work concurrently. This approach can be used to lower the burden placed on the simulation developer. A multi-core processor is best utilized when there is a low number of available parallelism that is identified due to the limited number of cores on a processor. Low-levels of parallelism can be identified between event scheduling and event execution within the simulation executive which creates a suitable environment to utilize a multi-core processor. With the parallelism being identified in the simulation executive, an increase in performance to a DES can be achieved without modifications to the application.

## 2 BACKGROUND

### 2.1 Discrete Event Simulation (DES)

Discrete event simulation is a system modeling technique that describes the behavior of the system as a series of state transitions at specific moments in time. These states are transitioned through a sequence of events that occur at a specific moments in time (Chen 2015). These events are executed in timestamp order therefore a DES contains an event list that holds all future events in timestamp order. There is no physical delay between event executions but rather the simulation time will instantaneously change when an event is executed. Figure 1 shows an ordered event list being executed by the simulation.

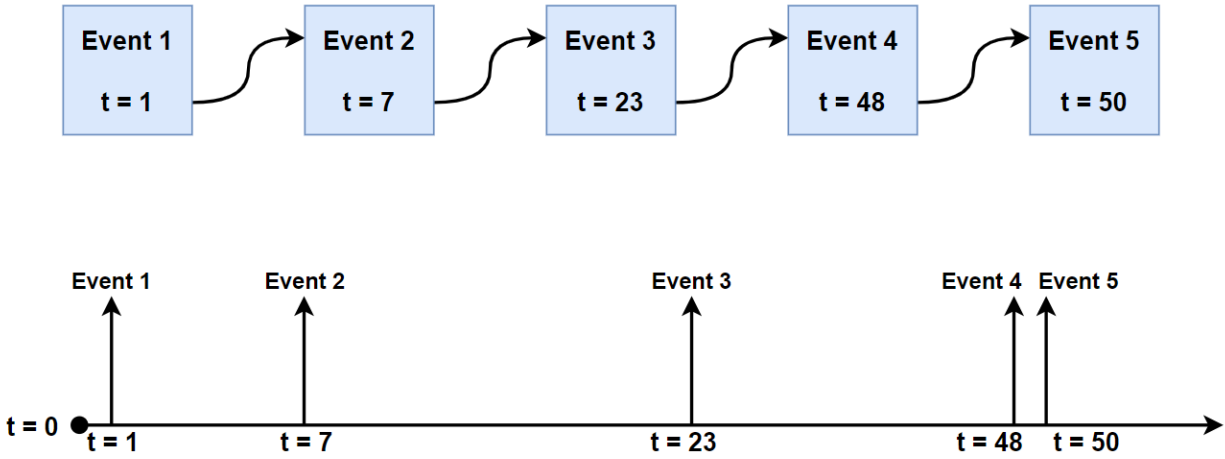


**Figure 1: Event List (top) and DES Execution (bottom)**

A standard approach to DES software development is to partition the simulation into the simulation application software and a reusable simulation executive as illustrated in the architecture in Figure 2. (Pidd 2004) The simulation executive is responsible for selecting the next event to execute in nondecreasing timestamp order, advancing simulation time to that of the currently executing event, and the scheduling of future events provided by the simulation application. The simulation application is responsible for executing the events which involves changing state information and scheduling future events. The simulation executive uses the control loop in Figure 3 to manage event execution. (Law 2004) Pidd provides the modified loop when handling conditional events in addition to scheduled events as found in the 3-phase worldview (Pidd 2004). The algorithm for scheduling future events by placing them in the event list in timestamp order is provided in Figure 4. The event list structure being used is a sorted linked list although alternative structures exist (Vaucher 1975) such as heaps, calendar queues (Brown 1988), and lazy queues (Ronngren 1991). These algorithms in Figures 3 and 4 are presented as the foundation upon which parallelism is identified.

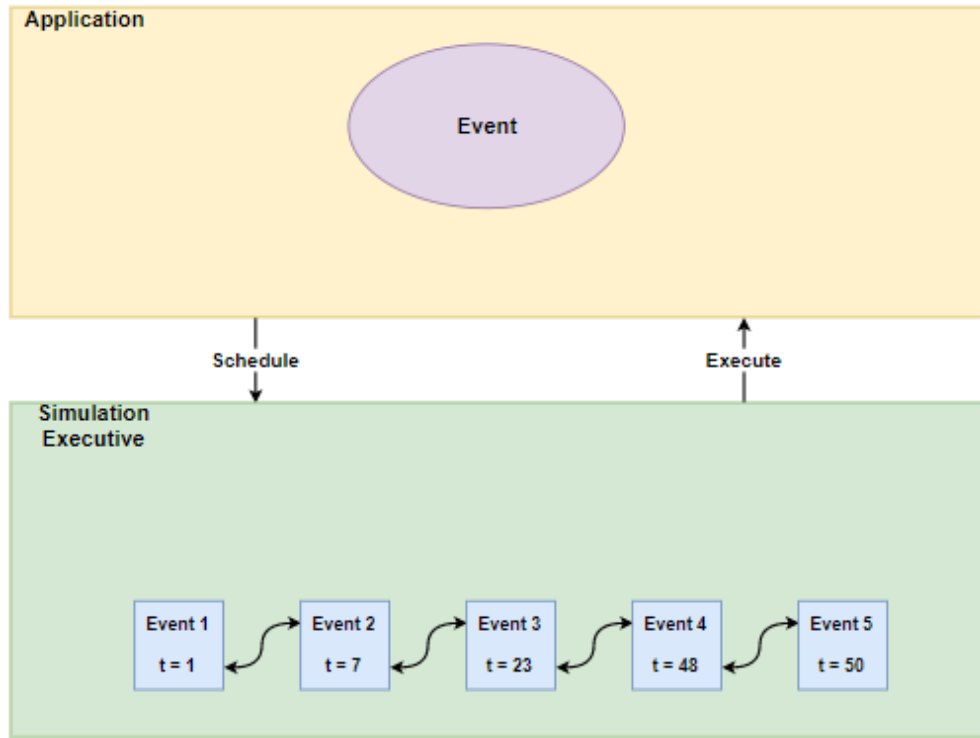


**Figure 2: Application and Simulation Executive Relationship**

```

While Simulation is not done
  Get the next event
  Simulation Time = Event Time
  Execute the event

```

**Figure 3: Run Simulation Algorithm**

```

If (NewEvent.Time < First.Event.Time)
  Add NewEvent as FirstEvent;
IteratorEvent = FirstEvent;
While (NewEvent.Time > IteratorEvent.Next.Time)
  IteratorEvent = IteratorEvent.Next;
Add NewEvent after IteratorEvent;

```

**Figure 4: Schedule New Event Algorithm**

## 2.2 Parallel Discrete Event Simulation Using Multi-Threading

In a single core processor only a single thread of execution is realizable at a moment in time. With the introduction of a multi-core processor architecture, a multi-threaded environment can provide true parallelism. A multi-threaded environment involves creating multiple threads of execution in a single program that work concurrently. A Parallel Discrete Event Simulation (PDES) can be created if a DES is partitioned into multiple threads of execution. Each thread in a PDES share a common program context, shared memory spaced, that allows each thread to access the same information shown in Figure 5. Taking advantage of the common program context reduces the burden placed on the developer when compared to distributed simulation. Parallelism between processes must be identified to gain a noticeable performance benefit. If one thread processes 95% of the work load, then all other created threads are much less valuable; partitioning the problem so that all threads are continuously processing is the key to parallel simulation. This research will focus on identifying parallelism within the simulation executive so that the simulation application can change while stilling maintaining a performance benefit.

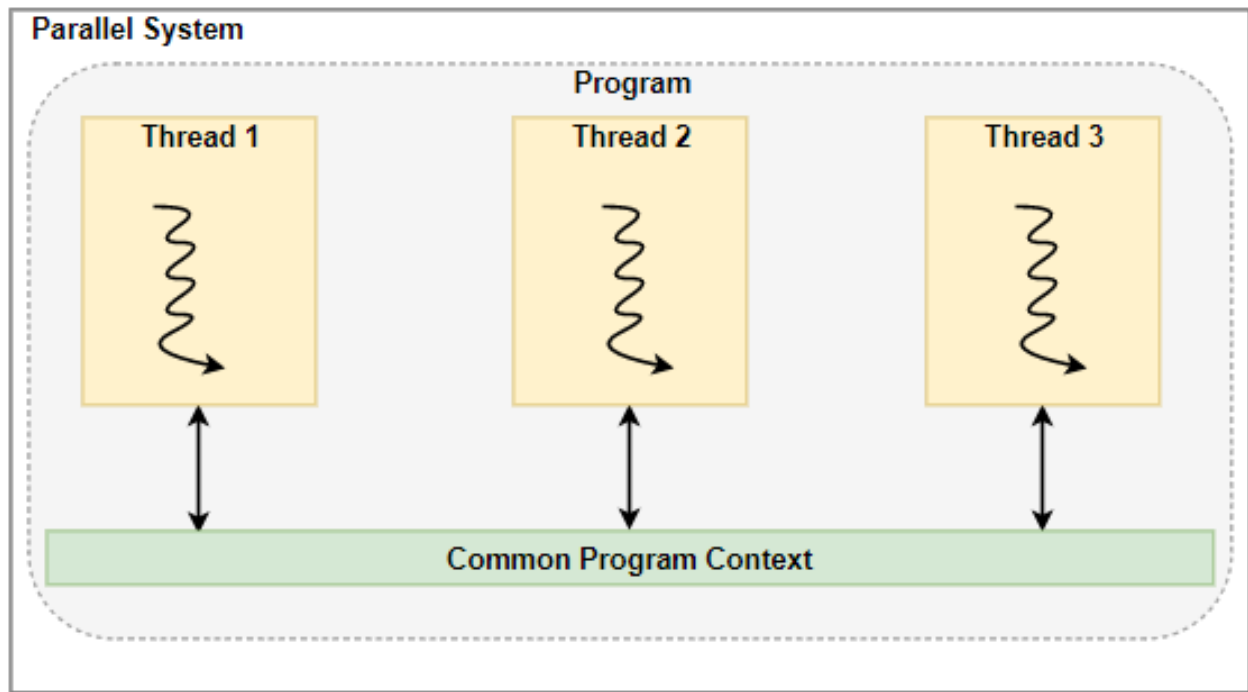
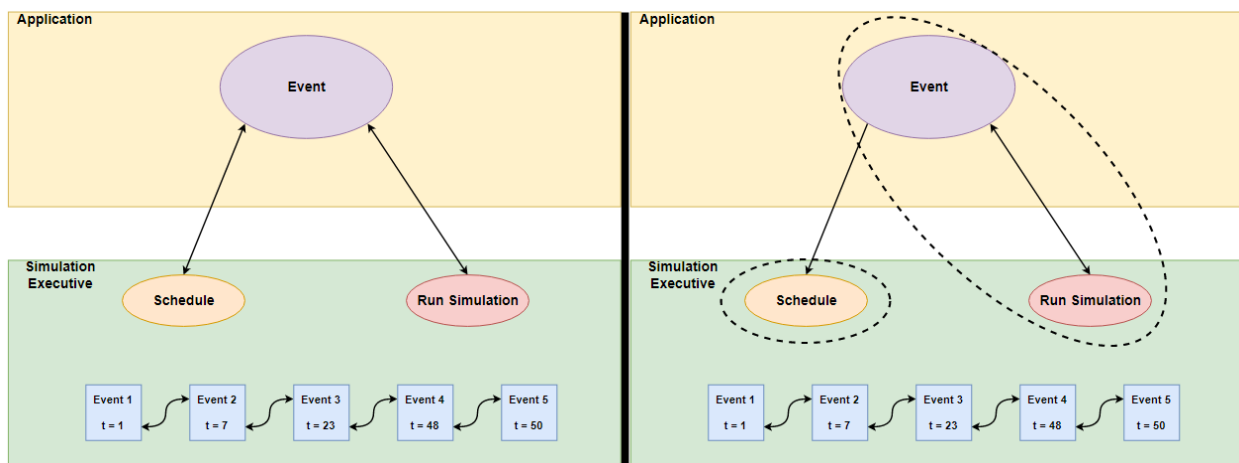


Figure 5: Multi-Threaded System

### 3 CURRENT WORK

#### 3.1 Parallelism Event Scheduling and Execution

Introducing parallelism in the simulation executive can increase the performance of a serial DES application without adding overhead to the application developer. Scheduling a future event, while initiated from the execution of an event, is independent from the continued execution of the event. This suggests that those actions can occur in parallel. Figure 6 on the left shows the relationship of executing an event selected by the simulation executive from the event list, and that event scheduling another event. On the right, the circled areas represent portions identified for potential parallelism; scheduling events and executing events can be run in parallel. Isolating the parallelism to the simulation executive allows for the simulation executive to remain reusable, with the same interface as the serial DES resulting in no intervention required by the simulation application developer.





**Figure 6: Serial (left) and Parallel (right)**

A serial simulation executive will continuously get events and execute them. During the execution of an event, a new event may be scheduled. This schedule must finish before the execution of the current event will continue as shown on the left in Figure 7. Parallelism between event scheduling and execution allows for future events to be scheduled while the current event continues to be executed as shown on the right in Figure 7. With event scheduling and execution working in parallel, the same number of events can be executed in a shorter amount of time when compared to its serial counterpart which can be deduced by comparing the left from the right in Figure 7.

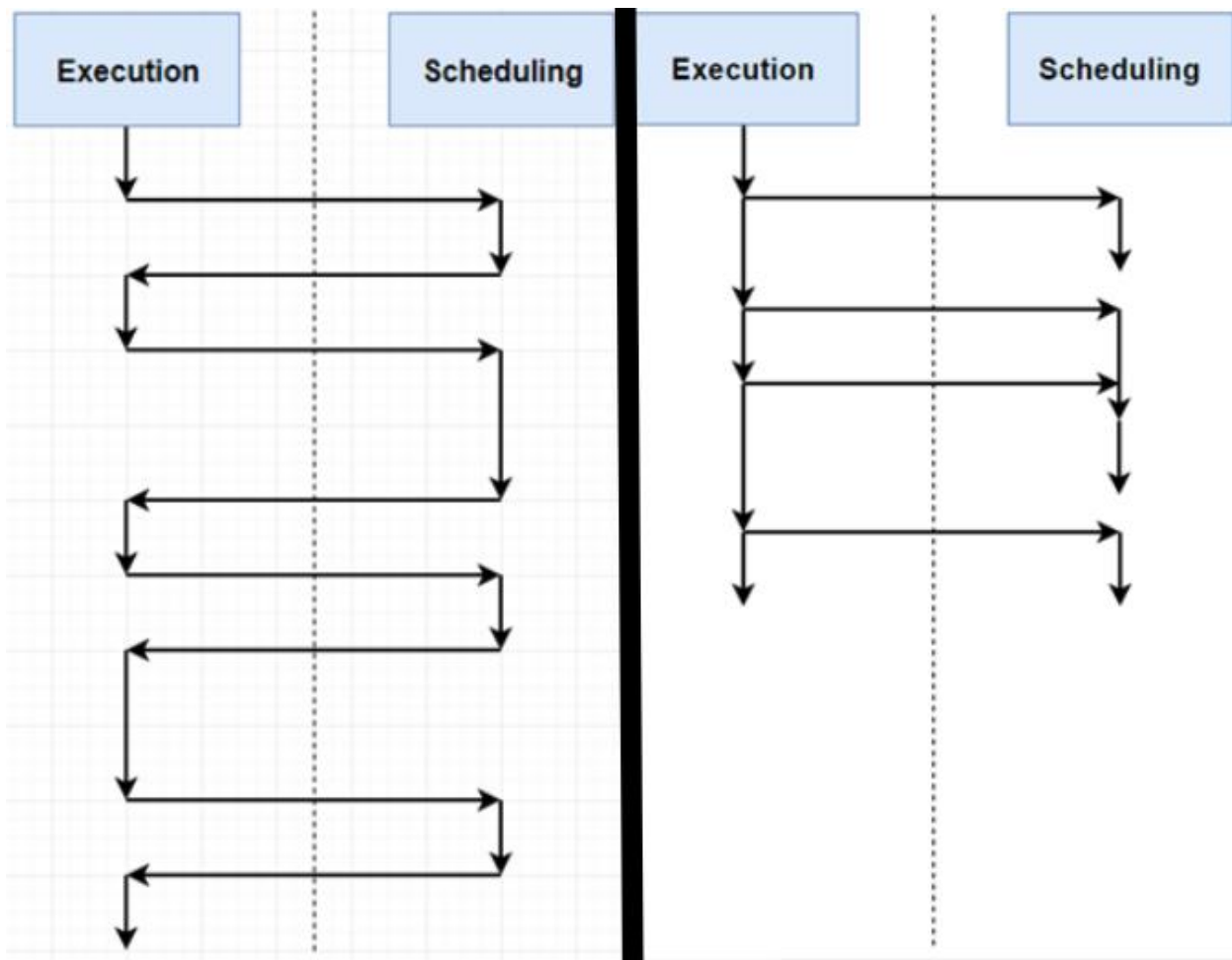


**Figure 7: Serial Execution (left) vs. Parallel Execution (right)**

In a serial simulation executive, only one event is scheduled at any moment in time because a schedule will finish before a new event will be executed. The concurrency between execution and scheduling in a parallelized simulation executive brings forth the potential that a new event wishes to be scheduled before the previous event has finished being scheduled. To circumvent this issue, an additional event list is created known as the scheduled event list; it holds all future events that are to be scheduled in the main event list as illustrated in Figure 8. On completion of scheduling an event, the scheduling thread checks this list to see if it has more events to schedule, else it goes to sleep, waiting for the next event to schedule.

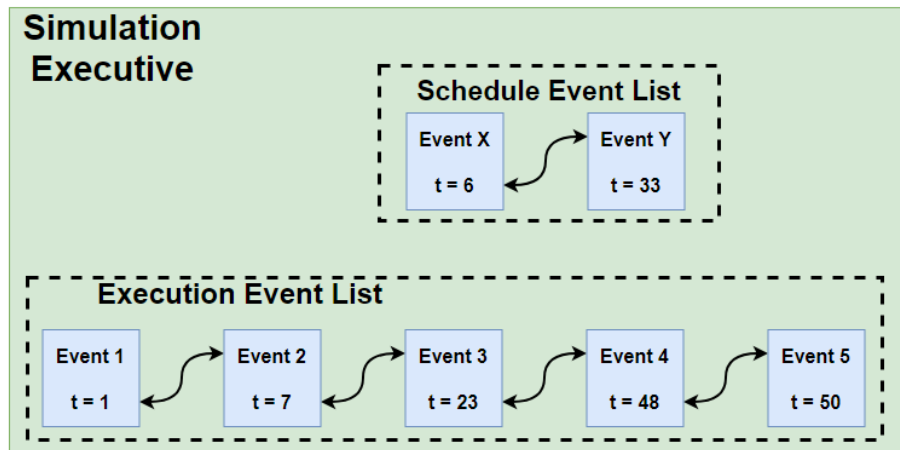


Figure 8: Schedule Event List

### 3.2 Identification of Resource Contention

One concern in parallel processing is resource contention (2005 Moseley, 2011 Dey). This occurs in multithreaded applications when multiple threads interact with the same piece of data at the same time. The proposed approach has two threads: event scheduling and event execution and they both access the event list. The execution thread always accesses the front of the list to get the next event, and only does so once per executed event. The scheduling thread begins at the front of the list and works its way through the list until finding the appropriate location to insert the event. Therefore the only event that is under contention is the first event as illustrated in Figure 9.

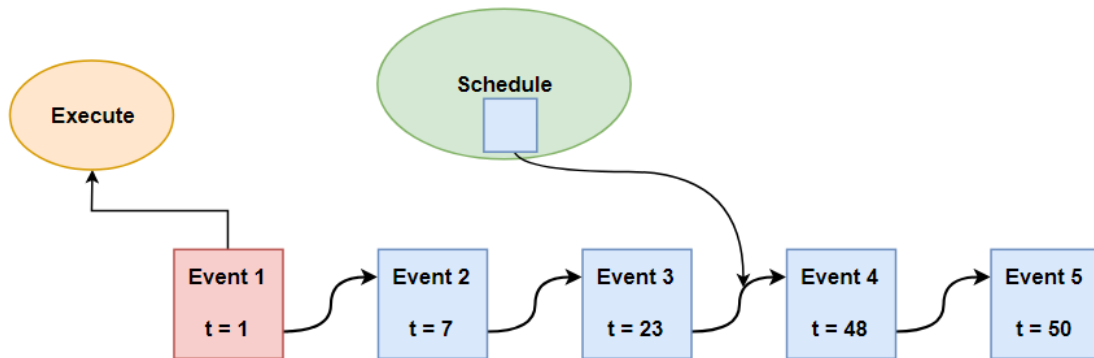
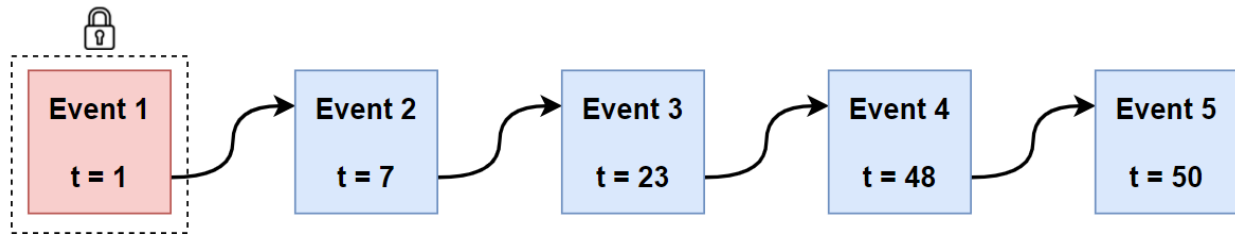


Figure 9: Resource Contention in the Event List

### 3.3 Solving Resource Contention with Mutex Locking

Mutex locking is used to solve the resource contention problem. A lock is placed around the first event in the list and is initially unlocked. When one of the threads needs to interact with the first event in the list, the thread checks if the mutex is locked or unlocked. If the mutex is unlocked, the thread will lock the mutex indicating that the first event is under use and will unlock the mutex when the thread is done interacting with the first event in the list. If the mutex is locked, then the thread will wait for the mutex to be unlocked before interacting with the first event in the list. The scheduling thread has to deal with the scheduling event list which may have more than one event waiting to be scheduled. The scheduling thread will only unlock the mutex if it is currently scheduling the last event the scheduling event list and the iterator is past the first event in the list as shown in Figure 11. The execution thread checks if the mutex is locked and if there are no events in the schedule event list then gets the first event as shown in Figure 12. Figure 10 shows a mutex lock placed around the first event in the event list. Figure 11 and figure 12 show the algorithms for the scheduling and execution threads when dealing with the mutex.



**Figure 10: Mutex Locking the First Event**

<pre> If (mutex is locked)     Wait for unlock Lock mutex While(Schedule Event List &gt; 0)     If (NewEvent.Time &lt; First.Event.Time)         Add NewEvent as FirstEvent;     If (Schedule Event List &lt;= 1)         Unlock mutex     IteratorEvent = FirstEvent;     While (NewEvent.Time &gt; IteratorEvent.Next.Time)         IteratorEvent = IteratorEvent.Next;     Add NewEvent after IteratorEvent; </pre>	<pre> While Simulation is not done     If (mutex is locked)         Wait for unlock     If(ScheduleEventList &gt; 0)         Wait until ScheduleEventList = 0     Lock mutex     Get first event     Unlock mutex     Simulation Time = Event Time     Execute Event </pre>
--	---

**Figure 11: Event Scheduling Thread**

**Figure 12: Event Execution Thread**

### 3.4 Testing

The parallel simulation executive can be tested by comparing the performance to its serial counterpart while using the same simulation application. The simulation application be will constructed as a test harness that allows the user to control the number of event in both the execution event list and the scheduling event list. This ability to control the amount of events in both events lists will allow for the control of the amount of work required for execution. Varying the number of events in both of these lists will allow us to see the performance benefits in systems with a large number of events as well as a sparse number of events. This type of testing will make it clear if a parallel simulation executive is worth taking advantage of and if so, under what conditions it should be utilized.

## 4 FUTURE WORK: ALTERNATIVE APPROACH TO HANDLING RESOURCE CONTENTION

Currently when the scheduling thread has control over the mutex, it keeps the mutex locked until the last event is being scheduled and the first event of the execution event list has already been checked. The execution thread must be cognizant of the not only the mutex but also if there are any events in the schedule event list; if there are events in the schedule event list then the first event in the execution event list is not considered safe for execution. Future work will investigate a method to identify when the first event in the execution event list is safe for execution regardless of the size of the scheduling event list. A much larger increase in performance is possible if the execution thread can continue executing events even when the scheduling event list is heavily populated.

## 5 CONCLUSION

When trying to increase the performance of DES many turn to distributed simulation. While distributed simulation will increase performance, the application developers are burdened with modifying the application to fit a distributed environment. This paper identifies a low-level inherit parallelism within the simulation executive that can be utilized through a multi-core processor. The performance can be increased using a multi-threaded approach by separating event scheduling and event execution into their own threads of execution. This modification to the simulation executive will increase the performance of a DES without any extra overhead to the application developer while still being reusable to many different applications.

## REFERENCES

- Brown, R. (1988). *Calendar Queues: A Fast  $O(1)$  Priority Queue Implementation For The Simulation Event Set Problem*. Communications of the ACM, 31(1), 1220-1227.
- Chen, W. (2015). *Out-of-order Parallel Discrete Event Simulation for Electronic System-level Design*. Cham: Springer International Publishing. doi: 10.1007/978-3-319-08753-5
- Dey, T., Wang W., Davidson J., and Soffa M. (2011). *Characterizing Multithreaded Applications Based on Shared-resource Contention*. Proceedings of the 2011 IEEE International Symposium on Performance Analysis of Systems and Software, 76-86. doi: 10.1109/ISPASS.2011.5762717
- Fujimoto, R. M. (1990). *Parallel Discrete Event Simulation*. Communications of the ACM, 33(10), 30-53.
- Fujimoto, R. M. (2000). *Parallel and Distributed Simulation Systems*. New York: John Wiley & Sons.
- Moseley T., Kihm J., Connors D., Grunwald D. (2005) *Methods for Modeling Resource Contention on Simultaneous Multithreading Processors*. Proceedings of the 2005 International Conference on Computer Design. doi: 10.1109/ICCD.2005.74
- Law, A. M., & Kelton, W. D. (2004). *Simulation Modeling and Analysis*. Boston: McGraw-Hill.
- Pidd, M. (2004). *Simulation Worldviews – So What?* Proceedings of the 2004 Winter Simulation Conference.
- Ronngren, R., Riboe, J., & Ayani, R. (1991). *Lazy Queue: An Efficient Implementation of the Pending-event Set*. In Proc. Of the 24<sup>th</sup> Annual Simulation Symposium, 194-204.
- Vaucher, J. G., & Duval, P. (1975). A Comparison of Simulation Event List Algorithms. *Communications Of The ACM*, 18(4), 223-230. doi: 10.1145/360715.360758

## AUTHOR BIOGRAPHIES

**BRANDON WADDELL** is a Ph. D student in the Department Modeling, Simulation, and Visualization Engineering at Old Dominion University. He received his bachelor's degree in Modeling, Simulation, and Visualization Engineering at Old Dominion University. His research interests include parallel simulation, collaborative autonomous systems, and networking. His email address is bwadd006@odu.edu.

**JAMES F. LEATHRUM Jr.** is an Associate Professor in the Department of Modeling, Simulation, and Visualization Engineering at Old Dominion University. He earned the Ph. D in Electrical Engineering from Duke University. His research interests include simulation software design, distributed simulation, and simulation education. His email address is jleathru@odu.edu.

# COMPARISON OF ASYNCHRONOUS HYBRID PARALLEL MPI-OPENMP JACOBI'S METHOD IMPLEMENTATIONS

Erik J. Jensen  
Department of Modeling,  
Simulation and Visualization Engineering  
Old Dominion University  
Norfolk, VA, USA  
ejens005@odu.edu

Masha Sosonkina  
Department of Modeling,  
Simulation and Visualization Engineering  
Old Dominion University  
Norfolk, VA, USA  
msosonki@odu.edu

## ABSTRACT

Asynchronous algorithms may increase performance of parallel applications. This work investigates strategies for implementing asynchronous hybrid parallel MPI-OpenMP Jacobi solvers, and generates a predictive performance model that suggests solver parameters that are well-suited to a specific problem. Results show that making efforts to equalize the number of iterations for all processing elements benefits performance and solution quality.

**Keywords:** asynchronous, hybrid, parallel, MPI, OpenMP

## 1 INTRODUCTION

Asynchronous parallel methods avoid the performance cost of synchronizing MPI processes and OpenMP threads that are working together to complete a calculation. Instead of waiting for the slowest processing component to complete a computation to proceed to the next step or iteration, the other processing components may independently continue to compute. Asynchronous systems have some advantages over synchronous systems, in that they may mitigate the effect of typical performance variations between similar computing elements, for example, from iteration to iteration; or they may harness the ability of a computing element to perform useful work while waiting for information from another computing element. As future high-performance computing (HPC) platforms continue to scale in the number of processing elements and calculations are increasingly parallelized, asynchronous methods may offer performance superior to synchronous methods.

Bethune, et al. present several asynchronous Jacobi's method implementations that solve LaPlace's equation in three dimensions, which are parallelized with MPI, SHMEM, or OpenMP (Bethune, Bull, Dingle, and Higham 2014). Their finding that asynchronous Jacobi implemented with OpenMP is 33% faster than the synchronous OpenMP application leads them to suggest the potential for OpenMP in a hybrid MPI-OpenMP implementation. This work implements some asynchronous hybrid MPI-OpenMP models that solve the discrete Laplace equation for a two-dimensional heat diffusion problem with Jacobi's method, similar to the work of Bethune, et al. Background information and related work are explored in section 2. The parallel solver models and implementations are described in section 3. Implementation performance testing results are examined in section 4. The predictive model is explained in section section 5, and model results are discussed in section 6. Section 7 concludes and projects future work.

## 2 BACKGROUND INFORMATION

In science and engineering, partial differential equations mathematically model systems in which continuous variables, such as temperature or pressure, change with respect to two or more independent variables, such as time, length, or angle (Smith 1985). LaPlace's equation in three dimensions,

$$\nabla^2 \phi = \frac{\partial^2 \phi}{\partial x^2} + \frac{\partial^2 \phi}{\partial y^2} = 0,$$

is fundamental for modeling equilibrium and steady state problems, such as incompressible fluid flow or heat transfer, and maintains that the rate at which a fluid enters a domain is equal to the rate at which a fluid leaves the domain. In practice, the partial differential equation is not used directly, but is discretized such that a finite difference operator computes difference quotients over a discretized domain. For example, the two-dimensional discrete Laplacian operator,

$$(\nabla_3^2 f)(x, y) = f(x-1, y) + f(x+1, y) + f(x, y-1) + f(x, y+1) - 4f(x, y),$$

approximates the two-dimensional continuous Laplacian using a five-point stencil (Lindeberg 1990). From this, a special case of the Jacobi algorithm,

$$(v_{l,m}^{k+1} = \frac{1}{4}(v_{l+1,m}^k + v_{l-1,m}^k + v_{l,m+1}^k + v_{l,m-1}^k),$$

may be applied to solve a two-dimensional sparse linear system of equations (Strikwerda 2004). This work uses the Jacobi algorithm to solve a simple two-dimensional heat diffusion problem, in which a plate is subject to Dirichlet-boundary-condition temperatures (Chapra and Canale 1998).

### 2.1 Related Work

Bahi et al. demonstrate the efficacy of asynchronous methods, especially for grid systems, and propose a system for classifying parallel iterative algorithms, based on computational and communication strategies (Bahi, Contassot-Vivier, and Couturier 2006) (Bahi, Contassot-Vivier, and Couturier 2003). Iterations and communications may be either synchronous or asynchronous. This work develops and tests implementations that are Synchronous Iterations - Synchronous Communications (SISC), Synchronous Iterations - Asynchronous Communications (AIAC), and also an unmentioned class, Asynchronous Iterations - Synchronous Communications (AISC). Jager and Bradley also demonstrate superior performance of asynchronous methods for solving large sparse linear fixed-point problems (de Jager and Bradley 2010). Voronin compares three parallel implementations using MPI and OpenMP, with asynchronous threads, and finds that utilizing a "postman" thread within each computational node to perform communications delivers superior performance, compared to the alternative hybrid MPI-OpenMP implementation (Voronin 2014).

## 3 HYBRID MPI-OPENMP MODELS AND IMPLEMENTATIONS

The implementations solve a heat diffusion problem, in which a two-dimensional heated plate has Dirichlet boundary-condition temperatures, using OpenMP for shared memory parallelization, and MPI for distributed-memory parallelization. Several types of implementations have been developed, falling into the AIAC, AISC, and SISC categories. Descriptions of the implementations follow, based on classification.

In addition to these implementations, an exclusively shared-memory-parallel implementation, SHRD, has been developed as a benchmark, to measure the effectiveness of the hybrid-parallel implementations.

### 3.1 Asynchronous Iterations - Asynchronous Communications (AIAC)

Two matrices,  $u_0$  and  $u_1$ , store grid point values that each thread reads, e.g. from  $u_1$ , to compute newer values to write, e.g. to  $u_0$ . As the method is asynchronous, each thread independently determines which matrix stores its newer  $u^{(t+1)}(i, j)$  values and older  $u^{(t)}(i, j)$  values. For an  $n + 2$  by  $n + 2$  grid that is equally divided among all  $n_p$  threads, each thread solves for  $n^2/nt$  grid points, such that the grid is evenly partitioned along the y-axis. When a thread copies grid point values above or below its domain for the computation, OpenMP locks are employed to ensure that data is captured accurately, from a single iteration. Further, locks are used when updating values on boundary rows and subdomain halos, and when copying subdomain boundaries. Each thread  $p_n$  computes its local residual value every  $k^{th}$  iteration, which it contributes to the set of residual values for the subdomain. Using an OpenMP atomic operation, a single thread copies the set of subdomain residuals, computes a sum, and sends the sum to the master MPI process.

Within the AIAC category, there are five variants:

1. Work-Scaling-1. In WS1, the subdomain is equally divided among all OpenMP threads, and one thread performs communication with the master MPI process.
2. Work-Scaling-X. In WSX, the subdomain is divided such that the communicating thread,  $p_c$  performs less computational work than the other threads. The size of the  $p_c$  compute region is  $(n + 2)/n_p/X$ , and the remaining threads equally divide the remainder of the subdomain.
3. Rotating-Incrementing. In RTINC, the subdomain is equally divided among all OpenMP threads, but communication with the master MPI process is rotated among the threads.
4. Rotating-Maximum-Iterations. Similar to RTINC, but RTMAXIT chooses the OpenMP thread that has performed the most iterations to communicate.
5. Rotating-Minimum-Residual. Similar to RTMAXIT, but RTMNRs chooses the OpenMP thread that has performed the most iterations to communicate.

### 3.2 Asynchronous Iterations - Synchronous Communications (AISC)

The Asynchronous-Direct implementation is similar to the AIAC implementations, but one OpenMP thread in each MPI process is reserved exclusively for synchronous communication. In ASYNCDIR, the communicating threads swap subdomain halo values directly, without the master MPI process intermediary.

### 3.3 Synchronous Iterations - Synchronous Communications (SISC)

The Synchronous-Direct implementation is a modification of a base AIAC implementation, in which iterations and communications have been synchronized across threads and subdomains. For SYNC DIR, one thread per subdomain communicates directly with other communicating threads regarding halo values, while the non-communicating threads are idle.

## 4 IMPLEMENTATION PERFORMANCE RESULTS

Data collected from empirical testing of the implementations demonstrates the efficacy of different solving strategies, as a function of problem size, subdomain size, and swap period. The swap period,  $P_{swap}$ , may



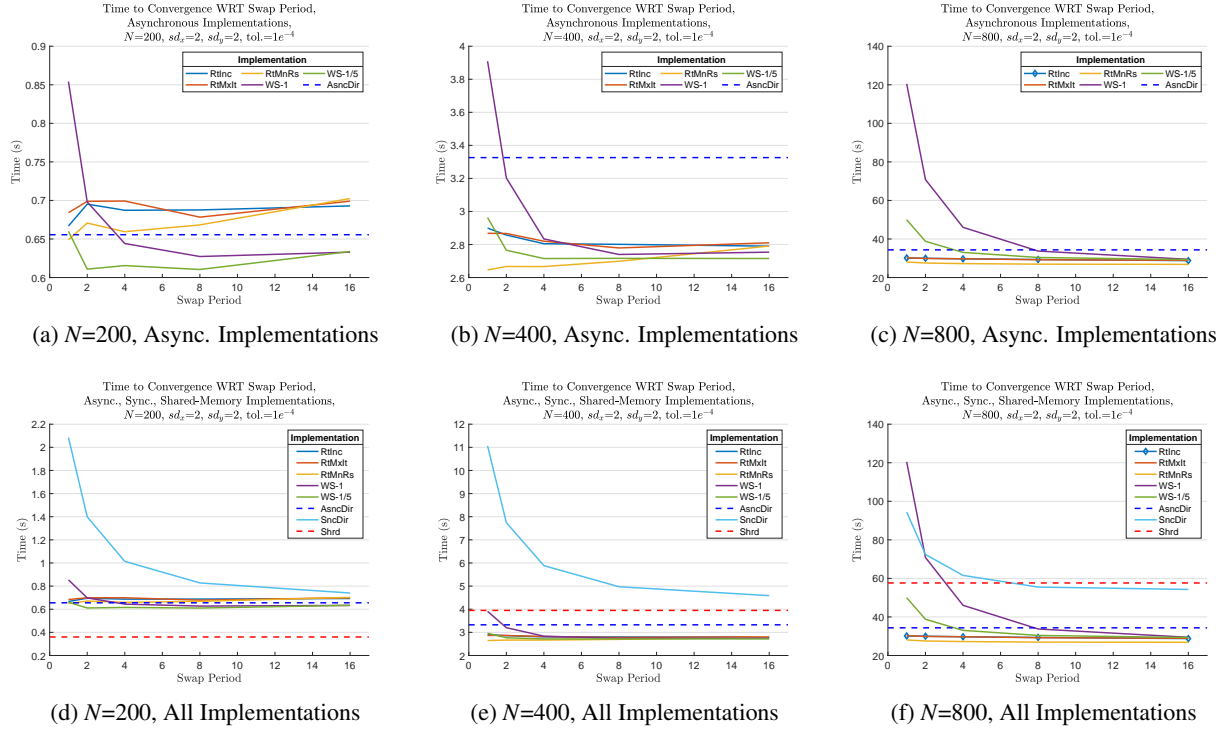


Figure 1: Time to convergence with respect to swap period, synchronous and asynchronous implementations compared, for three subdomain sizes.

be 1, meaning that halo values are exchanged after every iteration, or a number  $x > 1$ , meaning that halo values are exchanged only every  $x$  iterations. For a sufficiently small problem size, fig. 1(d) shows that the exclusively-shared-memory-parallel implementation SHRD outperforms the hybrid-parallel implementations. However, using larger subdomain sizes demonstrates that the hybrid implementations benefit from the additional complexity of distributed parallelization. When  $P_{\text{swap}}$  is sufficiently large, the AIAC implementations perform similarly, with minor variations. For these tested problems, the AISC implementation ASNCDir falls short of the other asynchronous implementations, perhaps because the advantage of quick communication and constant halo swaps does not outweigh the loss of a computational thread. The SISC implementation, SNCDIR, cannot match the performance of the asynchronous implementations under these conditions, likely because of the expense of lost computation during the communication phase.

Figure 2 demonstrates the scaling abilities of the tested implementations. Figure 2(c) and Figure 2(d) show that iteration rates remain fairly constant as a function of problem size, meaning that a significant communication bottleneck is not observed. Increasing the swap period improves the iteration rate, especially for SNCDIR, which suffers from a costly communication phase and fails to match the iteration rates of the asynchronous implementations.

Figure 3 and fig. 4 demonstrate the shortcomings of the work-scaling implementation WS. As a dedicated thread performs communications, as well as computations, the iteration rate may be less than the non-communicating threads, if care is not taken to balance the compute load with communication. Figure 3 implies this balance can be achieved by pairing the work-scaling factor  $X$  with an appropriate swap period, such that time, and therefore iterations, lost during the communication phase may be budgeted with a sufficiently small compute load. Equalizing iteration rates of master and non-master threads also avoids the error imbalance seen in fig. 4. Figure 4(a) shows that when a master thread does not match the iteration

rate of non-master threads, a disproportionately large amount of the solution error originates from the master thread. However, fig. 4(b) suggests this problem can be mitigated by increasing the swap period. The predictive model discussed in section 5 aims to investigate appropriate swap-period-work-scaling-factor pairings, for a given problem.

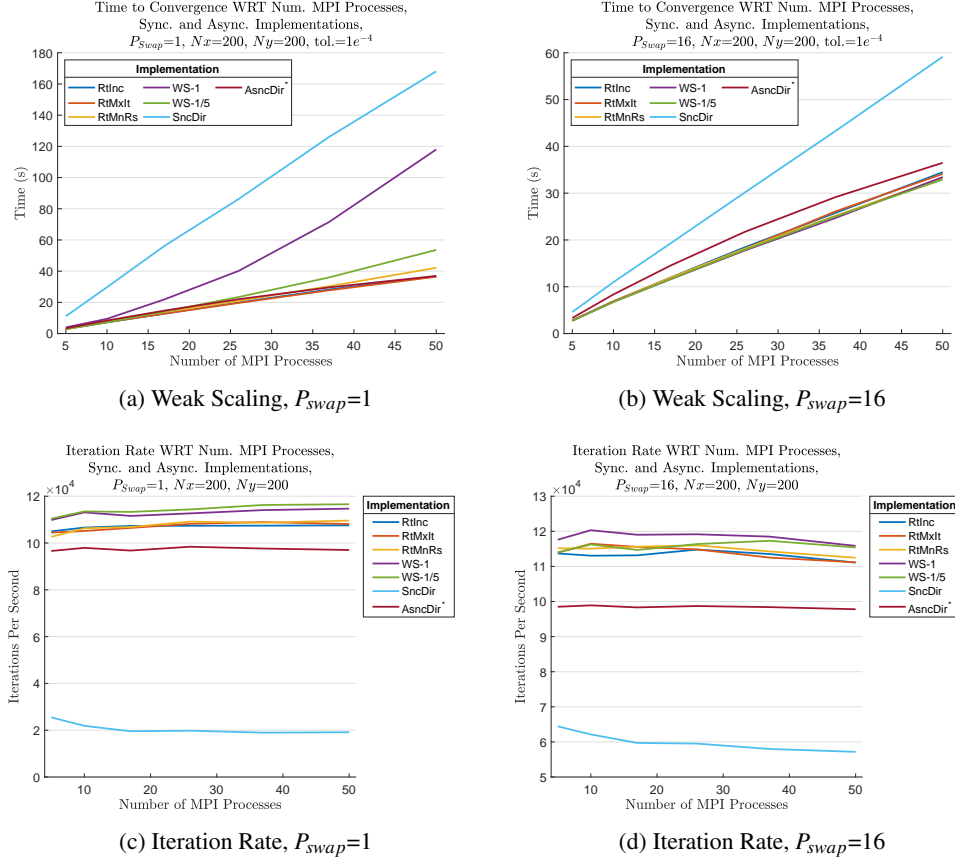


Figure 2: Weak scaling and iteration rates for swap periods 1 and 16. Individual weak-scaling trajectories may be interpreted only relative to other implementations.

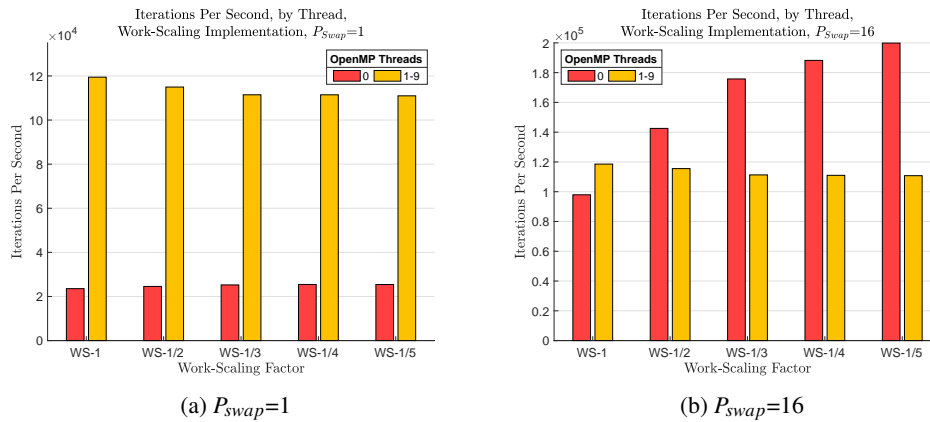


Figure 3: Iteration rates by thread number for swap periods 1 and 16, work-scaling implementation.

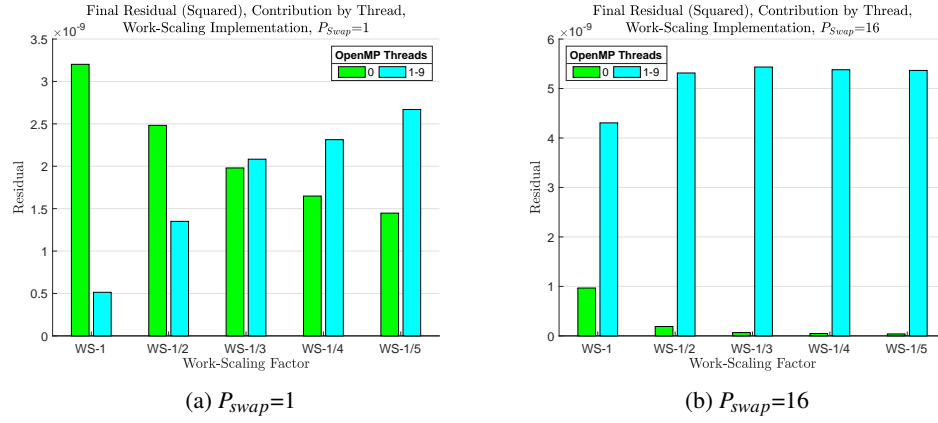


Figure 4: Residual contribution by thread number for swap periods 1 and 16, work-scaling implementation.

## 5 PREDICTIVE MODEL

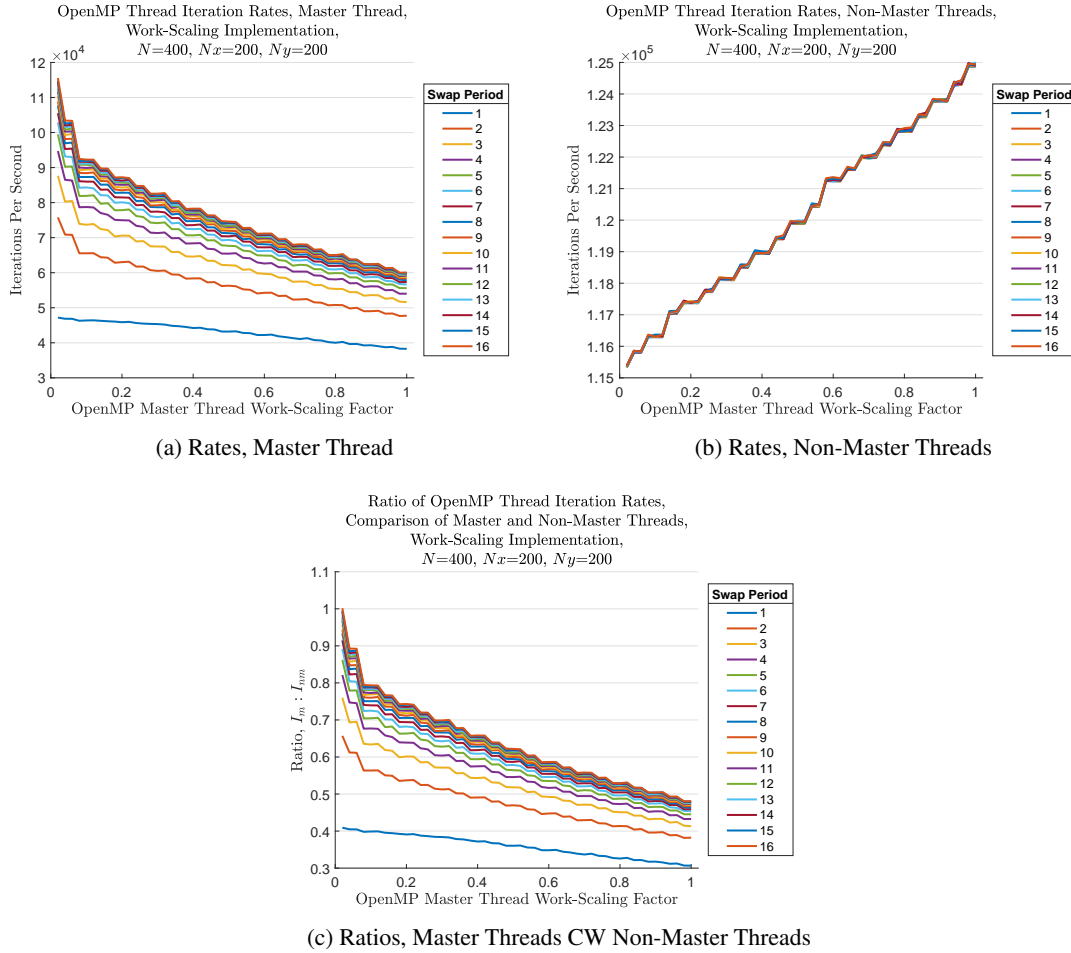


Figure 5: Predictive model results for work-scaling implementation. Iteration rates of master and non-master threads, as a function of swap period and work-scaling factor.

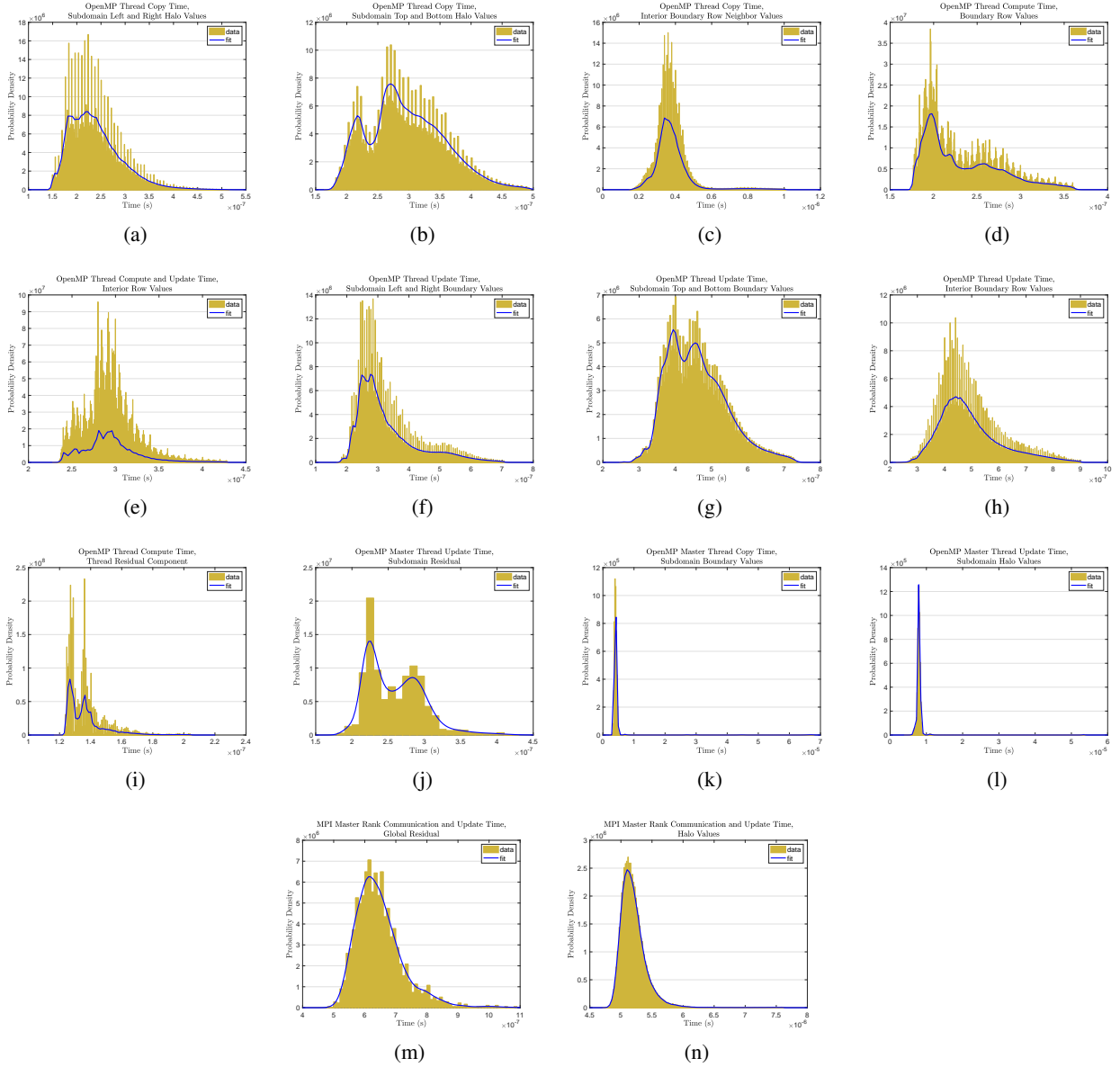


Figure 6: Empirically-measured histogram data and time distributions used in predictive model.

The predictive model utilizes the time distributions generated from empirical data, as shown in fig. 6. Similar to the method described in (Jensen and Sosonkina 2018), a MATLAB script models thread computation and master-worker communication for WS. The communicating thread computes an area of the subdomain ranging from 8% to 100% of  $(n + 2)/n_p$ , for swap periods ranging from 1 to 16.

## 6 MODEL RESULTS

Model results indicate mixed predictive power. Figure 5(b) shows non-master thread behavior is adequately modeled, but master-thread behavior under-performs, compared to actual performance on the Old Dominion University Turing cluster. The cause of this misbehavior is under investigation and is expected to be resolved in future work.

## 7 CONCLUSIONS AND FUTURE WORK

Modifying the halo swap strategy of the base hybrid-parallel model WS1 provides significant performance improvements and equalizes error quantity in subdomain regions. The asynchronous implementations outperform the synchronous implementation. The predictive model delivers mixed results, and will be improved in future work. Future work may also involve adapting the implementations and predictive model to a three-dimensional problem and a more powerful solving algorithm.

## REFERENCES

- Bahi, J. M., S. Contassot-Vivier, and R. Couturier. 2003, April. “Coupling dynamic load balancing with asynchronism in iterative algorithms on the computational grid”. In *Proceedings International Parallel and Distributed Processing Symposium*, pp. 9 pp.–.
- Bahi, J. M., S. Contassot-Vivier, and R. Couturier. 2006, Mar. “Performance Comparison of Parallel Programming Environments for Implementing AIAC Algorithms”. *The Journal of Supercomputing* vol. 35 (3), pp. 227–244.
- Bethune, I., J. M. Bull, N. J. Dingle, and N. J. Higham. 2014. “Performance analysis of asynchronous Jacobi’s method implemented in MPI, SHMEM and OpenMP”. *The International Journal of High Performance Computing Applications* vol. 28 (1), pp. 97–111.
- Chapra, S. C., and R. P. Canale. 1998. *Numerical methods for engineers*, Volume 2. McGraw-Hill New York.
- de Jager, D. V., and J. T. Bradley. 2010. “Extracting state-based performance metrics using asynchronous iterative techniques”. *Performance Evaluation* vol. 67 (12), pp. 1353 – 1372.
- Jensen, E., and M. Sosonkina. 2018. “Modeling a Task-Based Matrix-Matrix Multiplication Application for Resilience Decision Making”. In *Proceedings of the 26th High Performance Computing Symposium, HPC ’18*.
- Lindeberg, T. 1990, Mar. “Scale-space for discrete signals”. *IEEE Transactions on Pattern Analysis and Machine Intelligence* vol. 12 (3), pp. 234–254.
- Smith, G. D. 1985. *Numerical solution of partial differential equations: finite difference methods*. Oxford university press.
- Strikwerda, J. C. 2004. *Finite difference schemes and partial differential equations*, Volume 88. Siam.
- Voronin, K. V. 2014, 07. “A numerical study of an MPI/OpenMP implementation based on asynchronous threads for a three-dimensional splitting scheme in heat transfer problems”. *Journal of Applied and Industrial Mathematics* vol. 8 (3), pp. 436–443. Copyright - Pleiades Publishing, Ltd. 2014; Last updated - 2014-09-04.

## AUTHOR BIOGRAPHIES

**ERIK J. JENSEN** is a graduate student in the Department of Modeling, Simulation and Visualization Engineering at Old Dominion University working toward his Ph.D. His research interests include resilience in high-performance computing. His email address is [ejens005@odu.edu](mailto:ejens005@odu.edu).

**MASHA SOSONKINA** received her Ph.D. from Virginia Tech, and currently is Professor in the Department of Modeling, Simulation and Visualization Engineering at Old Dominion University. Her research interests include applied computational mathematics, high-performance computing and chemical and biological sciences. Her email address is [msosonki@odu.edu](mailto:msosonki@odu.edu).

# QUANTIFYING THE EFFECT OF AN UNACCUSTOMED GAIT PATTERN ON MOVEMENT VARIABILITY

Collin D. Bowersock  
College of Physical Therapy and Athletic Training  
School of Health Sciences  
Kinesiology and Rehabilitation  
Old Dominion University  
cbowe005@odu.edu

## ABSTRACT

Variability is an important characteristic of human movement. It allows for the adaptability to differing environments and attention to unpredicted perturbations. Changes in gait pattern may alter the natural variability seen during a habitual gait pattern, possibly leading to deleterious effects. Given the current trend to utilize different running styles to decrease injury risk, considerations of how the variability structure may change during different running styles should be made. This project aims to quantify the effect an unaccustomed running pattern has on center of pressure displacement variability using a novel method of non-linear analysis

**Keywords:** Non-linear analysis, movement variability, center of pressure, gait.

## 1 INTRODUCTION

In the field of human movement studies, there has been a rise in the use of non-linear measures to quantify movement variability and study its role in cyclical movements. We have come to understand the importance of variability in ambulatory tasks such as running and walking. The variability allows us to adapt to differing environments and attenuate unpredicted perturbations. Alterations in individuals' habitual gait patterns can lead to deviations in the structure and quantity of movement variability, possibly increasing the risk for disadvantageous gait issues.

Adopting an alternate foot strike pattern is a way in which individuals choose to modify their habitual gait pattern. Those who run long distances may choose to do adopt a different foot strike pattern in an attempt to reduce running related injuries. Research has found different running styles to result in decreased joint loads in the lower extremities which are common areas for running related injuries. However, no study has investigated the effect a novel running style has on movement variability. Moreover, the abrupt switch to a new running style commonly leads to sudden injury. Thus, this study aims to quantify the effect a change in running style has on movement variability. Specifically, center of pressure (COP) displacement patterns will be quantified using a novel non-linear analysis measure while healthy individuals run with their preferred foot strike pattern and a non-preferred foot strike pattern.

## 2 METHODS

Nineteen recreationally active individuals without prior lower extremity running related injuries participated in the study. Using an instrumented treadmill with Zebris pressure measurement system, COP

displacement paths (mediolateral, anterior-posterior) were recorded for 5 minutes, while subjects ran at their preferred pace and foot strike pattern. A subsequent trial was recorded at the same speed, but with an unaccustomed foot strike pattern. Mediolateral and anterior-posterior COP displacement from the two trials were analyzed using linear and non-linear measures. Standard linear analyses were used to quantify COP displacements, step length, stride time and cadence. A novel non-linear measure was used to quantify the rate of COP displacement divergence. Briefly, a nearest neighbor algorithm was created to find the smallest Euclidean distance between the first COP displacement sample and another sample, excluding the current step of interest. The two points were then tracked throughout the step to determine the rate of divergence. Each sample of each step was used to find an average rate of divergence over the entirety of the two trials for each subject.

### 3 RESULTS

In Progress

### 4 DISCUSSION

This study will increase our current knowledge about how movement variability changes when a novel task is being introduced into the system. We may find a greater amount of variability with decreased divergence rate, suggesting the use of an exploratory technique to acquire information about the new task. The results could also show the opposite, less variability with an increase in the divergence rate, suggesting a locking of degrees of freedom because of the introduction of an unfamiliar task.

The development of this novel non-linear analysis technique may be applied to other two-dimensional data sets along with the customary detrended fluctuated analysis (DFA) technique to quantify the persistence of a signal over time. The inclusion of additional measured dimensions may prove to be useful in three-dimensional movement analysis, without the need for construction of pseudo dimensions used in DFA. Additional comparisons will be completed to determine the utility of the proposed method.

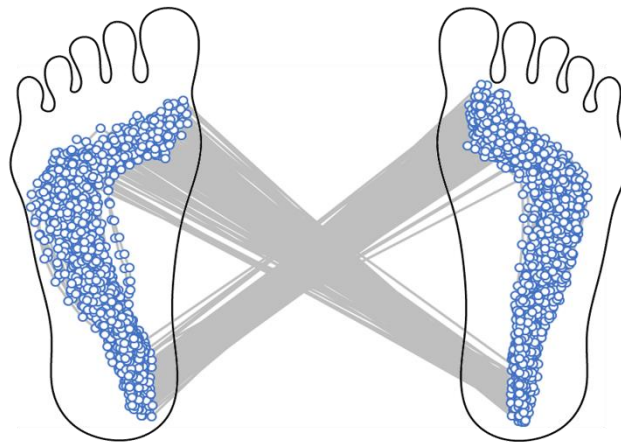


Figure 1: COP displacement traces between the left and right foot during running



# STABILITY ANALYSIS OF ACTIVE SUSPENSIONS OF LIQUID CRYSTALS

R. Anthony Williams

Dr. Ruhai Zhou

Department of Mathematics and Statistics  
Old Dominion University  
5115 Hampton Boulevard  
Norfolk, VA, USA  
ra1willi@odu.edu

Department of Mathematics and Statistics  
Old Dominion University  
5115 Hampton Boulevard  
Norfolk, VA, USA  
rzhou@odu.edu

## ABSTRACT

We first present kinetic model equations for active, anisotropic fluids arising from biological and materials science applications. The equations include transport equations for the polarity vector and the local concentration, as well as the Navier-Stokes equations. Then we examine the dynamics of the polar active liquid crystals near equilibrium in a uni-axial system. This is done by conducting a linear stability analysis about constant steady states in order to explore near equilibrium dynamics near the steady states. Numerical simulation results for different model parameters, including the parameters being perturbed, are provided.

**Keywords:** liquid crystals, stability analysis, numerical simulations.

## 1 INTRODUCTION

An active suspension can be described as a large-scale collection of self-propelled particles that interact with each other. Active suspensions have been the focus of many researchers throughout the years due to the complex dynamics they entail as well as the numerous applications. Some of the many applications of active suspensions include those in biology such as (Pedley and Kessler 1992), as well as those in technology (Dreyfus et al. 2005) and (Darnton et al. 2004) and many many others. Two of the most prominent applications of liquid crystals are liquid crystal displays (Gray, Harrison, and Nash 2007) and Kevlar (Zhang and Kumar 2008) which is used to produce many things including personal armor. The goal of this paper is to study the dynamics of polar active liquid crystals near equilibrium. This topic has been studied by many including (Xiao-Gang, Forest, and Wang 2014) as well as others, but these studies have mainly included a constant local concentration  $c$ . However, the local concentration is not constant generally and it depends on many things including the polarity vector, the potential for spatial inhomogeneity, and the polarity strength. Thus, in this paper we will examine the effects of allowing the local concentration to remain non-constant on the stability of the system near equilibrium. First we will present the mathematical model we will be studying, and then complete stability analysis on a linearized system. Within this analysis we will examine further a specific case of the wave number in the perturbation, and finally we present some numerical results from simulations that were conducted.

## 2 MATHEMATICAL MODEL

The dimensionless equation for the nanorod number density function (NDF)  $f(\mathbf{m}, \mathbf{x}, \mathbf{t})$  with constant translational diffusion coefficient  $D_s$  and rotational diffusion coefficient  $D_r$  is given by

$$\frac{\partial f}{\partial t} + \nabla \cdot ((\mathbf{v} + U_0 \mathbf{m})f) = D_s \nabla \cdot (\nabla f + f \nabla U) + D_r c^{-2} \mathcal{R} \cdot (\mathcal{R}f + f \mathcal{R}U) - \mathcal{R} \cdot (\mathbf{m} \times \dot{\mathbf{m}}f), \quad (1)$$

where the intermolecular potential  $U$  can be written as

$$U = N_1 c - \alpha \mathbf{p} \cdot \mathbf{m} - \frac{3N}{2} \mathbf{M} : \mathbf{m} \mathbf{m}, \quad (2)$$

with  $N_1$ ,  $\alpha$ , and  $N$  representing the strengths of the potentials for spatial inhomogeneity, polarity and nematic order, respectively. The nematic parameter  $N$  is proportional to the rod macromolecular volume fraction concentration. The local concentration  $c$ , the polarity director  $\mathbf{p}$  and the second moment orientation tensor  $\mathbf{M}$  are defined as the zeroth, first and second moment of  $f(\mathbf{m}, \mathbf{x}, \mathbf{t})$  on the unit sphere, respectively:

$$c(\mathbf{x}, t) = \langle 1 \rangle = \int_{||\mathbf{m}||=1} f(\mathbf{m}, \mathbf{x}, \mathbf{t}) \, d\mathbf{m}, \quad (3)$$

$$\mathbf{p}(\mathbf{x}, t) = \langle \mathbf{m} \rangle = \int_{||\mathbf{m}||=1} \mathbf{m} f(\mathbf{m}, \mathbf{x}, \mathbf{t}) \, d\mathbf{m}, \quad (4)$$

$$\mathbf{M}(\mathbf{x}, t) = \langle \mathbf{m} \mathbf{m} \rangle = \int_{||\mathbf{m}||=1} \mathbf{m} \mathbf{m} f(\mathbf{m}, \mathbf{x}, \mathbf{t}) \, d\mathbf{m}. \quad (5)$$

The Jeffery orbit  $\dot{\mathbf{m}}$  in (1) is

$$\dot{\mathbf{m}} = \mathbf{W} \cdot \mathbf{m} + a[\mathbf{D} \cdot \mathbf{m} - \mathbf{D} : \mathbf{m} \mathbf{m} \mathbf{m}], \quad (6)$$

where  $0 \leq a \leq 1$  is a geometric particle parameter,  $a = (r^2 - 1)/(r^2 + 1)$ , with  $r$  the particle aspect ratio, and  $\mathbf{D}$ ,  $\mathbf{W}$  are the symmetric and anti-symmetric parts of the velocity gradient tensor, also referred to as the rate of strain tensor and the vorticity tensor, respectively. In this work, the vorticity tensor is defined as  $\mathbf{W} = \frac{1}{2}(\nabla \mathbf{v}^\top - \nabla \mathbf{v})$  and  $[\nabla \mathbf{v}]_{i,j} = \frac{\partial v_j}{\partial x_i}$ . To close the system, the Smoluchowski equation (1) is coupled with the incompressible Navier-Stokes equations

$$\frac{D\mathbf{v}}{Dt} = \frac{\partial \mathbf{v}}{\partial t} + (\mathbf{v} \cdot \nabla) \mathbf{v} = \nabla \cdot (-\Pi \mathbf{I} + \tau_p + \tau_a), \quad \nabla \cdot \mathbf{v} = 0. \quad (7)$$

Here,  $\Pi$  is the hydrostatic pressure, and the constitutive equations for the passive nematic stress  $\tau_p$  and the active stress  $\tau_a$  are

$$\begin{aligned} \tau_p &= 2Re^{-1} \mathbf{D} + G[\mathbf{M} - \frac{1}{3}c\mathbf{I} - N\mathbf{M}^2 + N\mathbf{M} : \langle \mathbf{m} \mathbf{m} \mathbf{m} \mathbf{m} \rangle] \\ &\quad - \frac{1}{6}\alpha_0 G[2\mathbf{p} \mathbf{p} - (\langle \mathbf{m} \mathbf{m} \mathbf{m} \rangle \cdot \mathbf{p} + \mathbf{p} \cdot \langle \mathbf{m} \mathbf{m} \mathbf{m} \rangle)] + Re_2^{-1}[\mathbf{D} \cdot \mathbf{M} + \mathbf{M} \cdot \mathbf{D}], \\ \tau_a &= G \zeta_a (\mathbf{M} - \frac{1}{3}c\mathbf{I}), \end{aligned} \quad (8)$$

where  $\langle \mathbf{m} \mathbf{m} \mathbf{m} \rangle$  and  $\langle \mathbf{m} \mathbf{m} \mathbf{m} \mathbf{m} \rangle$  are third and fourth moments of  $f$ , the parameters  $Re$  and  $Re_2$  are Reynolds numbers for solvent and particle-solvent interactions,  $G$  is the anisotropic stress coefficient, and  $\zeta_a$  is the particle activation parameter that tunes the strength of the force dipole. Additionally,  $\alpha_0$  is the strength of the passive-nematic stress.

The mathematical model used in this work involves a system of equations including a transport equation for the polarity vector and the local concentration as well as the Navier-Stokes equations, all of which are

derived from the kinetic equations. Using the notations  $c = \langle 1 \rangle$ ,  $\mathbf{p} = \langle \mathbf{m} \rangle$ ,  $\mathbf{M} = \langle \mathbf{m}\mathbf{m} \rangle$ , and  $\mathbf{M}_3 = \langle \mathbf{m}\mathbf{m}\mathbf{m} \rangle$  where  $\mathbf{m}$  is a unit vector representing the axis of symmetry of the rod-like molecule, the equation for the polarity vector  $\mathbf{p}$  can be found by projecting (1) onto its first moment. Similarly, an equation for the local concentration  $c$  is derived by projection (1) onto its zeroth moment, both yielding

$$\begin{aligned} & \frac{\partial \mathbf{p}}{\partial t} + \mathbf{v} \cdot \nabla \mathbf{p} + U_0 \nabla \cdot \mathbf{M} \\ = & D_s \left( \nabla^2 \mathbf{p} + \nabla \cdot (N_1 \nabla c \mathbf{p} - \alpha \nabla \mathbf{p} \cdot \mathbf{M} - \frac{3N}{2} \nabla \mathbf{M} : \mathbf{M}_3) \right) \\ & - D_r (2\mathbf{p} + \alpha(\mathbf{M} - c\mathbf{I}) \cdot \mathbf{p} + 3N(\mathbf{M}_3 : \mathbf{M} - \mathbf{M} \cdot \mathbf{p})) \\ & + \boldsymbol{\Omega} \cdot \mathbf{p} + a(\mathbf{D} \cdot \mathbf{p} - \mathbf{D} : \mathbf{M}_3) \end{aligned} \quad (9)$$

$$\begin{aligned} & \frac{\partial c}{\partial t} + \mathbf{v} \cdot \nabla c + U_0 \nabla \cdot \mathbf{p} \\ = & D_s \left( \nabla^2 c + \nabla \cdot (N_1 c \nabla c - \alpha \nabla \mathbf{p} \cdot \mathbf{p} - \frac{3N}{2} \nabla \mathbf{M} : \mathbf{M}) \right) \end{aligned} \quad (10)$$

where  $U_0$  is the rod self-propulsion speed,  $\alpha$  is the polarity strength,  $D_s$  is the translational diffusion coefficient,  $D_r$  is the rotational diffusion coefficient,  $N_1$  is the strength of the potential for spatial inhomogeneity, and  $a$  is the geometric particle parameter for rods. At equilibrium in a uni-axial system, the orientation tensor  $\mathbf{Q}$  (symmetric and traceless) may be written as  $\mathbf{Q} = s(\mathbf{nn} - \frac{1}{3}\mathbf{I})$ , where  $s$  is the orientational order parameter (Doi and Edwards 1986). Also, the eigenvector  $\mathbf{n}$  of  $\mathbf{Q}$  is parallel to the direction of average orientation so that  $\mathbf{n} = \frac{\mathbf{p}}{\|\mathbf{p}\|}$ , and then let the order parameter be  $s = \|\mathbf{p}\|^2$ . Thus it is true that  $\mathbf{Q} = \mathbf{p}\mathbf{p} - \frac{1}{3}(\mathbf{p} \cdot \mathbf{p})\mathbf{I}$ . Since  $\mathbf{M} = \mathbf{Q} + \frac{1}{3}c\mathbf{I}$  (Yang et al. 2010) and  $\mathbf{Q}$  is traceless, we note that  $\text{tr}(\mathbf{M}) = c$ . This relationship gives rise to the closure rule  $\mathbf{M} = \mathbf{p}\mathbf{p} + \frac{1}{3}(c - \mathbf{p} \cdot \mathbf{p})\mathbf{I}$ . Additionally, we neglect the nematic strength  $N$ , so taking equations (9) and (10) and applying the closure rule results in the following governing system of equations

$$\begin{aligned} & \frac{\partial \mathbf{p}}{\partial t} + \mathbf{v} \cdot \nabla \mathbf{p} + U_0 \left[ \nabla \cdot \mathbf{p}\mathbf{p} + \frac{1}{3} \nabla (c - \mathbf{p} \cdot \mathbf{p}) \right] \\ = & D_s \left( \nabla^2 \mathbf{p} + \nabla \cdot (N_1 \nabla c \mathbf{p} - \alpha [\nabla \mathbf{p} \cdot \mathbf{p}\mathbf{p} + \frac{1}{3}(c - \mathbf{p} \cdot \mathbf{p}) \nabla \mathbf{p}]) \right) \\ & - 2D_r \left( 1 - \frac{1}{3}\alpha c + \frac{1}{3}\alpha \mathbf{p} \cdot \mathbf{p} \right) \mathbf{p} + \boldsymbol{\Omega} \cdot \mathbf{p} + a(\mathbf{D} \cdot \mathbf{p} - \mathbf{D} : \mathbf{p}\mathbf{p}\mathbf{p}) \end{aligned} \quad (11)$$

$$\frac{\partial c}{\partial t} + \mathbf{v} \cdot \nabla c + U_0 \nabla \cdot \mathbf{p} = D_s (\nabla^2 c + \nabla \cdot (N_1 c \nabla c - \alpha \nabla \mathbf{p} \cdot \mathbf{p})) \quad (12)$$

$$\frac{d\mathbf{v}}{dt} + (\mathbf{v} \cdot \nabla) \mathbf{v} = \nabla \cdot (-\Pi \mathbf{I} + \tau_p + \tau_a), \quad \nabla \cdot \mathbf{v} = 0 \quad (13)$$

$$\begin{aligned} \tau_p = & 2Re^{-1} \mathbf{D} + G[\mathbf{p}\mathbf{p} - \frac{1}{3}(\mathbf{p} \cdot \mathbf{p})\mathbf{I}] \\ & - \frac{1}{6}\alpha_0 G[2\mathbf{p}\mathbf{p} - (\mathbf{p}\mathbf{p}\mathbf{p} \cdot \mathbf{p} + \mathbf{p} \cdot \mathbf{p}\mathbf{p}\mathbf{p})] \\ & + Re_2^{-1} [\mathbf{D} \cdot (\mathbf{p}\mathbf{p} + \frac{1}{3}(c - \mathbf{p} \cdot \mathbf{p})\mathbf{I}) + (\mathbf{p}\mathbf{p} + \frac{1}{3}(c - \mathbf{p} \cdot \mathbf{p})\mathbf{I}) \cdot \mathbf{D}] \end{aligned} \quad (14)$$

$$\tau_a = G\zeta_a(\mathbf{p}\mathbf{p} - \frac{1}{3}(\mathbf{p} \cdot \mathbf{p})\mathbf{I}). \quad (15)$$

Of interest is to find a relationship between the particle activation parameter  $\zeta_a$  and the strength of polarity parameter  $\alpha$ . The system of equations above will be analyzed for stability at different equilibrium states and different initial conditions in the proceeding sections.

### 3 LINEAR STABILITY ANALYSIS

#### 3.1 Stability

A solution to the preceding governing system of equations (13)-(17) can be found by perturbing the initial state using a plane wave perturbation as follows:

$$\mathbf{v} = \mathbf{v}_0 + \epsilon \mathbf{v}_1, \mathbf{p} = \mathbf{p}_0 + \epsilon \mathbf{p}_1, \Pi = \Pi_0 + \epsilon \Pi_1, c = c_0 + \epsilon c_1$$

where  $\epsilon \ll 1$  and the perturbations are  $\mathbf{v}_1 = e^{i\mathbf{k} \cdot \mathbf{x}} \mathbf{v}_1(t)$ ,  $\mathbf{p}_1 = e^{i\mathbf{k} \cdot \mathbf{x}} \mathbf{p}_1(t)$ ,  $\Pi_1 = e^{i\mathbf{k} \cdot \mathbf{x}} \Pi_1(t)$ , and  $c_1 = e^{i\mathbf{k} \cdot \mathbf{x}} c_1(t)$  (Xiao-Gang, Forest, and Wang 2014). Here  $\mathbf{k} = (k_1, k_2, k_3)$  is the wave number vector,  $\Pi_1$  and  $c_1$  are constant unknown scalars, and  $\mathbf{v}_1$  and  $\mathbf{p}_1$  are constant unknown vectors. If we truncate at the linear order of  $\epsilon$ , then from equation (11) we arrive at an equation for the first order correction  $\mathbf{p}_1$  which is given by

$$\begin{aligned} \mathbf{p}_1' + & \left[ S_1 \mathbf{I} + iU_0 \mathbf{p}_0 \mathbf{k} - \frac{2i}{3} U_0 \mathbf{k} \mathbf{p}_0 + \frac{4}{3} \alpha D_r \mathbf{p}_0 \mathbf{p}_0 \right] \mathbf{p}_1 \\ & + \left[ S_2 \mathbf{I} + \frac{i}{2} (1-a) \mathbf{k} \mathbf{p}_0 + ia(\mathbf{k} \cdot \mathbf{p}_0) \mathbf{p}_0 \mathbf{p}_0 \right] \mathbf{v}_1 \\ & + \left[ \frac{i}{3} U_0 \mathbf{k} + D_s N_1 \|\mathbf{k}\|^2 \mathbf{p}_0 - \frac{2}{3} \alpha D_r \mathbf{p}_0 \right] c_1 = 0. \end{aligned} \quad (16)$$

In a similar fashion, equation (12) yields

$$c_1' + S_3 c_1 + (\mathbf{k} \cdot \mathbf{p}_1) S_4 = 0. \quad (17)$$

The Navier-Stokes equations (13) together with the passive nematic stress  $\tau_p$  (14) and the active stress  $\tau_a$  (15) will result in

$$\begin{aligned} & \left[ S_5 \mathbf{I} - \frac{2i}{3} \alpha_0 G \left( (\|\mathbf{p}_0\|^2 - \frac{1}{2} \alpha_0) \mathbf{p}_0 \mathbf{k} + 2(\mathbf{p}_0 \cdot \mathbf{k}) \mathbf{p}_0 \mathbf{p}_0 \right) \right. \\ & \quad \left. + \frac{iG}{3} (1 + \zeta_a) (2\mathbf{k} \mathbf{p}_0 - \mathbf{p}_0 \mathbf{k}) \right] \mathbf{p}_1 + \mathbf{v}_1' \\ & + \left[ S_6 \mathbf{I} + \frac{1}{2Re_2} \left( \|\mathbf{k}\|^2 \mathbf{p}_0 \mathbf{p}_0 + (\mathbf{p}_0 \cdot \mathbf{k}) (\mathbf{p}_0 \mathbf{k} + \mathbf{k} \mathbf{p}_0) \right) \right] \mathbf{v}_1 \\ & + i\mathbf{k} \Pi_1 = 0, \\ & \mathbf{k} \cdot \mathbf{v}_1 = 0. \end{aligned} \quad (18)$$

All of the constants  $S_i, i = 1, 2, 3, 4, 5, 6$  are defined in the appendix. From the linearized momentum equation above, we can see that  $\Pi_1$  can be eliminated from the system. This is done by taking the dot

product of both sides of the equation with  $\mathbf{k}$  and solving for  $\Pi_1$  and then substituting in for the result, which is

$$\Pi_1 = \frac{(C\mathbf{p}_1 + D\mathbf{v}_1) \cdot \mathbf{k}}{i\|\mathbf{k}\|^2}.$$

The linearized system of equations can now be written in the following way:

$$\begin{pmatrix} c_1' \\ \mathbf{p}_1' \\ \mathbf{v}_1' \end{pmatrix} = \begin{pmatrix} -S_3 & -S_4\mathbf{k}^\top & 0 \\ \mathbf{z} & A & B \\ 0 & C' & D' \end{pmatrix} \begin{pmatrix} c_1 \\ \mathbf{p}_1 \\ \mathbf{v}_1 \end{pmatrix}$$

where  $\mathbf{z} = \frac{i}{3}U_0\mathbf{k} + (D_sN_1\|\mathbf{k}\|^2 - \frac{2}{3}\alpha D_r)\mathbf{p}_0$ ,  $C' = (\mathbf{I} - \frac{1}{\|\mathbf{k}\|^2}\mathbf{k}\mathbf{k}) \cdot C$  and  $D' = (\mathbf{I} - \frac{1}{\|\mathbf{k}\|^2}\mathbf{k}\mathbf{k}) \cdot D$ . The matrices  $A, B, C$ , and  $D$  are defined in the appendix. For simplicity, we will denote the above system by  $\mathbf{y}' = F\mathbf{y}$  where  $\mathbf{y}$  is the vector of unknown quantities,  $\mathbf{y}'$  is the time derivative of the unknown quantities, and  $F$  is the  $7 \times 7$  coefficient matrix operating on  $\mathbf{y}$ . In order to examine the stability of this system, we need to determine the eigenvalues of the matrix  $F$ . Specifically, we are interested in finding the instances which lead to unstable states of the system. This occurs when at least one, but not all, eigenvalue has positive real part (Sanchez 1968). The eigenvalues are dependent on the equation parameters and the initial equilibrium state to be perturbed.

### 3.2 Equilibrium

We seek to study the stability of this system near equilibrium. The system is at equilibrium when the flow velocity  $\mathbf{v} = 0$  and the polarity vector  $\mathbf{p}$  is homogeneous in space. If we examine equation (13), we can see that there will be two different equilibrium states depending on  $\mathbf{p}$ . The first equilibrium is when  $\mathbf{p} = \mathbf{0}$  and  $\alpha$  takes any value, and this is known as the isotropic state. The second equilibrium occurs when  $1 - \frac{1}{3}\alpha c + \frac{1}{3}\alpha\mathbf{p} \cdot \mathbf{p} = 0$ . At this equilibrium,  $c = \langle 1 \rangle = \int_{\|\mathbf{m}\|=1} 1 \cdot f(\mathbf{m})d\mathbf{m} = 1$  since the nanorod number density function  $f$  is normalized, so the polar state will be when

$$\|\mathbf{p}\|^2 = \frac{\alpha - 3}{\alpha}.$$

The goal is to determine what values for the parameters  $\alpha$  and  $\zeta_a$  will result in a positive real part of the eigenvalue. These states are very interesting dynamically, so we wish to find situations where this is true. In addition, we are interested in the case for  $\zeta_a < 0$  which is referred to as the pusher case (Saintillan and Shelley 2008). We will examine the stability of this system near the isotropic equilibrium state ( $\|\mathbf{p}\|^2 = 0$ ) and the polar equilibrium state ( $\|\mathbf{p}\|^2 = \frac{\alpha-3}{\alpha}$ ).

#### 3.2.1 Isotropic Equilibrium State

For the isotropic equilibrium case, the initial state of the polarity vector,  $\mathbf{p}_0$ , will be zero along with the initial velocity vector  $\mathbf{v}_0$ . Additionally, the initial local concentration  $c_0 = 1$ , and the rod self-propulsion speed  $U_0$  will be set to zero. With these initial conditions, the coefficient matrix  $F$  has the following eigenvalues:

$$\lambda_{1,2,3} = -S_1 = (D_s\|\mathbf{k}\|^2 + 2D_r)(\frac{\alpha}{3}c_0 - 1)$$

$$\lambda_4 = iU_0(k_1 - k_2 + k_3) - D_s\|\mathbf{k}\|^2(1 + N_1c_0)$$

$$\lambda_{5,6} = -\frac{1}{Re||\mathbf{k}||^2}$$

$$\lambda_7 = \frac{1}{Re} (||\mathbf{k}||^2 - \frac{1}{||\mathbf{k}||^2}).$$

Since  $N_1, D_s, ||\mathbf{k}||^2$  and  $c_0$  are guaranteed positive, it is clear that  $\lambda_4$  will always have negative real part. Also,  $\lambda_{5,6}$  are completely real and guaranteed negative as well because  $Re$  is always positive. However,  $Re(\lambda_7) > 0$  if  $||\mathbf{k}||^2 > 1$ . Given that  $c_0 = 1$ ,  $\lambda_{1,2,3}$  will also have positive real part if  $\frac{\alpha}{3}c_0 - 1 > 0$ , or equivalently,  $\alpha > 3$ . Results showing some patterns observed for the unstable states are shown in section 4.2.1.

### 3.2.2 Polar Equilibrium State for a Specific Case of the Wave Number $\mathbf{k}$

The polar equilibrium state occurs when  $||\mathbf{p}_0||^2 = \frac{\alpha-3}{\alpha}$ . Without loss of generality we can take an initial polarity vector to be  $\mathbf{p}_0 = (p, 0, 0)$ , where  $p = \sqrt{\frac{\alpha-3}{\alpha}}$ . As in the isotropic equilibrium state, an additional assumption made is that the initial velocity of the surrounding fluid  $\mathbf{v}_0 = 0$ . Also, we will let the rod self-propulsion velocity  $U_0 = 0$  for this analysis.

This section addresses a specific case of the wave number vector  $\mathbf{k}$  for when  $k_2 = k_3 = 0$  but  $k_1 \neq 0$ , or  $\mathbf{k} = (k_1, 0, 0)$ . Thus, this case leads to the coefficient matrix  $F$  having eigenvalues equal to

$$\begin{aligned} \lambda_1 &= 0 \\ \lambda_{2,3} &= -\frac{1}{2} \left[ \frac{4}{3} \alpha D_r p^2 + D_s k_1^2 (N_1 - \alpha p^2) \right. \\ &\quad \left. \mp \sqrt{\left( D_s k_1^2 (1 + \alpha p^2) - \frac{4}{3} \alpha D_r p^2 \right)^2 + 4 D_s p^2 k_1^2 \left( D_s N_1 k_1^2 - \frac{2}{3} \alpha D_r \right)} \right] \\ \lambda_{4,5} &= \lambda_{6,7} = -\frac{1}{2} \left\{ k_1^2 \left[ D_s (N_1 - \alpha p^2) + \frac{1}{Re} + \frac{p^2}{Re_2} \right] \right. \\ &\quad \left. \mp k_1 \sqrt{k_1^2 \left[ \frac{1}{Re} + \frac{p^2}{Re_2} - D_s (N_1 - \alpha p^2) \right]^2 + G p^2 (1 + a) \left[ \frac{1}{3} \alpha_0 - \frac{2}{3} \alpha_0 p^2 - 1 - \zeta_a \right]} \right\}. \end{aligned}$$

We will let  $k_1 = 1$  because the magnitude of  $k_1$  has no significant impact on whether the eigenvalue has positive real part or not. We discovered that the eigenvalue  $\lambda_4$  listed above will be positive for  $\alpha > 3$  provided that  $\zeta_a < 0$  and  $|\zeta_a|$  is large enough. In this case,  $-\zeta_a$  dominates the eigenvalue  $\lambda_4$ . The relationship between  $\zeta_a$  and  $\alpha$  which represents when  $\lambda_4 = 0$  can be seen in Figure 1 below. When  $\alpha > 3$ ,  $\lambda_4 > 0$  whenever  $\zeta_a < 0$  and smaller than a critical value  $\zeta_{a,c}$  which will be visibly apparent in Figure 2 below. Thus, under these circumstances the system will have an unstable state. Results showing some patterns observed for the unstable states are shown in section 4. [need to be more specific]

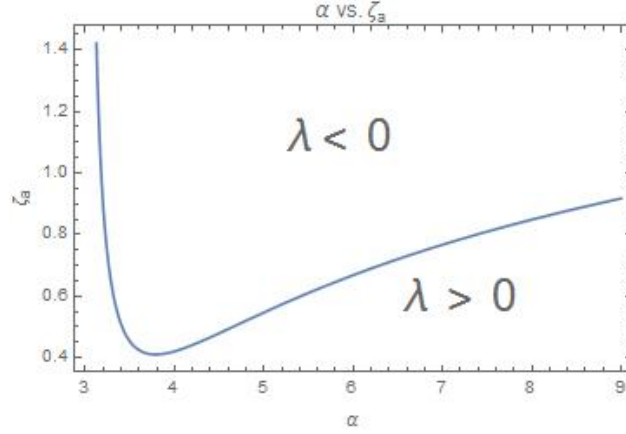


Figure 1: A depiction of the relationship for  $\zeta_{a,c} = \zeta_{a,c}(\alpha)$ . Along this curve, the eigenvalue  $\lambda_4 = 0$ .

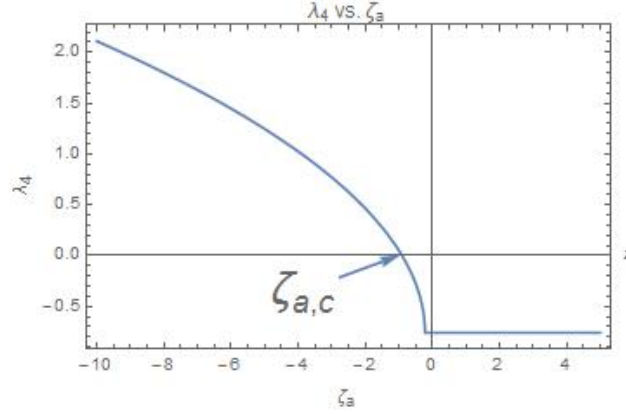


Figure 2: A special case of  $\text{Re}(\lambda_4)$  vs.  $\zeta_a$  for when  $\alpha = 5$ , showing the critical value  $\zeta_{a,c}$ .

## 4 NUMERICAL SIMULATIONS

### 4.1 Outline of Numerical Method

The Navier-Stokes equations were solved using the finite difference method on a staggered grid as in (Griebel, Dornsiefer, and Neunhoffer 1998). The horizontal velocity component  $v_1$  is located at the midpoints of the vertical edges of each cell, and the vertical velocity component  $v_2$  is located at the midpoints of the horizontal edge of each cell. Both the pressure  $\Pi$  and  $v_3$  are located at the cell centers. One reason a staggered grid might be used is to prevent possible pressure oscillations.

Once the solution to the Navier-Stokes equations is found numerically, which yields the velocity and pressure, these values are input into the transport equations for the polarity vector and local concentration. These equations are subsequently solved using a semi-implicit method where the time derivative is represented by a forward Euler scheme, resulting in the following two elliptic equations:  $[1 - D_s \Delta t \nabla^2] \mathbf{p}^{n+1} = \mathbf{p}^n + \Delta t \mathbf{F}^n$



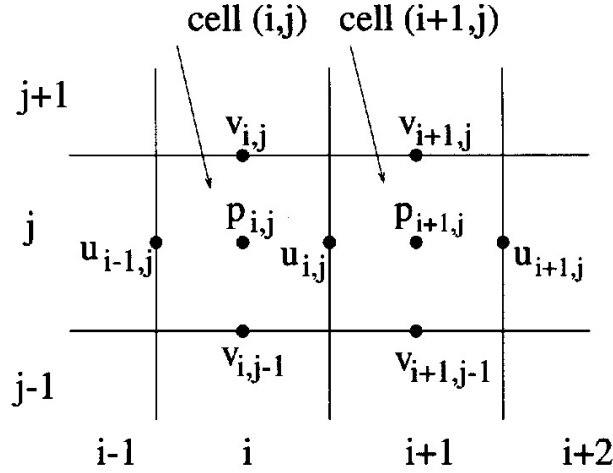


Figure 3: An illustration of the staggered grid deployed in (Griebel, Dornsiefer, and Neunhoeffer 1998), where  $p$  is pressure in this context.

and  $[1 - D_s \Delta t \nabla^2] c^{n+1} = c^n + \Delta t H^n$  where

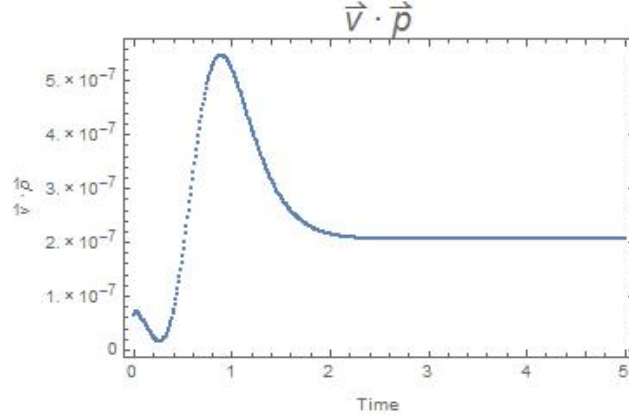
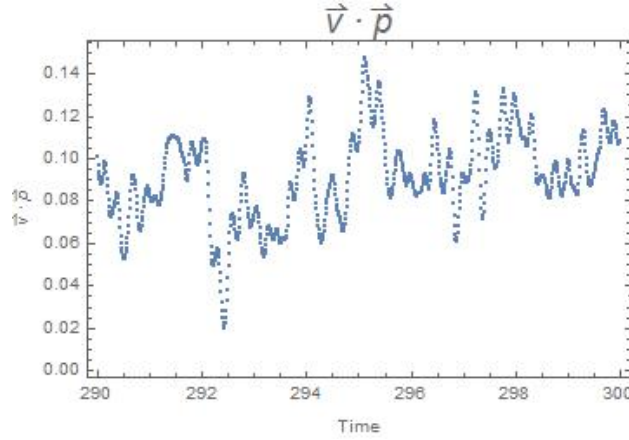
$$\begin{aligned} \mathbf{F} = & D_s \left( \nabla^2 \mathbf{p} + \nabla \cdot (N_1 \nabla c \mathbf{p} - \alpha [\nabla \mathbf{p} \cdot \mathbf{p} \mathbf{p} + \frac{1}{3} (c - \mathbf{p} \cdot \mathbf{p}) \nabla \mathbf{p}]) \right) \\ & - 2D_r \left( 1 - \frac{1}{3} \alpha c + \frac{1}{3} \alpha \mathbf{p} \cdot \mathbf{p} \right) \mathbf{p} + \boldsymbol{\Omega} \cdot \mathbf{p} + a \left( \mathbf{D} \cdot \mathbf{p} - \mathbf{D} : \mathbf{p} \mathbf{p} \mathbf{p} \right) \\ & - \mathbf{v} \cdot \nabla \mathbf{p} - U_0 \left[ \nabla \cdot \mathbf{p} \mathbf{p} + \frac{1}{3} \nabla (c - \mathbf{p} \cdot \mathbf{p}) \right] \end{aligned}$$

$$H = D_s (\nabla^2 c + \nabla \cdot (N_1 c \nabla c - \alpha \nabla \mathbf{p} \cdot \mathbf{p})) - \mathbf{v} \cdot \nabla c + U_0 \nabla \cdot \mathbf{p}.$$

With this setup of the equations, there are now 4 equations (one for the local concentration and one for each component of the polarity vector) that need to be solved in order to get the solution for the polarity vector and the local concentration. These elliptic equations are solved using the MUDPACK Multigrid solver (Adams 1989) at each time iteration to update the values of the polarity vector and local concentration.

## 4.2 Results From Numerical Simulations

The computational domain in this work is a 2D square cavity. The boundary conditions used for the simulations done here are periodic boundary conditions. The parameters other than  $\alpha$  and  $\zeta_a$  will be fixed and will be equal to  $D_s = 0.02$ ,  $D_r = 5$ ,  $G = 4$ ,  $\alpha_0 = 1$ ,  $Re = 5$ ,  $Re_2 = 5$ , and  $a = 0.95$ . For positive values of  $\zeta_a$  or values that are negative but close to zero, the system will be stable and will converge to a stable state. To present this graphically, we have chosen to plot the average value of the velocity vector dotted with the polarity vector after nearly two million iterations of the solver were run. At this point, if  $\langle \mathbf{v} \cdot \mathbf{p} \rangle$  remained at some constant value, then the system is seen as stable. However, if this is not the case, then the system is seen as unstable. In Figure 4, an example of a stable state is shown while in Figure 5 an unstable state is shown.

Figure 4: Stable state for the case where  $\zeta_a = -1$ .Figure 5: Unstable state for the case where  $\zeta_a = -10$ .

#### 4.2.1 Patterns Observed for Isotropic Equilibrium State

For the isotropic equilibrium state, multiple excitable patterns are observed. A periodic 1D banded structure is shown in Figure 6, and it is considered 1D banded since the norm of the polarity vector only changes in one linear direction. Then as  $\alpha$  increases to 3.9, the pattern converts to a steady 1D banded structure. The most interesting pattern observed is the 2D periodic structure when  $\alpha = 4.2$  and  $\zeta_a = -5$ . The average value of the in-plane angle is shown in Figure 9, and it is obvious that this is an oscillatory state given how the in-plane angle is changing over time. The maximum and minimum of the average in-plane angle are relatively close to each other which implies that the system is in a wagging state, i.e. each polymer is "wagging" back and forth in short, simple motions.

#### 4.2.2 Patterns Observed for Polar Equilibrium State

For the polar equilibrium state, multiple excitable patterns are observed. A pattern occurs where majority of the time the solution is parallel to the polarity vector, but then for short bursts of time there is a large increase in activity. This is when  $\alpha = 3.9$  and  $\zeta_a = -9$  and it is depicted in Figure 10, where the time difference between the 3 plots shown is only 1 time unit. Then as  $\alpha$  increases to 4.2, the pattern converts to a 2D periodic/oscillatory structure. A similar plot to Figure 9 was not included but provided the same insights.

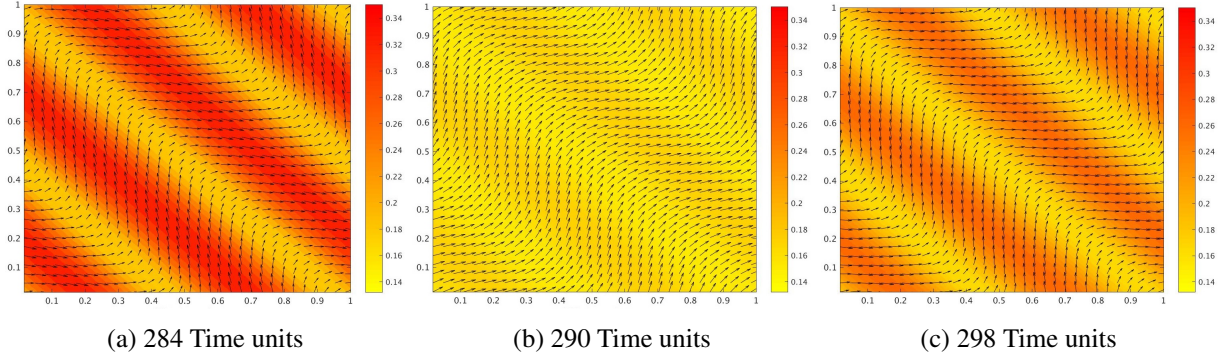


Figure 6: Polarity vector norm superimposed on the polarity vector quiver plot. 1D oscillatory structure for  $\alpha = 3.4$  and  $\zeta_a = -5$ .

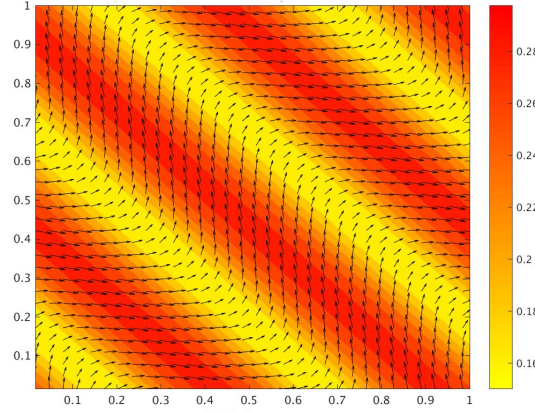


Figure 7: Polarity vector norm superimposed on the polarity vector quiver plot. Steady 1D Banded structure for  $\alpha = 3.9$  and  $\zeta = -5$ .

This state that was brought on by perturbing the polar equilibrium state is a wagging state. Additional, less interesting patterns were neglected in this work.

## 5 CONCLUSION

In this paper, we have presented our mathematical model for polar active liquid crystals which include the implementation of certain closure rules. Then we presented a method of linear stability analysis in order to examine the dynamics of the system near equilibrium. While doing this, we observed that for a specific case of the wave number  $\mathbf{k}$ , there are stable and unstable states of the system based on the values of the particle activation parameter  $\zeta_a$  and the polarity strength  $\alpha$ . Next, we provided some results from the numerical simulations that were conducted which confirmed our results from the linear stability analysis. The goal of future work in this subject matter is to explore different values of the wave number  $\mathbf{k}$  including allowing  $k_2, k_3 \neq 0$ , as well as continue to conduct numerical simulations using different parameter values to determine the full effect of this (and numerical boundary conditions) on the stability of the liquid crystal system. Additionally, simulations where more physical boundaries are applied will be pursued.

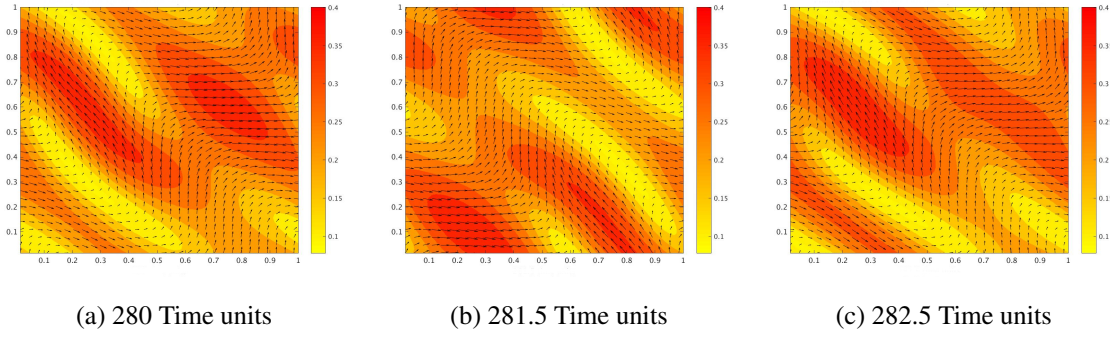


Figure 8: Polarity vector norm superimposed on the polarity vector quiver plot. 2D periodic structure for  $\alpha = 4.2$  and  $\zeta_a = -5$ .

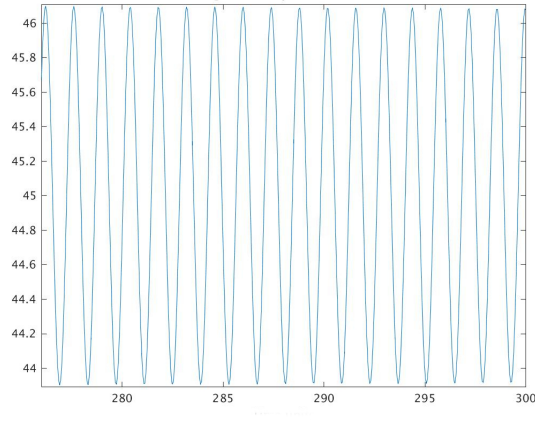


Figure 9: Average value of the in-plane angle for  $\alpha = 4.2$  and  $\zeta = -5$ .

## ACKNOWLEDGMENTS

This research is supported by the National Science Foundation, NSF-1517519. I would also like to acknowledge and thank the Modeling and Simulation Department at ODU for funding my work through a Modeling and Simulation assistantship.

## A APPENDIX

The constants that were defined in 16, 17, and 18 are as follows:

$$\begin{aligned}
 S_1 &= i(\mathbf{v}_0 + U_o \mathbf{p}_0) \cdot \mathbf{k} + D_s [|\mathbf{k}|^2 (1 - \frac{\alpha}{3}(c_0 - \|\mathbf{p}_0\|^2) + N_1 c_0) - \alpha(\mathbf{k} \cdot \mathbf{p}_0)^2] \\
 &\quad + 2D_r (1 - \frac{1}{3}\alpha c_0 + \frac{1}{3}\alpha \|\mathbf{p}_0\|^2) \\
 S_2 &= -\frac{i}{2}(1 + a)(\mathbf{k} \cdot \mathbf{p}_0) \\
 S_3 &= i(\mathbf{v}_0 \cdot \mathbf{k}) + D_s |\mathbf{k}|^2 (1 + N_1 c_0)
 \end{aligned}$$

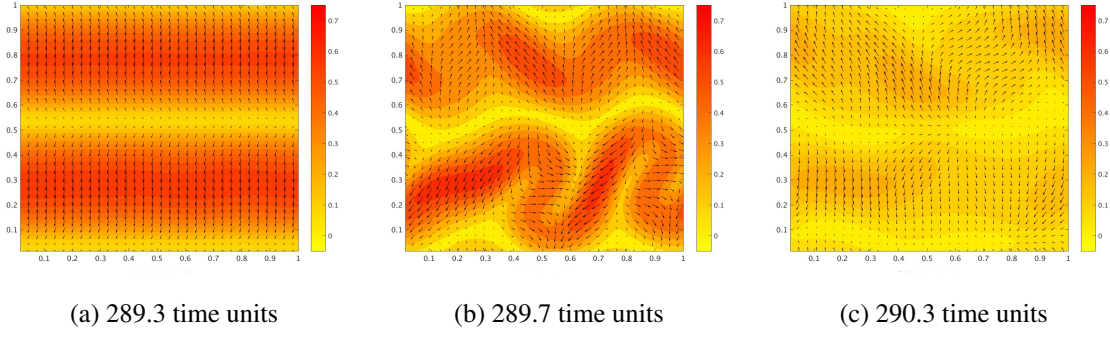


Figure 10: Polarity vector norm superimposed on the polarity vector quiver plot. Extremely fast pattern changes when  $\alpha = 3.9$  and  $\zeta_a = -9$ .

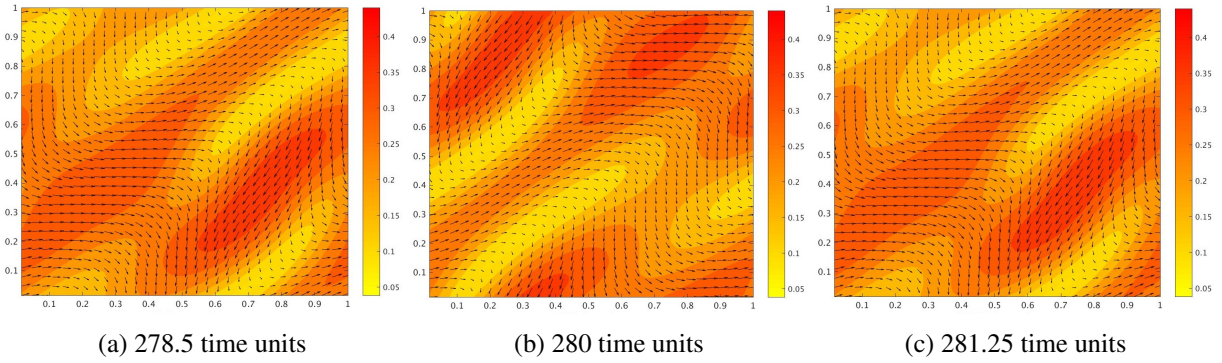


Figure 11: Polarity vector norm superimposed on the polarity vector quiver plot. 2D periodic structure when  $\alpha = 4.2$  and  $\zeta_a = -5$ .

$$S_4 = U_0 - \alpha D_s(\mathbf{k} \cdot \mathbf{p}_0)$$

$$S_5 = iG(\mathbf{p}_0 \cdot \mathbf{k}) \left( \frac{1}{3}\alpha_0 - (1 + \zeta_a) - \frac{2}{3}\alpha_0 \|\mathbf{p}_0\|^2 \right)$$

$$S_6 = i(\mathbf{v}_0 \cdot \mathbf{k}) + \frac{1}{Re} \|\mathbf{k}\|^2 + \frac{1}{2Re_2} (\mathbf{p}_0 \cdot \mathbf{k})^2 - \frac{1}{3Re_2} \|\mathbf{p}_0\|^2 \|\mathbf{k}\|^2.$$

The matrices  $A$ ,  $B$ ,  $C$ , and  $D$  from the system of equations are defined as:

$$A = - \left( S_1 \mathbf{I} + iU_0 \mathbf{p}_0 \mathbf{k} - \frac{2i}{3} U_0 \mathbf{k} \mathbf{p}_0 + \frac{4}{3} \alpha D_r \mathbf{p}_0 \mathbf{p}_0 \right)$$

$$B = - \left( S_2 \mathbf{I} + \frac{i}{2} (1 - a) \mathbf{k} \mathbf{p}_0 + ia(\mathbf{k} \cdot \mathbf{p}_0) \mathbf{p}_0 \mathbf{p}_0 \right)$$

$$C = - \left[ S_5 \mathbf{I} - \frac{2i}{3} \alpha_0 G \left( (\|\mathbf{p}_0\|^2 - \frac{1}{2} \alpha_0) \mathbf{p}_0 \mathbf{k} + 2(\mathbf{p}_0 \cdot \mathbf{k}) \mathbf{p}_0 \mathbf{p}_0 \right) + \frac{iG}{3} (1 + \zeta_a) (2\mathbf{k} \mathbf{p}_0 - \mathbf{p}_0 \mathbf{k}) \right]$$

$$D = - \left[ S_6 \mathbf{I} + \frac{1}{2Re_2} \left( \|\mathbf{k}\|^2 \mathbf{p}_0 \mathbf{p}_0 + (\mathbf{k} \cdot \mathbf{p}_0) (\mathbf{p}_0 \mathbf{k} + \mathbf{k} \mathbf{p}_0) \right) \right].$$

## REFERENCES

- Adams, J. C. 1989. “mudpack: Multigrid portable fortran software for the efficient solution of linear elliptic partial differential equations”. *Applied Mathematics and Computation* vol. 34, pp. 113–146.
- Darnton, N., L. Turner, K. Breuer, and H. C. Beng. 2004. “Moving Fluid with Bacterial Carpets”. *Biophysical Journal* vol. 86, pp. 1863–1870.
- Doi, M., and S. Edwards. 1986. *The Theory of Polymer Dynamics*. 1st ed. New York, New York, Oxford University Press.
- Dreyfus, R., J. Baudry, M. Roper, M. Ferminger, H. Stone, and J. Bibette. 2005. “Microscopic artificial swimmers”. *Nature* vol. 437, pp. 862–865.
- Gray, G., K. Harrison, and J. Nash. 2007. “New family of nematic liquid crystals for displays”. *Electronics Letters* vol. 9, pp. 130–131.
- Griebel, M., T. Dornsiefer, and W. Neunhoeffler. 1998. *Numerical Simulation in Fluid Dynamics*. 1st ed. Philadelphia, Society for Industrial and Applied Mathematics.
- Pedley, T. J., and J. O. Kessler. 1992. “Hydrodynamic Phenomena in suspensions of swimming microorganisms”. *Annual Review of Fluid Mechanics* vol. 24, pp. 313–358.
- Saintillan, D., and M. J. Shelley. 2008, Apr. “Instabilities and Pattern Formation in Active Particle Suspensions: Kinetic Theory and Continuum Simulations”. *Phys. Rev. Lett.* vol. 100, pp. 178103.
- Sanchez, D. A. 1968. *Ordinary Differential Equations and Stability Theory: An Introduction*. 1st ed. New York, New York, Dover Publications.
- Xiao-Gang, Y., M. G. Forest, and Q. Wang. 2014. “Near equilibrium dynamics and one-dimensional spatial-temporal structures of polar active liquid crystals”. *Chinese Physics B* vol. 23, pp. 1187011–1187037.
- Yang, X., M. G. Forest, W. Mullins, and Q. Wang. 2010. “2-D lid-driven cavity flow of nematic polymers: an unsteady sea of defects”. *Soft Matter* vol. 6, pp. 1138–1156.
- Zhang, S., and S. Kumar. 2008. “Carbon Nanotubes as Liquid Crystals”. *Small* vol. 4, pp. 1270–1283.



# **SIMULATION OF SOUND ABSORPTION BY SCATTERING BODIES TREATED WITH ACOUSTIC LINERS AND THE ASSESSMENT OF ITS HIGH-PERFORMANCE PARALLEL COMPUTING CAPABILITIES**

Michelle E. Pizzo and Fang Q. Hu

Old Dominion University  
Department of Mathematics and Statistics  
2300 Engineering and Computational Sciences Building  
Norfolk, VA, 23529, USA  
[mpizzo@odu.edu](mailto:mpizzo@odu.edu), [fhu@odu.edu](mailto:fhu@odu.edu)

## **ABSTRACT**

Aircraft noise reduction is a major goal within the field of aviation research. When designing next generation quiet aircraft, it is important to be able to accurately and efficiently predict the acoustic scattering by an aircraft body from a given noise source. Acoustically treated liners are an effective tool for aircraft noise reduction. The objective of this work is to study the modeling and simulation of acoustic wave scattering by prototype geometric bodies treated with acoustic liners. Moreover, fast algorithms and high performance computing are considering to both assess and reduce the computational cost of the simulation. Carried out by large scale parallel computing, the scalability, speedup, and efficiency of the acoustic simulation will be studied. Preliminary results are included for modeling the acoustic wave scattering by non-treated geometries from a given point source. Geometries include a flat-plate and sphere.

**Keywords:** aeroacoustics, wave scattering, high performance computing, acoustic liners, admittance

## **1 INTRODUCTION**

Aircraft noise reduction is a major goal within the field of aviation research. When designing next generation quiet aircraft, it is important to be able to accurately and efficiently predict the acoustic scattering by an aircraft body, both rigid as well as lined, from a given noise source (Hu 2013, Hu 2014, Hu et al. 2016). Acoustic scattering problems can be modeled using boundary element methods (BEMs) by reformulating the linear convective wave equation as a boundary integral equation (BIE), both in the frequency domain and the time domain (Chappell et al. 2006, Ergin et al. 1999, Jones and Hu 2007, Marburg 2015, Marburg and Schneider 2001).

Although frequency domain solvers are the most commonly used and researched within literature, there are several distinct advantages (Hu 2013) to using a time domain solver. For example, a time domain solution allows for the simulation and study of broadband sources and time-dependent transient signals, scattering solutions at all frequencies to be obtained within a single computation, and the avoidance of needing to invert a large dense linear system (as is required in the frequency domain). Additionally, a time domain solution is more naturally coupled with a nonlinear computational fluid dynamics simulation of noise sources.

Time domain boundary integral equations (TDBIE) have an intrinsic numerical instability and carry a high computational cost. In recent years, numerical techniques for modeling acoustic wave scattering by complex



geometries using the TDBIE have been under development (Hu 2013, Hu 2014, Hu et al. 2016). It has been shown that stability can be realized using a Burton-Miller type reformulation of the BIE. Moreover, the computational cost can be reduced using fast algorithms and high performance computing (HPC). This work uses a time domain BEM (TDBEM) approach, in which the scattering solution is obtained using temporal and surface basis functions and a March-On-in-Time scheme in which a sparse matrix is solved iteratively. The March-On-in-Time scheme reduces computational complexity.

The numerical formulation of the stable TDBEM is detailed in Section 2. The formulation is valid for both rigid and lined acoustic surfaces with a mean flow  $\mathbf{U}$ . The incorporation of an impedance boundary condition, valid for surfaces with acoustically treated liners, is detailed in Section 3. Preliminary results are included in Section 4 for modeling the acoustic wave scattering by non-treated geometries, i.e. geometries with a rigid surface, from a given point source. Concluding remarks are given in Section 5, and future work is detailed in Section 6.

## 2 FORMULATION OF THE STABLE TIME DOMAIN BOUNDARY ELEMENT METHOD

The convective wave equation with constant mean flow  $\mathbf{U}$  is given by:

$$\left(\frac{\partial}{\partial t} + \mathbf{U} \cdot \nabla\right)^2 p - c^2 \nabla^2 p = q(\mathbf{r}, t) \quad (1)$$

where  $q(\mathbf{r}, t)$  is the source term,  $p(\mathbf{r}, t)$  is the acoustic pressure, and  $c$  is the speed of sound. Consider a homogeneous initial condition  $p(\mathbf{r}, 0) = \partial p / \partial t(\mathbf{r}, 0) = 0$ . By introducing free-space adjoint Green's function:

$$\begin{aligned} \tilde{G}(\mathbf{r}, t; \mathbf{r}', t') &= \frac{1}{4\pi c^2 \bar{R}} \delta\left(t' - t + \beta \cdot (\mathbf{r}' - \mathbf{r}) - \frac{\bar{R}}{c\alpha^2}\right) \\ \alpha &= \sqrt{1 - M^2}, \quad \beta = \frac{\mathbf{M}}{1 - M^2}, \quad \mathbf{M} = \frac{\mathbf{U}}{c} \\ \bar{R} &= \sqrt{|\mathbf{M} \cdot (\mathbf{r} - \mathbf{r}')|^2 + \alpha^2 |\mathbf{r} - \mathbf{r}'|^2} \end{aligned} \quad (2)$$

where  $M = |\mathbf{M}|$  and  $\mathbf{r}$  is a point on scattering body surface, the wave propagation problem can be reformulated into a TDBIE.

To reformulate the wave propagation problem into a TDBIE, we consider the Kirchhoff integral representation of the acoustic field in the presence of a mean flow:

$$p(\mathbf{r}', t') = \int_V \frac{q(\mathbf{r}, t'_R)}{4\pi c^2 \bar{R}} d\mathbf{r} + \int_0^{t'^+} \int_S \left[ c^2 \left( \tilde{G} \frac{\partial p}{\partial \bar{n}} - p \frac{\partial \tilde{G}}{\partial \bar{n}} \right) - U_n \left( \tilde{G} \frac{\partial p}{\partial t} - p \frac{\partial \tilde{G}}{\partial t} \right) \right] d\mathbf{r}_S dt \quad (3)$$

where  $\partial / \partial \bar{n} = \partial / \partial n - M_n(\mathbf{M} \cdot \nabla) = (\mathbf{n} - M_n \mathbf{M}) \cdot \nabla$  denotes a modified normal derivative,  $\bar{\mathbf{n}} = \mathbf{n} - M_n \mathbf{M}$  and  $M_n = \mathbf{M} \cdot \mathbf{n}$  such that  $\mathbf{n}$  is the inward normal vector on the scattering body,  $t'_R = t' + \beta \cdot (\mathbf{r}' - \mathbf{r}) - \bar{R}/(c\alpha^2)$ , and  $S$  denotes the surfaces of both the scattering body and acoustic source. Figure 1 illustrates the relationship between the mean flow, the surface of the scattering body, and the surface of the acoustic source.

In Eq. (3), the left integral is representative of direct sound and the right integral is representative of the sound contribution from the surface of both the scattering body and acoustic source. The TDBIE results by taking the limit of Eq. (3) as  $\mathbf{r}' \rightarrow \mathbf{r}'_S$  where  $\mathbf{r}'_S$  is a point on the boundary and  $\mathbf{r}_S$  is some arbitrary point:

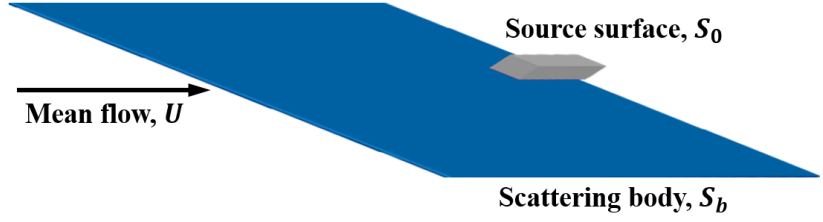


Figure 1: Schematic diagram illustrating the relationship between the mean flow, the surface of the scattering body, and the surface of the acoustic source.

$$C_S p(\mathbf{r}'_S, t') = \int_V \frac{q(\mathbf{r}, t'_R)}{4\pi c^2 R} d\mathbf{r} + \int_0^{t'^+} \int_S \left[ c^2 \left( \tilde{G} \frac{\partial p}{\partial \bar{n}} - p \frac{\partial \tilde{G}}{\partial \bar{n}} \right) - U_n \left( \tilde{G} \frac{\partial p}{\partial t} - p \frac{\partial \tilde{G}}{\partial t} \right) \right] d\mathbf{r}_S dt \quad (4)$$

where  $C_S = 1$  if  $\mathbf{r}'_S$  is on the exterior of  $S$  and  $C_S = 1/2$  if  $\mathbf{r}'_S$  is on  $S$ . Using the relation that  $\partial/\partial \bar{n} = \partial/\partial n - M_n(\mathbf{M} \cdot \nabla) = (\mathbf{n} - M_n \mathbf{M}) \cdot \nabla$  in Eq. (4),  $\partial p/\partial \bar{n}$  can be expressed with the term  $\partial p/\partial n$ . For rigid acoustic surfaces,  $\partial p/\partial n = 0$ .

The resulting TDBIE has intrinsic numerical instabilities due to resonant frequencies resulting from nontrivial solutions in the interior domain. Using a Burton-Miller type reformulation of Eq. (4), resonant frequencies can be eliminated and stability achieved (Hu 2013, Hu 2014, Hu et al. 2016). The stable Burton-Miller type reformulation of Eq. (4) is discretized by dividing  $S$  into boundary elements using surface element basis functions  $\phi_i(\mathbf{r}_S)$  at node  $i$  and temporal basis functions  $\psi_j(t)$  at time  $j$ :

$$p(\mathbf{r}_S, t) = \sum_{i=1}^{N_e} \sum_{j=0}^{N_t} u_i^j \psi_j(t) \phi_i(\mathbf{r}_S) \quad (5)$$

In Eq. (5),  $N_e$  denotes the total number of surface nodes,  $N_t$  denotes the number of time-steps, and  $u_i^j$  denotes the solution at node  $i$  and time-step  $j$ . Equation (5) yields the collocation March-On-in-Time scheme:

$$\mathbf{B}_0 \mathbf{u}^j = \mathbf{q}^j - \sum_{m=1}^{j_M} \mathbf{B}_m \mathbf{u}^{j-m} \implies \mathbf{u}^j = \lambda^j \mathbf{e}_0 \quad (6)$$

which reduces computational complexity. In Eq. (6),  $\mathbf{u}^j$  denotes the vector of all coefficients  $u$  at time  $j$ . The solution is obtained by iteratively solving the system of equations. In the system (6),  $B_m$ ,  $m = 0, \dots, j_M$  is sparse. Stability is realized if and only if the magnitude of the largest eigenvalue of  $B_m$  is less than or equal to 1, i.e.,  $\max|\lambda| \leq 1$ .

### 3 INCORPORATION OF AN IMPEDANCE BOUNDARY CONDITION

Consider a geometric body with a surface that is treated with an acoustic liner. In this case,  $\partial p/\partial n \neq 0$  unlike rigid acoustic surfaces where  $\partial p/\partial n = 0$ . Without the presence of mean flow,  $\partial p/\partial n$  can be represented (Marburg and Schneider 2001) in the frequency domain by:

$$P_n(\mathbf{x}, \omega) = \frac{\partial p}{\partial n}(\mathbf{x}, \omega) = i\omega \rho_0 Y(\omega) p(\mathbf{x}, \omega) \quad (7)$$

where  $\rho_0$  is the density,  $Y(\omega) = 1/Z(\omega)$  is the surface admittance, and  $Z(\omega)$  is the surface impedance. It can be shown that (refer to Appendix A):

$$P_n(\mathbf{x}, t) = \frac{\partial p}{\partial n}(\mathbf{x}, t) = \frac{\rho_0}{2\pi} \int_{-\infty}^t \frac{\partial y}{\partial t}(t - \tau) p(\mathbf{x}, \tau) d\tau \quad (8)$$

where  $\partial y / \partial t$  is the time derivative of  $y(t)$ , the inverse Fourier transform of  $Y(\omega)$ .

The ability to translate the acoustic liner admittance from the frequency domain to the time domain is heavily motivated by the work of Rienstra (Rienstra 2006), in which a frequency domain impedance boundary condition is translated to the time domain using Fourier transforms. Using experimentally determined admittance data and methodology similar to Rienstra (Rienstra 2006), a time domain solution of  $y(t)$  can be calculated. Then, Eq. (8) can be coupled with the BIE that provides the framework for accurately calculating sound scattering from acoustically large bodies. This coupling will allow for the study of sound absorption by acoustic liners regarding both the spatial resolution of the TDBEM with respect to the surface element basis functions and the far field acoustic impedance behaviors of treated vs. non-treated surfaces. Additionally, this coupling will allow for the study of the scalability and computational performance by assessing the algorithmic speedup and efficiency. Refer to Section 6 for further details.

#### 4 PRELIMINARY RESULTS FOR THE ASSESSMENT OF RIGID SURFACES

Preliminary work has been completed to assess the spatial resolution of the TDBEM with respect to the surface element basis functions  $\phi_i(\mathbf{r}_s)$  in Eq. (5) by considering the scattering of an acoustic point source by prototype geometric bodies with rigid surfaces (Hu et al. 2016). Geometries considered include a flat plate and sphere. The flat plate has dimension  $[-0.5, 0.5] \times [-0.5, 0.5] \times [-0.1, 0.1]$  and the point source is located at  $\mathbf{x} = (x, y, z) = (0, 0, 1)$ . The sphere is centered at  $\mathbf{x} = (0, 0, 0)$  with radius 0.5 and the point source is located at  $\mathbf{x} = (0, 0, 1)$ . For the spherical geometry, we consider both a standard and rotated orientation as shown in Fig. 2a and Fig. 2b. For both the flat plate and sphere, we limit the study to the observed far field solution.

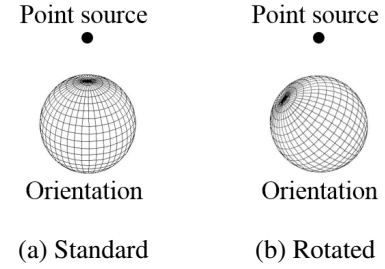


Figure 2: Orientation of the rigid body spherical elements with relation to the point source.

##### 4.1 Flat Plate with Rigid Body

To assess the spatial resolution of the TDBEM with respect to the spatial basis functions, we consider the scattering of an acoustic point source by the flat plate with rigid body. The contour plots of the frequency domain solutions converted from the time domain solution at  $\omega = 5\pi$  and  $\omega = 15\pi$  are given in Fig. 3. The solution in Fig. 3 was computed using 80 elements in both the  $x$ - and  $y$ - directions and 16 elements in the  $z$ -direction.

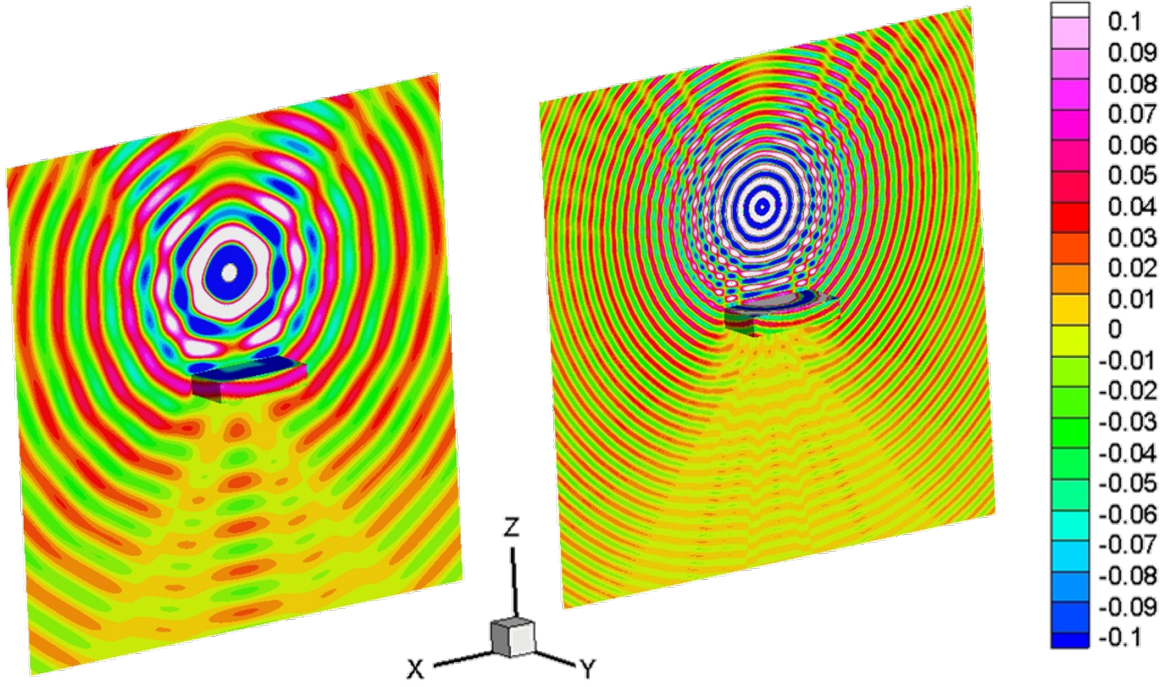


Figure 3: Rigid body flat plate contour plots of the frequency domain solution converted from the time domain solution at  $\omega = 5\pi$  [left] and  $\omega = 15\pi$  [right].

By discretizing the surface of the plate in the  $x$ ,  $y$ , and  $z$  directions with  $N_x$ ,  $N_y$ , and  $N_z$  elements respectively, a series of computations were carried out by increasing the number of elements used from  $N_x \times N_y \times N_z = 20 \times 20 \times 4$  to  $80 \times 80 \times 16$ . Figure 4 depicts the converted frequency domain solution at  $\omega = 15\pi$  along a field line of coordinates where  $-2.5 \leq x \leq 2.5$ ,  $y = 0$ , and  $z = -2.5$ , as the number of surface elements increased from  $20 \times 20 \times 4$  to  $80 \times 80 \times 16$ . The spatial resolution is measured along one direction on the surface using the metric of points-per-wavelength (PPW). PPW is computed by:

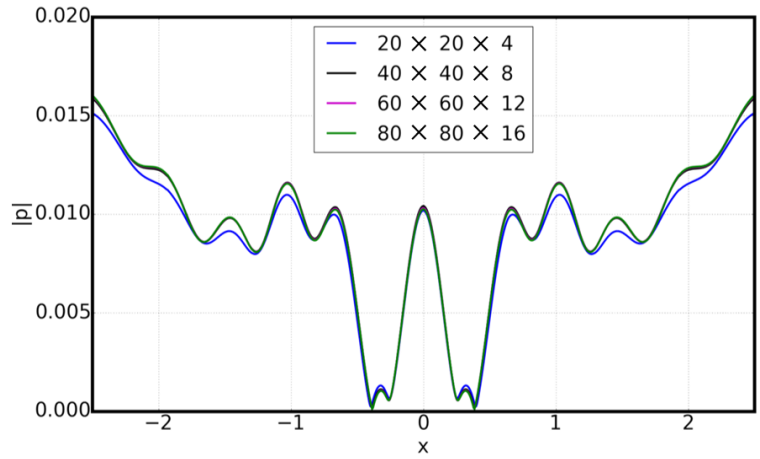


Figure 4: Rigid body flat plate frequency domain solution converted from the time domain solution at  $\omega = 15\pi$  along a field line of coordinates  $-2.5 \leq x \leq 2.5$ ,  $y = 0$ , and  $z = -2.5$ .

$$PPW = \frac{2\pi(p+1)N_x}{kL_x} \quad (9)$$

where  $p$  is the order of the basis function,  $k = \omega/c$  is the wavenumber,  $L_x$  is the plate length along the  $x$ -direction, and  $N_x$  is the number of elements along the  $x$ -direction (Hu et al. 2016). Using the solution

computed by  $100 \times 100 \times 20$  as the reference, the relative error in the L2 norm is plotted as a function of PPW. The results of the far field solution with constant basis functions are given in Fig. 5. For constant basis functions,  $p = 0$ . As indicated in the figure, the relative error measured in the L2 norm becomes as small as 2% with only 5 PPW. The excellent spatial resolution is likely due to the integration over a closed, hence periodic, domain. Although the basis functions being used are of zeroth order, the integrations over each element are computed by high-order Gauss quadrature on a  $6 \times 6$  grid.

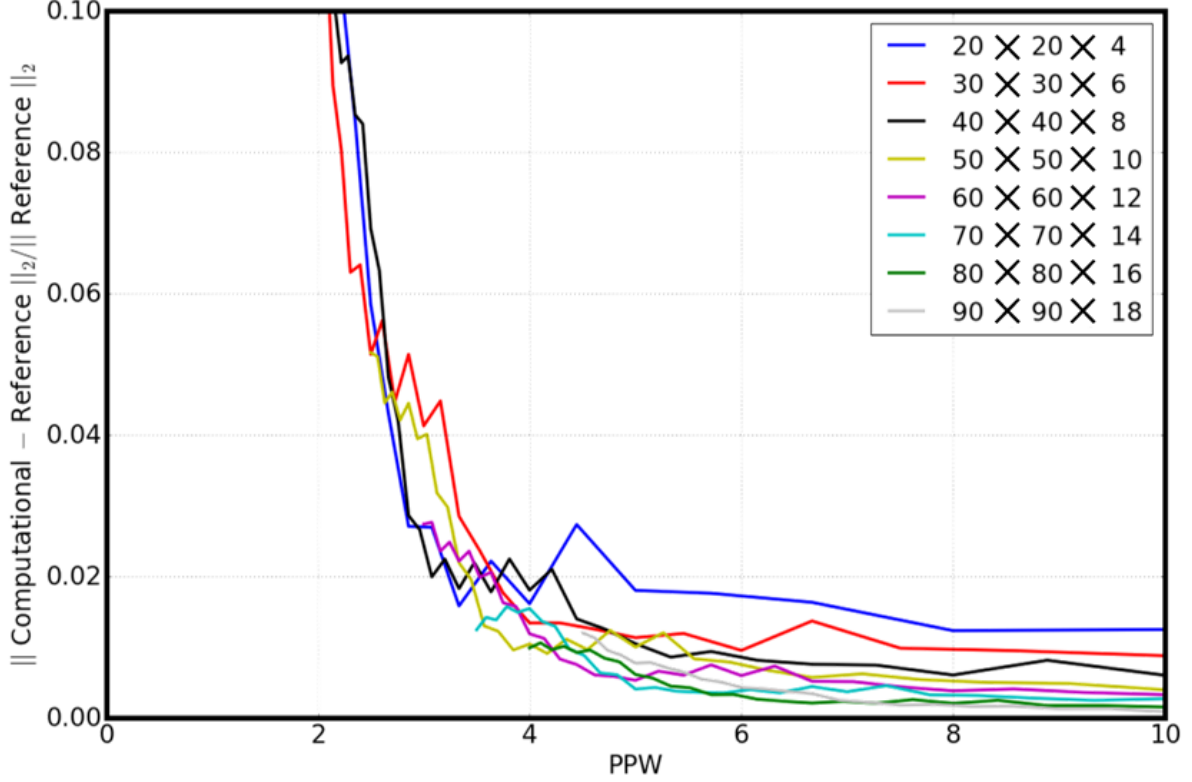


Figure 5: PPW results of the flat plate with rigid body far field scattering solution obtained with constant basis functions.

Moreover, the spatial resolution is measured along the entire surface using the metric of points-per-wavelength-squared (PPW2). PPW2 is computed by:

$$PPW2 = \frac{4\pi^2(p+1)^2[2N_xN_y + 2(N_x + N_y)N_z]}{k^2[2L_xL_y + 2(L_x + L_y)L_z]} \quad (10)$$

where  $L_y$  and  $L_z$  are the plate lengths along the  $y$ - and  $z$ - directions, and  $N_y$  and  $N_z$  are the number of elements along the  $y$ - and  $z$ - directions (Hu et al. 2016). Equation (10) is equivalent to  $(4\pi^2 \times \text{degrees of freedom})$  divided by  $(k^2 \times \text{surface area})$ . Using the solution computed by  $100 \times 100 \times 20$  as the reference, the relative error in the L2 norm is plotted as a function of PPW2. The results of the far field solution with constant basis functions are given in Fig. 6. As indicated in the figure, the relative error measured in the L2 norm of the far field solution becomes as small as 2% when PPW2 is only 25 with constant basis functions being used. This results are similar to the PPW results of the flat plate.

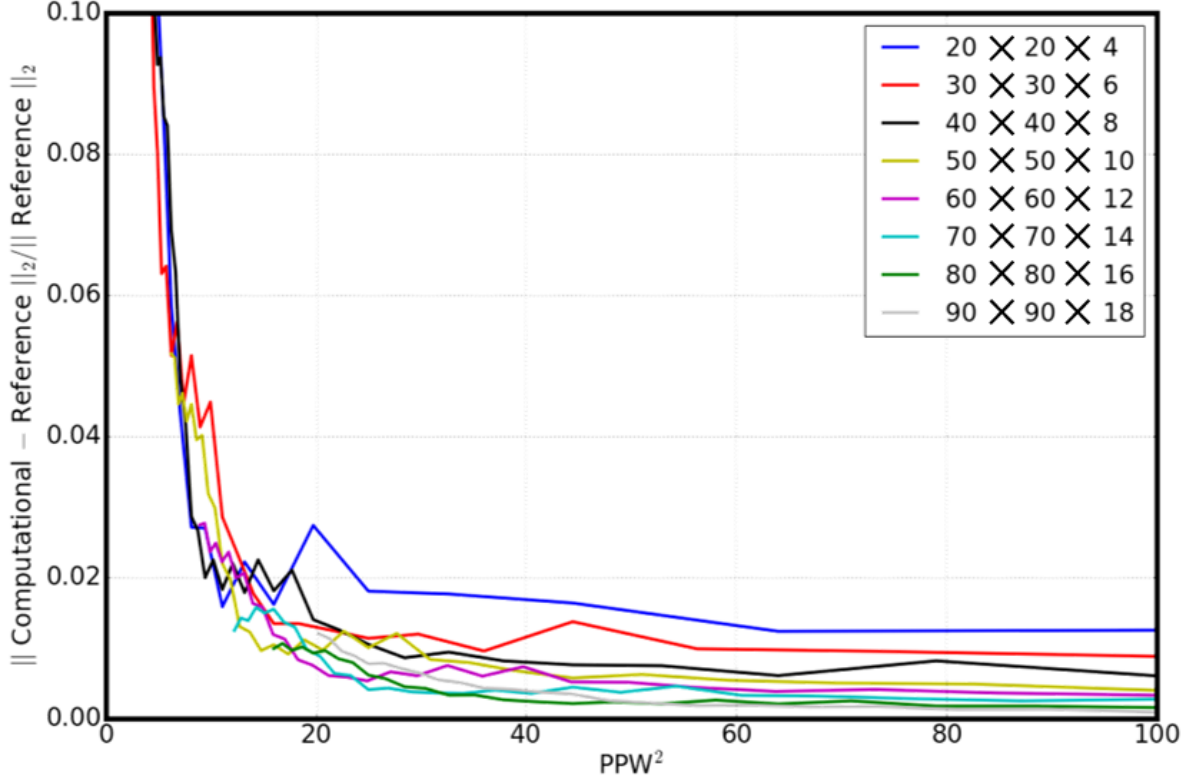


Figure 6: PPW2 results of the flat plate with rigid body far field scattering solution obtained with constant basis functions.

#### 4.2 Sphere with Rigid Body

To further assess the spatial resolution of the TDBEM with respect to the spatial basis functions, we consider the scattering of an acoustic point source by the sphere with rigid body. Both the standard and rotated orientations were considered as illustrated in Figs. 2a and 2b, respectively. A series of computations were carried about by increasing the number of surface elements used from 729 to 32,389. The spatial resolution is measured along the entire surface using the metric of PPW2.

Using the exact solution, the relative error in the L2 norm is plotted for both the standard and rotated orientations as a function of PPW2. The results of the far field solution with constant basis functions are given in Fig. 7 for the standard orientation sphere and Fig. 8 for the rotated orientation sphere. As indicated in the figures, the relative error measured in the L2 norm of the far field solution becomes as small as 4% when PPW2 is only 25 with constant basis functions being used, for both orientated spheres. It appears that, at least for the far field problem, the use of constant elements can keep the overall problem size small while the high-order integration helps to maintain accuracy.

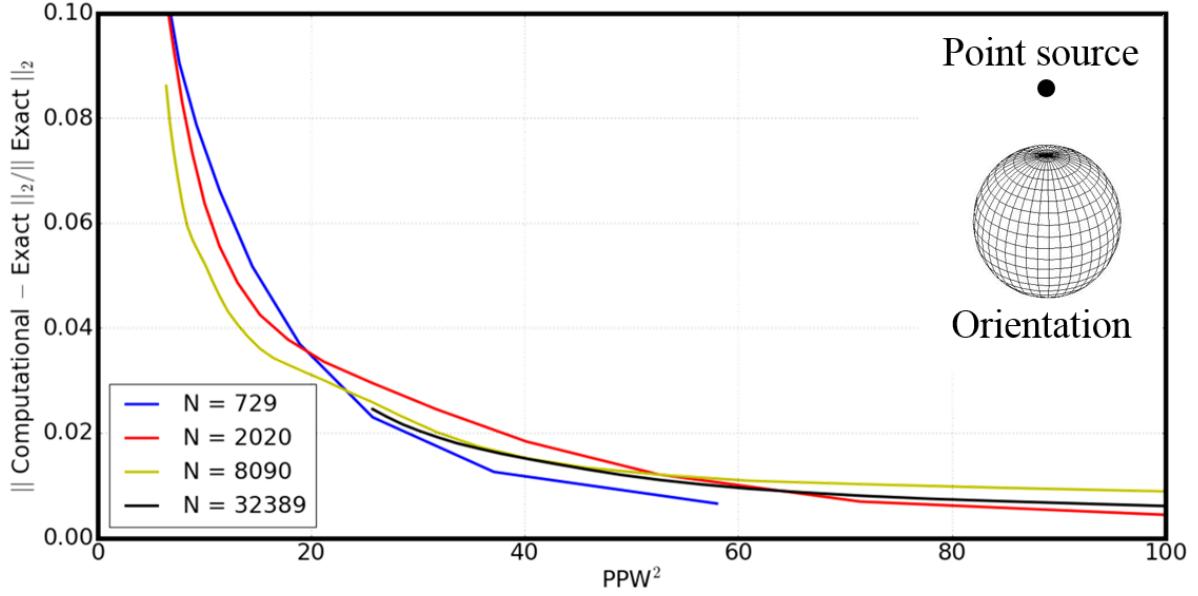


Figure 7: PPW2 results of the standard orientation sphere with rigid body far field scattering solution obtained with constant basis functions.

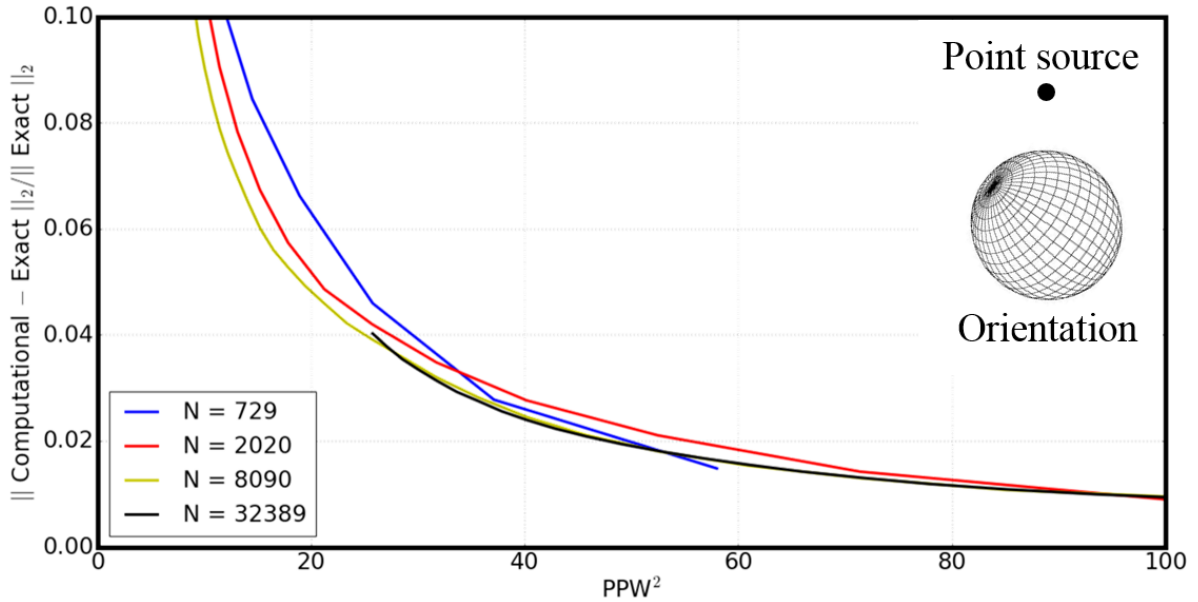


Figure 8: PPW2 results of the rotated orientation sphere with rigid body far field scattering solution obtained with constant basis functions.

### 4.3 High Performance Scalability Using Central Processing Units

Preliminary work has been completed to assess the scalability of the numerical algorithm by once more considering the scattering of an acoustic point source by the sphere with rigid body. The computations were run using standard compute nodes available through the Old Dominion University Turing Cluster (J. Pratt



2017). Each standard compute node carries 128 GB of memory and contains between 16 and 32 central processing unit (CPU) cores. Using the Turing Cluster, a series of computations using 8,090 and 32,389 surface elements were carried out by doubling the processing power from 8 CPU cores to 16, 32, 64, etc. With each simulation, the average time per iteration was calculated. The expectation was to obtain an inverse relationship between the time per iteration and the number of CPU cores.

The scalability results of using 8,090 surface elements are shown in Fig. 9a and using 32,389 surface elements are shown in Fig. 9b. As indicated in the figures, the numerical results closely match the expected outcome that the time per iteration would be inversely proportional to the number of CPU cores. It should be noted that in both assessments, the numerical results tapered off. This is likely due to an increase in parallel overhead, i.e. an increase in the time associated with performing parallel communications.

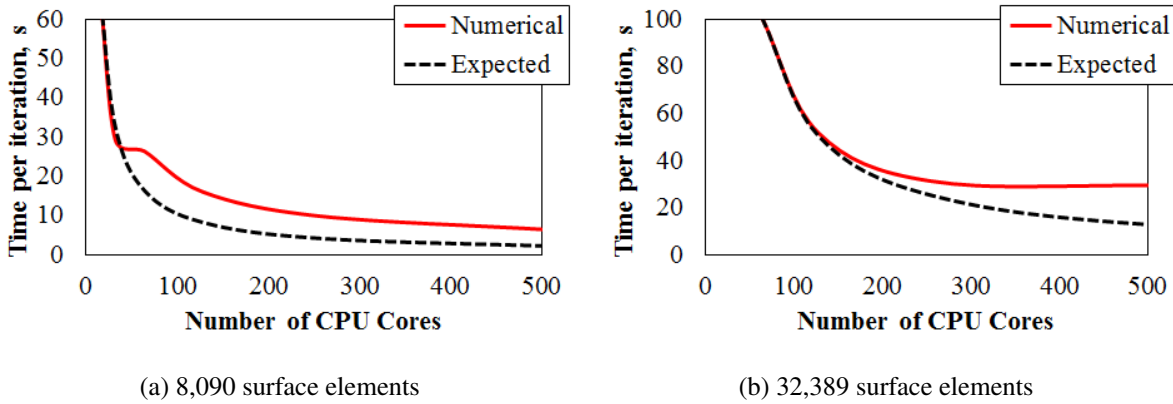


Figure 9: CPU scalability results obtained from modeling the scattering of an acoustic point source by a sphere with rigid body.

#### 4.4 Algebraic Eigenvalue Stability Analysis

Preliminary work has also been completed to assess the numerical stability of the TDBEM by again considering the scattering of an acoustic point source by the sphere with rigid body. In this assessment, we consider a rotated orientation as illustrated in Fig. 2b. With Mach numbers  $M = 0.0, 0.3$ , and  $0.6$ , the magnitudes of the largest eigenvalue  $\lambda$  in Eq. (6) were calculated to be, respectively: 1.000000, 0.999994, and 0.999938 using 729 surface elements and 1.000000, 1.000000, and 1.000000 using 2,020 surface elements. These results demonstrate numerical stability since the condition  $\max|\lambda| \leq 1$  is satisfied in each case.

## 5 CONCLUDING REMARKS

When designing next generation quiet aircraft, it is important to be able to accurately and efficiently predict the acoustic scattering by an aircraft body, both rigid as well as lined, from a given noise source. Acoustic scattering problems can be modeled using BEMs by reformulating the linear convective wave equation as a BIE. A TDBIE formulation, as well as its Burton-Miller type reformulation was discussed for solving acoustic wave scattering problems in the time domain using a BEM. The TDBEM formulation is valid for both rigid and lined acoustic surfaces with a mean flow  $U$ . Moreover, the incorporation of an impedance boundary condition in the formulation of the TDBEM was introduced. Impedance boundary conditions are assumed when assessing the scattering of an acoustic point source by a geometric body whose surface is treated with an acoustic liner. Further work will be completed to study the implementation of an impedance boundary condition as outlined in Section 6.



Preliminary work has been completed to assess the spatial resolution of the TDBEM with respect to the surface element basis functions by considering the scattering of an acoustic point source by prototype geometric bodies with rigid surfaces. Geometries considered include a flat plate and sphere. The study was limited to the observed far field solution and spatial resolution was measured using the metrics of PPW and PPW2. Results demonstrate that with constant basis functions, the relative errors measured in the L2 norm becomes as small as 2% when PPW2 is only 25 (PPW is only 5) for the flat plate and as small as 4% for the sphere. The scalability of the numerical algorithm was additionally assessed. A series of computations were carried out using standard compute nodes that carry 128 GB of memory and contain between 16 and 32 CPU cores. The scalability results using 8,090 and 32,389 surface elements both demonstrate the expected inverse relationship between the time per iteration and the number of CPU cores. Finally, numerical stability was demonstrated by considering a spherical geometry with rotated orientation. With Mach numbers  $M = 0.0, 0.3, \text{ and } 0.6$ , the magnitudes of the largest eigenvalue  $\lambda$  in Eq. (6) all satisfied the condition  $\max|\lambda| \leq 1$  for both 729 and 2,020 surface elements.

## 6 FUTURE WORK

Future work includes further studying the:

1. Analytical representation of experimentally determined admittance data and its connection to time domain implementations
2. Coupling of the admittance boundary condition with the TDBIE, including the stable reformulation of the integral equation
3. Analytical stability of the coupled system with respect to the (a) non-existence of resonant frequencies and (b) algebraic eigenvalue stability analysis
4. Simulation of acoustic wave scattering by prototype geometric bodies treated with liners and comparison with analytical and experimental results whenever possible
5. Scalability and computational performance by assessing the algorithmic speedup and efficiency

## ACKNOWLEDGMENTS

F. Q. Hu and M. E. Pizzo are supported by a NASA Cooperative Agreement, NNX11AI63A. M. E. Pizzo is also supported in part by an Old Dominion University Modeling and Simulation graduate fellowship. This work used the computational resources at the Old Dominion University ITS Turing cluster and the Extreme Science and Engineering Discovery Environment (XSEDE), which is supported by the National Science Foundation grant number OCI-1053575.

## A APPENDIX

Let  $p(\mathbf{x}, \omega) = Z(\omega)v(\mathbf{x}, \omega)$  where  $p(\mathbf{x}, \omega)$  is the acoustic velocity,  $v(\mathbf{x}, \omega) = \mathbf{v} \cdot \mathbf{n}$ ,  $\mathbf{v}$  is the acoustic velocity vector,  $\mathbf{n}$  is the inward normal vector on the scattering body, and  $Z(\omega)$  is the surface impedance. Then,

$$v(\mathbf{x}, \omega) = Y(\omega)p(\mathbf{x}, \omega) \quad (11)$$

where  $Y(\omega) = 1/Z(\omega)$  is the surface admittance (Rienstra 2006). In the frequency domain,  $v$  can be represented (Marburg and Schneider 2001) by:

$$v(\mathbf{x}, \omega) = \frac{1}{i\omega\rho_0} \frac{\partial p}{\partial n}(\mathbf{x}, \omega) \quad (12)$$

### A.1 Method

By setting Eq. (11) equal to Eq. (12), we obtain a relation for  $\partial p / \partial n(\mathbf{x}, \omega)$ . Using the inverse Fourier transform convolution property and causality condition which states that  $y(t - \tau) = 0$  for all  $t - \tau > 0$ , i.e.  $y(t - \tau) = 0$  for all  $t > \tau$ , we see that:

$$\begin{aligned}
 Y(\omega)p(\mathbf{x}, \omega) &= \frac{1}{i\omega\rho_0} \frac{\partial p}{\partial n}(\mathbf{x}, \omega) \implies \frac{\partial p}{\partial n}(\mathbf{x}, \omega) = i\omega\rho_0 Y(\omega)p(\mathbf{x}, \omega) \\
 \mathcal{F}^{-1} \left\{ \frac{\partial p}{\partial n}(\mathbf{x}, \omega) \right\} &= \mathcal{F}^{-1} \{ i\omega\rho_0 Y(\omega)p(\mathbf{x}, \omega) \} \\
 P_n(\mathbf{x}, t) = \frac{\partial p}{\partial n}(\mathbf{x}, t) &= \mathcal{F}^{-1} \{ i\omega\rho_0 Y(\omega) \} * \mathcal{F}^{-1} \{ p(\mathbf{x}, \omega) \} = \rho_0 \frac{\partial y}{\partial t}(t) * p(\mathbf{x}, t) \\
 &= \frac{\rho_0}{2\pi} \int_{-\infty}^{\infty} \frac{\partial y}{\partial t}(t - \tau) p(\mathbf{x}, \tau) d\tau = \frac{\rho_0}{2\pi} \int_{-\infty}^t \frac{\partial y}{\partial t}(t - \tau) p(\mathbf{x}, \tau) d\tau \\
 \implies P_n(\mathbf{x}, t) &= \frac{\partial p}{\partial n}(\mathbf{x}, t) = \frac{\rho_0}{2\pi} \int_{-\infty}^t \frac{\partial y}{\partial t}(t - \tau) p(\mathbf{x}, \tau) d\tau
 \end{aligned}$$

### A.2 Method

Using the inverse Fourier transform convolution property and causality condition which states that  $y(t - \tau) = 0$  for all  $t - \tau > 0$ , i.e.  $y(t - \tau) = 0$  for all  $t > \tau$ , we see that from Eq. (11):

$$\begin{aligned}
 v(\mathbf{x}, \omega) &= Y(\omega)p(\mathbf{x}, \omega) \\
 \mathcal{F}^{-1} \{ v(\mathbf{x}, \omega) \} &= \mathcal{F}^{-1} \{ Y(\omega)p(\mathbf{x}, \omega) \} = \mathcal{F}^{-1} \{ Y(\omega) \} * \mathcal{F}^{-1} \{ p(\mathbf{x}, \omega) \} \\
 v(\mathbf{x}, t) &= \frac{1}{2\pi} \int_{-\infty}^{\infty} y(t - \tau) p(\mathbf{x}, \tau) d\tau = \frac{1}{2\pi} \int_{-\infty}^t y(t - \tau) p(\mathbf{x}, \tau) d\tau
 \end{aligned}$$

Hence by invoking the differentiation property and commutativity of convolution, we see that from Eq. (12):

$$\begin{aligned}
 v(\mathbf{x}, \omega) &= \frac{1}{i\omega\rho_0} \frac{\partial p}{\partial n}(\mathbf{x}, \omega) \implies \frac{1}{\rho_0} \frac{\partial p}{\partial n}(\mathbf{x}, \omega) = i\omega v(\mathbf{x}, \omega) \\
 \mathcal{F}^{-1} \left\{ \frac{1}{\rho_0} \frac{\partial p}{\partial n}(\mathbf{x}, \omega) \right\} &= \mathcal{F}^{-1} \{ i\omega v(\mathbf{x}, \omega) \} \\
 \frac{1}{\rho_0} P_n(\mathbf{x}, t) = \frac{1}{\rho_0} \frac{\partial p}{\partial n}(\mathbf{x}, t) &= \frac{\partial v}{\partial t}(\mathbf{x}, t) = \frac{\partial}{\partial t} \left[ \frac{1}{2\pi} \int_{-\infty}^t y(t - \tau) p(\mathbf{x}, \tau) d\tau \right] \\
 &= \frac{1}{2\pi} \int_{-\infty}^t \frac{\partial}{\partial t} [y(t - \tau) p(\mathbf{x}, \tau)] d\tau = \frac{1}{2\pi} \int_{-\infty}^t \frac{\partial y}{\partial t}(t - \tau) p(\mathbf{x}, \tau) d\tau \\
 \implies P_n(\mathbf{x}, t) &= \frac{\partial p}{\partial n}(\mathbf{x}, t) = \frac{\rho_0}{2\pi} \int_{-\infty}^t \frac{\partial y}{\partial t}(t - \tau) p(\mathbf{x}, \tau) d\tau
 \end{aligned}$$

## REFERENCES

- Chappell, D. J., P. J. Harris, D. Henwood, and R. Chakrabarti. 2006. "A Stable Boundary Element Method for Modeling Transient Acoustic Radiation". *Journal of Acoustical Society of America* vol. 120 (1), pp. 74–80.
- Ergin, A. A., B. Shankar, and E. Michielssen. 1999. "Analysis of Transient Wave Scattering from Rigid Bodies Using a Burton-Miller Approach". *Journal of Acoustical Society of America* vol. 106 (5), pp. 2396–2404.
- Hu, F. Q. 2013. "An Efficient Solution of Time Domain Boundary Integral Equations for Acoustic Scattering and Its Acceleration by Graphics Processing Units". *19th AIAA/CEAS Aeroacoustics Conference* (2013-2018).
- Hu, F. Q. 2014. "Further Development of a Time Domain Boundary Integral Equation Method for Aeroacoustic Scattering Computations". *20th AIAA/CEAS Aeroacoustics Conference* (2014-3194).
- Hu, F. Q., M. E. Pizzo, and D. M. Nark. 2016. "On the Assessment of Acoustic Scattering and Shielding by Time Domain Boundary Integral Equation Solutions". *22nd AIAA/CEAS Aeroacoustics Conference* (2016-2779).
- Jones, A. D., and F. Q. Hu. 2007. "A Three-Dimensional Time-Domain Boundary Element Method for the Computation of Exact Green's Functions in Acoustic Analogy". *13th AIAA/CEAS Aeroacoustics Conference* (2007-3479).
- Marburg, S. 2015. "The Burton and Miller Method: Unlocking Another Mystery of Its Coupling Parameter". *Journal of Computational Acoustics* vol. 23 (1550016).
- Marburg, S., and S. Schneider. 2001. "Influence of Element Types on Numeric Error for Acoustic Boundary Elements". *Journal of Computational Acoustics* vol. 11 (3), pp. 363–386.
- J. Pratt 2017. "Turing Community Cluster General Information". <http://www.odu.edu/hpc>. Accessed Apr. 14, 2017.
- Rienstra, S. W. 2006. "Impedance Models in Time Domain Including the Extended Helmholtz Resonator Model". *12th AIAA/CEAS Aeroacoustics Conference* (2006-2686).

## AUTHOR BIOGRAPHIES

**MICHELLE E. PIZZO** is a Ph.D. Candidate in the Department of Mathematics and Statistics at Old Dominion University. She holds a M.S. in Computational and Applied Mathematics from Old Dominion University, M.S. in Mechanical Engineering from Embry-Riddle Aeronautical University, and B.D. in Aerospace Engineering from Embry-Riddle Aeronautical Engineering. Her research interests lie in modeling and simulation, high performance computing, aeronautics, astronautics, and aeroacoustics. Her email address is [mpizzo@odu.edu](mailto:mpizzo@odu.edu).

**FANG Q. HU** is a Professor in the Department of Mathematics and Statistics at Old Dominion University. He holds a Ph.D. in Mathematics from Florida State University, M.S. in Engineering from Zhejiang University, and B.S. in Mathematics from Zhejiang University. His research interests include scientific computing, computational aeroacoustics, computational biology and geochemistry, and numerical simulation of fluids and sound. His email address is [fhu@odu.edu](mailto:fhu@odu.edu).

## MEDICAL SIMULATION

- Page 89 Nishant Kumar Srivastava, Sanjay Kumar Singh , Umesh Singh  
**Banaras Hindu University**  
Frailty Models for Modelling Heterogeneity Based on Multiplicative and Additive Baseline Hazards
- Page 91 Narendra Banerjee and Lin Chen  
**Elizabeth City State University**  
Matching miRNA IDs to Gene Expressions with a Web Crawler
- Page 94 Haben G. Yhdego  
**Old Dominion University**  
Fall Detection Using Long Short Term Memory (LSTM)
- Page 101 Defu Cui and Frederic D. McKenzie  
**Old Dominion University**  
Stress Analysis of Chest Wall During Inspiration
- Page 103 Austin Tapp and Michel Audette  
**Old Dominion University**  
Practical Applications of Neurosurgical Ontologies for Various Craniotomic Approaches Through Computer Assisted Surgery
- Page 114 J. P. Asija, Brian Dilinila, Minh Dong, Michael Poteat, Jacob Richardsom, Thomas Tracey and Jake Webster  
**Old Dominion University**  
ODU MSVE Capstone 2018: Medical Workstation Evaluation Process
- Page 128 Shrabani Ghosh and Michel Audette  
**Old Dominion University**  
Towards Deformable Cranium & Foramen Surface Model
- Page 130 Eric Jenkins  
**Old Dominion University**  
Modeling the Soft Tissues of the Lower Body During a Landing Task

# FRAILTY MODELS FOR MODELLING HETEROGENEITY BASED ON MULTIPLICATIVE AND ADDITIVE BASELINE HAZARDS

**Nishant Kumar Srivastava, Sanjay Kumar Singh , Umesh Singh**

Department of Statistics, Institute of Science, Banaras Hindu University

email: nishantpark@gmail.com

## **Abstract**

In the analysis of lifetime data, heterogeneity may be present in many situations. This heterogeneity is referred to as frailty. If the frailty is ignored and it is present then the inferences are incorrect. Frailty models are extensions of the proportional hazards model which is best known as the Cox model (Cox, 1972), the most popular model in survival analysis. Normally, in most clinical applications, survival analysis implicitly assumes a homogeneous population to be studied. This means that all individuals sampled into that study are subject in principle under the same risk (e.g., risk of death, risk of disease recurrence). In many applications, the study population cannot be assumed to be homogeneous but must be considered as a heterogeneous sample, i.e. a mixture of individuals with different hazards. For example, in many cases it is impossible to measure all relevant covariates related to the disease of interest, sometimes because of economical reasons, sometimes the importance of some covariates is still unknown. The frailty approach is a statistical modelling concept which aims to account for heterogeneity, caused by unmeasured covariates. In statistical terms, a frailty model is a random effect model for time-to-event data.

In this paper we have studied the performance of Gamma distribution taken as frailty distribution with Exponential and Weibull distribution taken as multiplicative and additive baseline hazards. The performances of the estimates of the parameters have been evaluated and effects of increasing the sample size and cluster size were also studied through Monte Carlo Simulations. The biases and MSEs of the estimates were also computed. The Akaike Information Criteria (AIC) and Bayesian Information Criteria (BIC) are used to compare the gamma frailty models based on different baseline hazards and also to compare the performance of multiplicative baseline hazards and additive baseline hazards frailty models and a better model is proposed. We apply these models to a real-life survival data set of McGilcrist and Aisbetts related to the kidney infection

data and estimates of the parameters and standard error of the estimates are calculated. We performed Wald test to test the significance of the covariate effects. Simulation and Analysis are done using R software.

Results of simulation study show that the biases and MSE values in estimates are more in additive hazards model than multiplicative hazards model. When we increase the cluster size keeping the total sample size same then there are no effects on the biases and MSEs. The AIC and BIC values are slightly less for additive hazards model as compared to multiplicative hazards model. We perform Wald test to test the significance of the covariate effects. The results indicate that sex has significant effect ( $p\text{-value} \leq 0.05$ ) on the hazard of infection which means that males have more risk to infection than females. The results show that age has no significant effect ( $p\text{-value} \leq 0.05$ ) on the hazard of infection.

Key Words: Heterogeneity, frailty, Monte Carlo simulation, AIC.

## References

- alen, O. O. (1987). Two examples of modelling heterogeneity in survival analysis. *Scandinavian Journal of Statistics*, 14:19-25.
- Aalen, O. O. (1994). Effects of frailty in survival analysis. *Statistical Methods in Medical Research* 3:227-243.
- Andersen, P.K., Borgan, O., Gill, R.D. and Keiding, N. (1993). *Statistical models based on counting processes*. Springer-Verlag, New York.
- Balakrishnan, N. and Peng, Y. (2006). Generalized gamma frailty model. *Statistics in Medicine*, 25:2797-2816.

# Matching miRNA IDs to Gene Expressions with a Web Crawler

Narendra Banerjee

Department of Technology

[nnbanerjee014@students.ecsu.edu](mailto:nnbanerjee014@students.ecsu.edu)

Elizabeth City State University

1704 Weeksville Rd

Elizabeth City, NC, USA

Lin Chen

Department of Mathematics & Computer Science

[lchen@ecsu.edu](mailto:lchen@ecsu.edu)

Elizabeth City State University

1704 Weeksville Rd

Elizabeth City, NC, USA

## ABSTRACT

A web crawler was developed to match miRNA IDs to corresponding gene expressions. A miRNA ID usually corresponds to multiple expressions and an expression can be from multiple miRNAs. The complexity of connecting miRNA IDs and their gene expressions is  $O(n^3)$ . In the study of searching cancer gene for African American, matching miRNA IDs and gene expressions is a major step of targeting cancer genes. Two input files collected by experiments contain miRNA IDs and gene expressions respectively. A Python web crawler was used to align records in those two files by automatically searching and matching input records with the records deposited at mirbase.org and targetscan.org. The matching time was reduced to a few hours from several months that it used to be.

**Keywords:** miRNA, gene expression, web crawler

## 1 INTRODUCTION

The research in Dr. Hirendra Banerjee's group at Elizabeth City State University (ECSU) is searching cancer gene for African American [1]. Both miRNA and gene expression were collected with experimental techniques. One miRNA may have multiple gene expressions; on the other side, one gene expression may correspond to several miRNAs. We can search the gene expressions for a miRNA or search the miRNA ids for a specific gene expression in some databases [2, 3]. However, there is no tools to matching miRNA and gene expression for our African American data. The manual procedure of implementing matching is extremely time-consuming and is easy to make mistakes. The African American cancer data contains 35344 miRNA ids and 2180 gene expressions. If conduct searching at mirbase.org and targetscan.org, over  $10^9$  records have to be searched, which will take over 1,700 working hours.

In this project, we designed and conducted a Python web crawler to implement the matching between miRNA ids and gene expressions in African American cancer data set. It is also able to be used to other similar data sets.

## 2 METHOD

The web crawler was designed to match each miRNA record to its gene expression by searching mirbase.org and targetscan.org (Figure 1). A miRNA.csv including 560 miRNAs records was generated by Dr. Hirendra Banerjee's group. Each record in miRNA.csv contain transcript IDs, fold change values (FC\_I), and other related information. The web crawler searches each of those transcript IDs at mirbase.org and fetches Uniform Resource Locators (URLs) pointing to targetscan.org. Usually each transcript ID relates to several URLs. Then the webpage for each of those URLs is searched by the web crawler. A table containing target gene is generated from each webpage at targetscan.org. At the end, each record in the table is compared with the records in Expression.csv. The records in Expression.csv was also collected by Dr. Hirendra Banerjee's group. Each of those records contains gene expressions, their fold change values

(FC\_II), and other related information. If a target gene in the table at targetscan.org matches the gene symbol of a record in Expression.csv, the miRNA id and fold change value in miRNA.csv, the gene symbol and the fold change value in Expression.csv are saved into the output file.

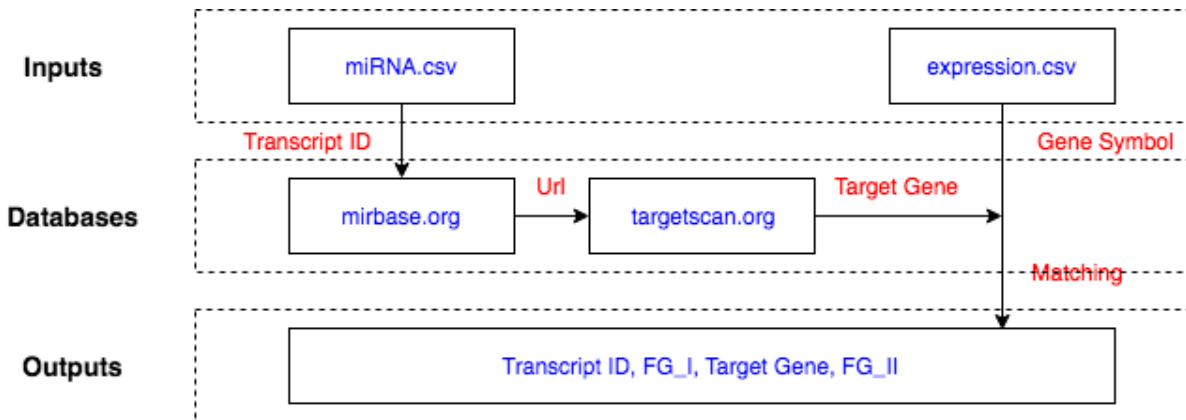


**Figure 1.** The flowchart of align the records in two inputs by searching two online database.

### 3 RESULTS AND DISCUSSION

Total 74946 matched records were generated using the web crawler for the African American data set from Dr. Hirendra Banerjee's group. It took 2.5 hours on a notebook with an Intel 4 core CPU and 8 Gb memory.

The transcript ID has-mir-361 in miRNA.csv have two miRNA ids at mirbase.org, hsa-mir-361-5p and has-mir-361-3p. Each miRNA id has one URL linking to targetscan.org. Open the URL links of two miRNA ids at targetscan.org, 5161 and 375 records are found respectively. For each of those records, search the target gene in Expression.csv. For instance, a record (has-mir-361, -2.40987, LURAP1L, 7.76052) in the output file represents the match between has-mir-361 in miRNA.csv and LURAP1L in Expression.csv, which is one of 445 matched pairs for has-mir-361. Table 1 shows several matched records in the output file for hsa-mir-361.

**Table 1.** Several sample records in the output file of the web crawler for miRNA hsa-mir-361.

Transcript ID	FC_I	Target Gene	FC_II
hsa-mir-361	-2.40987	LURAP1L	7.76052
hsa-mir-361	-2.40987	VEGFA	5.72351
hsa-mir-361	-2.40987	SCAF8	5.59933
hsa-mir-361	-2.40987	STX7	6.17386

### 4 ACKNOWLEDGEMENT

This project is supported by NIH 4T34GM100831-05. Thanks Dr. Hirendra Banerjee's discussion and Rayshaw Walker's manually demo.

### REFERENCES

- [1] H. Banerjee, B. Bazemore, A. Barfield, D. Crummit, C. Krauss, G. Payne, J. Rousch, V. Maglik, Immunol Disord Immunother, 2016, 1(3), p109.



[2] miRBase, <http://mirbase.org/>, accessed on March 12, 2018.

[3] TargetScanHuman, [http://www.targetscan.org/vert\\_71/](http://www.targetscan.org/vert_71/), accessed on March 12, 2018.

# FALL DETECTION USING LONG SHORT TERM MEMORY(LSTM)

HABEN G. YHDEGO  
HYHDE001@ODU.EDU

DR. MICHEL AUDETTE  
MAUDETTE@ODU.EDU

Modeling, Simulation and Visualization Engineering  
Old Dominion University, Norfolk, USA

## Abstract

*Falls are a major cause of injuries and hospital admissions among elderly people. Thus, the care giving process and the quality of life of older adults can be improved by enabling detection of falling events for the elderly, monitoring the patient and consequently provides emergency support in the event of falling. This paper presents a fall detection method using one of recurrent neural network(RNN) algorithms called long short-term memory(LSTM). As fall is sequence of action from imbalance to hitting the floor, it takes advantage of RNN which has the ability to encode and process sequential data, such as acceleration measurements from wearable sensors. The datasets are preprocessed using median filter and feature extraction is performed using non-overlapping sliding windows. We use the accelerometer data from the URFD datasets and the reported results are very promising which is comparable to the SVM method that uses both the accelerometer and kinetic data.*

**Keywords:** Fall detection, RNN, LSTM, Wearable sensors

## I. INTRODUCTION

Fall is defined as an event which results in a person coming to rest inadvertently on a lower level [5]. The reasons why falls occur and some people are more likely to fall may be intrinsic or extrinsic. The occurrence of fall incidence increases by the chronic problems and diseases such as Alzheimer, Parkinson, arthritis and visual impairment. And also, environments like slippery surfaces and dangerous daily activities may cause a fall. Those cause of fall may effect into various problems from severe physical injuries to psychological issues, depression and avoidance of the activity that caused the fall.

Fall is a precipitous drop from a height, or from a higher position, which may be accompanied by injuries. This is one of the most dangerous and fearful situation in the elderly living [13]. Falls are a serious medical and social problem among the elderly. This has led to the development of automatic fall-detection systems [14]. The elderly, especially those above the age of 65, are exposed to falls owing to the deterioration of their physical functions [15]. When an elder person falls and becomes unconscious or is unable to move his/her body, he/she may succumb to the injuries that caused the fall. Each year, there are more than one third of people aged 65 years old falling [16]. This is the reason; fast and early detection of the fall is very important to save and rescue the people and avoid the badly prognosis. Thus, research and development of a system that can automatically detect falls in the elderly or other patients has been actively studied [14]. The identified fall-detection systems can be classified primarily into two categories: context-aware systems and wearable devices. Most of the wearable automatic sensors utilize accelerometers,

gyroscopes, or tilt sensors and set thresholds of their outputs to detect the large impact of body with ground or near horizontal orientation of trunk, or both [14].

## II. RELATED WORKS

There are various methods of fall detection methods but the most common implementations are based on both threshold and machine learning techniques [6]. The procedure to detect falls using those two methods consists of four parts. The first one is detection component collects data from the accelerometer which are preprocessed using a series of magnitude and time thresholds as implemented in [7] to identify fall-like segments. A second part extracts features from these segments that are used by a different machine learning classifiers like k-Nearest Neighbor (kNN) to distinguish between falls and activities of daily living (ADL). There are also two auxiliary components; one that monitors the activation level of the sensor and aims keeping battery consumption as low as possible and another that adjusts the model to the user activity patterns.

Nowadays, a lot of machine learning algorithms are used to further improve the detection rate accuracy. We have to extract feature data from the sensor input signals that are inputs to the machine learning techniques. After that, those machine learning classifier takes advantage of these characteristics to construct a mathematical model acceptance from the a distinguishes between two or more classes. Activity recognitions and pattern recognitions have been interested academic research and industry over the last decades. Fall detection is one of the activity recognitions that has been studied and several methods has been developed with varying different value of accuracy. Some use only wearable inertial sensors, while others have cameras and ambient sensors to be used in our living environment.

Different works like [8] and [9] are proposed thresholding the magnitude of the acceleration and the acceleration at the vertical direction. Which means when both thresholds are exceeded within a time window, a fall is detected. This paper [9] uses angular velocities in addition to acceleration magnitude as input data. When both values are greater than the specified thresholds a fall is detected. This method collect data by placing the sensor in the middle of chest. In this work [10] they use both upper and lower thresholds for the acceleration magnitude. If the upper and lower is exceeded in less than 1s, a fall template using wavelet transform is used to compare with the acceleration signal. Then a fall is detected if the transformation yields high similarity. Even though most works depend on thresholds, it is difficult to use threshold methods to predict unseen data. Due to this, recent approaches [12] employ feature extraction engineering and machine learning classifiers to improve detection accuracy.

The machine learning implementations differ in many aspects. Some of of them like [7] and [10] use both thresholds and machine learning methods. There is promising machine learning techniques like RNN that introduce sequence modeling to be used in activity recognitions. Furthermore, smoothing the sensor data using various filtering methods such as first and second order low-pass filters [11] helps us to got good results. But, the main problem of the current fall detection algorithm is the lack of an approved database of realistic falls and ADLs. The dataset used in different papers use different sensor position and it also selects a different set of activity patterns on which they evaluate the detection algorithm. The most common activities performed are walking, running, standing up and sitting down, while forward, and backward fall types are

simulated. However, in most cases, these data are not collected in real fall situations. Therefore, not only is a reasonable comparison almost impossible, but the results are not reproducible as well.

### III. METHODOLOGY

Neural networks are powerful for pattern classification and base of deep learning techniques. A feed forward neural network or multilayer perceptron (MLP), is a computational model that process information through a series of interconnected computational nodes. These computational nodes are grouped into layers and are associated with one other using weighted connections as shown below. A limitation of the MLP architectures is that it assumes that all inputs and outputs are independent of each other. In order for an MLP to model a time series(such as sensor signal), it is necessary to include some temporal information in the input data.

Recurrent neural networks(RNNs) are neural networks specifically designed to tackle this problem, making use of recurrent connection in every unit. This work describes a fall detection using long short term memory(LSTM) and tri-axial accelerometer, through analyzing the features of human motion series during fall processes. Old machine learning algorithms like Support vector Machine(SVM) process their data with out any notion of sequential order but recurrent neural network(RNN) has the ability to encode and process sequential data. RNNs as shown in figure 1 are neural networks making use of recurrent connection in every unit. In RNN, the activation of a neuron is fed back to itself with a weight and a unit time delay and it provides with a memory(hidden values) of past activations, which allows it to learn the temporal dynamics of sequential data. The number of layers that is traversed by back-propagation grows dramatically. Thus, using RNN for training our data introduces a vanishing gradient problem. RNN amplify this problem because they are trained by back-propagation through time (BPTT).

LSTM neural networks are recurrent networks that includes a memory to model temporal

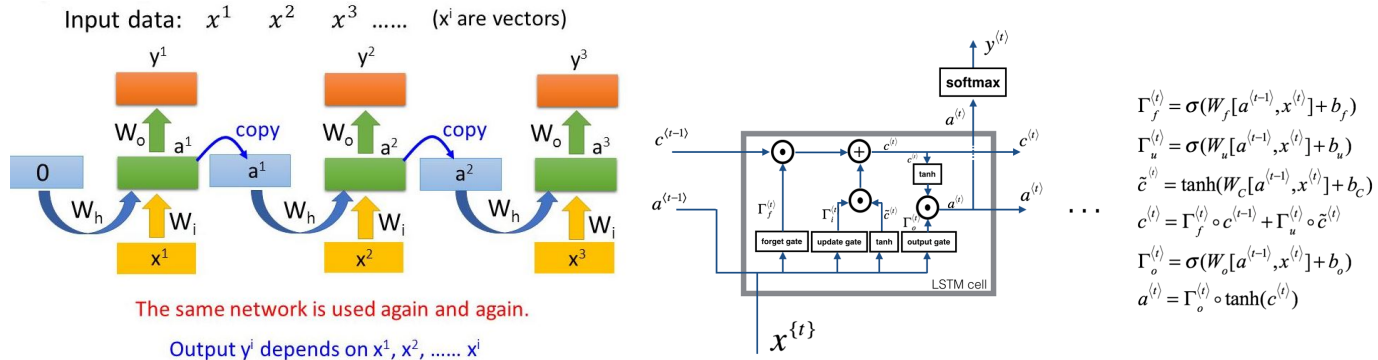


Figure 1: RNN architecture and Single Cell of LSTM

dependencies in time series problems. LSTM architecture avoids the problem of vanishing gradients by introducing error gating. The recurrent LSTM cell is an extension of RNNs, where the internal memory can be updated, erased or read out as shown in figure 1.

A dataset from the UR fall detection dataset [1] is used. This dataset contains 70 (30 falls + 40 activities of daily living) sequences. They recorded the data from two Microsoft Kinect cameras and corresponding accelerometer data. For our application, we use the accelerometer data only. Those data are preprocessed using median filter with sampling rate of 256 HZ to remove the noise (high frequency). We can see the sample of the dataset after performing the preprocessing for the fall and ADL (Non-Fall) in figure 2 respectively, where SV is the magnitude of the three axis acceleration.

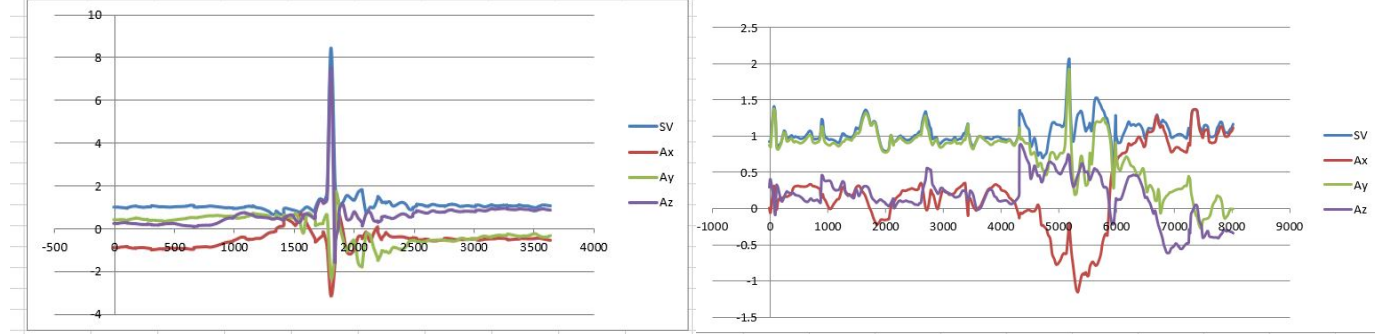


Figure 2: Fall and Non-Fall sample datasets

The feature vector input for the LSTM of  $X_1, X_2, \dots, X_n$  is created by segmenting using fixed size non-overlapping sliding window. Our total sequences of feature vectors are 60 which has 500 ms length window each and looks like as shown in figure 3. Those feature vectors are the input for our proposed architecture which is given in figure 4. The three LSTM layers of the network have each 128 size feature vector and the last soft-max classifier is used for binary classification.

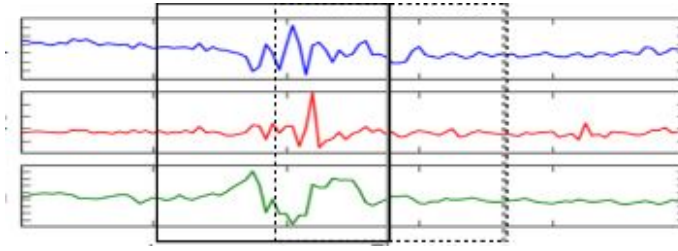


Figure 3: Sliding window sample

#### IV. EXPERIMENTAL RESULTS

The datasets is divided into training and testing with 80% and 20 % respectively. After we train and test based on the proposed simple model architecture above, our training progress over the training iteration number is shown in figure 5.

The experimental evaluation on the URFD dataset gives us the results shown in the table below based on the formulas of  $\text{Accuracy} = \frac{TP+TN}{TP+TN+FN+FP}$ ,  $\text{Precision} = \frac{TP}{TP+FP}$ ,  $\text{Sensitivity} = \frac{TP}{TP+FN}$ , and  $\text{Specificity} = \frac{TN}{TN+FP}$ , where TP is true positive, TN is true negative, FN is false negative and FP is

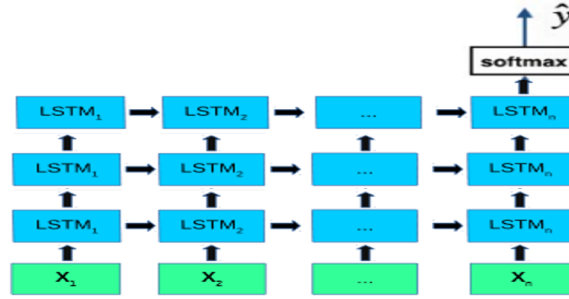


Figure 4: The proposed model architecture

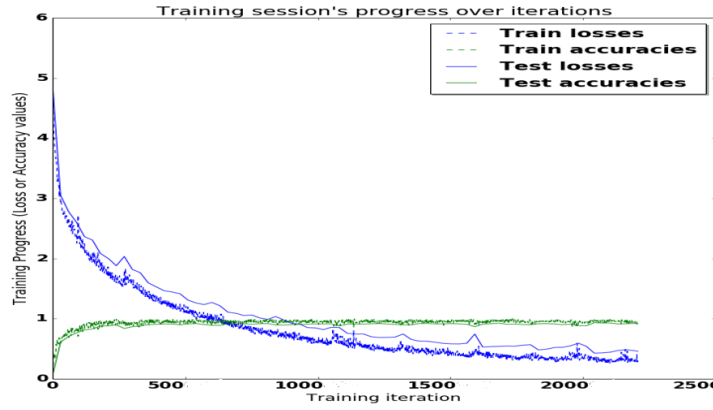


Figure 5: Accuracy of training and testing over the training iteration

false positive.

## V. CONCLUSION

In this paper, a sequential based models of LSTM is used for fall detection. Those type of RNN algorithms helps us to process time series data due to the capability of the algorithms to model and process sequential data. We use the accelerometer data only but the results are comparable to the SVM method that uses both the kinect and accelerometer data.

## VI. FUTURE WORKS

In the future, I am planning to use different handcrafted feature engineering methods such as overlapping windows, cascade-classifier approach(CCA) [3] and Event-Triggered machine learning approach [2], and automatic feature extraction using Convolutional neural networks(CNN) as used in this paper [4]. It is also recommended to use other data with the accelerometer data like gyroscope, magnetometer data. We are planning to test on different existing datasets and also we

	Results
Accuracy	90.91
Precision	90.01
Specificity	92
Sensitivity	90.13

Table 1: Experimental Results

will collect datasets from students and patients. Moreover, we will use other model, parameters and deep learning algorithms with LSTM for training.

## REFERENCES

- [1] M. Kepski, <http://fenix.univ.rzeszow.pl/~mkepski/ds/uf.html>, UR fall detection dataset, Interdisciplinary Center for Computational Modeling, University of Rzeszow. 2014.
- [2] Putra, I Putu Edy Suardiyana and Brusey, James and Gaura, Elena and Vesilo, Rein, *An Event-Triggered Machine Learning Approach for Accelerometer-Based Fall Detection*, Sensors, 18, 2018,
- [3] Putra, I.P.E.S.; Brusey, J.; Gaura, E, A Cascade-Classifer Approach for Fall Detection In Proceedings of the 5th EAI International Conference on Wireless Mobile Communication and Healthcare, MOBIHEALTH'15, London
- [4] Ming Zeng, Le T. Nguyen, Bo Yu, Ole J. Mengshoel, Jiang Zhu, Pang Wu, Joy Zhang, *Convolutional Neural Networks for Human Activity Recognition using Mobile Sensors*, Department of Electrical and Computer Engineering, Carnegie Mellon University, Moffett Field, CA, USA.
- [5] "Falls I WHO", <http://www.who.int/mediacentre/factsheets/fs344/en/>, WHO, Nov 2016,
- [6] P. Tsinganos, *Smartphone-based Fall Detection System for the Elderly*, Jun. 2017
- [7] S. Abbate, M. Avvenuti, F. Bonatesta, G. Cola, P. Corsini, A. Vecchio, *A smartphone-based fall detection system*, Pervasive and Mobile Computing, vol. 8, no. 6, pp. 883-899, Dec. 2012
- [8] J. Dai, X. Bai, Z. Yang, Z. Shen, D. Xuan, *PerFallD: A pervasive fall detection system using mobile phones*, Proceedings of the 8th IEEE International Conference on Pervasive Computing and Communications (PERCOM 2010), 29 Mar.-2 Apr. 2010.
- [9] R. Y. W. Lee, A. J. Carlisle, *Detection of falls using accelerometers and mobile phone technology*, Age and Ageing, vol. 40, no. 6, pp. 690-696, 2011.
- [10] V. Viet, D. Choi, *Fall Detection with Smart Phone Sensor*, The 3rd International Conference on Internet (ICONI) 2010, pp. 27-31, Dec. 2011.
- [11] I. N. Figueiredo, C. Leal, L. Pinto, J. Bolito, A. Lemos, *Exploring smartphone sensors for fall detection*, The Journal of Mobile User Experience, vol. 5, no. 2, 2016.
- [12] A. Ozdemir, B. Barshan, *Detecting Falls with Wearable Sensors Using Machine Learning Techniques*, Sensors, vol. 14, no. 6, pp. 10691-10708, Jun. 2014.

- [13] She T., Sun X., Xia Z., Chen L., Liu J., *Fall Detection Algorithm Based on Triaxle Accelerometer and Magnetometer*, The Journal of Mobile User Experience, Engineering Letters, 2016.
- [14] Lim D., Park C., Kim N., Kim S., Yu Y., *Fall-Detection Algorithm Using 3-Axis Acceleration: Combination with Simple Threshold and Hidden Markov Model*, Journal of Applied Mathematics, 2014.
- [15] Park B., Shin I., Ha J., et al, *Senior Survey 2008: life and welfare service needs of the elderly in Korea*, Ministry for Health and Welfare, 2009.
- [16] Ageing W., Unit L., *WHO global report on falls prevention in older age.*, World Health Organization, 2008,



# STRESS ANALYSIS OF CHEST WALL DURING INSPIRATION

Defu Cui and Frederic D. McKenzie  
Modeling, Simulation and Visualization Department  
Old Dominion University  
4700 Elkhorn Avenue, Norfolk, VA 23529, USA  
dcui001@odu.edu and rdmckenz@odu.edu

## ABSTRACT

Pectus excavatum is the most common congenital chest wall deformity. However, the pathogenesis is still unknown and its related research results are inconsistent. Since the chest wall is subject to a negative intrapleural pressure which pulls the chest wall inward, the negative intrapleural pressure may be a pathogenetic factor for pectus excavatum. The purpose of this study is to investigate the stress distribution in the chest wall during inspiration. A 2D model of chest wall including lungs and diaphragm is first built, and COMSOL Multiphysics, a finite element commercial software, is utilized to analyze the stress distribution in the chest wall during inspiration. The results indicate that the stress in the sternum increases significantly during the process of the inspiration. Moreover, the sternum is subject to higher stress for an elongated torso.

**Keywords:** pectus excavatum, stress distribution, inspiration.

## 1 INTRODUCTION

Pectus excavatum (PE) is the most frequent congenital chest wall deformity. However, its pathogenesis is still unknown. There are several hypotheses regarding the formal pathogenesis of PE, which can be divided into two categories: intrinsic pathogenetic factors and extrinsic pathogenetic factors[1]. Most of hypotheses of pathogenesis of PE are about intrinsic pathogenetic factors, which include cartilage overgrowth, overgrowth of the ribs, ligamentum substernale, dysfunction of the lung parenchym, weak cartilage through metabolism, intrathoracic tension, and muscular imbalance of muscles of respiration[1]. The hypotheses about the extrinsic pathogenetic factors are intrauterine pressure of different causes, and exogen overstrengthening from work[1]. The inner surface of the chest wall and the outer surface of the lungs are lined with pleural membranes. The chest wall is subject to the intrapleural pressure, which is usually sub-atmospheric due to the chest wall expansion and elastic lung recoil acting in opposite directions. During inspiration, the contraction of the diaphragm and intercostal muscles causes expansion of the thorax. As a result, the intrapleural pressure will decrease[2]. Since the negative intrapleural pressure pulls the chest wall inward, the negative intrapleural pressure may be a pathogenetic factor of PE. To have a better understanding of the influences of the intrapleural pressure, this study investigates the stress distribution in the chest wall during inspiration. A 2D model of chest wall including lungs and diaphragm is first built. Then, COMSOL Multiphysics is used to analyze the stress distribution in the chest wall.

## 2 DESCRIPTIONS OF CHEST WALL MODEL

Figure 1 shows a 2D chest model. The lung is represented as a single balloon inside a sealed chamber connected to the atmosphere via a tube. The pleural cavity is a small liquid filled space. The intrapleural pressure during breathing is modeled using the air pressure confined inside a sealed container.

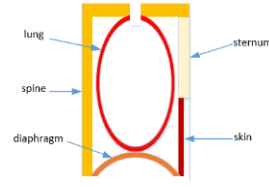


Figure 1: A 2D Model of Chest.

### 3 RESULTS AND DISCUSSIONS

COMSOL Multiphysics is used to compute the stress distribution during the inspiration. All materials are assumed linear elastic. The intrapleural pressure is assumed to be  $-10KPa$  at the beginning of inspiration. Figures 2 and 3 demonstrate the stress distributions of chest wall at the beginning and end of inspiration, respectively. The stress distributions are also shown when the height of chest wall is  $H = 0.4m$  and  $H = 0.5m$ , respectively. At the beginning of inspiration, the stress at the tip of the sternum is  $2.67e6 Pa$  when  $H = 0.4m$ , while the stress at the tip of the sternum is  $3.12e6 Pa$  when  $H=0.5m$ . At the end of inspiration, the stress at the tip of the sternum is  $3.95e6 Pa$  for  $H = 0.4m$ , while the stress at the tip of the sternum is  $4.05e6 Pa$  for  $H = 0.5m$ . The results show that the stress in the sternum increases significantly during the inspiration. Moreover, the sternum is subject to a higher stress for a higher ribcage. The large stress in sternum during inspiration will pull the sternum inward, which may make the sternum buckle inward and develop PE. Besides, this can also explain that most PE patients have an elongated ribcage.

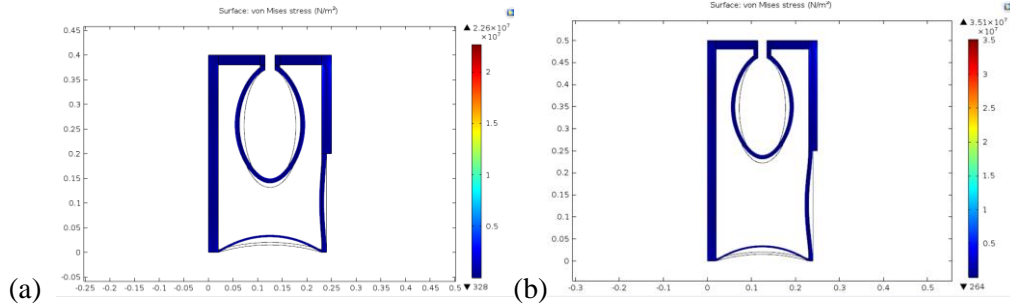


Figure 2: Stress distribution at the beginning of inspiration: (a)  $H=0.4m$ ; (b)  $H=0.5m$ .

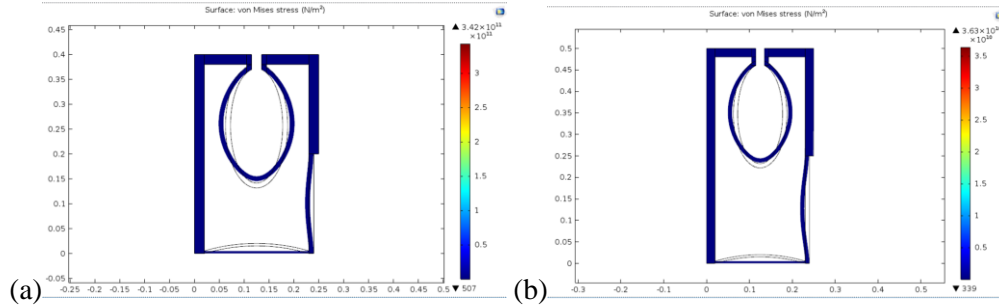


Figure 3: Stress distribution at the end of inspiration (diaphragm contraction): (a)  $H=0.4m$ ; (b)  $H=0.5m$ .

### REFERENCES

- [1] Brochhausen C., Turial S., Müller F. K. P., Schmitt V. H., Coerdts W., Wihlm J.-M., et al., Pectus excavatum: history, hypotheses and treatment options, Interactive CardioVascular and Thoracic Surgery, vol. 14, 2012, pp. 801-806.
- [2] Levitzky M.G. Pulmonary physiology. McGraw-Hill Medical Publishing; 2013.

# **PRACTICAL APPLICATIONS OF NEUROSURGICAL ONTOLOGIES FOR VARIOUS CRANIOTOMIC APPROACHES THROUGH COMPUTER ASSISTED SURGERY**

Austin Tapp  
Biomedical Engineering Ph.D. Student  
Old Dominion University  
5115 Hampton Blvd  
Norfolk, VA, USA  
atapp001@odu.edu

Advisor: Michel Audette, Ph.D.  
Modeling, Simulation and Visualization Engineering  
5115 Hampton Blvd  
Old Dominion University  
Norfolk VA, USA  
maudette@odu.edu

## **ABSTRACT**

The development of imaging devices has enabled the delivery of multimodal information, leading to descriptive patient specific data sets and simulated planning of surgical procedures. These substantial influxes of medical imaging information have the potential to be harnessed, processed and utilized in Computer Assisted Surgery (CAS). As CAS becomes increasingly common for a variety of surgical fields, there is a need for representation, storage and processing of surgical knowledge in a structured, integrated and standardized format that can easily be adapted to match case-specific imaging information. One such format, represented in this study as an ontological model, supports coarsely defined intracranial and intranasal neurosurgical approaches which will display discrete and well-understood steps based on patient information obtained during a surgical procedure. Through various manipulations, these ontologies, which will be ratified by neurosurgeons, are reproduced in a Semantic Web format, and allow integration of modern imaging analysis and medical modeling software that provide live feedback and utilize algorithms to suggest surgical approaches with the highest rates of success based on information obtained and analyzed in real time. Semantically mapped neurosurgical approaches can be interpreted by both humans and machines and uncover vast possibilities of potential real-time data analysis, integration, and processing of intra-operative medical images (MRI, CT, ultrasound) to greatly expand the ability for surgeons to provide ideal care for any patient. These intraoperatively obtained images are then applied to preoperative models, thereby updating and accounting for brain shift and estimating resected tumor volumes. Every step of a surgical procedure may include annotated medical images of each patient, display additional personalized anatomical landmark information along the patient's surgical corridor, and guide a surgeon through any combination of procedures with a "surgical GPS"-like display, allowing the physician to elect for the best surgical approach, exponentially increasing the chances of a successful outcome.

**Keywords:** Ontology, RDF, Semantic Web, CAS, Neurosurgery

# 1 INTRODUCTION

## 1.1 Background

Computer Assisted Surgery (CAS) is becoming increasingly common for various types of surgical interventions, such as neurosurgery, orthopedic surgery, and maxillofacial surgery. CAS utilizes computer-based technology in all phases of the surgery, starting with pre-operative planning, and continuing through intraoperative procedures, and into post-operative analysis. In the pre-operative phase, CAS receives data from various sources related to surgical knowledge, which is gathered from discrete databases. In particular, CAS for neurosurgery involves a guide based on diagnostic images of patients such as computed tomography (CT), magnetic resonance images (MRI), angiography and tractography (Perrone, 2012). Merging the information accumulated by multiple images platforms creates a patient unique atlas that includes segmented anatomical structures, which are labeled based on the risk of damaging functionalities in crossing them (Vivani 2016). CAS domain includes other areas of medical expertise such as engineering of surgical devices, modeling of surgical procedures and assessment of various surgical methods complied and adopted into a computable manner. It is critical to interface CAS application data with the latest knowledge representation system in order to integrate and unify heterogeneous data. For neurosurgical approaches, pre-operative, intra-operative and post-operative analysis is needed to perform appropriate diagnoses, procedures and patient health maintenance. This analysis may include the use of medical imaging, anatomical and pathological data, and past diagnostic records of patients. Within these vast sources of medical knowledge, there lies the opportunity for representation, storage, and processing of surgical knowledge of a system, which keeps track of all information to utilize it for specific task demanding applications (Guarino & Giaretta, 1995).

An ontological model provides the means to represent conceptual knowledge using expressive formal logics (Guarino & Giaretta, 1995). Ontologies, defined as an explicit formal specification of a shared conceptualization, allows a representation in a semantically, systematic and interoperable manner. Ontological models, which provide insight into a specific domain of interest, in this case neurosurgical approaches, allow for representation that is comprehensible for humans and software alike (Perrone 2012). The models of any particular domain require definitions of persons, devices, tasks, systems, states, and information of the process involved. Protégé, used to model surgical planning, allows the number of steps to be defined for each surgical procedure (Noy & McGuinness 2001). Surgeons are able to access descriptions of surgical procedures and query ontologies using patient-specific parameters, based on a template provided by the general ontology model. Parameter variations processed by combinations of modeling software, ontologies, and pre/intra-operative imaging provides the best surgical approach depending on specific case analysis.

The goal of this project is to design and develop multiple ontologies for neurosurgical approaches that are often used for a variety of target, usually malignant body, removal. A representation of knowledge on this scale can help to standardize, unify and advance healthcare and surgical practices across the globe. A culmination of domain knowledge and medical records and procedures paired with patient-specific ontological guidance information yields a more accurate diagnosis and treatment. The surgical domains operate at various levels of granularity, which allows for the flexibility of ontologies to be generalized but also fine-tuned to assist in each individual study. The ontologies are linked to knowledge repositories from various neurosurgical information sites, including those that provide neurosurgical techniques, lexicons, and terminological agreements.

## 1.2 Ontologies

Ontologies can be used to model a domain and support reasoning about entities. This format represents knowledge as a set of concepts within a domain, and the relationships between pairs of concepts, particularly for representing and sharing knowledge. Ontologies may be defined as explicit and formal specifications of a conceptualization, in which the typology of concepts and relative restrictions

are well defined, and machines are able to read and conceptualize an abstract and simplified model of the domain of interest. Representation of knowledge in ontologies is based on conceptualization of objects, concepts and other entities that could belong to certain areas of interest, and the subjects of ontologies must be related to a category of things that exist or may exist within a single domain (Noy & McGuinness 2001).

In order to build an ontology, it is necessary to: identify the domain of interest, evaluate the possibility of re-using existing ontologies, identify basic terms, define taxonomy, properties and rules, individualize new terms resulting from rules, define instances and identify errors and inconsistencies (Noy & McGuinness 2001). Following construction, ontologies would be used to share knowledge between users and machines through a software, which would extract and merge data from various ontologies to answer a user's questions or use the answers to further provide input for processing. Therefore, building the ontology requires basic knowledge of two languages: Resource Description Framework and Ontology Web Language.

The ontologies in the focus of this study are largely considered surgical workflow ontologies. These types of ontologies are utilized in computer assisted surgery and can be improved using surgical models and patient specific models created from multimodal images. A methodological framework for these models includes the definition of a surgical ontology, the development of a planning software for surgical procedure based on the ontology and the analysis of these descriptions to generate knowledge about the surgical practice. The surgical work defined as "the automation of a business process in the surgical management of patients, in whole or part, during which documents, information, images or tasks are passed from one participant to another for action, according to a set of procedural rules" (Perrone, 2012). By breaking the procedure into steps to create a surgical script, with a list of relevant image entities assigned to each step, the surgical process may be successfully annotated. When a procedure is the basic entity of the ontology, it may be defined with significant information including patient info, surgical steps, descriptions of the steps, etc. Each step is described as an action with associated attributes, while each structure will be represented by an image from multimodal imaging software of the patient. Each image may include information about the target area, areas around the target to be avoided, landmarks, and other anatomical features critical for appropriate surgical success.

### **1.3 Use of Ontologies**

After producing and understanding these logical connections, a classified knowledge-based model is created that may answer specific types of questions. Answering questions is done through the use of a querying language called SPARQL, SPARQL Protocol and RDF Query Language. Resource Description Framework (RDF) is the basic language for coding, reusing structured metadata, and providing interoperability with other applications that exchange machine-readable information. The basic unit to represent information is the statement, or the triple subject-predicate-object, and each element of the triple is a resource. The RDF model may be displayed as a graph in which nodes are resources or primitive types and branches are properties (Berners-Lee & Jaffe, 2018). Ontology Web Language (OWL) is a language adopted as standard by W3C, the World Wide Web consortium, from 2002. OWL was based on the RDF model and adds a larger vocabulary in order to describe the properties and classes, combining concepts to logic rules.

The questions that SPARQL may answer, could in theory be answered by a website, but the ease of manipulating, adding, modifying and deleting concepts within the preview of an ontology allows for a much more fluid and consistently maintained knowledge base. Websites are not meant to be so frequently revised and edited, which would need to occur every time a patient came in to undergo a surgical procedure in order to match the specific needs and interests of the patient (HP Labs, 2010).

## 2 METHODS

### 2.1 Creation of Ontologies

The production of the ontologies is based on information mined and processed from 3D Neuroanatomy, a Spanish website dedicated to detailing potential approaches helpful in developing ontologies (Cornejo, et al., 2014). The approaches described include: pterional craniotomy, endoscopic endonasal, lateral supraorbital, anterior interhemispheric transcallosal, infratentorial supracerebellar, far lateral, presigmoid, frontotemporal and many more. 3D Neuroanatomy also details the anatomy of the ventricular system, sellar and parasellar regions, and the orbit. Following the conversion of these approaches, often described in chapters, to a more skeletal procedure, terms were cross referenced for concepts found on NeuroLex, SNOWMED, and OpenGALEN. After the confirmation of these concepts, ontologies can then be formed through Protégé to construct domain models and knowledge-based applications with full support for the OWL 2 Web Ontology Language (Figure 1). Protégé contains a direct in-memory connection to description logic reasoners such as HermiT and Pellet, that ensure the compatibility of classes', object properties' and data properties' relationships (Stanford Center for Biomedical Informatics Research, 2000). The ontologies created may then be produced or saved in .owl or .rdf formats for appropriate compatibility. The ontologies themselves may be built as smaller sections, because they can later be integrated and combined, which may produce repeat concepts, but establishing a greater quantity of individuals relationship can only improve the accuracy, connectivity and effectiveness of the ontology. The use of the Ontology Lookup Service was useful in drafting ontologies, as there are many ontologies in production or complete that may provide a base for an ontology looking to be created.

### 2.2 Karma

Once an ontology has been formed through Protégé, they may be integrated using a software known as Karma. Karma is an open-source ontology model developer program to be used for the mapping of ontologies in their .owl or .rdf formats (Knoblock et al., 2016). The use of Karma requires the most up to date versions of Java and MAVEN 3.0. A Java\_Home file should be established, and MAVEN must be added to a path. This will create a virtual machine and allow Karma to launch a local host window in an internet browser, where the map may be manipulated. The settings for Karma include a Max Heap compactly, 16GB in this case, and files used are mainly UTF-8. Once initialized, the ontologies in .owl or .rdf formats may be used. Data is required to produce the map, and that data may be uploaded as .json, .csv, or .xml files. Columns, that include the identifier, title and language of the object, will appear after this data upload and the structure of the ontology can be developed. To create the model, "PyTransform" will allow a URI identifier for each ontological object to be made. A minimal python-based code that identifies the URL of the link through Karma must be established to form a copy column listed with a '\_uri' extension. At this point, data types may be mapped, and the model can be formed. The user may link columns to decide how the model will take its shape (Figure 2/3). After some use, Karma will begin to produce similar suggestions and ease the user workload by providing predictive mapping connections.

### 2.3 RDF & SPARQL

After a model is created, Karma provides options to publish the model and convert the model to a series of triple outputs. These triple outputs are described in the above section of about RDF's. The triples that Karma constructs are difficult to understand, and are better utilized with the use of a query software known as SPARQL (Apache Software Foundation 2011). SPARQL is used to retrieve the data embedded in the triples and can be run off a local server, similar to Karma. To initialize SPARQL, a path file should again be created using the command window every time this type of query is to be initialized. The query has significant filtering and retrieving capabilities, and any aspects entered into Karma: classes,

csv data values, object properties, etc. can be retrieved based on the input parameters. More specifically, SPARQL is able to extract values from structured or semi-structured data. It has the ability to explore data between unknown relationships and can execute complex joins of disparate databases in a query. SPARQL may also transform the RDF data from one vocabulary to another, which remains to be a critical part of the use of RDF in surgical preparation and consultation. By providing a simple way to allow for vocabulary adjustments, data from SNOWMED and NeuroLex have the potential to be integrated seamlessly into existing RDF models.

## **2.4 VIVO**

Following the successful testing of outputs of an RDF model through SPARQL queries, it may be published, uploaded or further edited on websites like VIVO. VIVO supports the recording, editing, analysis of the content of ontologies, and is currently primarily used to display researcher's information and their studies. This site, or other related services have the potential to host a variety of surgical ontologies, that may be continuously uploaded, downloaded, edited, and viewed by the medical community. Furthermore, the ontological information the server gathers can be manipulated using a simple website interface by surgeons all over the world. Any physician may access and consult this semantic web, which will also allow significant contributions to pre-operative surgical planning. A surgeon may upload the parameters of a patient's surgical needs onto this software, which will then recommend the most appropriate route and ontology for the surgeon to download. This download includes only surgical steps for now but will eventually produce a patient specific model related to patient's pre-operative medical images that are conformed to a generalized digital atlas. The atlas will be morphed to fit the patient based on these images and can contribute to the ease of surgical planning and the procedure itself, as along the patient's surgical corridor, various anatomical landmarks will be highlighted by the ontology and conserved in fine detail to produce a "surgical GPS". Similar to a GPS, the driver, or surgeon, has the ability to take their own route, but the ontology will continue to suggest information about the patient, surgical procedure, and anatomical landmarks based on any intraoperative images accessed at that time. These images taken during surgery can be constantly analyzed by software during the CAS procedure to provide continuous, powerful feedback relating to the present status of the patient and the next suggested step of the procedure.

## **3 RESULTS**

### **3.1 Verification**

After a consultation by surgeons at Mount Sinai in New York, we were able to produce an accurate, responsive and coarsely defined RDF triple set for an Endoscopic Endonasal Approach. The approach is defined below, with a series of anatomical landmark "outputs" that suggest movement to the next step of the surgery:

"ENT approach: Lateralizes nasal components-inferior turbinates and medial turbinates to visualize the medial orbital wall (output 1).

Isolate the sphenopalatine vasculature bilaterally. Identification of vomer (output 2).

Open the sphenoid ostiums (output3).

Open the sphenoid sinus to create one cavity (output 4).

Un-obstructed Identification of the OCR bilateral (Output 5).

Identification of the tuberculum and Sella bone(output6).

Identification of clival recess in pre-sellar space (output7).

Open bone of the sella and often tuberculum to identify dura (output8).

Neurosurgery: Intra-capsular approach. De-bulking of the intra-capsular tumor (output1). Identification of the cavernous sinus wall bilaterally (output2).

Identification of the normal gland (output 3).

Identification of the descending diaphragm (output4).

Doppler the carotid within the cavernous sinus an (output5)".

Figures 2 and 3 show the results of a rather large Karma RDF model that was produced based on these recommendations, and Figure 5 displays a subsequent query for the output landmarks of the procedure. The code that displays when SPARQL is initiated is shown here:

```
ATsMBP:~ Austin$ cd ~/Documents/Research/Research_Audette/Fuseki/apache-jena-fuseki-3.6.0
ATsMBP:apache-jena-fuseki-3.6.0 Austin$ ./fuseki-server --update --mem/ds
[2018-03-19 01:08:21] Server  INFO  Dataset: in-memory
[2018-03-19 01:08:21] Server  INFO  Apache Jena Fuseki 3.6.0
[2018-03-19 01:08:22] Config  INFO
FUSEKI_HOME=/Users/Austin/Documents/Research/Research_Audette/Fuseki/apache-jena-fuseki-3.6.0
[2018-03-19 01:08:22] Config  INFO
FUSEKI_BASE=/Users/Austin/Documents/Research/Research_Audette/Fuseki/apache-jena-fuseki-3.6.0/run
[2018-03-19 01:08:22] Config  INFO  Shiro file:
file:///Users/Austin/Documents/Research/Research_Audette/Fuseki/apache-jena-fuseki-3.6.0/run/shiro.ini
[2018-03-19 01:08:22] Config  INFO  Template file: templates/config-mem
[2018-03-19 01:08:23] Config  INFO  Register: /ds
[2018-03-19 01:08:23] Server  INFO  Started 2018/03/19 01:08:23 EDT on port 3030
```

### **3.2 Potential**

This code demonstrates the use of a local host to provide a platform for the triples to be searched. Within a query of this kind, we have the potential to further edit the posted triples, and update any relationships within the RDF model to greater enhance the specificity of the surgical steps for any procedure. As discussed above, this RDF will be uploaded onto a semantic web server, like VIVO, where it can be accessed and manipulated by a variety of individuals. Finding the ideal platform for the appropriate use of these models is critical and is the next step in the process of this research.

## **4 CONCLUSION**

### **4.1 Summary & Discussion**

Surgical ontologies have the potential to provide an excellent way to conceptualize, organize, and represent procedures in a format understood by both computers and individuals working in synchronization in an operating room. The use of these ontologies leads toward a standardization and unification of advancing healthcare and surgical practices, which can be shared and edited across the globe. Physicians will soon have the ability to upload patient parameters and download surgical ontologies of varying specificity, and utilize these ontologies with a SPARQL query to guide themselves through an ideal procedure. RDFs and the semantic web are exciting and powerful tools that can be easily equipped to a healthcare providers arsenal to allow extensive knowledge and understanding of the benefits and weaknesses of a variety of patient interventions. These interventions have the potential to be patient specific, but will stem from a generic and coarse model, eventually being streamlined down into an ideal therapy.

As the field of imaging software and various imaging modalities continues to expand, the capability to provide patient specific pre-operative models, enhanced intraoperative care, and significant increases in medical success through CAS has the potential to progress with similar strides. Through the use of surgical ontologies and a semantic web framework, physicians are provided with a significant array of tools that would exponentially enhance the individualized care of any patient. A creation of surgical ontologies is only the first of many cutting-edge innovations that take advantage of the growing power of



simulation software, artificial intelligence and surgical modeling to provide significantly enhanced healthcare outcomes.

## 4.2 Future Work

Future directions of this work include applications of these ontologies to a hierarchical and lexical representation of the brain that will be coupled with a digital anatomical atlas. This atlas will be initially generic but can be warped patient specific imaging data. There is also significant evidence that these ontologies will act as a successful tool for neurosurgical training through virtual reality simulations. As the surgeon is guided through the process within the GPS view, there will a lighting of anatomical landmarks along the surgical corridor. This corridor would be simulated in virtual reality for training purposes and also highlighted intraoperatively when meshed with patient imaging data (Figure 6).

Another area of future interest plays off of the idea of a semantic web platform to host a variety of neurosurgical and other surgical ontologies. Creating an open-source platform that would allow physicians to upload images of patient data, and retrieve from that same server a sequence of verified surgical approaches, complete with interventions that are specific to the anatomy of single patients and that would consider potential shifts in tissue, would allow for a greater level of pre-operative preparation and considerable collaboration on patient procedures. Due to the nature of this platform, any surgeon could have an influence on a surgical procedure for a patient that is not their own by enhancing this community of surgical workflows through verification and consideration of procedures. The influence of other doctors would come from constant data influxes relating to the planning, conditions, success rates, and other significant information relating to a patient's case that can then be processed and added into this semantic web.

## FIGURES

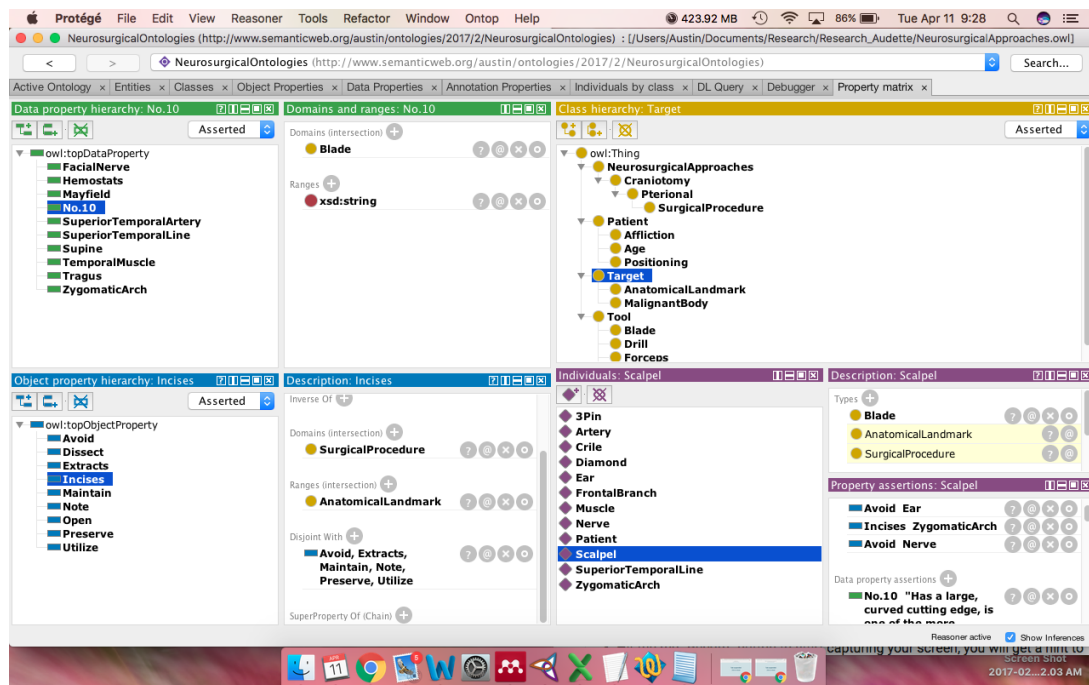


Figure 1. This figure is a screenshot that demonstrates the use of Protégé, an open-source software from Stanford, that is used in the creation of neurosurgical ontologies.

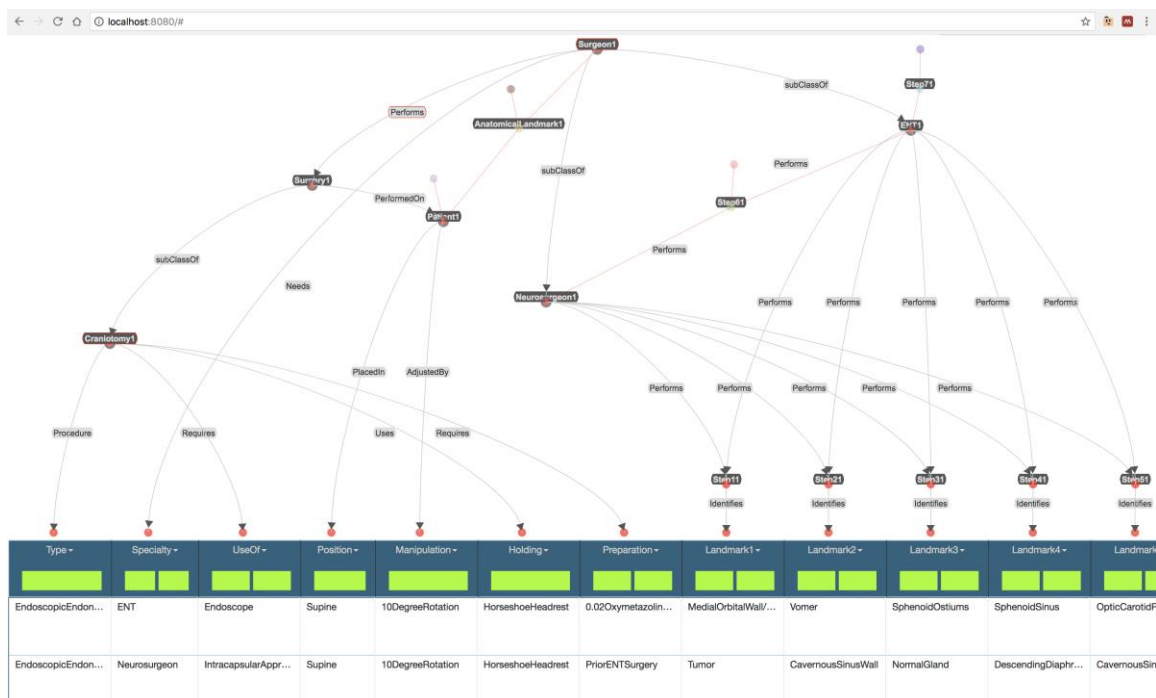


Figure 2. (1/2) A screenshot from Karma, developed by USC, that is used to create a sequence of RDF triples for the endoscopic endonasal approach.

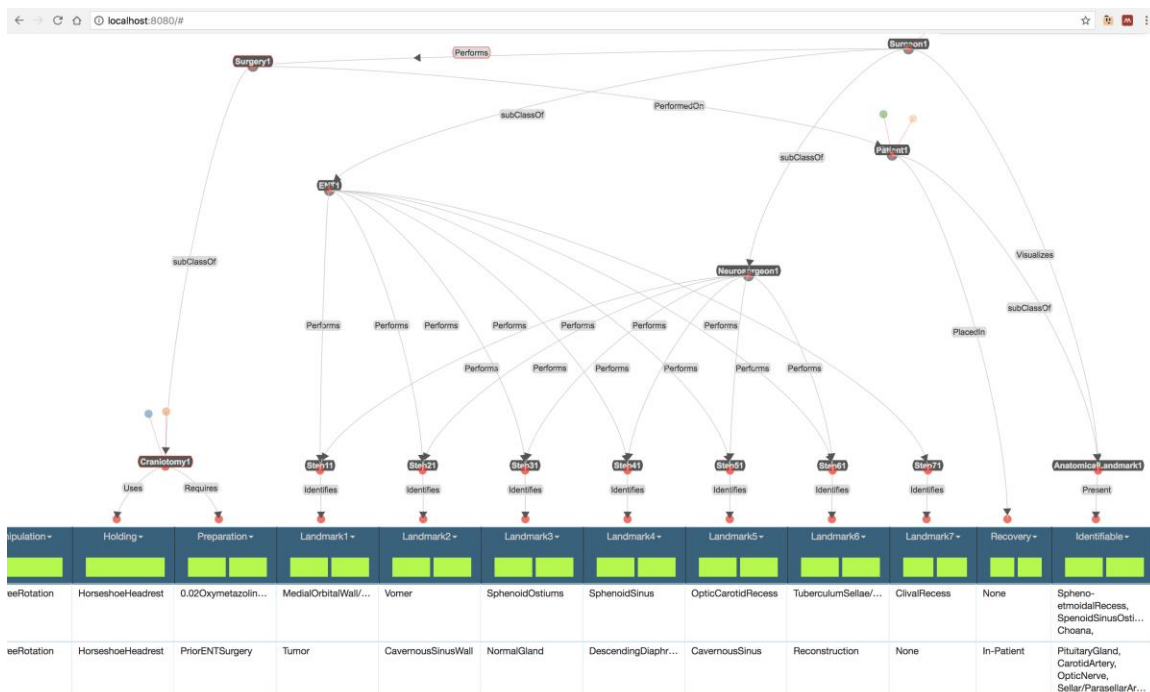


Figure 3. (2/2) This second screenshot is a continuation of the Karma model for an endoscopic endonasal craniotomy.

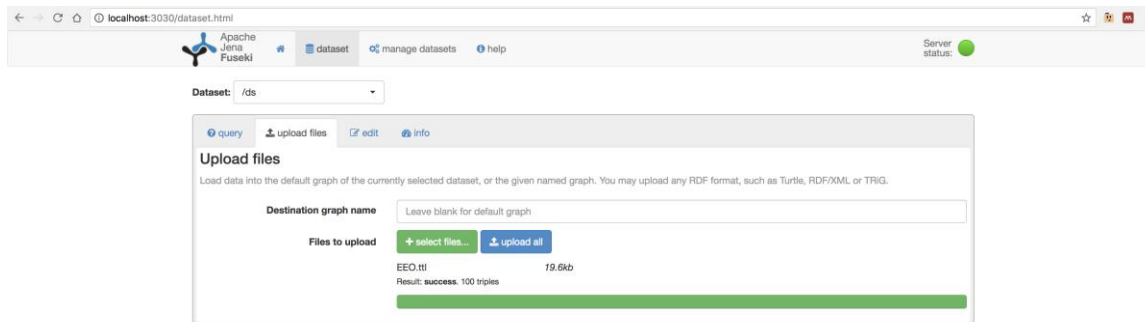


Figure 4. This screenshot shows the use of the Apache Jena Fuseki server to run SPARQL, a query engine for RDF triple values. The number of data points, or triples, gathered can be visualized and reports a successful acceptance of the above Karma model.

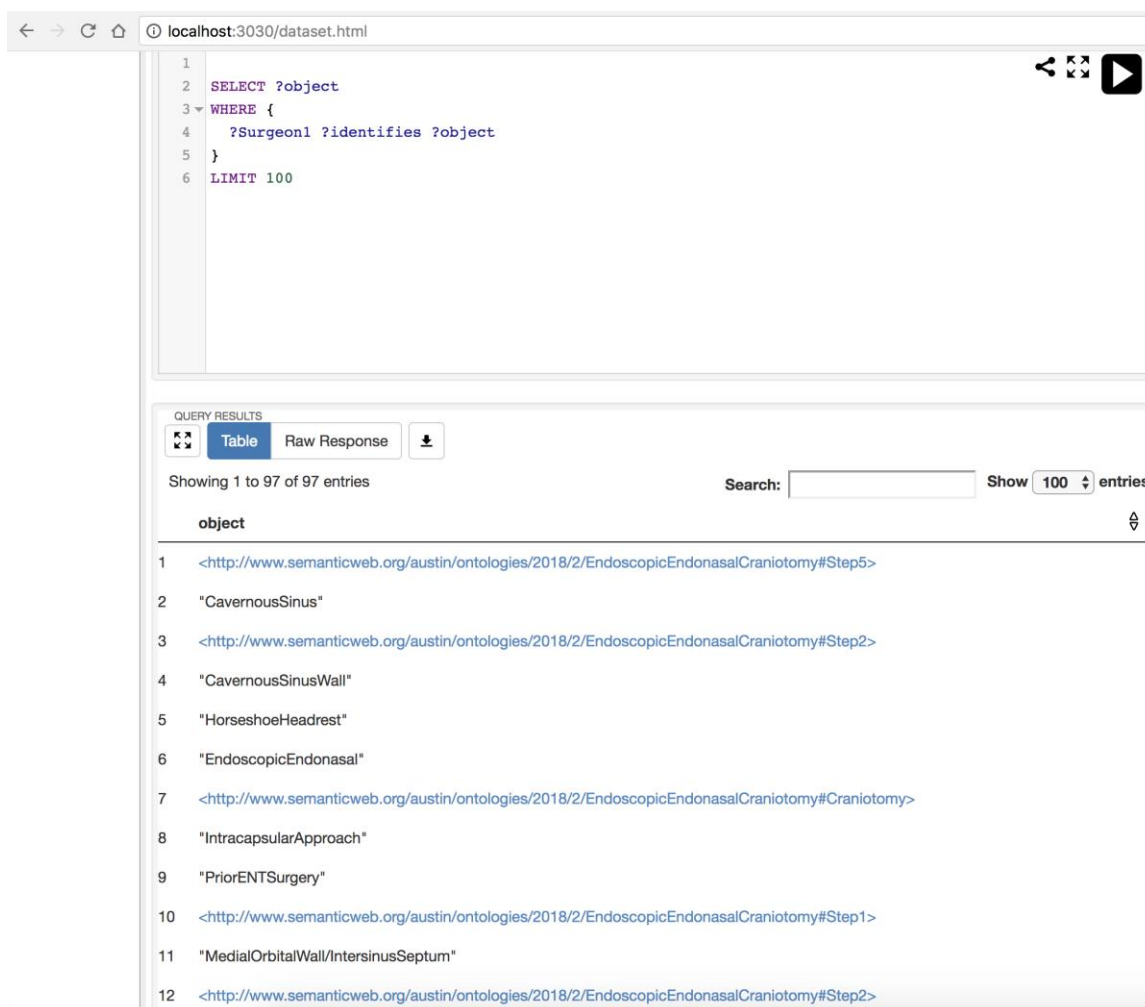


Figure 5. The output values of the SPARQL query. These values are the ‘object’ or the third part of the triple. In most instances, we strive for this string value to be that of an anatomical landmark. A sequential display of these outputs based on procedural step number is ideal and easily attainable based on the search filter/parameters.

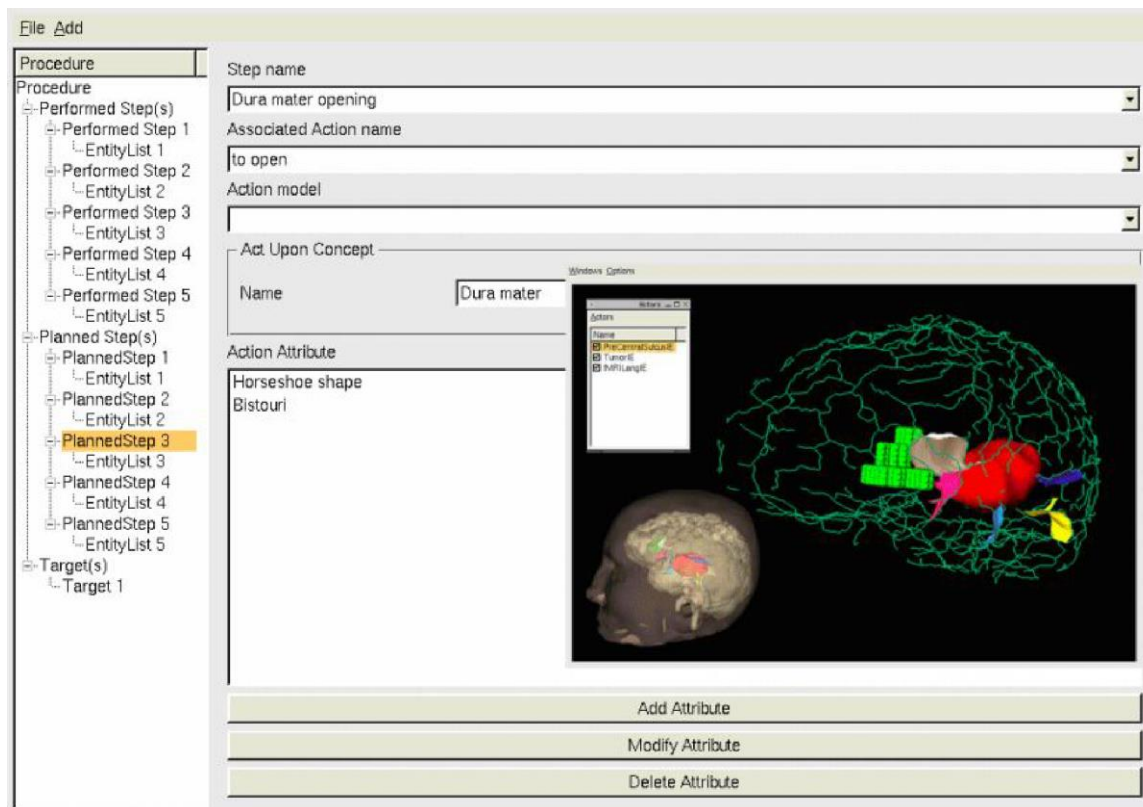


Figure 6. An example of a coarsely mapped 3D anatomical patient model with landmarks of the surgical corridor highlighted to show their importance as they relate to the procedure ontology. (Perrone 2012)

## ACKNOWLEDGMENTS:

I would like to express my appreciation to Professor Michel Audette, under whose guidance this investigation was conducted. Thank you for your support, supervision and criticisms regarding this study and its many related and future prospects.

I am also indebted to Drs. Raj Shrivastava and Alfred Illoreta, of Mount Sinai Medical Center, NY, for their careful consideration and review of the endoscopic endonasal approach's critical view and landmark outputs. Thank you for your time, and belief in the potential and clinical applications of this project.

I would also like to thank to Anthony Costa, Ph.D., a professor at Mt. Sinai, for facilitating communication and providing much needed assistance between ODU and Mount Sinai, as well as his support of our present and future collaborations.

Finally, I wish to thank the Biomedical Engineering department at ODU because without their funding, continuous work on this project would not have been possible.

## AUTHOR BIOGRAPHY

**AUSTIN TAPP** is a Ph.D. student in Biomedical Engineering at Old Dominion University. He received his B.S. in Neuroscience from the College of William and Mary. His research interests include modeling and simulation efforts for neurosurgical planning. His email address is [atapp001@odu.edu](mailto:atapp001@odu.edu).

## REFERENCES

- Apache Software Foundation. "Apache Jena." A free and open source Java framework for building Semantic Web and Linked Data applications (2011) [jena.apache.org/index.html](http://jena.apache.org/index.html).
- Berners-Lee, T., Jaffe, J., W3C, The World Wide Web Consortium (2018). Retrieved from <https://www.w3.org/>.
- Case, J., "Leading Healthcare Terminology, Worldwide." SNOMED International, (2011). Retrieved from [www.snomed.org/](http://www.snomed.org/).
- Cornejo, V. F., Lopez, P. G., Olivas, J. A., Alshafai, N. S., Cardenas, E., Elbabaa, S.K., Kaen, A., & Verdu, I. (2014, October 1). 3D Neurosurgical Approaches – ISSN 2254-9595. Retrieved from <http://3dneuroanatomy.com/category/3d-neurosurgical-approaches/page/2/>
- DBpedia. Wikipedia. "Ontology." Ontology | DBpedia, (Mar. 2017) [wiki.dbpedia.org/services-resources/ontology](http://wiki.dbpedia.org/services-resources/ontology).
- HP Labs. "Jena Ontology API." Apache Jena - Jena Ontology API, Nov. (2010) Retrieved from [jena.apache.org/documentation/ontology/](http://jena.apache.org/documentation/ontology/).
- Guarino, N., & Giarretta, P. (1995). Ontologies and Knowledge Bases: Towards a Terminological Clarification. *Towards Very Large Knowledge Bases. Knowledge Building and Knowledge Sharing*, 1(9), 25–32. <https://doi.org/10.1006/ijhc.1995.1066>
- Knoblock, C., Szekely, P., & Burns, G. (2016). "Karma." Karma: A Data Integration Tool, University of Southern California, 2016, [usc-isi-i2.github.io/karma/](https://github.com/usc-isi-i2/karma).
- Mudunuri, R., Burgert, O., & Neumuth, T. (2009). Ontological Modelling of Surgical Knowledge. In *GI Jahrestagung*. Retrieved from <http://subs.emis.de/LNI/Proceedings/Proceedings154/gi-proc-154-61.pdf>
- Neurolex., Term Dashboard (2018). University of California. Retrieved from <https://scicrunch.org/scicrunch/interlex/dashboard>.
- Noy, N. F., & McGuinness, D. L. (2001). Ontology Development 101: A Guide to Creating Your First Ontology. *Stanford Knowledge Systems Laboratory*, 25. <https://doi.org/10.1016/j.artmed.2004.01.014>
- Perrone, R. (2012). *Ontological modeling for Neurosurgery : application to automatic classification of temporal and extratemporal lobe epilepsies*. <https://www.politesi.polimi.it/handle/10589/77823>
- Porter, B., van Zyl, J., & Lamy, O., "Apache Maven Project." Maven – Welcome to Apache Maven (2000) [maven.apache.org/index.html](http://maven.apache.org/index.html).
- Stanford Center for Biomedical Informatics Research. "Protégé." Protégé (2000) [protege.stanford.edu/products.php](http://protege.stanford.edu/products.php).
- Viviani, R. (2016). A Digital Atlas of Middle to Large Brain Vessels and Their Relation to Cortical and Subcortical Structures. *Frontiers in Neuroanatomy*, 10, 12. <https://doi.org/10.3389/FNANA.2016.00012>
- Whetzel PL, Noy NF, Shah NH, Alexander PR, Nyulas C, Tudorache T, Musen MA. BioPortal: enhanced functionality via new Web services from the National Center for Biomedical Ontology to access and use ontologies in software applications. Epub 2011 Jun 14.
- Zaveri, A., Shah, J., Pradhan, S., Rodrigues, C., Barros, J., Ang, B. T., & Pietrobon, R. (2012). Center of excellence in research reporting in neurosurgery--diagnostic ontology. *PloS One*, 7</i

## **ODU MSVE CAPSTONE 2018: MEDICAL WORKSTATION EVALUATION PROCESS**

J.P. Asija

Department of Modeling, Simulation, &  
Visualization Engineering  
Old Dominion University  
1300 Engineering & Computational Sciences  
Building  
Norfolk, VA 23523  
jasij001@odu.edu

Brian Dilinila

Department of Modeling, Simulation, &  
Visualization Engineering  
Old Dominion University  
1300 Engineering & Computational Sciences  
Building  
Norfolk, VA 23523  
bdili002@odu.edu

Minh Dong

Department of Modeling, Simulation, &  
Visualization Engineering  
Old Dominion University  
1300 Engineering & Computational Sciences  
Building  
Norfolk, VA 23523  
mdong004@odu.edu

Michael Poteat

Department of Modeling, Simulation, &  
Visualization Engineering  
Old Dominion University  
1300 Engineering & Computational Sciences  
Building  
Norfolk, VA 23523  
mpote001@odu.edu

Jacob Richardson

Department of Modeling, Simulation, &  
Visualization Engineering  
Old Dominion University  
1300 Engineering & Computational Sciences  
Building  
Norfolk, VA 23523  
jrich087@odu.edu

Thomas Tracey

Department of Modeling, Simulation, &  
Visualization Engineering  
Old Dominion University  
1300 Engineering & Computational Sciences  
Building  
Norfolk, VA 23523  
ttrac005@odu.edu

Jake Webster

Department of Modeling, Simulation, &  
Visualization Engineering  
Old Dominion University  
1300 Engineering & Computational Sciences  
Building  
Norfolk, VA 23523  
jwebs001@odu.edu

## ABSTRACT

The Exploration Medical Capability (ExMC) element at NASA Langley Research Center desires a process for evaluating designs for medical workstations capable of supporting long-duration space exploration. The authors, as part of their senior capstone design experience, are charged with designing an evaluation process and implementing a prototype of that process. A key component of the evaluation process is a simulation having the capability to assign quantitative values to dynamic performance measures. Dynamic performance measures are evaluated by observing the conduct of an activity or task over a period of time. An example of a dynamic performance measure would be action completion time. The design team has determined that using a discrete event simulation, in which avatars are monitored while performing representative medical tasks, is the best approach for evaluating dynamic performance measures. The focus of this paper is performance metric calculation to provide evaluation scores for medical workstation designs.

**Keywords:** Discrete Event, Process, Metrics, Evaluation

## 1 INTRODUCTION

As of 2018, many advanced challenges in astronautics have been achieved. This includes the challenge of sending numerous space exploration vehicles to Mars. However, the National Aeronautics and Space Administration views this as only the beginning. One of the many near-horizon goals of NASA is that of advancing deep space exploration, as well as sending humans to Mars. Advancements in deep space exploration have in turn resulted in a new and innovative space capsule design, which will facilitate future voyages. On the other hand, these advancements raise many questions. One of these questions involves the logistics involved in maintaining crew health and safety. NASA aims to further develop its ability to accommodate medical needs and provide preventive measures aboard the deep space capsule in future manned voyages.

As the ability to send astronauts on deep space voyages becomes more of a reality, the ability to keep astronauts safe and healthy becomes more of a priority. The effects of microgravity on the human body for extended durations is still an area in which many questions are unanswered. Because of this, NASA must ensure that its medical capabilities are fit for long-duration, deep-space exploration. One of the current challenges that NASA is facing is how to distinguish between two medical workstations so that comparisons and differences can be highlighted when comparing designs. A medical workstation is a dedicated area where medical operations will occur during the space travel duration. A series of medical procedures performed in each medical workstation would provide a foundation for determining how the astronauts move around within the confined space, how they access the supplies within the workstation, and the ability to carry out a given procedure.

The Capstone Team is implementing its designed solution prototype system to produce this evaluated metric data that highlights those differences for NASA. NASA will be able to use the Capstone Team's solution prototype to effectively compare and evaluate between medical workstation designs from contractors. With NASA's future space travel ambitions, a candidate medical workstation design is required for NASA use. Performance measures related to the medical process being studied provide data used to differentiate aspects between workstation designs. The major focus of this paper is the development and simulation-based evaluation of performance measures targeting dynamic aspects of using a medical workstation.

## 2 DOCUMENT OVERVIEW

The document is structured in the following manner. The first section is the *Introduction*, where the authors introduce the problem description and present a general idea of the Capstone Team's solution. Next, a *Document Overview* is presented. This section briefly describes the sections and highlights their pieces of key content. Third, the concept and purpose of *Performance Measures and Metrics* are explained. This section details the purpose of using performance measures for the evaluation of medical workstation designs, defines metrics and the importance of their calculation, and provides examples of the Capstone Team's current list of performance measures and metrics. Following the section on performance measures and metrics, the next section presents the Capstone Team's *System Architecture*. Here, a high-level view of the entire project solution is visually introduced and explained describing how the system inputs and outputs provide the raw data necessary for metric calculation – and thus, information for medical workstation design evaluation.

The next three sections introduce and describe the three modular software components of the project solution. Immediately after the system architecture is explained, the next section introduces the *Input Editor* software component of the Capstone Team's solution. By using this piece of software, the user can modify inputs to the system, such as changing a workstation design being studied or the medical process being implemented. Following the input editor, the next section focuses on the *Simulation* software component of the system. This section renews dialogue of dynamic performance measures in the system, and it illustrates why and how simulation is needed and utilized to obtain quantitative output data relevant to dynamic aspects of the system under study. The final software component of the system is the *Output Analysis* tool. This output analysis section describes how output information from the simulation component is utilized to evaluate metrics of performance from dynamically studying the system, and it explains how this calculated metric data is used to compare and analyze medical workstation designs. The last section is a *Conclusion* of the document, where the authors present their current stage of completion and illustrate the path to the final milestone of the project.

## 3 PERFORMANCE MEASURES AND METRICS

Performance measures are the qualities by which a workstation design is assessed and compared with other designs. Performance measures can be divided into two categories dynamic and static. Dynamic Performance measures are directly tied to scenarios. A scenario is a set of related tasks that are representative of expected use. Usually an entire scenario is simulated at once. Some scenarios may be more important or more likely to occur in actual operation than other scenarios. This means that there must be a way to group or rank and weight scenarios such that given a numerical value for a design's ability to support each scenario in the set of scenarios a final score for the goodness of the design can be achieved. The output analysis tool described later in this paper supports this functionality.

When developing a scenario a set of expected use cases is translated to a simulation-ready model in this case a process flow. Performance measures are then developed for the model. This process begins by identifying all the points at which an actor interacts with the environment. I.e. moves through the environment, grab an object or uses an object etc. etc. These are the locations where information like the number of times a tool is used, the time it takes to retrieve a tool, time it takes to move to the point of care, can be collected. This information is used to calculate the performance metrics which are later weighted and organized to develop a final score for the scenario on that design. The weighting and organizing of the performance metrics is also performed in the output analysis tool.

Static performance measures have no need for simulation and are treated differently. Usually a static performance measure will be evaluated by one or more subject matter expert(s), but it is conceivable that some static performance measures could be evaluated by a computer acting as a sort of automatic yardstick. Static performance measures can be integrated into the scoring of a design at the same level as scenarios and also as a factor in a scenario score.



## 4 SYSTEM ARCHITECTURE

The major system employed by the Capstone Team operates on three major software components: the Input Editor, the Simulation, and the Output Analysis Tool. The Input Editor utilizes a graphical user interface (GUI) to allow the user to customize inputs to the system, such as workstation design models, the current medical process flow, or the current tools and resources. Once input information is finalized, the user can press a launch button from the Input Editor to launch a simulation for as many runs as chosen in the specified input information. The simulation completes as many runs of the current medical process flow and outputs raw data of time-stamped events, spatial and time-based constraint violations, and data focused on performance measures being recorded and studied as specified by the user.

The performance measure-focused output data recorded is utilized by the Output Analysis Tool to calculate the metric data for medical workstation design evaluation. The Output Analysis Tool implements a GUI to allow the user to provide the weighting and grouping of metrics. The evaluation of these metrics and the application of user-specified metric weights allows the user to receive a total score for each design. A visual representation of the system architecture is shown in Figure 1.

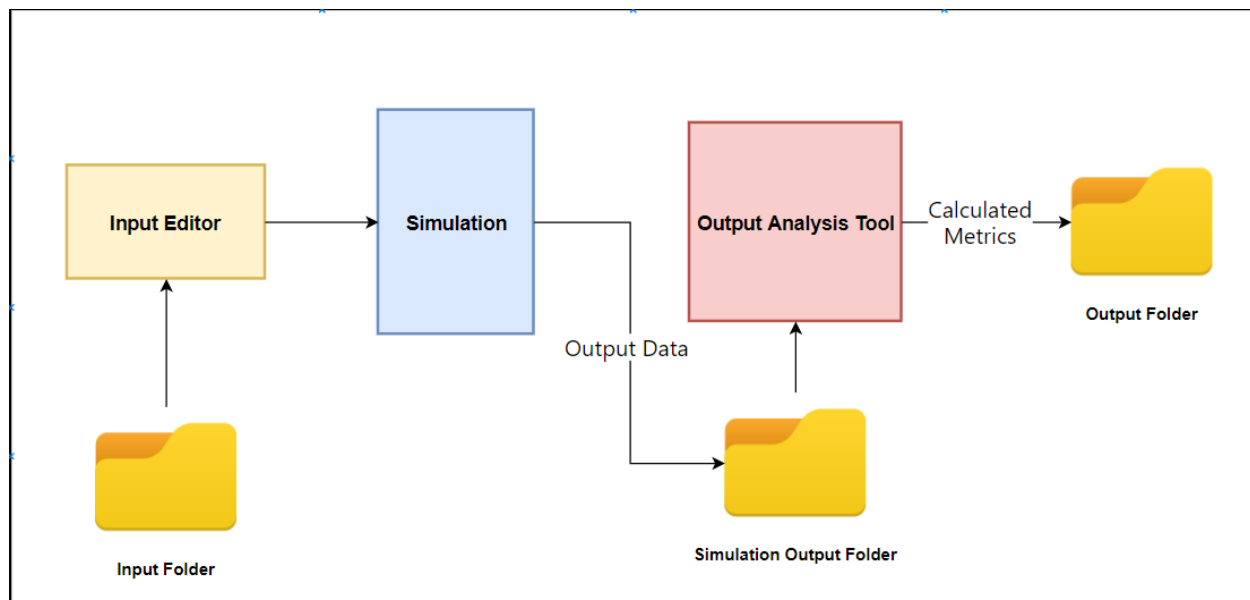


Figure 1: System Architecture

Medical scenarios are modeled as process flows using the process-oriented modeling paradigm. Every process in the medical process flow models represent an action related to the medical scenario being studied and implemented. In the simulation module, each process is modeled as a process block. Blocks are representative steps or actions linked in a sequence to form a task. An example task is “Conducting CPR” with example blocks “Prepare AED for shock” and “Move caregiver to the position of the AED”.

**Definition 1.** A block represents a processing step, generally an action, in the process flow.

**Definition 2.** A process consists of one or more tasks in a given order.

Different processing steps call for different process blocks:

- Decision
- Fork
- Join
- Move To
- Prepare

- Record
- Retrieve
- Use Tool
- Wait For

Decision blocks represent decisions in the process flowchart that lead a branch of block activities depending on a condition. Forks and Joins allow concurrency of block activities in the flowchart. Move To blocks contain the logic for checking whether an actor must move and calculate when the actor will suddenly appear at a target location. A Prepare block contains the logic of an actor preparing an item after a given time. A Retrieve block covers the retrieval of an item from its storage location. A Use Tool block covers the use of reusable tools after a given time. Wait For blocks are more generic in the sense that they are activities that occur over a time duration. They are generic and do not cover low-level detailed actions such as checking for blockage in the patient’s throat. Wait For blocks cover actions that are outside the resolution of the simulation.

Record blocks do not affect the system state in any way. Rather, they are responsible for creating or appending to a separate output file for raw data for metrics. Some metrics require a beginning and an end while others require a one-time update in information. Record blocks are divided into two categories: Paired and Solo Record blocks (Figure 2). Paired Record blocks handle these beginnings and ends to record differences in, say, time or distance travelled. These Record blocks are typically used for Time- and Distance-related performance metrics. They must exist together in the Process Flow to correctly provide information for calculation for metrics in the Output Analysis Tool. Solo Record blocks focus on one-time information gathering. Currently, they handle count of the usage of tools or the remaining amount of resources.

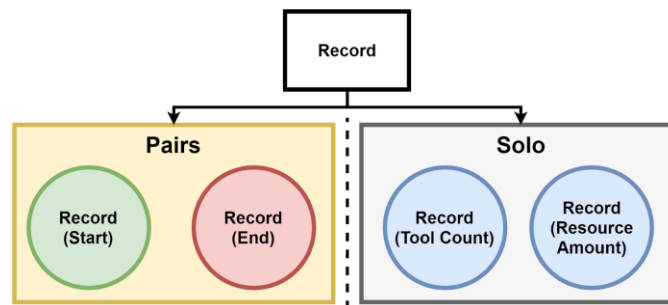


Figure 2: Categories of Record Blocks

## 5 INPUT EDITOR

### 5.1 Overview

The “Input Editor” module of the MWEP application is composed of a set of user-interface pages. These pages facilitate specification of various datum necessary for fully defining both a “design” and a “scenario” in accordance with the previous discussion on the design/scenario dichotomy.

There is a total of six pages associated with the input editor. One page is associated with launching the application. Two pages are associated with the design definition. The final three pages are associated with the scenario definition. In diagrammatic form, we provide this specification:

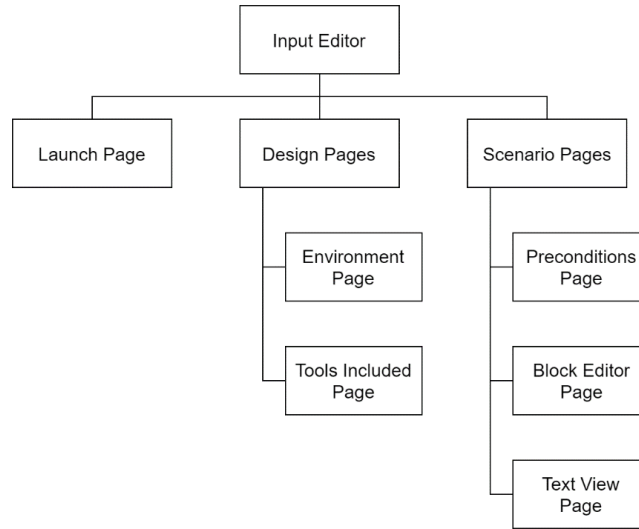


Figure 3: Input Editor System Architecture

## 5.2 User Experience (UX)

The purpose of the input editor is to facilitate the formal specification of both the scenario and design involved in characterizing the quality differences between medical workstations. Initially, the cubic dimensions of both the habitat and workstation are specified; This data may either be input manually or through an importing process of two volumetric .OBJ files. Upon invocation of the input editor, the user inputs the “design” in the corresponding section of the program. The environment tab is composed of fields corresponding to the following coordinate inputs:

- Habitat Dimensions
- Workstation Dimensions
- Workstation Position with respect to Habitat
- Position of Caregiver(s)
- Position of Patient
- 

The environment interface that encapsulates this input is displayed below in Figure 4.

Figure 4: Environment Interface

Now that the user has the Environment defined, the tools may be placed in the habitat or the workstation spaces. The “Tools Included” section is the tab that allows the user to input the set of tools needed for the scenario. The tab allows the user to insert the name, position, and the radius of the tool. For each tool, the user may specify a table of use conditions, whose individual rows correspond to a particular method of using a tool. These rows allow a set of predefined distribution types (e.g. uniform, normal, etc.). Next, there is a button that allows the user to insert the resources consumed via the usage of each tool. (e.g. the ‘fluid’ consumed by a syringe). In order to add new tools to the input editor, the user clicks on the “Add Tools” button, causing a blank row to appear. The user will have to then insert the parameters of the tool that will be added. This tab will be displayed below in Figure 5.

Figure 5: Tools Included Tab

The scenario section allows the user to both specify preconditions and the process flowchart that represents this conceptual scenario. For each precondition, a name and a real number between zero and one are provided. The real number is associated with the probability of the boolean precondition being “true” during a particular instance of the simulation.

A user may add more than one precondition by clicking on the corresponding “Add Precondition” button. Clicking this button will result in an empty parameters row being generated, as shown below in Figure 6.

Figure 6: Preconditions Tab

The flowchart editor is the most involved portion of the input editor. This facilitates the user to specify the process flow via a drag-and-drop interface. In this interface, the user may create a block by double-clicking the left mouse button. Those corresponding blocks are connected through a dragging action on the right mouse button. While in the white space, the user may scroll the mouse to change the currently selected block type. On the other hand, if the mouse is hovering over an edge, the currently selected metric type will be changed.

Metric markers are associated with edges between blocks. To create a metric, the user double-clicks an edge. An instance of the currently selected metric will be spawned on that edge. An example of this can be seen in Figure 7.

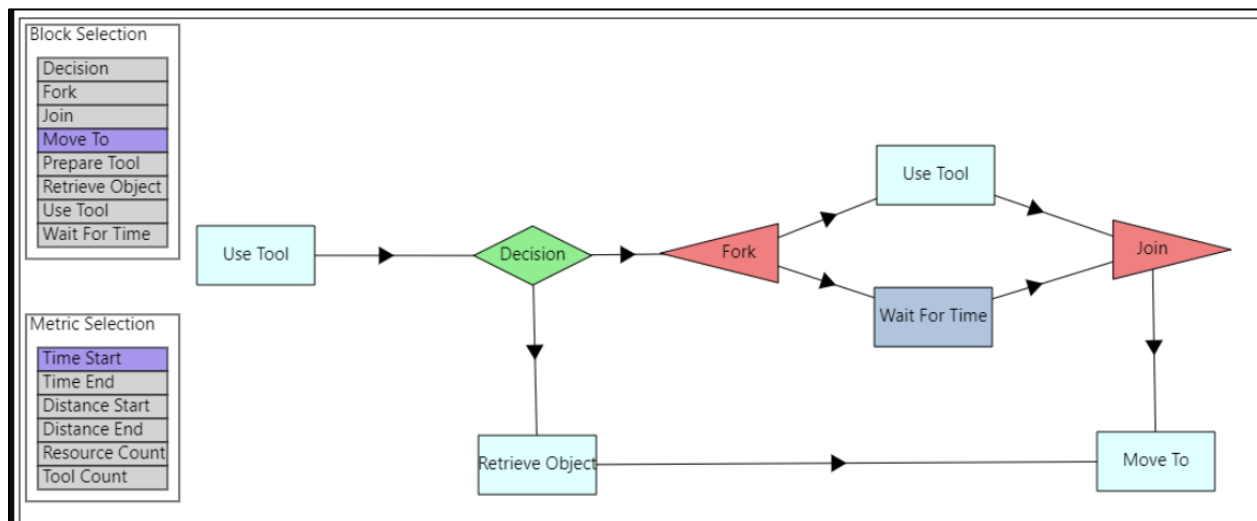


Figure 7: Flowchart Editor

Finally, If the user wants to see the output file to the Simulation, the tab that is labeled Text View. This has a specified outline to it so that the simulation can read the input. The user may not edit the file but may change the parameters in the above tabs to change parameters. The file will be able to be saved for future reference.

## 6 SIMULATION

The Simulation Tool's main purpose is to generate raw data necessary to calculate metrics for dynamic performance measures. The raw data is then saved in output files to be accessed by the Output Analysis Tool. To accomplish this, it takes the responsibility of running through the user-defined process flow. The Simulation Tool can take in any user-defined process flow with the use of blocks representing generic actions.

### 6.1 Simulation Representation of the Process Flow

Within the Simulation Tool exists a Process Builder. This Process Builder utilizes a file parser that can read in the generated file from the Input Editor. The file parser uses the information to provide the Process Builder to construct a system state for the process flow as well as construct a software representation of the process flow (Figure 8).

The information read in from the generated file contains information necessary for the system state and the process flow (Figure 9). Information for the system state consists of:

- Conditions and their probabilities;
- Consumable resources;
- Reusable tools;
- Workstation and habitat information; and
- Actor information.

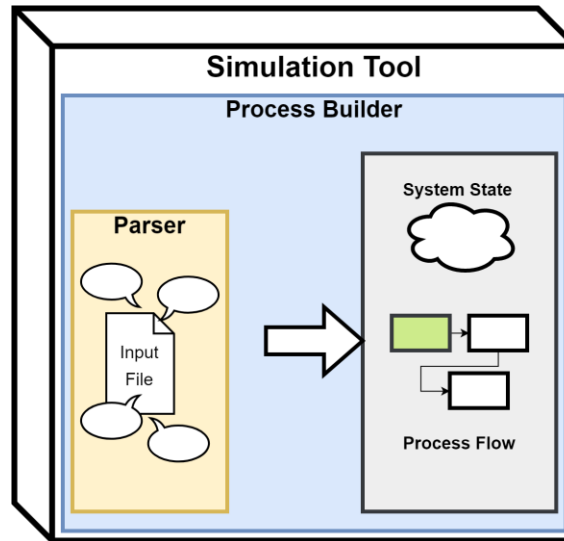


Figure 8: Simulation Tool Process Builder

Conditions are circumstances in the system that may lead necessary actions if they occur. An example condition is the presence of fluid in the patient's lungs. The information taken in for a condition is its name and its chance of occurring – a probability. The chances of conditions occurring are predefined as probabilities between zero and one. Within a workstation exists a set of items that can be used for medical procedures. These items are divided into two groups: Resources and Tools. Resources are consumable. They are items that are disposable and cannot be reused. This covers anesthetic fluid or bandages. Information read from the generated file consist of the resource's name, the resource's position, and its initial amount. Tools are reusable items that can be utilized multiple times. Tools have names, positions, and counts of their usage. Workstation and habitat information is used as a reference for the location and dimensions of the workstation and habitat. Actor information covers the positions, names, and velocities of actors. These actors are individuals acting within the workstation and are divided into two groups: Caregivers and Patients. The Caregiver carries out the actions in the defined in the process flow while the Patient is acted upon by one or more Caregivers.

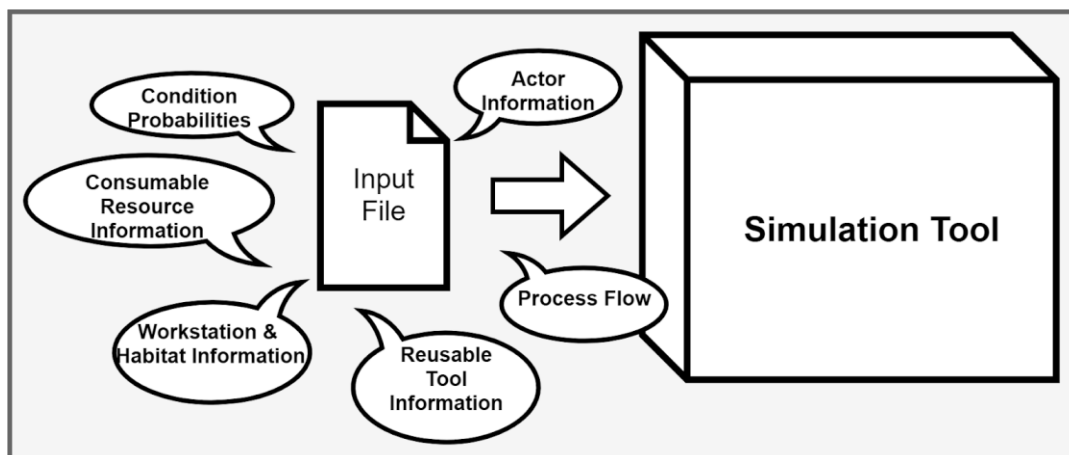


Figure 9: Information from Generated File

The Process Builder's file parser uses the Input Editor's generated file to create a software representation of the Process Flow. The software representation consists of coded logic representing the linked blocks. These blocks access the information of the system state upon activation and carry out their internal functionality. Certain blocks represent activities that involve time passing and modification of portions of the

system state. These blocks are: Move To, Prepare, Retrieve, Use Tool, and Wait For blocks. These causes are “events.”

**Definition 3.** *An event is the cause of instantaneous changes of the system under study and/or schedule future events.*

## 6.2 Events and the Concept of Time

To handle events and the concept of time, the Simulation Tool is divided into two bodies: The Model and the Simulation Executive (Figure 10). The model, a.k.a. “the Tracker”, is the combination of the system state and the Process Flow constructed by the Process Builder. It tracks the activation of blocks within the Process Flow. The model contains the code for block logic as well as the implementation of events. It interacts with the Simulation Executive by providing it defined events that are ready to be scheduled. On the other hand, the Simulation Executive acts as “the Manager” in the sense that it is solely responsible for scheduling and executing events as well as managing the advancement of time. It contains an Event Set which consists of events sorted in ascending order, the simulation’s current time, and an interface to be interacted with by the Model.

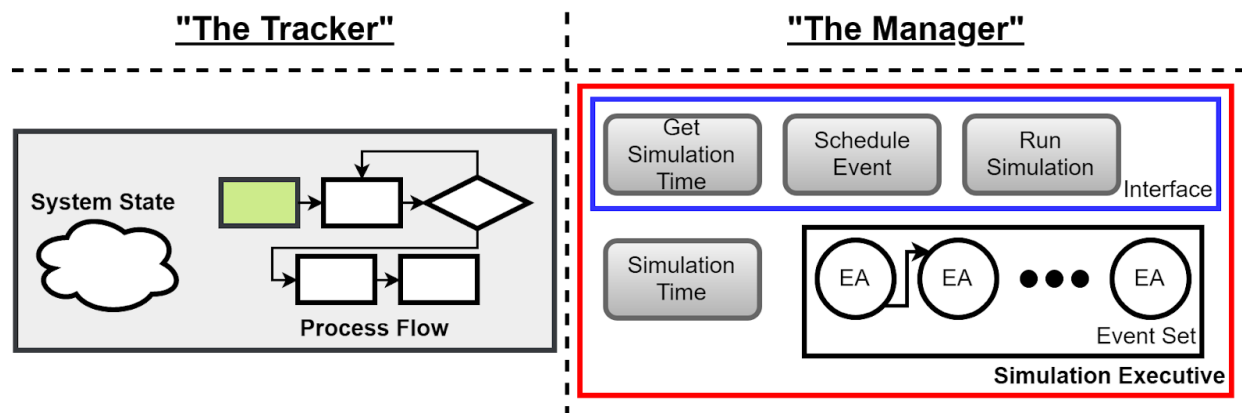


Figure 10: The Model (“The Tracker”) and the Simulation Executive (“The Manager”)

The Simulation Executive interacts with the Model by accepting events and placing them in time-stamped order into the Event Set (Figure 11, left). This is done when the Model wishes to schedule an event through the interface.

**Definition 4.** *“Time-stamped order” refers to ordering events in ascending order of the time that they are to be executed. An event to occur before the current simulation time cannot be executed.*

The Simulation Executive executes events in time-stamped order (Figure 11, right). When this occurs, the event is popped off the beginning of the Event Set and the Simulation Executive advances the simulation time to the time-stamp of the executing event. The event is then executed, allowing it to modify the state of the system.

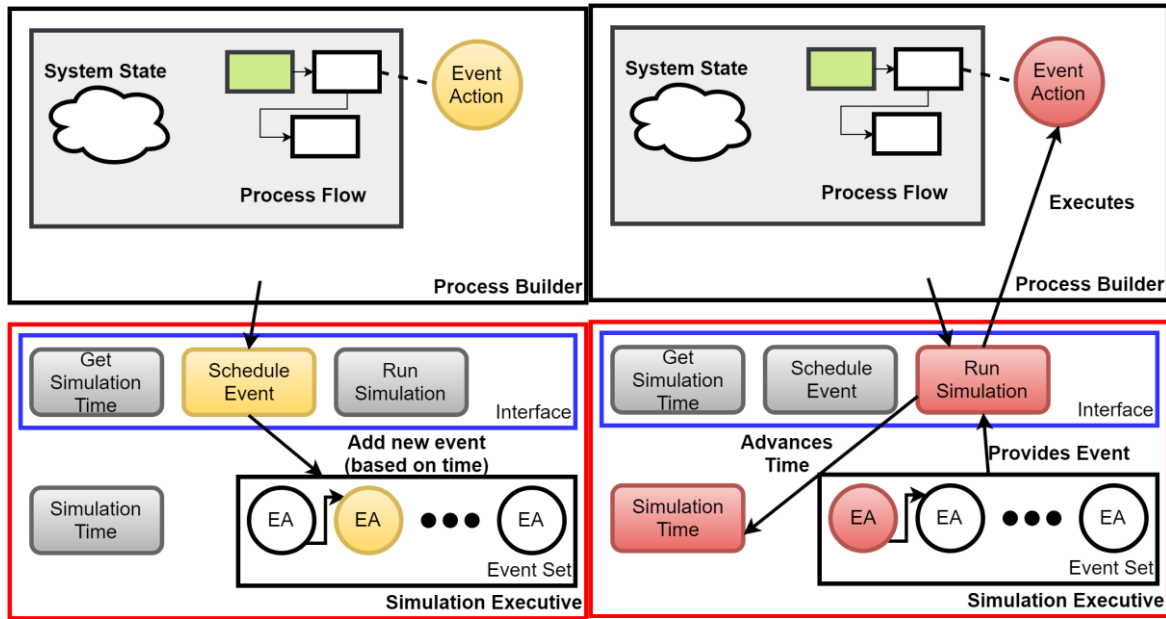


Figure 11: The Scheduling and Execution of Events

To allow the Model to see what the current simulation time is, the Simulation Executive contains a method to get the current simulation time which accesses its variable of the simulation time.

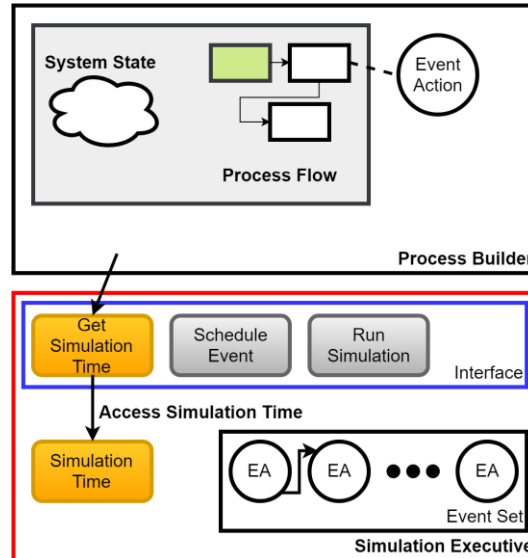


Figure 12: The Scheduling and Execution of Events

### 6.3 Generating Raw Output

The Simulation Tool has the functionality to walk through a Process Flow multiple times for a workstation.

**Definition 5.** These “walkthroughs” of the behavior within a Process Flow are referred to as runs.

Each run starts with the same system state. To introduce randomness between raw output, stochastic time distributions are used by the blocks to generate sample points. When one run has been completed, only one sample point is taken from a time distribution. However, when multiple runs are completed, multiple



sample points are taken. This allows the creation of confidence intervals when generating the values for metrics.

The information generated by the simulation fall under three categories:

1. Time-stamped events;
2. Record Block Output; and,
3. Constraint Violations.

Time-stamped event information covers the current simulation time, the current run number, the name of the process, and the entire system state. Time-stamped event information is generated and saved in a dedicated output file for that given run after the execution of an event. This information can be used by NASA to create visualizations and use each time-stamped event for a step in an animation. Record output files contain the information necessary to calculate metrics. The information covers the identifier of the type of Record block, the name of the target metric, the type of metric, the name of the target (e.g. a tool) where the information is gathered from, and the information needed for calculations. Constraint violations are detected when a system constraint has been violated during the simulation. There are different types of constraint violations: time, spatial, tool, and resource. For example, when a process has gone over a user-defined time limit, a time constraint has been violated. If a resource has been consumed entirely or if the required amount to be depleted is greater than the remaining amount, a resource-related constraint is violated. These time constraints are collected in a separate file for use by the Output Analysis Tool.

## **7 OUTPUT ANALYSIS**

The overall goal of the simulation is to eliminate and or refine candidate workstation designs until there is a single design to be built and used. In support of this effort, a specialized tool to view simulation output has been designed and is being implemented. This Output Analysis tool has many functions.

1. It parses simulation output into human readable formats such as tables and graphs
2. It calculates performance metrics and performance statistical analysis
3. It facilitates the user grouping and weighting performance metrics to arrive at a final scenario score
4. It facilitates the user grouping and weighting scenario scores and static performance measures to arrive at a final design score

The Output Analysis tool consists of several modules that line up with the functions all contained within a single GUI wrapper. First is the Parsing module which allows the user to specify files containing simulation output consisting of raw time stamped events, once provided with these files the parser will move the information into a data structure that the analysis module will transform into data the other modules can use. The analysis module will from the raw data structure will create a data structure containing metric values and statistical analysis of those modules. The third module is the visualization module which reads the data structure produced by the analysis module and produces human-readable output, such as tables and various graphs. The GUI allows for the user to specify different table layouts and to generate graphs in multiple formats. The fourth module is the weighting and grouping interface. The final module is an exporter. Once performance metrics have been weighed and grouped for a scenario, the user will be able to save that information and import it when the same scenario is run on another workstation design preventing the work of weighting and grouping from having to be done twice. Once the user has the final scores for the scenarios and designs the user can compare the design scores and only investigate the properties of the high scoring designs. A user when investigating a design can use the output tool to look at performance metrics of individual runs for scenario allowing the user to find exactly how the differences of designs influence the ability to complete the scenarios.

## **8 CONCLUSION**

The Capstone Team is currently in the final stages of implementing its solution prototype for the problem. Performance measures and metrics are being iteratively improved upon and defined in more detail as the project nears completion. The three modular software components will be implemented to match their design specifications throughout the rest of March and April. The solution prototype is scheduled for completion and delivery to NASA around late April to early May 2018. The delivery of the prototype solution to NASA will include the entirety of the prototype software, detailed technical documentation for the solution and software, a user manual, and a final presentation. This project is also scheduled to be presented by the Capstone Team at MODSIM World 2018 and the ODU Engineering Department's first internal Capstone Conference.

## ACKNOWLEDGMENTS

The ODU Capstone Team would like to thank Dr. Kara Latorella of NASA, Dr. Roland Mielke, Dr. James Leathrum, and the entirety of the MSVSCC 2018 board and staff.

## AUTHOR BIOGRAPHIES

**J.P. ASIJA** is a research assistant in the Darden College of Education at ODU funded by the NSF GEODE grant. His email address is [jasij001@odu.edu](mailto:jasij001@odu.edu).

**BRIAN DILINILA** is currently an intern under Combat Direction Systems Activity Dam Neck representing NAVSEA and providing assistance to Joint Staff J7. His email address is [bdili002@odu.edu](mailto:bdili002@odu.edu).

**MINH DONG** is interested in game development and is currently working on a personal video game project. His email address is [mdong004@odu.edu](mailto:mdong004@odu.edu).

**MICHAEL POTEAT** is a research assistant at Old Dominion University working on computational recognition and segmentation of secondary structure elements embedded within a larger protein image. His email address is [mpote001@odu.edu](mailto:mpote001@odu.edu).

**JACOB RICHARDSON** is currently an intern at Jefferson Applied Research funded by the DOE as well as a tutor for the Modeling, Simulation, and Visualization Engineering department at ODU. His email address is [jrich087@odu.edu](mailto:jrich087@odu.edu).

**THOMAS TRACEY** is both a teaching assistant for Modeling and Simulation courses at ODU and a research assistant working on a graphical user interface used for assisting in the education of discrete event simulations. His research interests include discrete event modeling and simulation, continuous simulation, distributed systems and communication, machine learning, and artificial intelligence, particularly genetic algorithms for optimization. His email address is [ttrac005@odu.edu](mailto:ttrac005@odu.edu).

**JAKE WEBSTER** is focused on game development and has interests in mobile app and mobile game development. His email address is [jwebs001@odu.edu](mailto:jwebs001@odu.edu).

# Towards Deformable Cranium & Foramen Surface Model

Shrabani Ghosh, Dr. Michel Audette  
Modeling, Simulation & Engineering  
Old Dominion University  
1300 Engineering & Computational Sciences Building,  
Norfolk, VA 23529  
{sghos003,maudette}@odu.edu

## ABSTRACT

Recent development in segmentation on medical imaging has advanced medical diagnosis in a broader way. This project centers on the segmentation of the human skull. Human skull tissue has two parts: bones and foramina. There are numerous holes in which many nerves and blood vessels exit the skull. It is important to identify cranium and foramina in CT image for neurosurgical planning and operation. We have used image super resolution approach in order to enable a high-resolution skull and foramina model. The segmentation exploits a residual convolution neural network(CNN) model which reconstructs by interpolation high resolution 3D volumes from 2D image stacks for more accurate image analysis. We applied a surface extraction on 3D image to segment bones and holes of the cranium. This paper will introduce our approach to create a deformable surface model of foramina of the cranium.

**Keywords:** Cranial foramen, Contour model, Marching cubes, Simplex Mesh, Super-resolution.

## 1 INTRODUCTION

A foramen is an opening that allows passage of structures from one region to another. Human skull has 34 cranial foramina that transmit cranial nerves, blood vessels and other structures- these are collectively referred to as the cranial foramina. To prevent complications in skull base neurosurgery, the cranial foramen of the patient must be presented in the planning and patient specific simulation of the procedure.

## 2 METHODS

3D skull CT imaging enables accurate analysis of skull physiology. Using super-resolution approach that is based on a residual convolution neural network (CNN) model, a high resolution 3D image volumes from 2D image stacks has been reconstructed for more accurate image analysis[2]. This model allows the use of multiple input data acquired from different viewing plane for improved performance. We have dense sagittal, coronal and axial CT data. Dense images are subsampled along three axes, where each one is sparser than the original data along one axis. The synthesized axial, sagittal and coronal images and original cadaveric CT data is used to train the super-resolution reconstruction. The SR method recovers the missing information through the examples observed in training images.

Now the ambiguous super-resolution voxels in the image are labeled using the expert labeling segmented images of foramina. The foramina labeled image will be used to identify the boundary of the cranial foramina. Later, we will identify foramina surface using two-simplex deformable surface model[1].

### 3 RESULTS

In the result, Figure 1 is the 3D image generated from the super resolution reconstruction. Surface extraction has done for holes and bones on the 3D image. Figure 2 is surface extraction for bones and Figure 3 is for holes. But in that case all the holes are not extracted properly. The super resolution 3D image is labeled with expert labeled segmented images of foramina. Figure 4 is a segmented image of foramen magnum. It is labeled pixel by pixel in the super resolution slices of 3D image. Figure 5 is before the labeling and Figure 6 shows a slice of the 3D image after the labeling. After labeling with all the foramina and canals, we will do the surface extraction with multi-material 2-simplex surface.

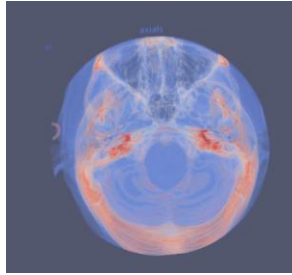


Figure 1: Reconstructed High Resolution Image

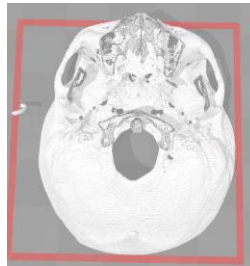


Figure 2: Surface Extraction in bone label

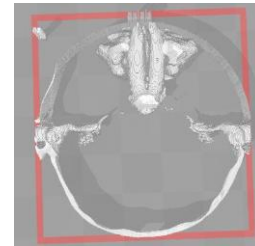


Figure 3: Surface Extraction in hole label



Figure 4: Segmented Magnum Foramen

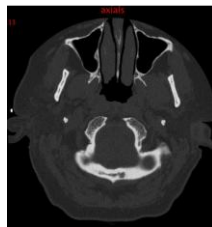


Figure 5: CT Image

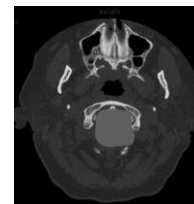


Figure 6: Expert Labeled with Magnum Foramen

### 4 CONCLUSION AND DISCUSSIONS

Our model will be able to differentiate the cranial nerves and holes in the skull. It will also be able to identify the endpoints of nerves. It will automate deformable 3D contour and surface model of segmented cranium nerves by giving the nerve endpoints information.

### REFERENCES

- [1] Rashid, T., et al. "Deformable Multi-material 2-Simplex Surface Mesh for Intraoperative MRI-Ready Surgery Planning and Simulation, with Deep-Brain Stimulation Applications." *Imaging for Patient-Customized Simulations and Systems for Point-of-Care Ultrasound*. Springer, Cham, 2017. 94-102.
- [2] Oktay, Ozan, et al. "Multi-input cardiac image super-resolution using convolutional neural networks." *International Conference on Medical Image Computing and Computer-Assisted Intervention*. Springer, Cham, 2016.

# **MODELING THE SOFT TISSUES OF THE LOWER BODY DURING A LANDING TASK**

Eric Jenkins, M.S.  
College of Health Sciences, Old Dominion University  
ejenk002@odu.edu

## **Abstract:**

Females are at an increased risk of ACL injury as compared to their male counterparts. Furthermore, females sustain noncontact ankle sprains at a higher incidence as compared to males. Previous research has investigated the relationship between taping/bracing at the ankle and its influence on the kinetic chain; however, there is not much evidence investigating the relationship of unilateral taping on bilateral lower extremity kinetics and kinematics. A purpose of this study is to utilize a 3D human body model to further elucidate the behavior of the lower body during a drop landing. Using human body modeling software, it is possible to delve deeper into the anatomy of the lower limbs. Initial results suggest higher ground reaction forces, with a shorter time to peak on the side of the taped limb. Bilateral ground reaction forces remained similar; however, the taped limb experienced higher forces when compared to the un-taped limb.

## **Introduction:**

Adolescent and young females are at an increased risk of ACL injury as compared to their male counterparts. Furthermore, females sustain noncontact ankle sprains at a higher incidence as compared to males. Previous research has investigated the relationship between taping/bracing at the ankle and its influence on the kinetic chain; however, there is not much evidence investigating the relationship of unilateral taping on bilateral lower extremity kinetics and kinematics. A purpose of this study is to utilize a 3D human body model to further elucidate the behavior of the lower body during a drop landing. Using OpenSim software (Stanford, CA, USA), it is possible to delve deeper into the functional anatomy of the lower limbs, including ligaments, bone, and muscle. From previous human cadaver research, we know the mechanical properties of soft tissue. This allows the implementation of that data into a modeling software whereby it is possible to simulate mechanical loading responses using a non-intrusive in-vivo research design.

## Methods:

Twenty participants were healthy, recreationally active females without a history of orthopedic injury to the lower limb. A lower body 3D model was utilized for kinematic assessments combined with two force plates for kinetic analysis of both limbs during the bilateral drop landing task from heights of 30, 45, and 60 cm. Participants were assessed on two occasions during the protocol one taped session and non-taped (control) session. The dominant ankle was taped to examine biomechanical effects on both the ipsilateral and contralateral limbs. Standard protocol for stepping off the platform asked participants to extend their dominant foot horizontally, before stepping off, without raising the body COM. Fifteen successful trials were gathered at each height under both control and taped conditions for a total of 90 total trials. Utilizing OpenSim software, the lower limbs were modeled with the anthropomorphic measures gathered from participants using previous research findings for inertial properties.

## Results:

Initial results suggest higher ground reaction forces, with a shorter time to peak on the side of the taped limb, combined with a reduced range of motion at the ankle. These effects were present at 45 and 60 cm heights, but not at 30 cm. Bilateral ground reaction forces remained similar; however, the taped limb experienced higher forces when compared to the un-taped limb. Higher peak knee moments were also observed on the taped limb. However, these effects are reduced after completion of the exercise protocol. The initial data indicates that taping the dominant ankle influences not only that ankle, but the rest of the kinetic chain ipsilaterally, as well as contralaterally.

# STUDENT CAPSTONE CONFERENCE

2018

## TRANSPORTATION, INFRASTRUCTURE SECURITY & MILITARY

- Page 133 Mahmud Hasan, Daniel Perez, Yuzhong Shyen and Hong Yang  
***Old Dominion University***  
Interactive M3 Visualization of Microscopic Traffic Simulation
- Page 135 Paulo O. Almeida, Andre J. Bergstein, Billingsley G. Pogue IV and Marisa Reyes  
***Westpoint Military Academy***  
Discrete Event Simulation and Analysis of the Planting Facility at the Corpus Christi Army Depot
- Page 144 Md Ariful Haque and Sachin Shetty  
***Old Dominion University***  
Analysis of Bulk Power System Resilience by Ranking Critical Nodes in the Vulnerability Graph
- Page 146 Zhenyu Wang and Hong Yang  
***Old Dominion University***  
Integrating Sensor Data for Identifying Secondary Crashes



# INTERACTIVE $M^3$ VISUALIZATION OF MICROSCOPIC TRAFFIC SIMULATION

Mahmud Hasan, Daniel Perez, Yuzhong Shen, Hong Yang  
Department of Modeling, Simulation & Visualization Engineering  
Old Dominion University  
Norfolk, VA

## ABSTRACT

Existing microscopic traffic simulation (MTS) models only provide limited visualizations that always restrict users' viewpoint to a flat screen. The downscaled scenes neither provide a realistic representation of the environment nor allow different users to simultaneously experience the simulation model from different perspectives. This largely prevent analysts from effectively demonstrating and disseminating their simulation results to various stakeholders of different background and knowledge. In light of these issues, this extended abstract develops a framework that enables **multi-user, multi-perspective, and multi-mode ( $M^3$ )** visualization architecture for MTS. A client-server architecture allows multiple users at distributed physical locations to view the same simulation from multiple perspectives simultaneously and supports a variety of virtual/augmented reality devices. A prototype of the proposed  $M^3$  visualization framework is implemented and demonstrated by simulating and visualizing a model of typical traffic operation in a high-density urban area.

**Keywords:** microscopic traffic simulation, virtual reality, augmented reality

## 1 INTRODUCTION

Microscopic traffic simulation (MTS) is the analysis of various traffic entities (e.g., vehicles, pedestrians, etc.) traveling through a virtual road network. MTS models are warranted because of their high accuracy and fidelity to actual traffic conditions. Traffic engineers generally use statistical analysis, animation and photo-montage to show the simulation output. However, it is often challenging for stakeholders with different backgrounds to easily perceive the stories and anticipate issues that may occur in each modeled scenario. Driven by the increasing need for illustrating complex scenarios for decision makings and public outreach, the main objective of this paper is to develop a framework that leverages recent development in cloud computing and virtual reality to advance the visualization of MTS. The proposed study distinguishes itself from traditional 2D and 3D implementations in the way that it provides a truly interactive, **multi-user, multi-perspective, and multi-mode ( $M^3$ )** visualization solution for MTS.

## 2 METHODOLOGY

Empowered by the latest advances in computer hardware, software, and networking, this study proposes a novel framework for interactive visualization of microscopic traffic simulations. The proposed framework offers a truly **multi-user, multi-perspective, and multi-mode ( $M^3$ )** visualization architecture for MTS. **M1**: “Multi-user” means that different model users (e.g., engineers, analysts) that intend to explore the simulation models. **M2**: “Multi-perspective” represents that these users can view the models in different roles (e.g., pedestrians and drivers). **M3**: “Multi-mode” denotes that the users can apply different types of devices to view the simulation model.

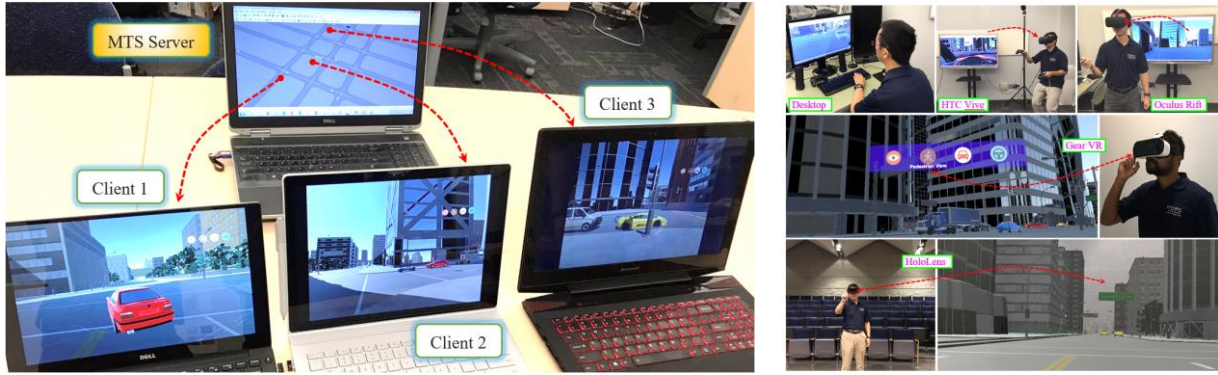
Different from existing MTS visualizations that run on the same computer as the MTS itself, the proposed  $M^3$  visualization framework employs a distributed architecture based on the client-server model where the MTS is the server and various visualizations are the clients. The server executes simulation as a service (SaaS) and at each simulation time step, sends the vehicle information (ID, position, speed, and bearing) and other traffic information such as traffic signals (IDs, location, and signal states) to the clients. The

clients present a realistic rendering of the 3D environment that contains the road network used by the MTS server and a graphical user interface (GUI) for users to interact with the visualization.

### 3 RESULTS

Figure 1 shows the prototype developed following the proposed  $M^3$  framework. It was built upon a hypothetical city model covering an area of 2.0 miles  $\times$  2.0 miles, with approximately 1,000 buildings, road network, and other facilities (e.g., bus stops, trees, signs, etc.) that typically present in an actual city. It should be emphasized that users can freely replace it by any city models of their interest. In this prototype, Paramics and Vissim have been used as the MTS server. To create virtual environment (VE) in the clients' end, Unity, one of the leading game engines, has been used.

To test the feasibility of the distributed client-server framework, each MTS model was turned into the MTS server by incorporating networking communications using TCP/IP protocols. Each virtual environment visualization client connects to the server using the server's domain name or IP address. The server does not need to know the clients' IP. Up to five clients in different networks were connected to the server in this prototype. Each user is offered the capability to explore the visualized environment from different perspectives. For the current prototype, four different perspective modes are supported, including Bird's-eye view, Pedestrian view, Car Follower view, and Driver view. To offer a multi-mode visualization, we adapted the visualization to VR and AR environments, which offer immersive views of the scene. The implementation of the scene in virtual reality was deployed in a HTC Vive, an Oculus Rift and a Gear VR with a Samsung Galaxy Note 4, while the Microsoft HoloLens headset was used to implement the scene in augmented reality.



(a) Distributed multi-user visualization.

(b) Multi-mode visualization.

**Figure 1: Developed prototype for  $M^3$  Visualization. Different users can visualize the scene in real time (a) with different devices (b). The simulation can be visualized from different perspectives.**

### 4 CONCLUSION

In this contribution, we presented a framework for enhanced visualization of MTS in a truly 3D virtual environment. The proposed  $M^3$  visualization framework was established by developing a distributed application structure that networks traditional microscopic traffic simulation models with different virtual/augmented reality platforms. The method was based on the mirror and enhancement of the key simulation components, including road network, vehicle trajectories, traffic control, etc., to create a more realistic 3D environment in 1:1 scale. A prototype that implemented the  $M^3$  visualization framework was developed and demonstrated. It used Paramics and Vissim as the server to test the multi-user, multi-perspective, and multi-mode visualization of a typical city traffic model.

# DISCRETE EVENT SIMULATION AND ANALYSIS OF THE PLATING FACILITY AT THE CORPUS CHRISTI ARMY DEPOT

Paulo O. Almeida  
Department of Systems Engineering  
United States Military Academy  
Building 606  
West Point, NY, USA  
[paulo.almeida@usma.edu](mailto:paulo.almeida@usma.edu)

Andre J. Bergstein  
Department of Systems Engineering  
United States Military Academy  
Building 606  
West Point, NY, USA  
[andre.bergstein@usma.edu](mailto:andre.bergstein@usma.edu)

Billingsley G. Pogue IV  
Department of Systems Engineering  
United States Military Academy  
Building 606  
West Point, NY, USA  
[billingsley.pogue@usma.edu](mailto:billingsley.pogue@usma.edu)

Marisa Reyes  
Department of Systems Engineering  
United States Military Academy  
Building 606  
West Point, NY, USA  
[marisa.reyes@usma.edu](mailto:marisa.reyes@usma.edu)

## ABSTRACT

The Corpus Christi Army Depot (CCAD) is one of the largest rotary wing repair facilities worldwide, performing essential maintenance for the U.S. military. The objective of this effort is to model the capacity of the CCAD Plating Shop to maximize productivity and efficiency. The Plating Shop is a vital entity in CCAD's repair process, with multiple implications for successful aircraft maintenance. We developed a discrete event simulation in ProModel™ that allows a user unfamiliar with the software to generate and analyze production scenarios via an Excel based user interface that measure throughput and utilization rates of the Plating Shop. These scenarios and their metrics allow CCAD to understand the capacity of the Plating Shop, identify bottlenecks, and make informed decisions to increase throughput and decrease cost. The model enables a crucial component in the U.S. defense industry to increase production and efficiency in its continuing efforts to support the American military.

**Keywords:** Corpus Christi Army Depot, discrete event simulation, ProModel™

## 1 INTRODUCTION

### 1.1 Background

“A [helicopter] fleet that was relatively young when the U.S. invaded Afghanistan has grown old, and thus needs to be renewed by either buying new helicopters or remanufacturing old ones to a like-new condition” (Thomas, Forbes). Regardless of how the Army decides to handle their aging helicopters, an organization that will surely be part of the solution is the Corpus Christi Army Depot (CCAD). Established in 1961, CCAD is one of the largest rotary wing repair facilities in the world, and is the Army’s leader in helicopter repair, maintenance, recapitalization, and overhaul capability. As the Army’s only organic avionic maintenance depot, CCAD receives helicopters from deployed and non-deployed units all over the world,

including foreign military operations (History of CCAD). Since inception, CCAD has processed approximately 13,000 aircraft, 72,000 engines and 1,400,000 components (Graves, 1999).

## 1.2 Plating and Shop Description

A major step in CCAD's helicopter repair process is the plating, or metal treatment, of helicopter parts. Benefits of plating the parts through different treatment recipes, such as chromium treatment, include "its inherent protective and decorative characteristics [...] resistance to tarnish, corrosion, wear and scratches" (Snyder). These features are important in helicopter part performance, improving safety of flight and preventing unplanned maintenance. Plating treatment occurs in CCAD's Plating Shop, a 126,000 square foot workspace that supports 18 processing lines with 25 metal finishing processes, depicted below in Figure 1. Since renovation completed on the Plating Shop in 1996, operator labor has been reduced by 20%, water consumption by 90%, and hazardous waste disposal by 90% (Keyport, 1994). Considered one of the most important processes within depot maintenance, CCAD believes improving efficiency within the Plating Shop will decrease maintenance processing time, maximize throughput, and optimize total performance of the facility.

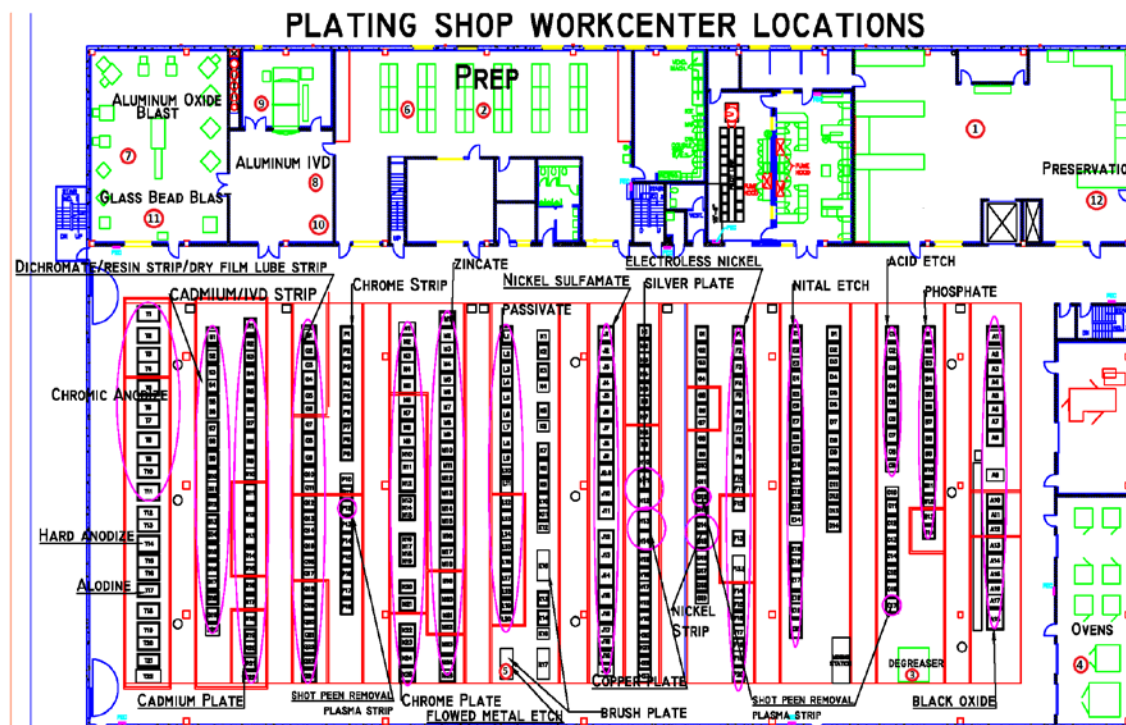


Figure 1. Plating Shop Layout

## 1.3 Problem Statement

The purpose of this effort is to model and analyze CCAD's Plating Shop capacity in order to identify facility capacity, prioritize resource allocation, and maximize shop productivity/efficiency.

## 2 METHODOLOGY

Efforts to improve and model the Plating Shop at CCAD were organized into a four-phase process. The methodology diagram can be seen below in Figure 2.

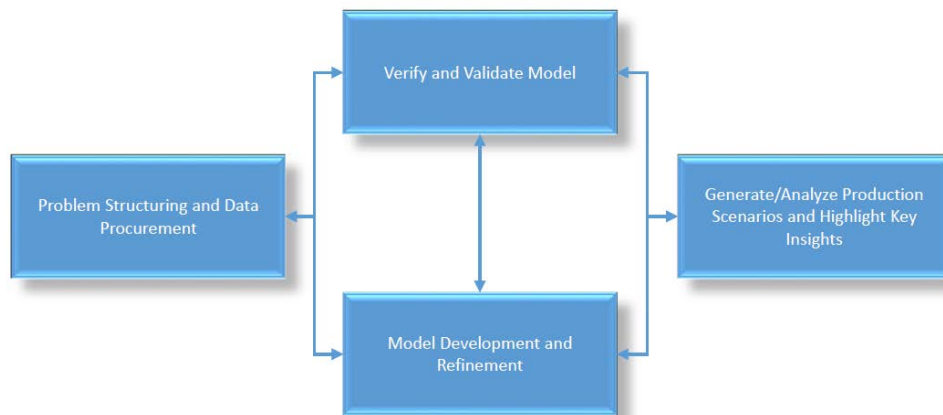


Figure 2: Methodology

As seen in the diagram, the first phase of the methodology is problem structuring and data procurement. To structure the problem stakeholder analysis was conducted to establish the scope, requirements, and end state of the project. An iterative data-collection process was utilized to generate process maps, understand business rules, and identify values such as batch sizes, processing times, etc.

The next two phases, verifying and validating the model and model development and refinement, occurred simultaneously and made up the duration of the project. The modeling strategy was to develop a single process line at a time and verify its accuracy. In two week intervals, we verified and validated the model as well as overall project progress with the stakeholders.

The final phase, generating/analyzing production scenarios and highlighting key insights, occurred once the model was in its end state. Scenarios were scored based on the results of the simulation and its subsequent outputs. These scenario results allowed the project team to analyze the scenarios and make a recommendation to the stakeholders on how to most effectively and efficiently operate the Plating Shop.

### 3 STAKEHOLDER IDENTIFICATION & ANALYSIS

#### 3.1 Stakeholder Identification

In order to understand the context and importance of the Plating Shop to larger organizations, stakeholders to the facility were identified and organized below in Figure 3.

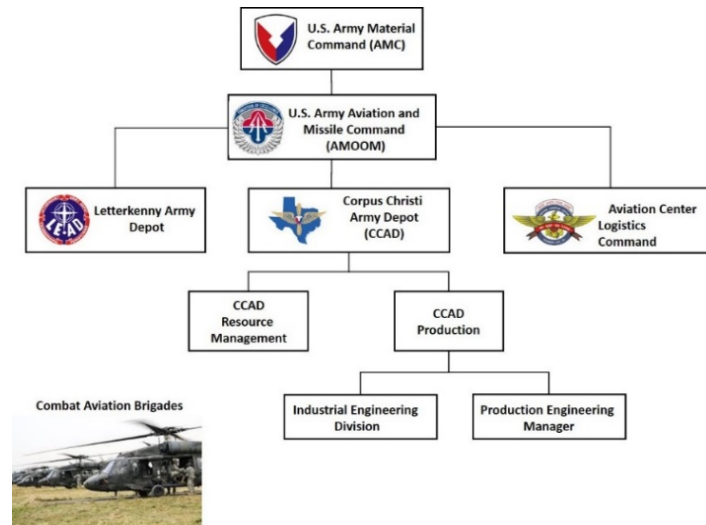


Figure 3: Stakeholder Identification

The following organizations are stakeholders in the Shop: Army Materiel Command (AMC), Aviation and Missile Command (AMCOM), the Corpus Christi Army Depot (CCAD), CCAD Resource Management, CCAD Production, CCAD Industrial Engineering, and Army Aviation Brigades (Delimarski et. al, 2017). AMC, one of the Army's three Major Commands, "develops and delivers materiel readiness solutions to ensure globally dominant land force capabilities" (Army Materiel Command). AMC is concerned with CCAD's Plating Shop because of the role it serves by providing the Army with combat ready aircraft. AMCOM is a subordinate organization of AMC that is concerned specifically with the readiness of aviation and missile materiel readiness of the Army. AMCOM's concern with the Plating Shop is nested within AMC's. CCAD as an organization focuses on returning aircraft and aircraft components to the Department of Defense and its various organizations cost and time effectively, while maintaining the highest quality. The three divisions from CCAD have the following interests in the Plating Shop:

- "Resource Management is responsible for providing financial and labor information to the depot, with the primary concern of how to develop innovative solutions while maintaining accountability and visibility of all resources" (Delimarski et. al, 2017).
- "CCAD Production orchestrates the efforts of global networks of organizations and manage programs coordinated to combat units. Their main concerns are managing their budget while producing aircraft for their representatives" (Delimarski et. al, 2017).
- "The Industrial Engineering Division is responsible for coordinating the different production lines within CCAD and ensuring their efficient operation" (Delimarski et. al, 2017).

Army Aviation Brigades are the stakeholders who utilize the aircraft and send their materiel (aircraft, engines, parts, etc.) to CCAD for overhaul and repair. Their primary concern is the operational readiness of their aircrafts in order to accomplish the mission.



### **3.2 Stakeholder Analysis**

To understand exactly what the stakeholders wanted from a model of the Plating Shop, we met with CCAD engineers in the Industrial Engineering Division. Through this communication, the following metrics were identified as essential outputs from the model: total part throughput, equipment utilization and worker utilization. Due to the complexity of the Plating Shop and time constraints, 3 of 18 process lines were modeled with the ability to add others at a later date. The three process lines modeled were those that receive the highest volume of parts: Aluminum IVD treatment, Cadmium treatment, and Chromium treatment. The structure of the additional 15 lines was included in the model, but not fully developed. The production scenarios for the model are entered in a user interface, developed in Microsoft Excel™, that allows a user to set the parameters of up to 15 unique production scenarios. The user interface was requested by the engineers at CCAD because it allows an individual with little or no experience with ProModel™ software to utilize the model. Examples of variables that can be adjusted in the user interface include number of workers, number of key stations available, batch sizes, material types, part size distribution, and key process station downtimes.

### **3.3 System Requirements**

Identifying requirements for a system is a critical step for systems design. Through synthesis and analysis of stakeholder input we were able to identify the fundamental requirements of the model. Below is a list of requirements that were identified as the most crucial for the model.

- The model shall replicate the work flow of the CCAD Plating Shop.
- The model shall be operable by a user with limited ProModel™ experience.
- The model shall have a Microsoft Excel™ user interface that passes appropriate inputs to ProModel™.
- The model shall allow user update of selected supporting data.
- The model shall depict selected outputs on a master scoreboard.
- The model shall have a Microsoft Excel™ module that retrieves appropriate output from ProModel™.
- The model shall have appropriate accompanying documentation.

## **4 LITERATURE REVIEW**

### **4.1 Theory of Constraints**

According to Kefeli and Uzsoy, a bottleneck, or constraint, can be defined as “the station to whose performance the performance of the overall production system is most sensitive” (2000). These bottlenecks become a limiting factor for a manufacturing process and limit the system’s ability to produce efficiently and effectively. There are likely many constraints that exist in the Plating Shop at CCAD; possible examples include unscheduled maintenance or equipment capacity. The Theory of Constraints, an idea first discussed by Eliyahu M. Goldratt, is based on the concept that a single constraint exists in any system and that system performance can only be improved when the constraint is improved (Goldratt). The five steps to the Theory of Constraints are to identify the constraint, exploit the constraint, subordinate and synchronize to the constraint, elevate performance of the constraint, and repeat the process as needed (Goldratt). By developing a discrete event simulation (DES) in ProModel™, we are able to identify possible constraints that we can recommend to CCAD for special attention and process improvement.

### **4.2 Simulation Modeling**

For the purposes of simulation, there are three major categories that serve different purposes: system dynamics, agent based simulation, and discrete event simulation. System dynamics has application to “urban, social, and ecological” systems and simulates of items such “material, people, and money”

(Borshchev). System dynamic simulation allows the modeler to model abstract systems and to determine how they perform over time. Agent based simulation is still a growing field, and the parameters of its applications are still being determined. The nature this simulation type, however, is to define a set of rules for a group of individuals and see how they interact with each other (Borshchev). Discrete event simulation involves moving entities such as people and objects “through the block of the flowchart where they stay in queues, are delayed, processed, seize and release resources, split, combined, etc.” (Borshchev). Discrete event simulation is highly applicable to manufacturing operations like the Plating Shop at CCAD, which moves parts from location to location, wait in queues and experience delays. The model developed to replicate the CCAD Plating Shop is a discrete event simulation.

A previous project team completed similar work that measured capacity for a Paint Shop that CCAD recently opened. In their model, the team created a user interface that allowed for the manipulation of variables such as the amount of helicopters, blades and containers, as well as the amount of artisans working in the Shop. Their model also provided the output of key metrics for analysis such as booth and artisan utilization, and total throughput of each item. Additionally, the physical movement of items in the Shop represented in the model, as well as statistical analysis enabled by ProModel™, allowed the team to identify bottlenecks in the Paint Shop.

For this project, we are using ProModel™ software to model the Plating Shop at CCAD. After considering the thousands of parts that receive chemical treatment at the Shop, the parts were simplified into three categories: small, medium and large sized parts. To further simplify the model, only 3 out of a total 18 lines are completely modeled: Aluminum IVD, Cadmium, and Chromium. These lines were chosen because they receive the highest volume of parts processed in the Shop. To lay the foundation for future work, we have developed process flows for the other 15 lines which are included in the model but not used for analysis at this time. By building this model and analyzing the results of the varying scenarios, CCAD will be able to see how the capacity of the shop changes, what potential bottlenecks exist, and determine what scenario provides the highest throughput, equipment and worker utilization, and equipment downtime.

### **4.3 Lean Six Sigma**

Lean Six Sigma is the combination of two different process improvement programs, Lean and Six Sigma. According to Rosa and Broday, “[t]he benefits of Lean Six Sigma in the industrial and service sectors [...] include: ensuring that services and products meet customer needs, removing waste from processes, reducing the cost of poor quality, reducing the incidence of defective products or services, reducing cycle time, and delivering the correct product or service at the right time and place” (Rosa). Lean Six Sigma is growing in popularity, primarily due to “global competition” which forces organizations to set themselves apart by focusing on “quality and customer[s]” (Rosa).

Through exposure to the principles of Lean Six Sigma, the team will be able to utilize its methodology in order to guide our actions toward improving the Plating Shop at CCAD. Lean Six Sigma will be useful in helping the team identify waste and bottlenecks in the system.

## **5 MODEL DEVELOPMENT**

### **5.1 Model Architecture**

To organize the model in a logical manner, we created a model architecture that depicts its components and how they are related. Within our model architecture, there are three main elements: a user interface spreadsheet, the base ProModel™ simulation, and a quantitative value model.

The user interface is a Microsoft Excel™ spreadsheet that allows the user to input selected production parameters for up to 15 unique scenarios. The parameters represent items in the Plating Shop such as number of workers, number of key process stations available, batch sizes, material types, part size distribution,



and key process station downtimes. The spreadsheet then acts as an input to the base model in ProModel™, which accepts the values and then when prompted by the user executes the simulation.

## 5.2 User Interface

The model user interface is displayed in Figure 4. The user interface is a Microsoft Excel worksheet within a larger workbook, directly tied into our ProModel™ simulation. All adjustments made within the user interface will populate into the ProModel™ simulation. The project utilizes the simplicity of Microsoft Excel™ to allow CCAD users to observe the effects of production requirements without having to be trained on ProModel™. Different rows within the user interface allow the user to specify production requirements for multiple production scenarios.

	A	B	C	D	E	F	G	H	I	J	K	L	M	N	O	P
1		Scenario 1	Scenario 2	Scenario 3	Scenario 4	Scenario 5	Scenario 6	Scenario 7	Scenario 8	Scenario 9	Scenario 10	Scenario 11	Scenario 12	Scenario 13	Scenario 14	Scenario 15
2		2	7	3	7	4	5	2	3	2	7	5	8	3	4	5
3	Oven 1	Open	Open	Open	Open	Open	Open	Open	Open	Open	Open	Open	Open	Open	Open	Open
4	Oven 2	Open	Open	Open	Open	Open	Open	Open	Open	Open	Open	Open	Open	Open	Open	Open
5	Oven 3	Closed	Open	Open	Open	Open	Open	Closed	Open	Closed	Open	Open	Open	Open	Open	Open
6	Oven 4	Open	Closed	Open	Open	Open	Open	Closed	Closed	Closed	Open	Open	Open	Closed	Open	Open
7	Oven 5	Closed	Open	Closed	Open	Closed	Open	Closed	Closed	Closed	Open	Open	Open	Closed	Closed	Open
8	Oven 6	Closed	Open	Closed	Open	Closed	Closed	Closed	Closed	Closed	Open	Closed	Open	Closed	Closed	Closed
9	Oven 7	Closed	Open	Closed	Open	Closed	Closed	Closed	Closed	Closed	Open	Closed	Open	Closed	Closed	Closed
10	Oven 8	Closed	Closed	Closed	Closed	Closed	Closed	Closed	Closed	Closed	Closed	Closed	Open	Closed	Closed	Closed
11																
12		3	3	3	3	3	3	3	3	3	3	3	3	3	3	3
13	Grit Blasting 1	Open	Open	Open	Open	Open	Open	Open	Open	Open	Open	Open	Open	Open	Open	Open
14	Grit Blasting 2	Open	Open	Open	Open	Open	Open	Open	Open	Open	Open	Open	Open	Open	Open	Open
15	Grit Blasting 3	Open	Open	Open	Open	Open	Open	Open	Open	Open	Open	Open	Open	Open	Open	Open
16	Grit Blasting 4	Closed	Closed	Closed	Closed	Closed	Closed	Closed	Closed	Closed	Closed	Closed	Closed	Closed	Closed	Closed
17	Grit Blasting 5	Closed	Closed	Closed	Closed	Closed	Closed	Closed	Closed	Closed	Closed	Closed	Closed	Closed	Closed	Closed
18	Grit Blasting 6	Closed	Closed	Closed	Closed	Closed	Closed	Closed	Closed	Closed	Closed	Closed	Closed	Closed	Closed	Closed
19	Grit Blasting 7	Closed	Closed	Closed	Closed	Closed	Closed	Closed	Closed	Closed	Closed	Closed	Closed	Closed	Closed	Closed
20																
21																
22		3	3	3	3	3	3	3	3	3	3	3	3	3	3	3
23	Glass Bead Blasting 1	Open	Open	Open	Open	Open	Open	Open	Open	Open	Open	Open	Open	Open	Open	Open
24	Glass Bead Blasting 2	Open	Open	Open	Open	Open	Open	Open	Open	Open	Open	Open	Open	Open	Open	Open
25	Glass Bead Blasting 3	Open	Open	Open	Open	Open	Open	Open	Open	Open	Open	Open	Open	Open	Open	Open
26	Glass Bead Blasting 4	Closed	Closed	Closed	Closed	Closed	Closed	Closed	Closed	Closed	Closed	Closed	Closed	Closed	Closed	Closed
27	Glass Bead Blasting 5	Closed	Closed	Closed	Closed	Closed	Closed	Closed	Closed	Closed	Closed	Closed	Closed	Closed	Closed	Closed
28																
29																
30	Small	0.50	0.30	0.30	0.30	0.30	0.30	0.30	0.30	0.30	0.30	0.30	0.30	0.30	0.30	0.30
31	Medium	0.25	0.30	0.30	0.30	0.30	0.30	0.30	0.30	0.30	0.30	0.30	0.30	0.30	0.30	0.30
32	Large	0.25	0.40	0.40	0.40	0.40	0.40	0.40	0.40	0.40	0.40	0.40	0.40	0.40	0.40	0.40
33																
34																
35	Batch Sizes															
36	Small	10	10	10	10	10	10	10	10	10	10	10	10	10	10	10
37	Medium	5	5	5	5	5	5	5	5	5	5	5	5	5	5	5
38	Large	2	2	2	2	2	2	2	2	2	2	2	2	2	2	2
39																
40	Quantity of Parts Input	8000	100	100	100	100	100	100	100	100	100	100	100	100	100	100
41																
42	Aluminum	100%	0%	0%	0%	0%	0%	0%	0%	0%	0%	0%	0%	0%	0%	0%
43	** % JUST Aluminum	35%	35%	35%	35%	35%	35%	35%	35%	35%	35%	35%	35%	35%	35%	35%
44	% with Cadmium Brush	50%	50%	50%	50%	50%	50%	50%	50%	50%	50%	50%	50%	50%	50%	50%
45	** % with Cadmium	30%	30%	30%	30%	30%	30%	30%	30%	30%	30%	30%	30%	30%	30%	30%
46	% with Cadmium Brush	33%	33%	33%	33%	33%	33%	33%	33%	33%	33%	33%	33%	33%	33%	33%
47	** % with Bare Metal	35%	35%	35%	35%	35%	35%	35%	35%	35%	35%	35%	35%	35%	35%	35%
48	% with Cadmium Brush	50%	50%	50%	50%	50%	50%	50%	50%	50%	50%	50%	50%	50%	50%	50%
49	Chromium	0%	0%	0%	0%	0%	0%	0%	0%	0%	0%	0%	0%	0%	0%	0%

Figure 4: Model User Interface

## 5.3 Base ProModel™ Simulation

The user can observe the simulation execute and observe how the parts physically move through the Plating Shop. Once the simulation is complete, the user can reference a scoreboard that highlights the number of batches of small, medium, and large parts plated as well as their associated material types. Additionally, ProModel™ has a results page which provides the user with information like throughput, line utilization by station, downtime, etc.

## 6 RESULTS AND ANALYSIS

Initial analysis of the model was performed in the model viewer, where a scoreboard displays the total number of parts batches processed by size category and by treatment (Aluminum IVD, Chromium, Cadmium). These values varied based on the variables in the user interface spreadsheet and by the time distributions coded into the model. Furthermore, once the model finishes the simulation an Excel file is generated that displays where parts traveled through the Plating Shop by locations and recipes. This file is

especially critical, because it allows the user to see how much time a part spends at different locations. With this information, bottlenecks can be identified for improvement. Finally, ProModel™ has a results page that provides the values for the key metrics.

Utilizing the log file, several bottlenecks were identified for the three treatments. Within the Aluminum treatment line, the Degreaser was the largest and most significant bottleneck. Other bottlenecks in the Aluminum line include the ion vapor deposition (IVD) chamber and the grit blast chamber. Within the Cadmium line, the largest bottleneck was again the degreaser; however, a dunk tank that comes later in the recipe acts like a bottleneck. Within the Chromium line, the largest bottleneck was again the degreaser. Additional steps that act like bottlenecks in the Chromium line are the grit blast chamber, one of the dunk tanks, and an oven.

Upon further analysis, the degreaser is a bottleneck in all of the lines for a couple of reasons. The first is that it only operates on parts in whole batches; therefore parts are queued while additional ones accumulate from the preparatory stage to start degreasing a batch. Secondly, the time it takes to degrease a batch takes significantly longer than any other step in each process. These two factors compound on each other to make the degreaser a legitimate bottleneck.

In order to mitigate the effects of the degreaser as a bottleneck, there are several steps CCAD can take. The first is to increase the batch sizes processed by the degreaser. This would allow more parts to move through the station at a time and prevent parts from being left in the queue. Another step is to reassign resources to the part preparation and degreaser locations. While the cooking time of the degreaser cannot be changed, the time spent preparing the parts to finish a full batch will prevent the parts from waiting to be degreased. Finally, scheduling downtimes around the degreaser, such as getting all the parts for a day through the degreaser and then shutting it down for maintenance would prevent the amount of times parts are waiting to be degreased.

## 7 CONCLUSIONS

The Plating Shop is a major focus for improvement in CCAD's aircraft repair process. This project provides a model that allows CCAD to analyze the results of multiple production scenarios within the Plating Shop's three most highly-trafficked metal-finishing processes. CCAD can immediately start analyzing production scenarios within the three processes to find bottlenecks, and identify key factors that increase productivity and decrease cost within the system. The model provides an invaluable service to CCAD personnel of all levels by allowing any user proficient in Microsoft Excel™ to alter specific production scenarios and observe each production result. The results of optimal production scenarios offer CCAD a framework for resource and equipment allocation to increase efficiency within the Plating Shop. CCAD has expressed the desire to potentially analyze all eighteen of the metal-finishing processes in the Plating Shop; this model offers CCAD the ability to build upon the existing framework to encompass all future analysis and production experimentation. This project delivers a living model, with detailed documentation, that CCAD will be able to continuously update based on the needs of the Plating Shop.

## REFERENCES

- Borshchev, A., & Filippov, A. (2004, July). From system dynamics and discrete event to practical agent based modeling: reasons, techniques, tools. In *Proceedings of the 22nd international conference of the system dynamics society* (Vol. 22). System Dynamics Society Oxford.
- Delimarski, P., Griffith, J., Howard, M., & McBryde, S. (2017). Discrete Event Simulation and Analysis of New ACCF. Technical Report prepared for the Corpus Christi Army Depot.
- Goldratt, E. (1999). *Theory of Constraints*. North River Press, Great.
- Graves, B. (1999, April 30). "Preparing for the Millennium." pfonline.com, accessed October 21, 2017. <https://www.pfonline.com/articles/preparing-for-the-millennium>.
- History of CCAD. <http://www.ccad.army.mil/history.html>.

- Kefeli, A., & Uzsoy, R. (2016). Identifying potential bottlenecks in production systems using dual prices from a mathematical programming model. *International Journal Of Production Research*, 54(7), 2000-2018. doi:10.1080/00207543.2015.1076182
- Keyport, W. (1994). Best Manufacturing Practices.
- Mission. Army Materiel Command. Accessed November 8, 2017. <http://www.amc.army.mil/>.
- Rosa, A., & Broday, E. (2018). Comparative Analysis Between the Industrial and Service Sectors: A Literature Review of the Improvements Obtained Through the Application of Lean Six Sigma. *International Journal For Quality Research*, Vol 12, Iss 1, Pp 227-252 (2018), (1), 227. doi:10.18421/IJQR12.01-13.
- Snyder, D. L. (2012). Decorative Chromium Plating Basics. *Metal Finishing*, 110(2), 14-21. doi:[https://doi.org/10.1016/S0026-0576\(13\)70110-7](https://doi.org/10.1016/S0026-0576(13)70110-7).
- Thompson, Loren. (2017, May 2). "Army Aviation Dodges a Bullet In Latest Budget Cliffhanger." <https://www.forbes.com/sites/lorenthompson/2017/05/02/army-aviation-dodges-a-bullet-in-latest-budget-cliffhanger/#5a0901d5db31>.

# ANALYSIS OF BULK POWER SYSTEM RESILIENCE BY RANKING CRITICAL NODES IN THE VULNERABILITY GRAPH

Md Ariful Haque, Sachin Shetty  
Dept. of Modeling, Simulation & Visualization Engineering  
Old Dominion University, Norfolk, VA 23529, USA  
mhaqu001@odu.edu

## ABSTRACT

This paper focuses on the ranking of the critical nodes in the network by constructing a vulnerability graph where the edges represent the vulnerabilities of the hosts. Ranking the critical nodes facilitates network administrator to concentrate on the security of the important hosts which are not possible to identify manually when the network size is large. We have used multi-stage directed acyclic graph model to generate the vulnerability graph and the MADM (multi-attribute decision making) method to rank the critical nodes in the network. The vulnerability graph is constructed keeping in mind the power system network and the node ranking is used to propose a systematic way to improve the cyber resilience of the bulk power system.

**Keywords:** Node ranking, Vulnerability graph, Cyber security, Bulk power system.

## 1 INTRODUCTION

Typical power grid network or substation network consists of thousands of hosts in the corporate and control subnetworks. The control network such as SCADA consists of the nodes to monitor the performance of the field location devices such as the programmable logic controller (PLC), remote terminal units (RTU) and intelligent electronic devices (IED). SCADA network performs the command and control through human-machine interface (HMI). On the other hand, corporate network hosts such as email servers and/or web servers are needed to keep the enterprise-wide business communications for smooth business operations. When the corporate network needs to communicate with the other business entities through some external communication media such as the internet, then the entire network is at risk of cyberattacks. In any network, an attacker needs to exploit multiple hosts sequentially before reaching a valued target. Typical cyberattack analysis consist of attack graph models where hosts are represented by system states and edges represent the transition between states. In the vulnerability graph nodes are hosts and edges directly represents the vulnerabilities that the host possesses. In this work, we have constructed vulnerability graph to analyze the sequential multi-step cyberattacks that can take place while exploring some valuable attack target. The nodes in the vulnerability graph are ranked using the relative criticality of those nodes respective to some valued target. The difference of this work from some other ranking is that it combines the effect of multiple vulnerabilities and their exploit and impact factors and severity rather than generating probability based on only exploitability factor.

## 2 METHODS

We have considered some of the factors that are important from cyber perspective to determine the relative criticality of the nodes in the vulnerability graph. The factors are asset value based on distance-based weight from the target node, the geodesic distance of the node from the target, CVSS (common vulnerability scoring system) exploit and impact metrics along with the severity level and degree centrality of those nodes in the graph. As we are applying the rank in bulk power system security analysis, so we have considered a

domain-specific physical impact factor which is the percentage of power outage possible by exploiting a target. Those factors are combined and a rank value is generated for each node which is compared to rank the critical nodes. To determine the rank value and comparison, we have applied MADM.

### 3 SIMULATION RESULTS

We have calculated the resilience of the target nodes using the method illustrated in (Shetty, Kamdem, Brijesh, & David, 2018) and used our ranking approach to compare the effects of using rank order and random order. It has found that the rank order of choosing the nodes reduces the cumulative simulation time almost half in a linear regression analysis when trying to improve the resilience of the particular BPS node.

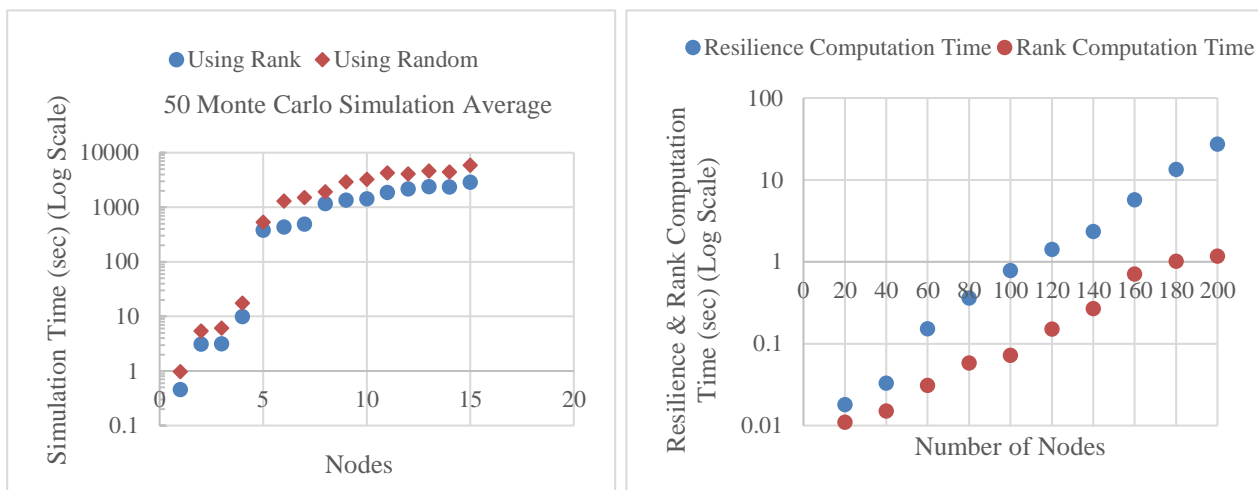


Figure 1: Comparison of simulation time (log scale) using random and ranked order of node selection (left) and comparison of resilience and rank computation time (right).

Sometimes, there may be questions regarding the time to compute the rank itself. The rank computation time is much less than the resilience computation time which is reflected in the above Figure 1 (right). This means that we can use the ranking method proposed here to find out the important nodes in the vulnerability graph respective to the power system network.

### 4 CONCLUSION

This work focuses on the ranking of critical network components or hosts using the vulnerability graph. By critical we mean the importance of the nodes from the cybersecurity perspective. The node ranking facilitates to identify the critical nodes in the network and thus, contributes to the improved security measure of the bulk power system network.

### ACKNOWLEDGEMENT

This paper is based upon work supported by the Department of Energy under Award Number DE-OE0000780.

### REFERENCES

Shetty, S., Kamdem, G., Brijesh, K., & David, N. (2018). *Cyber Resilience Metrics for Bulk Power System*, Risk Analysis Journal.

# PREDICTION OF TRAVEL MODE CHOICE BASED ON DEEP LEARNING

Zhenyu Wang

Dept. of Modelling, Simulation &  
Visualization Engineering, Old Dominion  
University  
Norfolk, VA 23529  
[zwang002@odu.edu](mailto:zwang002@odu.edu)

Hong Yang

Dept. of Modelling, Simulation &  
Visualization Engineering, Old Dominion  
University  
Norfolk, VA 23529  
[hyang@odu.edu](mailto:hyang@odu.edu)

## ABSTRACT

Travel mode choice prediction of individuals is important in planning new transportation projects. In this paper, we proposed to use an deep learning approach (convolutional neural network) for predicting travel mode of individuals. We examined the proposed approach's performance on two data sets such as the simulated data and Swiss Metro data. The results show that the deep learning approach can efficiently predict travel mode choice with relatively high accuracy rates. In addition, the impact of different variables is examined.

**Keywords:** Travel mode, deep learning, convolutional neural network

## 1 INTRODUCTION

Discrete choice modeling of travel behavior can help to estimate the proportion of competitive alternatives and hence the resulting travel demand and temporal distribution across different travel and activity patterns. Travel mode choice has received the most attention among discrete choice problems in travel behavior literature. However, unlike existing studies based on statistical models, researchers have attempted to use machine learning algorithms to account for the nonlinear relationship between factors such as income, gender, travel cost, etc and travel modes (walking, railway, motorcycle, and vehicle) of individual travelers. Data mining models have more flexible structures to represent the relationship between the attributes of alternatives and choices, and thus can learn and identify pattern characteristics extracted from sample data and form adaptive structures. Thus, the main objective of this study is to develop an deep learning approach to potentially offer insights to predict travel mode choice.

## 2 PROPOSED METHODOLOGY

Many existing studies sought to either parametric methods for predicting travel mode. However, various issues (e.g., weak model transferability and the inconsistency of model structures) have limited their applications. Alternatively, the deep learning approach is proposed in this paper to tackle the prediction issue. More specifically, the convolution neural network (CNN) is used. CNN is a deep learning approach that has been widely used in classification issues such as image classification and audio recognition. Lately, the applications of deep learning to address transportation issues such as the automated detection of ambulance in traffic videos are also emerging. Essentially, travel mode prediction is a classification problem. The versatility of the CNN makes it a suitable solution, especially when the causal relationship between a variety of contributing factors and the travel mode outcome is not clear. The CNN-based travel mode prediction structure is illustrated in Figure 1.

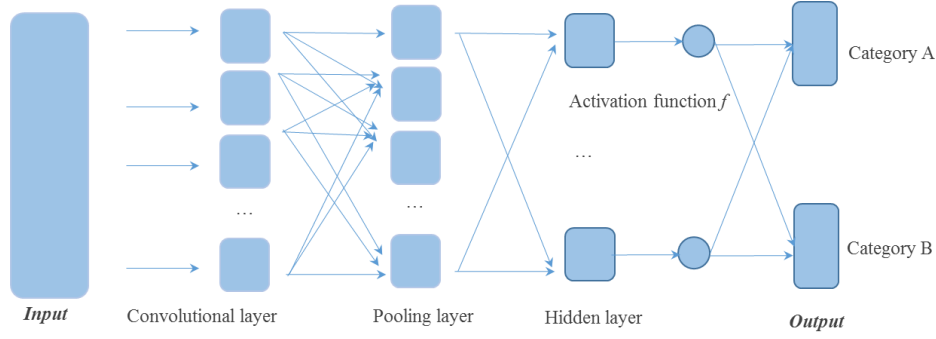


**Figure 1. Typical Modeling Structure of Convolutional Neural Networks.**

CNN is a neural network constituted by three types of layers: convolution layers, pooling layers, and hidden layers. The convolution layer takes a number of feature maps as input, and each neuron in the convolution layer does a convolution of the kernels with the lower layer activations. The output feature map  $X_n^{(i,j)}$  is represented as follows:

$$X_n^{(i,j)} = f(W_n^{(i,j)} \otimes X_{n-1}^{(i)} + b_n^{(i,j)}) \quad (1)$$

where,  $W_n^{(i,j)}$  is the weighted filters of layer  $n$ ;  $X_{n-1}^{(i)}$  is the output of layer  $n-1$  and serves as the input of layer  $n$ ;  $\otimes$  represents convolution operation;  $b_n$  denotes the bias for layer  $n$ ; and  $i = 1, 2, \dots, I$ ;  $j = 1, 2, \dots, J$ ;  $n = 1, 2, \dots, N$ . During the convolution, each neuron is connected to the patched subset of neurons in previous layer according to the following equation:

$$W_n^{(i,j)} \otimes X_{n-1}^{(i)} = \sum_{k=1}^K W_n^{(i,j,k)} \times X_{n-1}^{(i)} \quad (1)$$

where,  $k$  denotes the number of convolution patches.

After extracting the feature maps using the convolutional layer, a pooling layer is used to sub-sample the input from the convolution layer. Then, the hidden layer takes the sub-sampled output from the pooling layer and updates the weighting parameters in each layer to fit the model. Then the final output of the hidden layer is calculated. By normalizing the 2-dimensional output in layer  $N$ , the probability of a crash belonging to each category is calculated.

### 3 CASE STUDY AND RESULTS

Both simulated data in R and the case study data from Swiss Metro survey are used as the case study. Seven random normal distribution variables were linearly summed with the parameters of 0.14, 0.26, 0.21, 0.17, 0.15, 0.26 and 0.06. The multinomial travel mode data was simulated with three categories. Meanwhile, Swiss metro data consists of survey data collected on the trains between St. Gallen and Geneva, Switzerland, during March 1998 (<https://biogeme.epfl.ch/examples/swissmetro/swissmetro.pdf>). Variables include ticket, income, origin, and etc. Figure 2 shows the predictive performance of travel mode. The dotted line denotes the predictive accuracy of the baseline approach with all variables included, while the blue dots represent the predictive accuracy of models with relevant variable excluded.

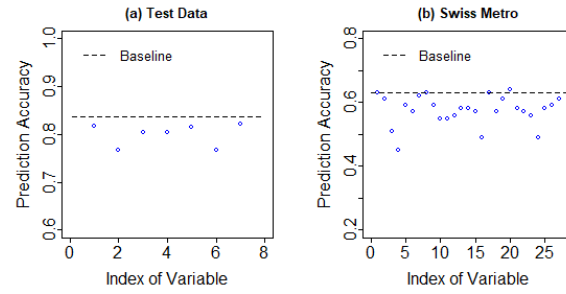


**Figure 2. Impact of Different Variables on the Prediction of Travel Modes**

#### 4 CONCLUSIONS

Our proposed approach can improve the predictive performance of travel mode. The CNN structure can better capture the nonlinear relationship between input variables and travel mode. The case study confirmed the efficiency and the performance of our proposed approach. It also should be noted that the exclude of certain variables can degrade the predicted performance.